

Performance Investigation and Enhancement of a Novel Oscillating Foil Based Building Integrated Wind Energy Harvesting System

Katrina Calautit

A thesis submitted in fulfilment of the requirements for the degree of

Doctor of Philosophy

Submitted to

Department of Mechanical and Aerospace Engineering

University of Strathclyde

April 2024

Declaration of authenticity and author's rights

This thesis is the result of the author's original research. It has been composed by the author and has not been previously submitted for examination which has led to the award of a degree.

The copyright of this thesis belongs to the author under the terms of the United Kingdom Copyright Acts as qualified by University of Strathclyde Regulation 3.50. Due acknowledgment must always be made of the use of any material contained in, or derived from, this thesis.

Signed: _____

Date: _____

Publications

Published journal papers

- Calautit, K., Johnstone, C., Investigation of the integration of an oscillating aerofoil energy harvester into the building roof structure. Energy Reports, 2024 <https://doi.org/10.1016/j.egy.2024.04.022>
- Calautit, K., Johnstone, C., State-of-the-art review of micro to small-scale wind energy harvesting technologies for building integration. Energy and Conversion Management: X, Vol, 20, 2023 <https://doi.org/10.1016/j.ecmx.2023.100457>
- Calautit, K., Mohammed, D., N., Hughes, B., R., Low energy harvesting systems: State of the art and future challenges. Renewable and Sustainable Energy Reviews, Vol., 147, 2021 <https://doi.org/10.1016/j.rser.2021.111230>
- Calautit, K., Aquino, A., Calautit, J., K., Nejat, P., Jomehzadeh, F., Hughes, B., R., A Review of Numerical Modelling of Multi-Scale. Computation. 6(1), 24, 2018 <https://doi.org/10.3390/computation6010024>

Conference papers

- Calautit, K., Johnstone, C., Evaluation of the impact of the aerofoil shape on the performance of an oscillating aerofoil energy harvester integrated into a building structure, 20th International Conference on Sustainable Energy Technologies, 2023.
- Calautit, K., Johnstone, C., A review on the state-of-the-art wind energy harvesting technologies and potential integration into building roof structure, 20th International Conference on Sustainable Energy Technologies, 2023.
- Calautit, K., Johnstone, C., A numerical CFD study on the integration and performance enhancement of oscillating aerofoil wind energy converters into buildings, uSIM Conference 2022.
- Calautit, K., Johnstone, C., Investigation of integrated design of oscillating

aerofoil energy harvester and roof building structure, 5TH SEE Conference on Sustainable Development of Energy, Water, and Environment Systems, 2022.

- Calautit, K., Johnstone, C., A review on small-scale building integrated-wind energy harvesting systems (BI-WEHS) for rural and decentralized communities, 5TH SEE Conference on Sustainable Development of Energy, Water, and Environment Systems, 2022.

Acknowledgements

Firstly, I would like to thank the Department of Mechanical and Aerospace Engineering Department at the University of Strathclyde for funding my Doctoral studies.

Thank you to my supervisor, Cameron Johnstone whose support and guidance have been instrumental in shaping my research career. His expertise, mentorship, and encouragement have not only contributed to my academic growth but have also played a significant role in moulding me into an experienced engineer. His belief in my abilities, coupled with invaluable insights and advice, have empowered me to navigate the complexities of research and academia with confidence and determination. I am profoundly grateful for his mentorship and support throughout my journey.

I also extend my sincere appreciation to our team in Energy Systems Research Unit (ESRU), including Song and Gavin, whose guidance and support have been invaluable throughout this journey. Their expertise, encouragement, and willingness to assist have greatly enriched my research experience and contributed to the success of my work. Moreover, I am grateful to my first year as PhD student colleagues in the research group, including Andrew, Diana, Hasan, and Sheen, for their collaboration and shared knowledge. Also, I would like to thank Ling, who generously shared her academic journey with me, providing support through challenges and attentively listening to my experiences as a student. Their friendship has made this journey both fulfilling and enriching, and I am thankful for their companionship along the way.

In addition, I would like to extend my heartfelt gratitude to my parents, Kaiser and Nida, whose support and guidance have been instrumental throughout my academic journey. From instilling a love for learning in my formative years to

providing invaluable encouragement and motivation during the challenging phases of my research, their belief in my abilities has been a constant source of strength. Their understanding and encouragement have played a vital role in shaping my academic and personal development.

Lastly, I would like to extend my appreciation to my brother, John, whose belief in my capabilities and support have been a constant source of inspiration. From the earliest stages of my academic journey, John has served as a role model, encouraging me to pursue excellence in all endeavours and providing invaluable guidance along the way. His confidence in my abilities and his encouragement to always strive for the best have motivated me to overcome challenges and achieve my goals. John's belief in me has been a driving force behind my academic and personal growth, and I am grateful for his support and encouragement.

Abstract

Integrating renewable energy into buildings enhances efficiency and reduces carbon footprints. Micro-wind turbines are promising but face challenges in low and turbulent wind conditions, especially in urban areas. Wind-induced vibration energy harvesters offer a solution. They enhance energy capture, reduce structural stress, and improve reliability by utilising wind-induced vibrations.

This thesis aims to investigate the feasibility and performance of integrating oscillating aerofoils into building structures for wind energy harvesting, addressing these challenges. The study introduces a novel building-integrated wind energy harvesting system comprising oscillating aerofoil and building roof structure. The study focuses on investigating the dynamic behaviour of oscillating aerofoil integration. Utilising Computational Fluid Dynamics (CFD) and a one-degree-of-freedom solver, it assesses the performance of an oscillating NACA 0012 aerofoil integrated into building roofs, serving as an alternative to traditional wind turbines. Validation of the CFD results was performed by comparing them with experimental data and previously published CFD studies. Comparisons were made for two scenarios: analysing the frequency of an oscillating aerofoil under pitch motion and examining airflow distribution within an atmospheric boundary layer velocity profile from a wind tunnel experiment detailed in the literature.

The results demonstrate that the optimal placement of oscillating aerofoils is crucial for maximising power output. For pitched and curved roof structures, the aerofoil should be positioned at the ridge or central mid-area with a spacing of 600 mm from the roof surface. On flat roofs, the edge on the windward side with at least 1000 mm spacing provides the highest mechanical power output. Moreover, the study shows that higher wind speeds correlate with increased mechanical power output that reaches 12

W at 9 m/s. However, the mechanical power output diminishes with changes in wind direction. Results also showed that the oscillating aerofoil integrated into a curved roof design yields the highest power output, with a significant increase of approximately 58% compared to a pitched roof.

In addition, a comparative analysis between NACA 0012 and SD7003 aerofoils integrated into roof buildings showed different results. The NACA 0012 aerofoil integrated into the curved roof achieved the highest mechanical power output, while the SD7003 aerofoil integrated into the pitched roof achieved a high mechanical power output. The investigation highlights the critical role of aerofoil and roof shape configuration and installation parameters in influencing system performance, providing practical insights for optimisation. Lastly, the aerofoil with a support arm achieved the highest power with 45 W output among the configurations, which is due to its high displacement and low frequency.

Advancing the study of building-integrated wind energy systems necessitates standardised experimental protocols and cross-disciplinary collaboration to enhance study comparability and system performance understanding. Future research should address sensitivity analyses of spring constants, the influence of adjacent structures, and the impact of turbulence and vortices. In addition, investigating various environmental case studies, implementing ducts for improved wind capture, and exploring aerofoil motion in both pitch and heave degrees of freedom will provide comprehensive insights. Lastly, focusing on transducers, power management, and energy storage will be crucial for developing efficient and sustainable self-charging power units.

Acronyms

AOA	Angle of attack
ABL	Atmospheric Boundary Layer
BIWT	Building Integrated Wind Turbine
BA-VAWT	Building Augmented Vertical-Axis Wind Turbine
CFD	Computational Fluid Dynamics
TSR	Tip-Speed Ratio
BEM	Blade-Element Momentum
HVAC	Heating, ventilation, and air conditioning
LED	Light-emitting diode
FSI	Fluid-structure interaction
WSN	Wireless Sensor Nodes
DOF	Degrees of Freedom
DOE	Design of Experiments
SIMPLE	Semi-Implicit Method for Pressure-Linked Equations
VPM	Vortex Particle Method
VIV	Vortex-Induced Vibration
CAWT	Cross-axis wind turbine
DAWT	Diffuser-Augmented Wind Turbine
VAWT	Vertical-Axis Wind Turbine
HAWT	Horizontal-Axis Wind Turbine

DWT	Ducted Wind Turbine
WLT	Wind Lens Turbine
VRGV	V-Shape Guide Vane
TENG	Triboelectric nanogenerator
EMS	Electromagnetic generators
MEMS	Micro electro-mechanical system
URANS	Unsteady Reynolds-averaged Navier-Stokes
ROMs	Reduced Order Models

Nomenclature

Symbols

U (m/s)	Velocity (metre per second)
P (Pa)	Pascal
g (m/s ²)	Gravitational acceleration
τ (N.m)	Torque
ω (rad/s)	Angular velocity
L (m/mm)	Length
F (N)	Force
f (Hz)	Frequency
t (s)	Time
kW	Power (kilowatt)
w	Power (watt)
W (kg)	Weight
mW	Power (milliwatt)
mW/cm	milliwatt per centimetre
μ W	Power (microwatt)
nW	Power (nanowatt)
k Ω	Electric resistance (kiloohm)

Ω Electric resistance (Ohm)

cm^3 Volume (Cubic centimetre)

V Electrical (Voltage)

N Force (Newton)

mm Length (Millimetre)

mJ Energy (Millijoule)

(x, y, z) Direction

Table of Contents

Publications	iii
Acknowledgements	v
Abstract	vii
Acronyms and Nomenclature	ix
Table of Contents	xiii
List of Figures	xx
List of Tables	xxxi
1.1 Introduction	1
1.1 Energy and climate change	1
1.2 Renewable energy in buildings	4
1.2.1 Solar energy.....	4
1.2.2. Wind Energy	5
1.3. Energy consumption in the built environment	6
1.4 Recent developments and global challenges on BIWT.....	7
1.5 Micro/small scale wind energy harvesting technologies challenges and advantages	9
1.5.1 Conventional wind turbines	9
1.5.2 Micro/small scale wind-induced vibration technologies.....	10
1.6 Urban and rural wind energy opportunities and challenges.....	11
1.7 Research questions	12

1.8 Research gaps and novelty	13
1.9 Research aim and objectives	15
1.10 Thesis structure	16
2 Literature Review	18
2.1 Methodology	18
2.2 Wind energy harvesting system for building integration	22
2.2.1.1 Horizontal-axis wind turbine (HAWT)	23
2.2.1.2 Vertical-axis wind turbine (VAWT)	28
2.2.1.3 Diffuser augmented wind turbine wind turbine	34
2.2.1.4 Other types of small-scale wind energy harvesting systems	38
2.2.2 Wind-induced vibration technologies	43
2.2.2.1. Galloping-type energy harvesting	44
2.2.2.2. Flutter-type low-energy harvesting	48
2.2.2.3 Vortex-induced vibration-type low-energy harvesting	52
2.3. Modelling methods for the evaluation and optimisation of wind energy harvesting systems	56
2.3.1 Wind resource assessment tool for wind energy harvesting systems technologies	56
2.3.2 Modelling of HAWT in building integration	59
2.3.3 Modelling of VAWT in building integration	61
2.3.4 Modelling of DAWT in building integration	63
2.3.5 Modelling of other configurations in building integration	65
2.3.6 Modelling of micro scale wind induced vibration technologies	67
2.3.7 CFD modelling of buildings and atmospheric boundary layer (ABL)	69
2.4 Recent developments with research methodology for dynamic mesh	79
2.5 Discussion	80
2.6 Summary	82
3.1 Research Methodology	84
3.1 CFD research methodology framework	85
3.2 Theory of CFD	87

3.2.1 CFD Equations	87
3.2.2 Transient modelling.....	89
3.2.3 Turbulence models	90
3.2.4 SIMPLE Algorithm	94
3.2.5 Residuals monitoring and convergence	95
3.3 Dynamic mesh.....	96
3.4 CFD geometry and domain	99
3.4.1 Aerofoil wind energy harvester – NACA 0012	100
3.4.2 Aerofoil wind energy harvester – SD7003	102
3.4.3 Building model	103
3.4.4 Building integrated wind energy harvesting system	104
3.5 Computational domain generation.....	105
3.6 Computational mesh and verification	107
3.6.1 Mesh generation for BI-WEHS model	108
3.6.2 Mesh sensitivity analysis	113
3.6.3 Time sensitivity analysis.....	116
3.7 CFD setup and boundary conditions.....	119
3.8 Solver methods and control.....	123
3.9 Computational method, analysis, and visualisation	123
3.9.1 Airflow characteristics and speed acceleration for isolated standalone NACA 0012 aerofoil	123
3.9.2 Airflow characteristics and speed acceleration for building roof structure	125
3.9.3 Atmospheric boundary layer velocity profile	126
3.10 Dynamic behaviour	128
3.10.1 Dynamic behaviour of the oscillating aerofoil energy harvester	128
3.10.2 Dynamic behaviour of the roof-integrated oscillating aerofoil energy harvester.....	131
3.10.2 Dynamic behaviour of the roof-integrated oscillating aerofoil energy harvester.....	131
3.10.3 Mechanical power output	132
3.10.4 Torque	134
3.10.5 Angular velocity	134

3.11 Summary of methodology	134
4 Model verification and validation	136
4.1 Structure of the verification/ calibration and validation	137
4.2 Verification and validation for aerodynamic characteristics	138
4.2.1 Lift coefficient	139
4.2.2 Drag coefficient	140
4.2.3 Effects of Reynolds number on lift and drag coefficient	140
4.2.4 Validation - Experimental and CFD set up	142
4.3 Validation for oscillating NACA 0012 aerofoil	147
4.3.1 Experimental and CFD set up for aerofoil	148
4.3.1 Experimental and CFD set up for aerofoil	150
4.3.2 Validation of the oscillating aerofoil frequency	150
4.4 Validation of the airflow around pitched, curved and flat roof building structure	151
4.4.1 Experimental and CFD set up for building roof structure.....	152
4.4.2 Validation of the airflow patterns for pitched, curved and flat roof building structure	156
4.5 Summary	159
5 Dynamic behaviour of BI-WEHS	161
5.1 Isolated standalone oscillating NACA 0012 aerofoil	162
5.1.1 CFD results for lift and drag forces	163
5.1.2 Torque and angular velocity of standalone oscillating NACA 0012	165
5.2 Evaluating the influence of building roof structures on accelerating wind flow	166
5.3 Building integrated wind energy harvesting system (BI-WEHS)	170
5.3.1 Velocity magnitude and static pressure distribution	170
5.3.1.1 Oscillating NACA 0012 aerofoil energy harvester on a flat roof building ..	170
5.3.1.2 Oscillating NACA 0012 aerofoil energy harvester on a pitched roof building	178
5.3.1.3 Oscillating NACA 0012 aerofoil energy harvester on a curved roof building	184
5.3.2 Velocity profile surrounding the aerofoil integrated into the flat, pitched,	

and roof building	189
5.3.3 Dynamic behaviour of the roof-integrated oscillating aerofoil energy harvester	191
5.3.3.1 Impact of wind speed	191
5.3.3.1.1 Aerofoil pitch angle	191
5.3.3.1.2 Torque and angular velocity of NACA 0012 integrated into the building roof	193
5.3.3.1.3 Effects on mechanical power output of NACA 0012 integrated into the building roof	196
5.4 Impact of wind directions	198
5.5 Impact of adjacent building	201
5.6 Case study for Basilan - Philippines	204
5.7 Power Spectral Density vs Frequency	206
5.8 Impact of SD7003 aerofoil shape on different roof configuration	209
5.8.1 Velocity magnitude and static pressure contours for SD7003 integrated into the flat roof at 3 m/s	211
5.8.2 Velocity magnitude and static pressure contours for SD7003 integrated into the flat roof at 6 m/s	213
5.8.3 Velocity magnitude and static pressure contours for SD7003 integrated into the flat roof at 9 m/s	215
5.8.4 Velocity magnitude and static pressure contours for SD7003 integrated into the pitched roof at 3 m/s	217
5.8.5 Velocity magnitude and static pressure contours for SD7003 integrated into the pitched roof at 6 m/s	219
5.8.6 Velocity magnitude and static pressure contours for SD7003 integrated into the pitched roof at 9 m/s	221
5.8.7 Velocity magnitude and static pressure contours for SD7003 integrated into the curved roof at 3 m/s	223
5.8.8 Velocity magnitude and static pressure contours for SD7003 integrated into the curved roof at 6 m/s	225
5.8.9 Velocity magnitude and static pressure contours for SD7003 integrated into the curved roof at 9 m/s	227
5.8.10 Torque and angular velocity of SD7003 aerofoil integrated into the	

building roof.....	229
5.8.11 Effects on mechanical power output of 1 m SD7003 integrated into the building roof.....	232
5.9 Comparison of NACA 0012 and SD7003 aerofoil shapes	234
5.9.1 Velocity magnitude contours for SD7003 and NACA 0012 aerofoil integrated into three roof shapes	235
5.9.2 Torque and angular velocity of NACA 0012 and SD7003.....	237
5.9.3 Effects on mechanical power output of NACA 0012 and SD7003 integrated into the building roof	240
5.10 Summary	242
6 Parametric analysis and impact on performance of BI-WEHS.....	244
6.1 Impact of oscillating aerofoil scale.....	245
6.1.2 Velocity magnitude and static pressure contours for 2 m NACA 0012	246
6.1.3 Velocity magnitude contours for 600 mm and 1000 mm 2 m SD7003	247
6.1.4 Torque and angular velocity of 2 m NACA 0012 and 2m SD7003	249
6.1.5 Effects on mechanical power output of 2m NACA 0012 and 2 m SD7003	252
6.2 Impact of placement on NACA 0012 performance.....	254
6.2.1 Velocity magnitude contours for 600 mm and 1000 mm NACA 0012	255
6.2.2 Torque and angular velocity of 600 mm and 1000 mm NACA 0012	257
6.2.3 Effects on mechanical power output of 600 mm and 1000 mm NACA 0012..	260
6.3 Impact of placement on SD7003 performance	261
6.3.1 Velocity magnitude contours for 600 mm and 1000 mm SD7003.....	262
6.3.2 Torque and angular velocity of 600 mm and 1000 mm SD7003	263
6.3.3 Effects on mechanical power output of 600 mm and 1000 mm SD7003	266
6.4 Impact of placement of NACA 0012 and SD7003 into the building roof.....	267
6.4.1 Torque and angular velocity of 1000 mm NACA 0012 and 1000 mm SD7003	268
6.4.2 Effects on mechanical power output of 1000 mm NACA 0012 and 1000 mm SD7003	272
6.5 Impact of support arm on oscillating aerofoil performance	274
6.5.1 Velocity magnitude contours for NACA 0012 with arm integrated into	

building roof.....	277
6.5.2 Torque and angular velocity of NACA 0012 with support arm	279
6.5.3 Effects on mechanical power output of NACA 0012 with support arm	282
6.6 Summary.....	283
6.7 Affirmations of research outputs.....	284
6.8 Research impact.....	289
7 Conclusion and Recommendations for Future Work	292
7.1 Conclusions	292
7.2 Recommendations for future works	293
7.3 Contributions to the knowledge.....	294
Bibliography	298
Appendices	296

List of Figures

1.1 Global energy-related greenhouse gas emissions, 2000-2022 [1].....	3
1.2 Schematic diagram of the oscillating NACA 0012 aerofoil integrated into the building roof structure [48].....	15
1.3 Overview of the thesis structure	17
2.1 The methodology framework for the review of micro/small-scale building integrated wind energy harvesting systems and wind-induced vibration technologies.....	19
2.2 Schematic diagrams of conventional small-scale wind turbines installed on the roof of a building (a) HAWT, (b) VAWT, and (c) DAWT	21
2.3 Schematic of Micro/Small-Scale Wind Energy Harvesters for Roof Building Integration: (a) flutter, (b) galloping, and (c) VIV.....	22
2.4 Wind turbine blades (a) design and schematic [62] of (b) HAWT installed into the building roof structure [64].....	23
2.5 Invelox (a) wind delivery system (b) computational domain of the installed HAWT inside the optimal Invelox [76].....	27
2.6 Principles of operation and rooftop wind turbines for buildings (a) Savonius [79] and (b) Darrieus [80-81]	29
2.7 Test configuration for cooling tower with VAWTs and enclosure by [89].....	34
2.8 Velocity contours of shroud and building test section in comparison with	

shroud case [93].....	36
2.9 (a) The velocity contour at the symmetry plane of the diffuser, (b) illustrates the velocity streamlines from a perspective view of the chosen building [94].....	37
2.10 CAWT (a) configuration and (b) CAWT on top of the building (c) CAWT CAD Model and (d) power coefficient plotted against the tip speed ratio for various pitch angles [96]	39
2.11 Comparison of the installation area between the (a) conventional BIWT and proposed system (b) structural aspect of the proposed system [63].....	40
2.12 VAWT with the VRGV (a) design and components (b) boundary condition and the domain size of the VAWT with the VRGV and (c) wind velocity contour distribution for the VRGV with pitch angle 19.5° [97].	41
2.13 Wind Booster (a) 3D model and fluid analysis [98]	42
2.14 Proposed design of galloping energy harvesting system (a) showing top and the side view and (b) experimental setup [101]	45
2.15 Design of the energy harvesting system based on galloping mechanism using cut corner prism [99]	46
2.16 Dimensions and schematic of the aeroelastic belt wind energy harvesting system prototype Aquino [105]	49
2.17 Schematic design of a piezo-electric energy harvesting system [108]	50
2.18 Maximum electrical power output obtained from the amplitude of plunge displacement was analysed and reported [111]	51
2.19 Actual image of (a) experimental setup (b) piezo-electric energy harvester in the circular flow arrangement [116].....	54
2.20 Vortex Bladeless (a) the configuration, (b) schematic design, and (c) VIV phenomenon in fluid dynamics [118]	55
2.21 CFD modelling of a) turbine-building at 13.5 m height streamlines	

b) turbine-building at 21 m height streamlines [126]	60
2.22 Wind turbine positioning. (a) most suitable wind energy exploitation systems for HAWT, VAWT, and DAWT (b) diffuser augmented wind turbine positioned at the upstream corner of the roof [134]	65
2.23 Graphical representation of (a) fitting the mean-velocity ABL log-law inlet profile to the wall function for mean velocity in the centre point P of the wall-adjacent cell, CFD simulation results for the streamwise gradients in the vertical profiles of (b) mean wind speed U; (c) turbulent kinetic energy k; (d) turbulence dissipation rate ϵ and (e) turbulence intensity [145]	72
3.1 CFD research methodology framework.....	85
3.2 CFD set up and process [159]	87
3.3 Monitoring of residuals	96
3.4 Sensitivity analyses of spring constant values for different parameters in (a) 3 m/s (b) 6 m/s, and 9 m/s wind speeds.....	99
3.5 Cl and Cd for NACA 0012 [171].....	101
3.6 Aerofoil centre of rotation	102
3.7 Reynolds number dependence on aerodynamic characteristics of SD7003 aerofoil (a) Cl, (b) Cd, (c) L/D [174]	103
3.8 3D pitched roof building structure [175].....	104
3.9 3D building integrated wind energy harvesting system [175].....	105
3.10 3D CFD model computational building and domain.....	107
3.11 Mesh of the (a) computational domain of the building with the oscillating 3D NACA 0012 aerofoil integrated into the pitched roof (b) 2D view of the mesh for BI-WEHS model (c) surface mesh around the oscillating aerofoil.....	111

3.12 Samples of results of mesh distribution at different positions of the aerofoil for dynamic mesh behaviour in different angles (a) 0 degree (b) 5 degrees (c) -10 degrees (d) 10 degrees	113
3.13 Mesh grid sensitivity analysis for the lift coefficient of NACA 0012 integrated into the (a) flat (b) pitched, and (c) curved roof building.....	116
3.14 Time sensitivity analysis for the lift coefficient of NACA 0012 installed into the (a) flat (b) pitched, and (c) curved roof structure.....	119
3.15 Velocity magnitude contour of NACA 0012 at 3 m/s with 0 angle of attack	125
3.16 Velocity magnitude contours of (a) flat (b) pitched (c) curved roof building....	126
3.17 Basilan Philippines (a) ABL velocity profile data imported to the CFD simulations using data from the [190] and (b) Map data: Google, Data SIO, NOAA, U.S. Navy, NGA, GEBCO, Maxar Technologies, Airbus [191] and (c) Map data: Google, Maxar Technologies, Data SIO, NOAA, U.S. Navy, NGA, GEBCO, TerraMetrics, Landsat / Copernicus [192].	127
4.1 A diagram of validation framework.....	137
4.2 Design of (a) NACA 0012 aerofoil profile [175] and (b) computational mesh and domain [171]	143
4.3 Aerodynamics characteristics – (a) C_l and (b) C_d – $Re=10,000$ and $Re=20,000$	145
4.4 Centre of rotation at $C=0.04$ centre and z axis [48]	147
4.5 Representation of the aeroelastic oscillating NACA0012 device in the wind tunnel [48]	149
4.6 Validation of (a) CFD results of frequency oscillation (b) plot diagram of frequency oscillation from the study of [10], (c) comparative analysis of current CFD results against experimental data from the research of [48]	151
4.7 3D CFD model of (a) pitched roof building with (b-c) mesh	

generation, (d) dimensions of computational domain and 3D model of (e) curved roof building with (f-g) mesh generation, (h) computational domain [21]	155
4.8 Set up of experimental model [198].....	156
4.9 Comparative analysis of CFD results, experimental data, and previous CFD results [21] for (a) curved and (b) pitched roof building, and averaged steam-wise velocity around the (c) curved and (d) pitched roof building	158
4.10 Comparative analysis of (a) experimental data, previous CFD results [198], and current CFD results for averaged steam-wise velocity around the flat roof building. The (b) velocity magnitude contours for the current CFD result	159
5.1 Diagram for (a) lift force, (b) drag force, and (c) lift-to-drag ratio under transient pitch oscillations in three different wind speeds	165
5.2 Isolated standalone NACA 0012 aerofoil in three different wind speeds	166
5.3 Wind speed acceleration velocity magnitude contours for flat roof at (a) 3 m/s (b) 6 m/s, (c) 9 m/s, pitched roof (d) 3 m/s, (e) 6 m/s, (f) 9 m/s, and (g) curved roof (h) 3 m/s, (i) 6 m/s, and (j) 9 m/s	169
5.4 Contours representing (a) velocity magnitude and (b) static pressure for an oscillating aerofoil with the NACA 0012 profile integrated into flat roof building at 3 m/s for time intervals of 0, 5, 20, and 30 seconds	174
5.5 Contours representing (a) velocity magnitude and (b) static pressure for an oscillating aerofoil with the NACA 0012 profile integrated into flat roof building at 6 m/s for time intervals of 0, 5, 20, and 30 seconds	176
5.6 Contours representing (a) velocity magnitude and (b) static pressure for an oscillating aerofoil with the NACA 0012 profile integrated into flat roof building at 9 m/s for time intervals of 0, 5, 20, and 30 seconds	178
5.7 Contours representing (a) velocity magnitude and (b) static pressure for an oscillating aerofoil with the NACA 0012 profile integrated into pitched	

roof building at 3 m/s for time intervals of 0, 5, 20, and 30 seconds	180
5.8. Contours representing (a) velocity magnitude and (b) static pressure for an oscillating aerofoil with the NACA 0012 profile integrated into pitched roof building at 6 m/s for time intervals of 0, 5, 20, and 30 seconds	182
5.9 Contours representing (a) velocity magnitude and (b) static pressure for an oscillating aerofoil with the NACA 0012 profile integrated into pitched roof building at 9 m/s for time intervals of 0, 5, 20, and 30 seconds	183
5.10 Contours representing (a) velocity magnitude and (b) static pressure for an oscillating aerofoil with the NACA 0012 profile integrated into curved roof building at 3 m/s for time intervals of 0, 5, 20, and 30 seconds	185
5.11 Contours representing (a) velocity magnitude and (b) static pressure for an oscillating aerofoil with the NACA 0012 profile integrated into curved roof building at 6 m/s for time intervals of 0, 5, 20, and 30 seconds	187
5.12 Contours representing (a) velocity magnitude and (b) static pressure for an oscillating aerofoil with the NACA 0012 profile integrated into curved roof building at 9 m/s for time intervals of 0, 5, 20, and 30 seconds	188
5.13 Velocity profile located at the (a) leading edge (b) mid span of the aerofoil (c) velocity profile points location for the three design parameters	190
5.14 Comparison of pitch angle for an oscillating aerofoil with the NACA 0012 profile integrated into(a) flat, (b) pitched, and (c) curved roof building at 3 m/s, 6 m/s, and 9 m/s.....	193
5.15 Comparison of the torque between an oscillating aerofoil integrated into flat, pitched, and curved roof at (a) 3, (b) 6, and (c) 9 m/s	195
5.16 Comparison of the angular velocity between an oscillating aerofoil Integrated into flat, pitched, and curved roof at (a) 3, (b) 6, and (c) 9 m/s	196
5.17 Average power output for three different models at different (a) wind speeds and (b) wind directions	200

5.18 Velocity magnitude contours for adjacent building and (a) flat, (c) pitched, and (e) curved roof building and static pressure contours for (b) flat (d) pitched, and (f) curved roof building structure	203
5.19 Comparison of average predicted power output for a NACA 0012 airfoil integrated into two different roof shapes with and without the presence of an adjacent building.	204
5.20 Average predicted power output for 1 day wind data on January 1, 2021	205
5.21 Power Spectral Density vs Frequency NACA 0012 integrated into (a) flat, (b) pitched, and (c) curved roof building at 3 m/s, 6 m/s, and 9 m/s.....	209
5.22 3D model of (a) non-symmetrical SD7003 airfoil integrated into the (b) flat, (c) pitched, and (d) curved roof building	210
5.23 Contours representing (a) velocity magnitude and (b) static pressure for an oscillating airfoil with the SD7003 profile integrated into flat roof building at 3 m/s for time intervals of 0, 5, 20, and 30 seconds	212
5.24 Contours representing (a) velocity magnitude and (b) static pressure for an oscillating airfoil with the SD7003 profile integrated into flat roof building at 6 m/s for time intervals of 0, 5, 20, and 30 seconds	215
5.25 Contours representing (a) velocity magnitude and (b) static pressure for an oscillating airfoil with the SD7003 profile integrated into flat roof building at 9 m/s for time intervals of 0, 5, 20, and 30 seconds	217
5.26 Contours representing (a) velocity magnitude and (b) static pressure for an oscillating airfoil with the SD7003 profile integrated into pitched roof building at 3 m/s for time intervals of 0, 5, 20, and 30 seconds	219
5.27 Contours representing (a) velocity magnitude and (b) static pressure for an oscillating airfoil with the SD7003 profile integrated into pitched	

roof building at 6 m/s for time intervals of 0, 5, 20, and 30 seconds	221
5.28 Contours representing (a) velocity magnitude and (b) static pressure for an oscillating aerofoil with the SD7003 profile integrated into pitched roof building at 9 m/s for time intervals of 0, 5, 20, and 30 seconds	223
5.29 Contours representing (a) velocity magnitude and (b) static pressure for an oscillating aerofoil with the SD7003 profile integrated into curved roof building at 3 m/s for time intervals of 0, 5, 20, and 30 seconds	225
5.30 Contours representing (a) velocity magnitude and (b) static pressure for an oscillating aerofoil with the SD7003 profile integrated into curved roof building at 6 m/s for time intervals of 0, 5, 20, and 30 seconds	226
5.31 Contours representing (a) velocity magnitude and (b) static pressure for an oscillating aerofoil with the SD7003 profile integrated into curved roof building at 9 m/s for time intervals of 0, 5, 20, and 30 seconds	228
5.32 Comparison of the torque between an oscillating SD7003 aerofoil integrated into flat, pitched, and curved roof at (a) 3 m/s, (b) 6 m/s, (c) 9 m/s with a distance of 600 mm and angular velocity at (d) 3 m/s, (e) 6 m/s, (f) 9 m/s with a distance of 600 mm	232
5.33 Average power output for the investigated 6 different parameters	234
5.34 SD7003 aerofoil integrated into (a) flat, (c) pitched, and (e) curved roof shapes at a distance of 600 mm and NACA 0012 aerofoil integrated into (b) flat, (d) pitched, and (f) curved roof shapes at a distance of 600 mm	237
5.35 Comparison of the torque between an oscillating NACA 0012 and	

SD7003 aerofoil integrated into (a) flat, (b) pitched, (c) curved roof with a distance of 600 mm and angular velocity for oscillating NACA 0012 and SD7003 aerofoil integrated into (d) flat, (e) pitched, (f) curved roof with a distance of 600 mm	240
5.35 Average power output for the investigated 6 different parameters	241
6.1 Velocity magnitude contours for 2 metres NACA 0012 with 600 mm distance between (a) flat and (c) pitched, (e) curved roof and 1000 mm distance between the aerofoil and (b) flat, (d) pitched, and (f) curved roof building.....	247
6.2 Velocity magnitude contours for 2 metres SD7003 with 600 mm distance between the (a) flat, (c) pitched, (e) curved roof and the aerofoil integrated into the (b) flat, (d) pitched, and (f) curved roof building with 1000 mm distance	248
6.3 Comparison of the torque between an oscillating NACA 0012 and SD7003 aerofoils integrated into (a) flat, (b) pitched, (c) curved roof with a distance of 600 mm a and angular velocity for oscillating NACA 0012 aerofoil integrated into (d) flat, (e) pitched, (f) curved roof with a distance of 600 mm	252
6.4 Average power output for the investigated 6 different parameters.....	253
6.5 Velocity magnitude contours for oscillating NACA 0012 aerofoil integrated into (a) flat, (c) pitched, and (e) curved roof at 3 m/s with a distance of 600 mm and for oscillating NACA 0012 aerofoil integrated into (b) flat, (d) pitched, and (f) curved roof at 3 m/s with a distance of 1000 mm	256
6.6 Comparison of the torque between an oscillating NACA 0012 aerofoil integrated into (a) flat, (b) pitched, (c) curved roof with a distance of 600 mm and 1000 mm and angular velocity for oscillating NACA 0012 aerofoil integrated into (d) flat, (e) pitched, (f) curved roof with a	

distance of 600 mm and 1000 mm	260
6.7 Average power output for the investigated 6 different parameters.....	261
6.8 SD7003 non-symmetrical low Reynolds number aerofoil integrated into (a) flat, (c) pitched, and (e) curved roof shapes at a distance of 600 mm and integrated into (b) flat, (d) pitched, and (f) curved roof shapes at a distance of 1000 mm	263
6.9 Comparison of the torque between an oscillating NACA 0012 and SD7003 aerofoil integrated into (a) flat, (b) pitched, (c) curved roof and angular velocity for oscillating NACA 0012 and SD7003 aerofoil integrated into (d) flat, (e) pitched, (f) curved with a distance of 600 mm and 1000 mm.....	266
6.10 Average power output for the investigated 6 different parameters with 600 mm distance.....	267
6.11 Comparison of the torque between an oscillating 2 m NACA 0012 and 2 m SD7003 aerofoil integrated into (a) flat, (b) pitched, (c) curved roof with a distance of 1000 mm and angular velocity for oscillating 2 m NACA 0012 and 2 m SD7003 aerofoil integrated into (d) flat, (e) pitched, (f) curved roof with a distance of 1000 mm.....	271
6.12 Average power output for the investigated 6 different parameters	273
6.13 Schematic 3D model of the oscillating aerofoil with support arm integrated into the building roof structure.....	276
6.14 Velocity magnitude contours for oscillating NACA 0012 with support arm integrated into the (a) flat, (c) pitched, and (e) curved roof building with a distance of 600 mm and NACA 0012 with support arm integrated into the (b) flat, (d) pitched, and (f) curved roof building with a distance of 1000 mm and at 3 m/s inlet velocity.....	278
6.15 Comparison of the (a-c) torque and (d-f) angular velocity for the	

case of oscillating NACA 0012 aerofoil with support arm integrated with a distance of 600 mm and 1000 mm	282
6.16 Average power output for the investigated 6 different parameter	283
6.17 Wind Panel in (a) Wind tunnel tests and (b) application in an environment of the Wind Panel [210] (c) Streamlines and (d) velocity contours for Glasgow Airport case study [211]	291

List of Tables

1.1 Wind turbine size classifications [35-36]	10
2.1 Summary of reviewed technical characteristics for reviewed building integrated horizontal axis wind turbine	73
2.2 Summary of reviewed technical characteristics for building integrated vertical axis wind turbine	74
2.3 Summary of reviewed technical characteristics for reviewed building integrated diffuser augmented wind turbine	75
2.4 Summary of reviewed technical characteristics for galloping based wind induced vibration technologies	76
2.5 Summary of reviewed technical characteristics flutter based wind induced vibration technologies	77
2.6 Summary of reviewed technical characteristics VIV based wind induced vibration technologies	78
3.1 Parameters of the oscillating NACA 0012 aerofoil applied in the CFD simulations	102
3.2 Mesh size details for three parameters	111
3.3 Time steps sensitivity analysis	117
3.4 CFD model set up and boundary conditions	120
4.1 Summary of percentage difference of CFD results against experimental data for (a) C_l and (b) C_d at $Re=10,000$ and (b) $Re=20,000$	145
5.1 Wind speed acceleration percentage increase	168
5.2 Parameters and material properties of SD7003 aerofoil profile	210

5.3 Parameters and material properties of NACA 0012 and SD7003 aerofoil profile.....	235
6.1 Parameters and material properties of 2 m NACA 0012 and 2 m SD7003 with 600 mm distance between the aerofoil and rooftop.....	246
6.2 Parameters and material properties of SD7003 with 1000 mm and 600 mm distance	262
6.3 Parameters and material properties of 2 m NACA 0012 and 2m SD7003 with 1000 mm distance between the aerofoil and rooftop.....	268
6.4 Parameters and material properties of NACA 0012 aerofoil with support arm integrated into the flat, pitched, and curved roof building.....	276

Chapter 1

Introduction

This chapter will introduce the current challenges faced by the energy and building sector including the increasing demand for energy and climate change associated with fossil fuels that are expected to be an ongoing crisis for the next decades. The ongoing challenges and limitations faced by recent developments in building integrated wind energy harvesters will be discussed. The oscillating aerofoil wind energy harvester will be introduced, and its potential integration with buildings will be highlighted. Lastly, the aims and objectives will also be discussed in this chapter to provide an overview of the purpose of the research. Lastly, the thesis content and structure will be summarised.

1.1 Energy and climate change

Over the past few decades, it has been reported that most of the world's energy is generated by burning fossil fuels, such as coal, oil, and natural gas, which release carbon dioxide and other greenhouse gases into the atmosphere [1]. Over the past few decades, the predominant source of global energy has been derived from fossil fuels like coal, oil, and natural gas. These fuels are burned to generate electricity, power transportation, and fuel industrial processes. However, this reliance on fossil fuels has significant environmental consequences. When burned, they release carbon dioxide (CO₂) and other greenhouse gases into the atmosphere. These gases contribute to the greenhouse effect, trapping heat and leading to global warming and climate change.

The environmental impact of fossil fuel use extends beyond greenhouse gas emissions. Mining and drilling for these fuels can cause habitat destruction and water pollution. In addition, the extraction and transportation of fossil fuels can have significant environmental and social impacts, affecting ecosystems and communities. Efforts to address these issues include promoting renewable energy sources like solar, wind, and hydroelectric power, which produce energy without emitting greenhouse gases. Transitioning to renewable energy is seen as crucial for reducing carbon emissions, mitigating climate change, and creating a more sustainable energy future. As shown in Figure 1, the total greenhouse gas emissions related to energy increased by 1.0%, reaching an unprecedented high of 41.3 Gt CO₂-eq in the year 2022. Many of these emissions (89%) came from CO₂ released during energy combustion and industrial processes. Another 10% came from methane emissions resulting from energy combustion, leaks, and venting. The primary sources of methane emissions were onshore oil and gas operations and steam coal production. Despite the cost-effectiveness of methane abatement technologies due to high natural gas prices, methane emissions still rose to almost 135 Mt CH₄, equivalent to around 4 Gt CO₂-eq [1]. These issues translate into global warming and climate change. Global warming and climate change have a significant influence on the availability and distribution of energy resources. Extreme weather events, such as hurricanes and wildfires, can also damage energy infrastructure, leading to disruptions in energy supply [2]. According to [3], the energy sector is a significant contributor to greenhouse gas emissions. In the year 2018, the energy sector accounted for approximately 72% of global greenhouse gas emissions, with electricity and heat generation accounting for the largest share [3]. This report addresses climate change and requires a transition to a low-carbon energy system. This includes reducing greenhouse gas emissions from the energy sector using renewable energy sources, such as solar and wind, and increasing energy efficiency in buildings, transportation, and industry [3].

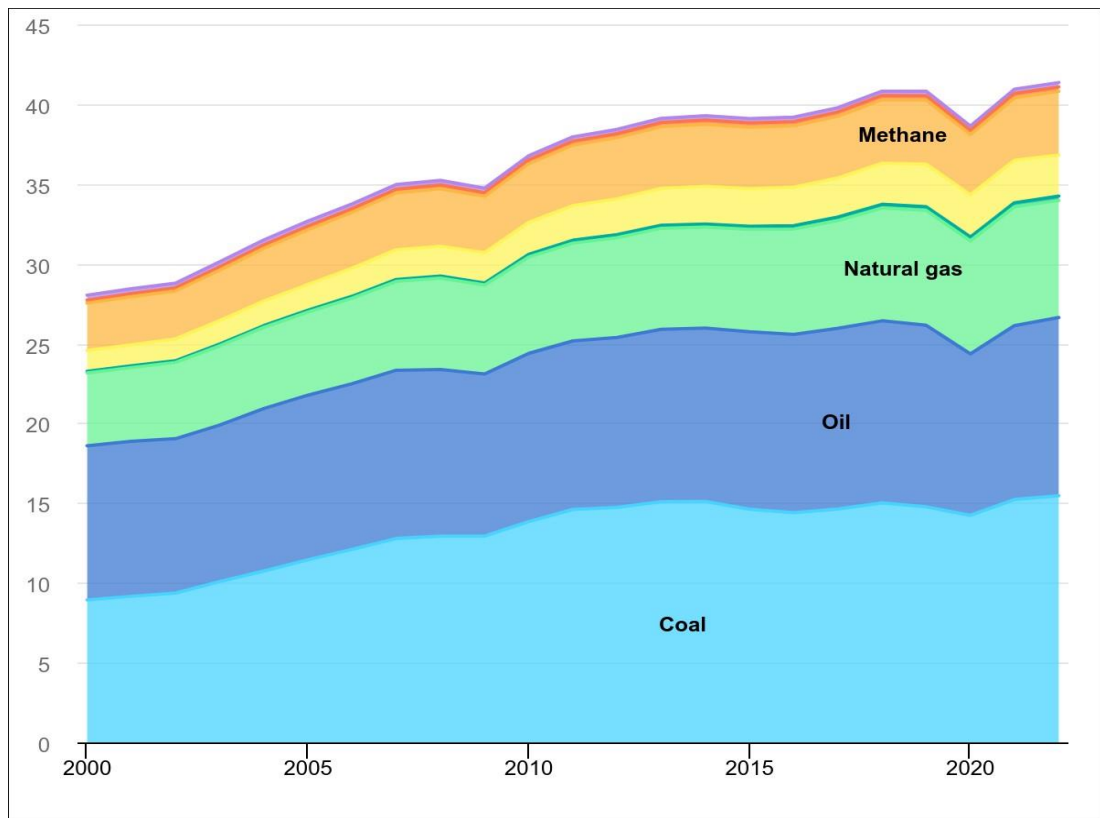


Figure 1. Global energy-related greenhouse gas emissions, 2000-2022 by IEA 2022; *CO2 Emissions in 2022*, <https://www.iea.org/reports/co2-emissions-in-2022>, License: CC BY 4.0; [1]

The Intergovernmental Panel on Climate Change (IPCC) reported in 2022 [4] that greenhouse gas (GHG) emissions, particularly carbon dioxide (CO₂), which accounts for about 80% of total GHG emissions have significantly contributed to climate change. Between 1970 and 2004, global GHG emissions increased by about 70%, a rise accompanied by a substantial increase in global energy consumption, which has grown by approximately 2.3% per year over the past decade. Despite renewable energy sources like hydropower, wind, and solar photovoltaics (PV) accounting for about 29% of global electricity production in 2020, fossil fuels still dominate, comprising about 84% of total energy consumption. This heavy reliance on fossil fuels has led to a global average temperature increase of about 1.1°C since the pre-industrial era, with projections indicating that the temperature could reach or exceed 1.5°C by around 2040-2050 [4]

To combat the effects of climate change, the Paris Agreement was adopted in 2015, aiming to limit global warming to well below 2°C above pre-industrial levels, with a concerted effort to cap the increase at 1.5°C. However, recent data shows that global temperatures have already reached 1.5°C above pre-industrial levels over the past 12 months. As of early 2024, reports from the Copernicus Climate Change Service (C3S) and the World Meteorological Organization (WMO) confirm that global temperatures have temporarily exceeded this critical threshold. January 2024, for example, was recorded as the warmest January on record, with temperatures 1.6°C above pre-industrial levels, driven by persistent GHG emissions and a strong El Niño event [4]

By June 2024, the global average temperature had risen even further, reaching 1.63°C above pre-industrial levels over the previous year. This period has witnessed a series of record-breaking monthly temperatures, primarily due to human-induced climate change and the ongoing effects of El Niño. These developments underscore the pressing need for more aggressive climate action, as the world is already experiencing temperature increases that the Paris Agreement sought to prevent.

Despite the adoption of the Paris Agreement, current pledges and actions by countries remain insufficient to achieve the goals set forth, emphasising the urgent need to transition to a low-carbon, sustainable, and resilient energy system. The continued over-reliance on fossil fuels and the insufficient implementation of renewable energy solutions are major barriers to mitigating the effects of climate change, making it clear that more immediate and substantial efforts are required to avoid further temperature rises and the accompanying environmental impacts.

1.2 Renewable energy in buildings

Renewable energy integration in buildings can provide substantial reductions in energy consumption and carbon emissions [5]. Through harnessing solar and wind, technologies, buildings can transition from conventional fossil fuel reliance to more sustainable and efficient energy sources.

1.2.1 Solar energy

Solar photovoltaic (PV) systems convert sunlight into electricity, which can power various building systems, thereby decreasing reliance on grid electricity. Moreover,

solar thermal systems can capture solar heat to provide domestic hot water and space heating, effectively reducing the need for conventional heating methods. Over the last few decades, solar panels have seen substantial improvements in efficiency and power output. In 2018, the efficiency of multi-crystalline PV panels reached 17%, while mono-crystalline panels achieved 18%. This positive trend is expected to continue through 2030 [6]. However, as the global PV market expands, there is an increasing need to address the degradation of panels and manage the volume of decommissioned PV panels, promoting circular economy practices. This involves developing innovative and alternative ways to reduce material use and mitigate module degradation, as well as exploring opportunities to reuse and recycle PV panels at the end of their lifecycle [6].

Despite its benefits, solar energy also has limitations. One major challenge is the intermittent nature of solar power, which depends on sunlight availability and weather conditions. This intermittency necessitates the integration of energy storage solutions or supplementary power sources to ensure a consistent energy supply. In addition, the initial cost of installing solar PV and thermal systems can be substantial, although long-term savings and incentives can help offset these expenses. The efficiency of solar PV systems remains relatively low compared to other solar energy technologies, with standard panels converting only about 15% to 22% of sunlight into usable electricity [7].

1.2.2. Wind Energy

Wind energy can contribute significantly to a building's energy needs using small-scale wind turbines. These turbines generate clean, renewable electricity by harnessing wind power, which can help reduce reliance on grid electricity and lower energy costs. Wind turbines typically operate with a practical efficiency ranging from 35% to 45%, while the theoretical maximum efficiency, known as the Betz limit, which is about 59.3%. This makes wind energy a potent option for buildings in areas with favourable wind conditions, offering a sustainable solution for electricity generation [8]. Nevertheless, wind energy also has its limitations. The generation of wind power is highly dependent on wind conditions, which can be variable and less predictable

compared to solar energy. This variability requires careful consideration of site-specific wind patterns and may necessitate backup power systems to ensure reliable energy supply. The installation of wind turbines involves high upfront costs and requires adequate space and appropriate wind conditions, which may not be available for all buildings. In addition, concerns related to noise and visual impact can affect the acceptability of wind turbines in urban or residential areas [8].

1.3. Energy consumption in the built environment

Energy consumption in the built environment is a global issue that has far-reaching environmental, social, and economic consequences. One of the most significant global issues related to energy consumption in the built environment is climate change. Buildings are responsible for a significant amount of global energy consumption and greenhouse gas emissions, which contribute to climate change. The use of fossil fuels for heating, cooling, and electricity in commercial and residential buildings accounts for approximately 40% of global energy consumption and 33% of global greenhouse gas emissions [9-12]. The building sector is responsible for approximately one-third of global energy and process-related CO₂ emissions, both directly and indirectly, making it a significant contributor to carbon emissions. To address this, emission restrictions are necessary across the entire value chain of buildings and building construction [9].

Fossil fuel dependence in buildings poses a risk to energy security due to volatile prices, highlighting the need for transitioning to renewable energy sources [3]. Energy poverty is also a problem where limited energy access, and high costs lead to negative health outcomes and reduced quality of life. Urbanisation' accelerating trend worldwide increases energy demand, greenhouse gas emissions, and air pollution, making sustainable urban development and energy-efficient buildings critical. Finally, resource depletion, such as deforestation and pollution, can have negative impacts on the environment, emphasising the importance of sustainable building practices. Addressing these global issues requires a comprehensive approach involving improved energy efficiency, renewable energy sources, energy access and affordability, sustainable building practices, and sustainable urban development [5].

The application of renewable power generation technologies in building codes, demonstrated by standards such as Passive House and the International Energy Conservation Code (IECC), marks a significant shift towards sustainability and energy efficiency in construction. Passive House Standards impose strict requirements on energy performance, insulation, airtightness, and ventilation, aiming to minimise energy consumption and environmental impact throughout a building's lifecycle. Through advocating for the adoption of renewable energy systems such as wind turbines, these standards provide self-sufficiency and resilience against energy cost fluctuations and disruptions. Moreover, these codes aid in reducing greenhouse gas emissions by lessening reliance on fossil fuels for heating, cooling, and electricity generation. Compliance with the IECC, enforced by state and local building codes, further advances these goals by promoting energy conservation and enhancing building sustainability through regulations covering insulation, windows, lighting, HVAC systems, and renewable energy integration. In essence, prioritising integrated renewable power generation technologies in building codes represents a crucial step towards creating more sustainable and environmentally conscious built environments [13-14].

1.4 Recent developments and global challenges on BIWT

The shift towards sustainable buildings and renewable energy are gaining momentum. Increasing energy efficiency requirements have led to innovative renewable energy solutions being integrated within buildings [15].

Over the years, the potential for building-integrated or roof-top renewable energy technology installations has drawn some attention [16]. Wind energy harvesting technologies have been a prevalent strategy for promoting the integration of renewable energy into the built environment for several decades Xu et al., 2021[17]. The integration of conventional micro or small-scale wind energy harvesting technologies with buildings, such as vertical axis wind turbines (VAWT), horizontal axis wind turbines (HAWT), and diffuser augmented wind turbines (DAWT), has been well researched. Studies [17-20] have shown that such technologies can take advantage of the accelerated wind flow around building structures [21] and buildings increasing the power output captured from the airflow [22-23]. Despite their potential, there are

challenges [24] associated with installing and operating conventional wind turbines in buildings, such as high costs, lower wind speeds and turbulence in the urban environment [18], vibration, and structural sitting issues [25]. Opportunities with conventional wind turbines placed on the rooftop, however, there are also challenges faced by these technologies. Building integrated wind turbines (BIWT) presents unique challenges that differ from those associated with standalone wind turbines. These challenges include the following:

- BIWT systems' efficiency drops in low wind speed conditions, which impacts the overall energy generation.
- Installing turbines on existing buildings is technically challenging, which requires structural reinforcements and consideration of building aerodynamics.
- Compatibility issues with architectural designs.
- Regular maintenance is critical for optimal performance but can be difficult in urban settings.
- Requires access to building rooftops and can involve disruptions to building occupants.

Addressing these challenges faced by BIWT requires innovative approaches and collaboration among stakeholders. Engineers, architects, city planners, and policymakers should work together to develop sustainable solutions for the deployment and maintenance of BIWT systems. As the demand for renewable energy continues to grow, finding solutions to overcome these challenges will be critical to unlocking the potential of BIWT and achieving a more sustainable future.

The [26] conducted a study on building-mounted wind turbines and identified several factors affecting wind speed, including geographic location, nearby obstructions, turbine height, and roof shape. Other publications, such as [27-32], have similarly emphasised the importance of roof shape in the success of roof-mounted wind turbines. [23] also conducted a study on wind flow around roof-mounted wind turbines, focusing on different roof shapes including pitched, pyramidal, and flat roofs, and concluded that the power density above the flat roof is greater and more consistent than above the other roof types. The authors suggested the need for further investigation to include other roof shapes.

In [33], the wind flow over a flat roof was analysed to develop guidelines for small wind turbine placement, highlighting the significance of roof shape in determining the optimal mounting location for the turbine. In the research conducted in [34], the recommended mounting location for a single wind direction on a pitched roof was investigated. The study suggested extending the investigation to include a variety of roof types and locations under different wind directions. The feasibility of wind power utilisation in high-rise buildings in Hong Kong suggested that studying the wind concentration effect due to building heights and optimal roof shape can increase the feasibility of urban wind turbines was investigated in the study of [22]. Given the complexity of the built environment, this research argues that multiple variables, including roof shape, wind direction, building height, and surrounding urban configuration, affect wind flow around buildings.

1.5 Micro/small scale wind energy harvesting technologies challenges and advantages

With the ongoing research and development of new wind energy harvesting technologies for sustainable and renewable energy technologies, many energy companies have taken an interest in micro/small-scale wind energy harvesting technologies which are designed to capture wind energy from the surrounding environment and convert it into electrical power. This wind energy harvesting technologies typically have a capacity of watts to kilowatts, which are suitable for residential or small-scale commercial applications [35-36].

1.5.1 Conventional wind turbines

The most common technology used is the conventional wind turbines, which include the horizontal axis wind turbine (HAWT) and vertical axis wind turbine (VAWT). Vertical-axis wind turbines (VAWTs) can be used for small-scale wind energy generation [37]. Unlike horizontal-axis wind turbines, which have a rotor shaft that is aligned parallel to the ground, VAWTs have a rotor shaft that is aligned perpendicular to the ground. This design allows them to capture wind energy from any direction and makes them more suitable for urban environments where wind direction is unpredictable [37].

Small-scale wind turbines can be installed on a pole or tower, allowing them to capture wind energy at a higher altitude where wind speeds are generally higher and more consistent [38]. Table 1 shows the size classifications of wind turbines. According to the [35], turbines with a rated capacity of over 100 kW are considered large, while those with a capacity below this are classified as small. The British Wind Energy Industry (BWEA) further subdivides the small category into micro wind (less than 1.5 kW), small wind (1.5 to 15 kW) [37] [39].

Table 1. Wind turbine size classifications [35-36]

Size	Swept area (m²)	Generating capacity (kW)	Applicable applications
Micro	Up to 7.5	<1.5	Provide power on-site for charging small batteries, and illuminating road signs, and streetlights
Small	7.5 to 75	1.5 to 15	Provide power on-site for small-scale commercial or residential buildings

Research on small-scale wind energy systems differs from that of large-scale systems, with a focus on aerodynamics and engineering methods for determining wind statistics at specific points of interest, such as rooftops. Recent work aims to simplify procedures and improve wind speed predictions, addressing reported errors ranging from 5% to 20% [39]. Studies also explore building aerodynamics, including the impact of flow phenomena on rooftops and rotor performance. While rotor aerodynamics for VAWT-type turbines have been extensively researched, further investigation is needed on turbulence and gust influences [39]. Novel designs for urban wind turbines exist but require expensive manufacturing and rigorous testing for certification. Building-integrated wind energy has potential, but buildings are not often optimised for wind energy generation. Limited studies have been conducted on noise emissions and visual impact, but economic studies show promise for small-scale wind energy. Overall, more integrated research and certification regulations are needed to advance the field synergistically with a multi-scale approach.

1.5.2 Micro/small scale wind-induced vibration technologies

Micro/small-scale wind energy harvesting technologies offer promising solutions for renewable energy generation in urban areas. These technologies encompass various

options such as building integrated wind turbines, rooftop wind turbines, hybrid wind-solar systems, and portable wind turbines [38]. These technologies, including innovative micro/small-scale turbines utilising wind-induced vibration mechanisms like vortex-induced vibration, flutter, and galloping, show potential for generating power output ranging from nanowatts to watts. Moreover, these designs are compact, which makes them suitable for space-constrained urban environments. Implementing these technologies can contribute to decentralised electrification, providing reliable and affordable electricity to remote communities. However, wind-induced vibration technologies are still in the early stages of development and face challenges such as lower power output and dependence on unpredictable factors like wind conditions [40-42]. Continuous research aims to refine and enhance these technologies, potentially making them cost-effective alternatives to traditional wind turbines, particularly in urban areas concerned with space and visual impacts. Overall, exploring the potential of micro/small-scale wind energy harvesting technology is worthwhile for meeting energy demand and facilitating decentralised electrification [38].

1.6 Urban and rural wind energy opportunities and challenges

When deciding about the placement and positioning of wind energy harvesting systems, urban and rural areas have different opportunities and challenges. Firstly, urban wind energy harvesting systems must be sized appropriately to fit into the limited space available in cities and towns, whereas rural wind turbines can be larger since there are fewer space constraints. Secondly, urban wind energy harvesting systems tend to operate at lower wind speeds compared to rural wind energy harvesting systems. This is because urban areas are often sheltered by surrounding buildings, which creates turbulent and slower wind conditions. Rural wind energy harvesting systems, on the other hand, can take advantage of open and unobstructed landscapes with stronger and more consistent wind speeds. Thirdly, the energy produced by urban wind energy harvesting systems are usually consumed locally, whereas rural wind turbines may supply electricity to regional grids. Therefore, the urban wind energy systems have more direct impact on local energy use and can help to reduce the carbon footprint of cities and towns. Finally, there are different challenges associated with the installation and maintenance of wind energy harvesting systems in urban and rural

environments. In urban areas, issues such as noise pollution and visual impact must be carefully managed, whereas in rural areas, access to remote locations and exposure to harsh weather conditions can be more challenging. In summary, while both urban and rural wind energy have their advantages and challenges, they serve different purposes and face different constraints depending on their location [42-46].

The study identified areas requiring further exploration and gaps in knowledge by critically analysing existing research, which results in the development of specific research question aimed at addressing these gaps. These questions were created to investigate the fundamental aspects such as the influence of building shapes, wind speed acceleration, optimal positioning of wind energy harvesting systems, the impact of varying wind conditions and turbulence, comparative analysis with existing micro/small scale wind energy harvesting systems, and the identification of key parameters. Each question presented in Section 1.7 were evaluated for its relevance and significance in advancing knowledge within the field, with an iterative refinement process ensuring clarity, focus, and alignment with the study's objectives.

1.7 Research questions

- What is the effect of different building shapes and configurations on the performance of an oscillating aerofoil integrated into the building roof structure?
- How can the wind flow around buildings be optimised to increase the power output of an oscillating aerofoil integrated into the building roof structure?
- What is the optimal placement of oscillating aerofoil integrated into the building roof structure to maximise power output?
- How do varying wind speeds and directions affect the performance of an oscillating aerofoil integrated into the building roof structure, and how can this be mitigated?
- What is the impact of turbulence on the performance of an oscillating aerofoil integrated into the building roof structure, and how can it be accounted for in simulations?
- What are the design parameters that affect the performance of building integrated wind turbines, and how can they be optimised?

This investigation will provide valuable insights into the optimal design and placement of such systems within different building structures, paving the way for more effective utilisation of wind energy resources in urban and built environments. This design is expected to provide a viable alternative to traditional wind turbines, avoiding high maintenance and transportation costs. It is expected to contribute significantly to decarbonisation efforts at a lower cost for end-users compared to current carbon-based solutions. The design can be easily integrated into existing buildings or retrofitted, providing direct power supply, and promoting decentralised grid systems. It features lightweight components, addressing concerns about increasing energy consumption in the built environment. Traditional wind turbines capture wind travelling in only one direction, making them inefficient in densely populated urban areas where wind is often trapped between buildings.

1.8 Research gaps and novelty

In response to the ongoing crisis with the increasing energy demand and carbon emissions, an alternative solution to extract energy from the wind flow around buildings is proposed in this research. This solution is an energy harvester device based on an oscillating aerofoil. From the review of relevant previous works, its integration into a building structure for energy harvesting has not yet been investigated. Even though there are existing research [47] on the technical performance of stand-alone [48] or isolated oscillating aerofoil devices [49-50], but not one of the studies has integrated these systems into the building structure, such as the roof [51-52]. Similarly, while there is research on aeroelastic belts [19] installed on building roofs, there is no study focusing on oscillating aerofoil wind energy harvesters integrated into building roof. Moreover, the effect of the building's shape on the oscillating aerofoil system for power extraction and energy harvesting efficiency has not yet been investigated [53-54]. Furthermore, the influence of the external wind environment [55-56] on these energy harvesters has not been widely explored. There is limited research on the influence of terrain and atmospheric boundary layer (ABL) profiles on the performance of such energy harvesting technologies) [56]. Finally, the experimental research on small or micro energy harvesting technologies integrated into the building is limited [56].

Regarding the evaluation of wind flow around buildings and energy harvesting technologies, CFD modelling has been widely used and validated by the research community for predicting and investigating the wind flow above and around buildings [57] and the aerodynamic characteristics of wind energy harvesters [58]. It is a cost-effective aid to wind tunnel testing and can be used to investigate various parameters at several wind and operating conditions [59].

The proposed design of a power capture system using an oscillating aerofoil to capture kinetic energy is a novel idea with the potential to contribute significantly to building-integrated wind energy harvesting. However, there are several research gaps in this area that need to be addressed. Firstly, there is a need to understand the fundamental dynamic behaviour of fluid-structure interaction when an oscillating aerofoil is integrated into the building structure. In addition, a new numerical approach using CFD dynamic mesh is proposed, which could help understand the dynamic behaviour of the building-integrated wind energy harvesting systems. The influence of the external wind environment on such energy harvesters has not been widely explored, and there is limited research on the influence of terrain and atmospheric boundary layer profile on the performance of these energy harvesting technologies. Finally, there is limited experimental research on small or micro energy harvesting technologies integrated into the building. One key research question that needs to be addressed is the turbulence kinetic energy of the proposed design, which can provide valuable insights into the potential energy output and efficiency of the system.

On the other hand, the integration of oscillating wind energy harvesting systems into building roof structures introduces potential vibrational issues that can stress the building. These issues include the resonance of new natural frequencies introduced by the oscillating system, dynamic loads from wind-induced oscillations impacting structural integrity, and the need for careful material selection and design optimisation to manage these vibrations effectively. Ensuring occupant comfort and safety involves mitigating excessive vibrations through strategic design measures to maintain structural stability and enhance energy harvesting efficiency.

Figure 2 shows the schematic and computational model of the introduced design presenting an oscillating NACA 0012 aerofoil integrated into a building roof for wind energy capture. The energy conversion process from wind kinetic energy to electrical energy using oscillating aerofoils. Wind flow imparts kinetic energy to the aerofoil, inducing oscillations, representing the conversion of wind kinetic energy into mechanical energy. This mechanical energy is then transferred through a system consisting of a motor and generator. The motor converts it into rotational motion, and the generator further transforms this into electrical energy through electromagnetic induction, serving as the final usable electrical output. In this configuration, airflow starts the oscillating motion of the NACA 0012 aerofoil, driven by wind-induced torque on the supporting rod, with contributions from the inertia and weight of the aerofoil. The configuration of the roof influences airflow velocities and turbulence intensity, impacting the potential power output of the proposed system, particularly at higher wind speeds [20]. The proposed solution of integration of oscillating aerofoil integrated into the building's roof structure, which captures wind energy through its oscillating behaviour will be investigated to further understand its potential for an energy harvesting system. This study will examine the influence of various roof configurations, including pitched, curved, and flat roof building structure. Through examining how these different roof shapes interact with wind flow dynamics and examine their impact on the performance of integrated wind energy harvesting systems. Specifically, the study aims to assess how each roof configuration affects wind speed, turbulence, and airflow patterns, ultimately determining their suitability for accommodating oscillating aerofoil-based energy harvesting technology.

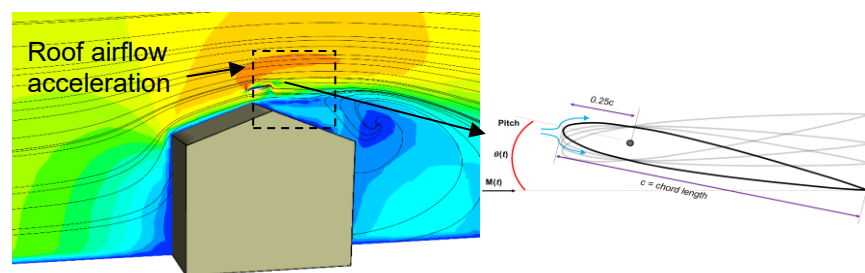


Figure 2. Schematic diagram of the oscillating NACA 0012 aerofoil integrated into the building roof structure [48]

1.9 Research aim and objectives

The aim is to develop a novel design approach and apply this to develop an oscillating aerofoil wind energy harvesting system integrated into the building roof structure. While objectives of the research include the following:

- Conduct a comprehensive review on building integrated wind energy harvesting systems (BI-WEHS) and evaluate literature gaps
- Develop a 3D numerical model of an oscillating aerofoil wind-induced energy harvester and the building roof structure to investigate its dynamic behaviour in transient simulations
- Validation of CFD results with experimental data for an oscillating aerofoil and the building roof structure to ensure its reliability by comparing its predictions with experimental data
- Integrate the 3D aerofoil wind energy harvester model into a building structure to improve its performance and assess the effects on overall efficiency
- Conduct parametric analysis to evaluate how changes in various parameters influence the performance and efficiency of the system

1.10 Thesis structure

Figure 3 shows the overview of the thesis structure. Chapter 2 presents a comprehensive literature review of various wind energy harvesting technologies, with a focus on building-integrated wind turbines and small-scale wind energy harvesting systems installed in building roof structures. The review includes theoretical, numerical, and experimental research to understand recent developments, current challenges, and limitations of these technologies. Knowledge gaps are identified, and potential solutions to address challenges faced by existing technologies are explored. Chapter 3 outlines the research methodology, including the use of ANSYS software for computational fluid dynamics (CFD) simulations to investigate energy harvesting performance. A full description of the numerical model used, including the governing equations, computational domain, mesh, grid adaption, boundary layer theory for building simulation and the boundary conditions has been provided. Five numerical studies were conducted. While the set-up of these studies was chiefly similar, the conditions and context for each have been described.

Chapter 4 discusses model verification and validation, comparing different aerofoil shapes and validating against previous experimental studies.

Chapter 5 investigates the dynamic behaviour of a single oscillating aerofoil, building roof structures, and their integration using ANSYS Fluent.

Chapter 6 focuses on the parametric analysis of the building-integrated wind energy harvesting system, exploring new designs and parameters.

Chapter 7 concludes the thesis with a summary of research findings, conclusions, and recommendations for future work, along with a list of references and appendices containing additional information used to support the studies presented.

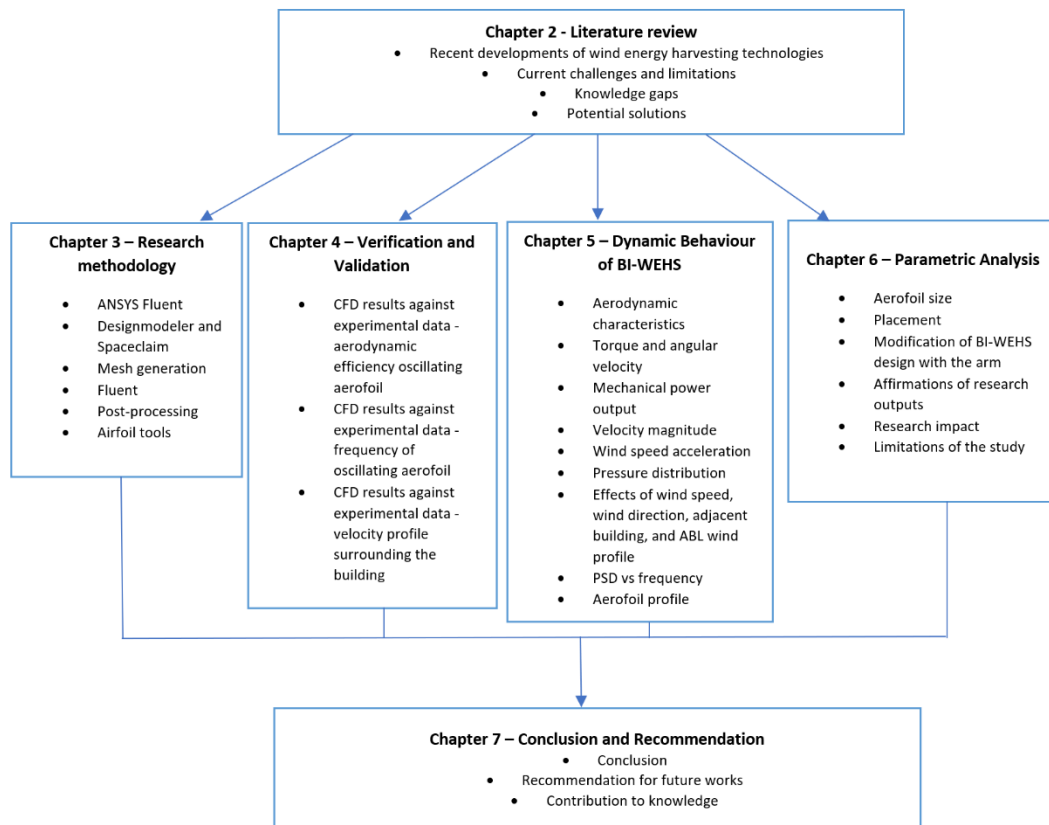


Figure 3. Overview of the thesis structure

Chapter 2

Literature review

This chapter will review the different types of wind energy harvesting technologies that are available in the literature. The study will provide different studies on different types of building-integrated wind turbines and other potential small-scale wind energy harvesting systems that can potentially be installed into the building roof structure. Different methods conducted in the literature, such as theoretical, numerical, and experimental research will be reviewed to further study the recent developments, current challenges, and limitations of these technologies. From this review, the knowledge gaps will be identified, and investigate the potential solutions and solve the current challenges faced by the existing technologies. Lastly, a summary of all the studied research will be discussed and analysed.

2.1 Methodology

Figure 4 shows the methodology framework for the review of micro/small-scale building integrated wind energy harvesting systems and wind-induced vibration technologies. This work will review the state-of-the-art for building integrated wind energy harvesting systems and wind-induced vibration technologies. As most current studies on building integrated wind turbines focus on conventional wind turbines such

as HAWT, VAWT, and DAWT, this review also explores different wind energy harvesting technologies, including wind-induced vibration technologies such as flutter, vortex-induced vibration, and galloping mechanisms. To achieve this, a comparative analysis of six different wind energy harvester systems was conducted. The review will examine the design, power, and harvesting performance of micro/small-scale wind energy harvesting systems, with the potential for integration into commercial and residential buildings.

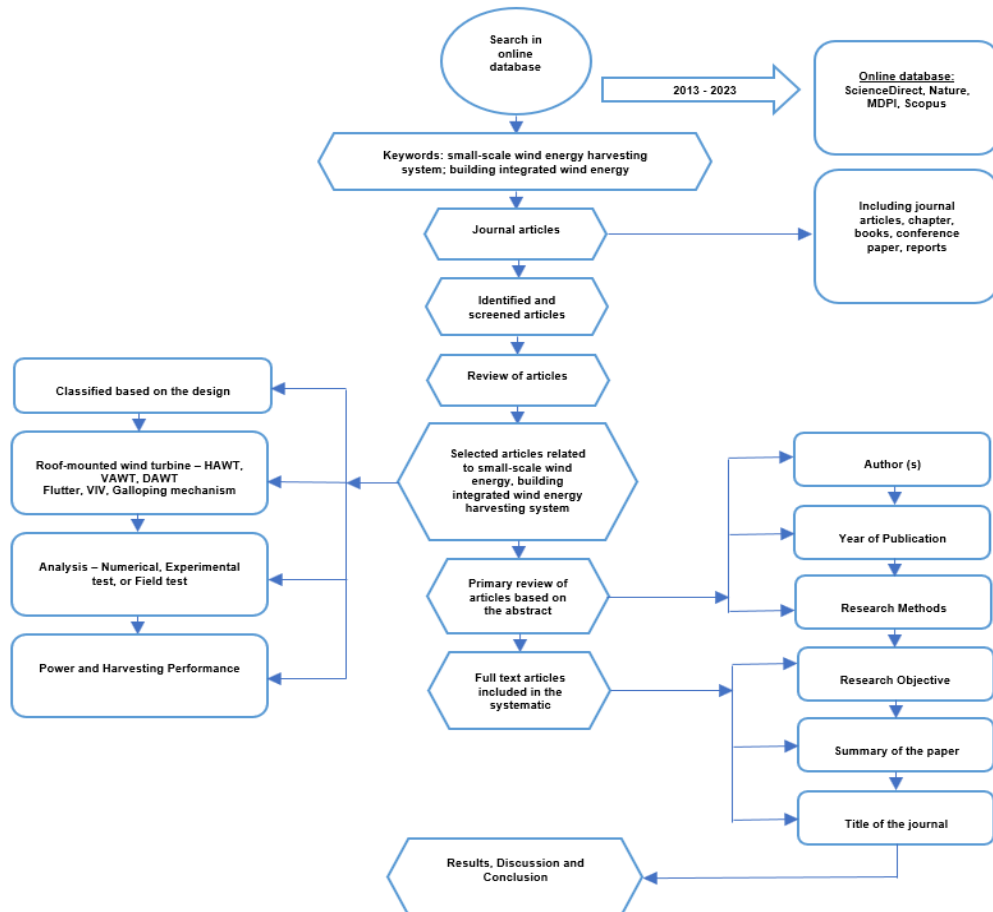


Figure 4. The methodology framework for the review of micro/small-scale building integrated wind energy harvesting systems and wind-induced vibration technologies

To conduct this review, an extensive search for relevant research materials was performed using a variety of keywords, such as "small-scale wind energy harvesting system," "building integrated wind energy harvesting system," "roof-mounted wind turbine," and "wind-induced vibration." Academic search tools such as ScienceDirect, MDPI, and Nature were utilised in this search, and only works published between 2013

and 2023 were considered. The selected papers explored various aspects of micro/small-scale wind energy harvesting systems, including their design, mechanisms, methods of analysis, and power and harvesting performance optimisation. Following a thorough examination of the literature, each technology was analysed in terms of its performance with different designs and environmental conditions.

The methodology framework employed to examine the current state of building-integrated wind energy harvesting systems and small-scale wind energy harvesting systems involves several steps. The first step was a comprehensive keyword search across a range of sources, including journal articles, books, conference papers, reports, and review papers. The second step involved the selection of relevant articles based on their abstract and relevance to the research topic. Next, the selected articles were thoroughly reviewed to identify various wind energy harvesting system designs that can be integrated into building structures, such as HAWT, VAWT, DAWT, flutter-based wind-induced vibration, vortex-induced vibration, and galloping mechanism. The research methods used in the articles, including numerical, experimental, or field tests, are then evaluated. The power and energy harvesting performance of both roof-mounted and small-scale wind energy harvesting systems were reviewed to identify a suitable wind energy harvester for a given application. Finally, a summary of the results, a discussion of the findings, and a conclusion on the state of the art of roof-mounted and small-scale wind energy harvesting systems are presented based on the reviewed literature.

Recent studies focusing on small-scale wind energy harvesting technologies have revealed two traditional wind turbine designs, HAWT and VAWT, that can be integrated into building structures [60]. However, these designs have limitations in capturing wind energy effectively, leading to the ongoing challenges with the developments. HAWTs and VAWTs each have limitations in wind energy capture. For HAWTs, these are requiring large spaces and alignment with wind direction, and VAWTs suffering from lower efficiency and maintenance issues. In response, building-integrated wind turbines (BIWTs) are being developed to address these challenges by

offering adaptable, space-efficient solutions suitable for urban environments and overcoming the specific constraints of traditional designs.

Another design was introduced which is called the DAWT. The design comprises of incorporating ducts or diffusers to better capture wind energy to the wind turbine and improve its power coefficient over time [61]. Figure 5 shows a building integrated with HAWT, VAWT, and DAWT. In Figure 5 (a), the commercial configurations of HAWT are presented. These turbines can operate either upwind or downwind, with upwind configurations being more prevalent due to their lower noise production and reduced rotor fatigue. HAWT systems can produce a variety of energy outputs [60]. Figure 5 (c) demonstrates the schematic diagram for DAWT.

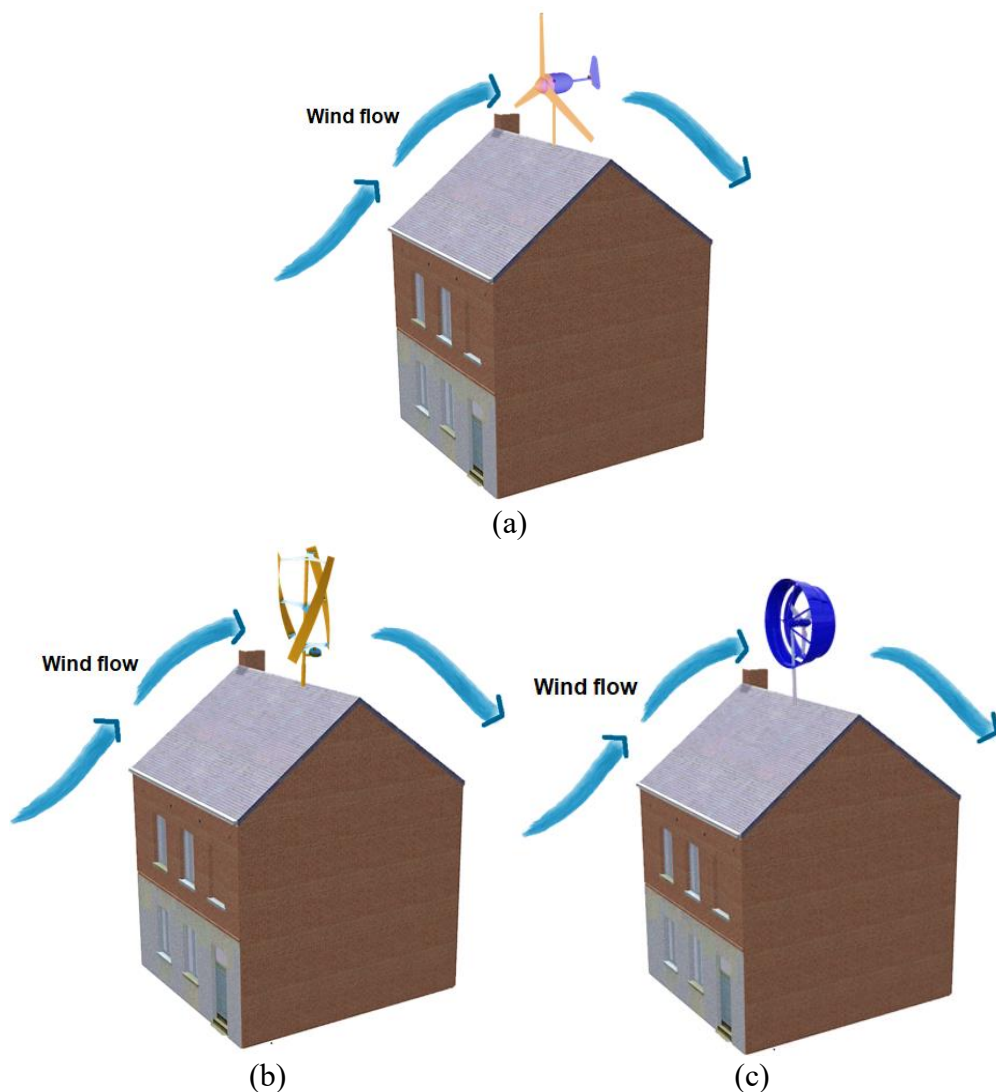


Figure 5. Schematic diagrams of conventional small-scale wind turbines installed on the roof of a building (a) HAWT, (b) VAWT, and (c) DAWT

Various micro/small-scale wind energy harvesting systems, such as wind-induced vibration technologies, are gaining popularity and being evaluated. These systems include galloping-based mechanisms, flutter-based wind-induced vibration, and vortex-induced vibration. However, their efficiency and performance are still in the early stages of testing, and they have not been widely adopted for real-world applications, particularly for building structures. Figure 6 (a-c) shows potential alternative design solutions for building-integrated wind energy harvesting systems that aim to overcome the challenges and limitations of traditional wind turbines. This also shows the schematic and integration of Figure 6 (a) flutter (b) galloping (c) vortex induced vibration into the building roof structure.

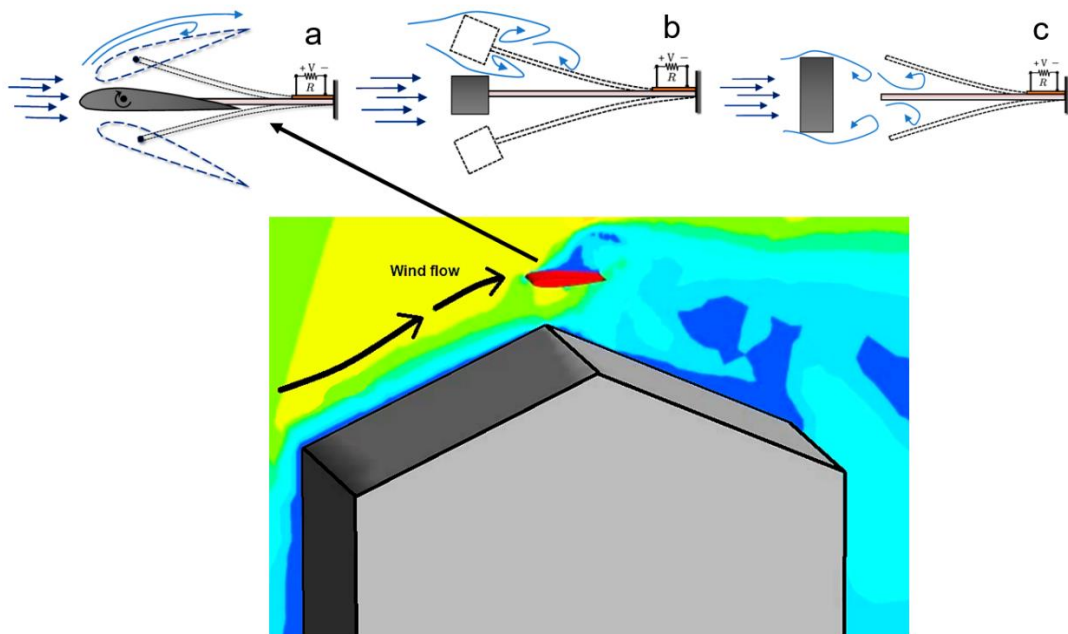


Figure 6. Schematic of Micro/Small-Scale Wind Energy Harvesters for Roof Building Integration: (a) flutter, (b) galloping, and (c) VIV

The evaluation of papers published in the past decade revealed a limited exploration of micro/small-scale wind-induced vibration technologies integrated or installed in building structures. Recent advancements in wind energy harvesting technologies have largely focused on building-integrated wind turbines, such as the horizontal-axis (HAWT), vertical-axis (VAWT), and diffuser-augmented wind turbines (DAWT). Therefore, this study also examines the potential and proposes an alternative wind energy harvesting system that can be integrated into building structures.

2.2 Wind energy harvesting system for building integration

This section provides an overview of the recent advancements in building-integrated wind turbines and micro/small-scale wind-induced vibrations as alternative sources of energy.

2.2.1.1 Horizontal-axis wind turbine (HAWT)

The HAWT is designed with a rotor shaft and electrical generator located at the top of a tower, with the rotor positioned perpendicular to the wind. It typically includes a gearbox, which increases the rotation speed of the rotor to generate electricity. HAWT systems are highly dependent on wind direction and therefore operate at greater heights compared to VAWT. Figure 7 provides an illustration of the (a) aerodynamic profile [62] and (b) schematic of a building integrated HAWT installed on a roof structure, as presented by [63].

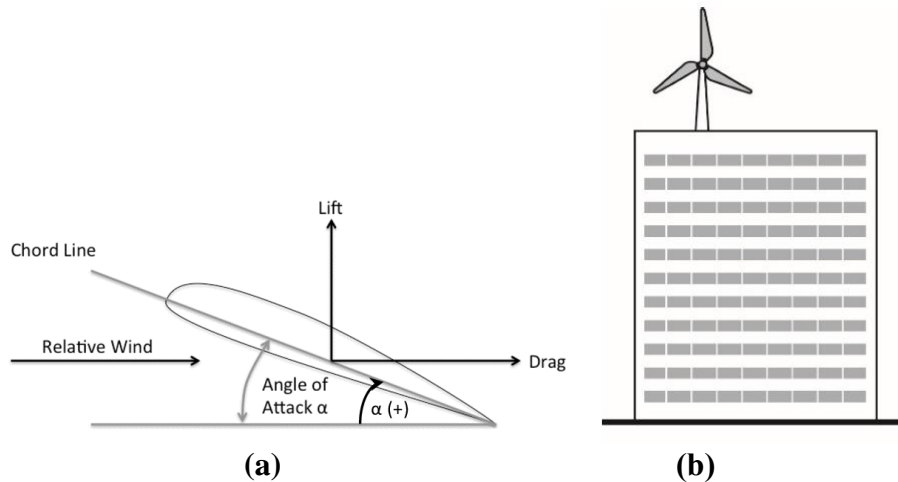


Figure 7. Wind turbine blades (a) design and schematic [62] of (b) HAWT installed into the building roof structure [64]

Several studies [65-73] have focused on the design and optimisation of HAWT rotors and blades, using methods such as CFD, Blade-Element Momentum (BEM), and genetic algorithms (GA) to investigate aerodynamic performance. These studies considered factors such as aerofoil profile, blade allowable stress, starting time, and output power. Many of the studies found that optimisation of the rotors led to improved power coefficient, starting performance, and annual energy production, with the use of linear distributions and 3D stacking lines also shown to improve performance.

Horizontal Axis Wind Turbines (HAWT) are extensively studied and widely used for building-integrated applications due to their historical significance, high efficiency, and superior power output. Originating from traditional windmill designs, HAWTs have benefited from extensive technological advancements, which makes them reliable and cost-effective. Their aerodynamic design optimises energy extraction, and their scalability allows for substantial energy production, which makes them suitable for integration into building structures. The well-established market presence, extensive research, and proven maintenance practices make HAWTs a highly viable option for incorporating wind energy into buildings.

The use of Computational Fluid Dynamics (CFD), Blade-Element Momentum (BEM), and genetic algorithms (GA) in designing and optimising wind turbine rotors and blades for building-integrated wind energy systems presents several advantages. These tools enhance aerodynamic performance by providing detailed airflow analysis and optimising blade shapes for maximum energy capture. BEM offers reliable predictions of rotor efficiency, facilitating precise design adjustments. Genetic algorithms identify optimal design configurations, balancing performance, cost, and durability. In addition, these tools allow for customisation of designs to specific building environments and wind conditions, improve overall system efficiency and reliability, and reduce the need for extensive physical prototyping and testing. This makes building-integrated wind energy systems more effective and better suited to urban environments with complex wind conditions. However, these benefits come with certain drawbacks. The software and computational resources necessary for these methods can be expensive, posing high initial costs. CFD simulations are computationally intensive and time-consuming. Moreover, there is a risk of over-optimising designs for specific conditions, which might not perform as well in varying real-world scenarios. Despite these challenges, the advantages of using these advanced tools often outweigh the disadvantages, making them valuable for developing efficient and reliable building-integrated wind energy systems.

The optimal blade design is critical for achieving high-performance HAWTs integrated into buildings, as highlighted in various studies. Singh et al. [74] designed a 2-bladed rotor with a special aerofoil and exponential twist and taper distribution to achieve

high aerodynamic performance at low wind speeds. Field tests demonstrated that the 2-bladed rotor performed better at a pitch angle of 18 degrees, achieving lower cut-in wind speeds and higher power coefficients compared to a baseline 3-bladed rotor. This optimisation led to improved performance, with a peak power coefficient of 0.29 at 6 m/s wind speed. However, the study did not address the practical aspects of integrating the turbine into building structures, which would be crucial for real-world applications.

Optimal blade design is critical for achieving high-performance HAWTs integrated into buildings, as highlighted in various studies. The peak power coefficient of 0.29 for the 2-bladed rotor at a 6 m/s wind speed is in the mid-range for small-scale HAWTs. Scientifically, the power coefficient C_p measures how efficiently a turbine converts the kinetic energy of wind into electrical power. For small-scale wind turbines, C_p values typically range from 0.2 to 0.35, with the theoretical maximum, known as the Betz limit, being 0.59. Therefore, a C_p of 0.29 is in the middle range, reflecting moderate efficiency within the practical range. The observed benefits, such as lower cut-in wind speeds and higher power coefficients in the 3-7 m/s wind speed range, suggest that the 2-bladed design is well-optimised for these conditions. However, since the study focuses solely on rotor design optimisation and does not address building integration, these results might not fully translate to a building-integrated context. Factors such as wind flow disturbances, structural vibrations, and spatial constraints could affect turbine performance when integrated into a building structure. Therefore, while a power coefficient of 0.29 indicates moderate efficiency, further research is needed to assess the turbine's performance in real-world, building-integrated environments.

Volkmer et al. [75] focused on the modification of blade design to reduce aerodynamic noise in small horizontal axis wind turbines. Three blade modifications were investigated, including an acoustically optimised blade profile, boundary layer tripping, and trailing edge serrations. Testing was conducted on a three-bladed research wind turbine, and all modifications resulted in a reduction of aerodynamic noise. The study found that the new KV200-profiled blades, with a thickness of 10%, had significantly lower overall sound power levels than the baseline S834-profile, and tripping and trailing edge serrations were effective in reducing noise but resulted in a reduction of turbine shaft power. Boundary layer tripping applied to the thicker S834-

profile led to the largest noise reductions but also the greatest degradation of turbine shaft power. A combination of tripping and trailing edge serrations had a similar effect to tripping alone, and the T-KV200 without trips but with trailing edge serrations was found to be the best option for noise reduction.

In the study by [76], the authors employed a multi-objective surrogate-based optimisation approach to investigate the optimised geometry of an Invelox wind delivery system. The study aimed to maximise wind power and net mass flow rate, while minimising backflow. The researchers used Kriging models to predict the outputs. These Kriging surrogate models are coupled with the Multi-Objective Particle Swarm Optimisation (MOPSO) algorithm. MOPSO, stimulated by collective behaviour in nature, guides particles through the search space to find optimal solutions that optimise multiple objectives simultaneously, such as maximising wind power and net mass flow rate while minimising backflow in the Invelox system. The Kriging models predict system performance for various geometries efficiently, aiding MOPSO in effectively exploring the design space to identify optimal or near-optimal configurations. This integrated approach combines the strengths of surrogate modelling and evolutionary optimisation to enhance engineering design outcomes.

Figure 8 demonstrates the (a) Invelox wind delivery design design with a funnel-shaped structure that captures wind from a wide area and accelerates it through a narrow throat where a turbine is located and (b) computational domain of the installed Invelox inside. In this system, the wind is captured by the funnel-shaped intake, and after passing through the piping system, the wind accelerates at the Venturi section. Invelox is a wind delivery system designed to efficiently capture and channel wind energy for electricity generation. Moreover, the system aims to increase the wind velocity at the turbine, thereby enhancing its power output compared to traditional wind turbines. Invelox systems are proposed as a potential solution to improve the efficiency and feasibility of wind energy capture, especially in locations where traditional turbines may face limitations due to wind speed or space constraints. The Invelox performance was found to improve by 64.7% for power throughput and 279.9% for swept ratio. The HAWT designed for the throat of the Invelox had a power coefficient of 0.46, and the optimal Invelox's entering mass flow rate was found to decrease by 49.6% when the turbine was not rotating.

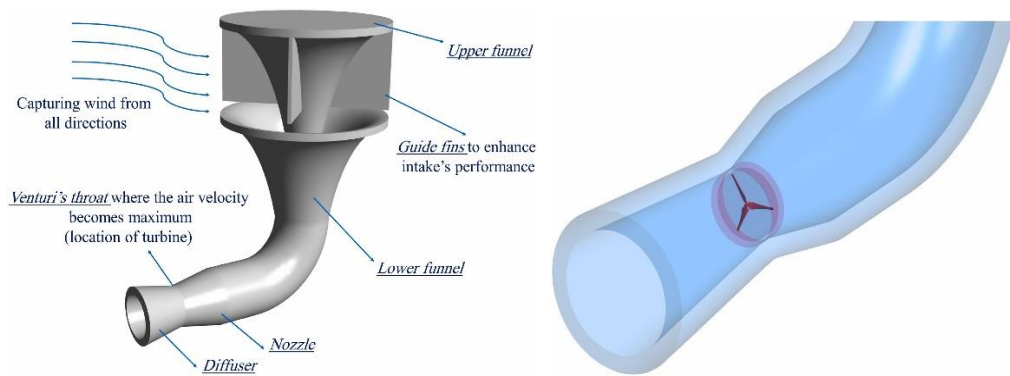


Figure 8. Invelox (a) wind delivery system (b) computational domain of the installed HAWT inside the optimal Invelox [76]

Dar et al. [77] investigated the impact of different roof edge shapes on the power performance and wake characteristics of a wind turbine installed on a roof in an urban environment. The study tested three roof edge configurations: a sharp 90° edge (cube), a slightly curved edge (round), and a roof with a boundary fence (fence). Among these, the round edge shape demonstrated the best performance, achieving the highest power production with the least turbulence intensity and shear. In contrast, the cube edge shape served as a middle-ground performer. While specific numerical values for power production and turbulence were not provided, it was implied that the cube edge shape performed better than the fence shape but not as well as the round edge. The study suggested that the cube edge shape offered a balanced performance, neither excelling nor underperforming significantly in any specific aspect compared to the other shapes.

The fence edge shape experienced the most significant drop in power production and exhibited the highest standard deviation and turbulence intensity. Despite the lack of exact values, the study highlighted that minor changes in roof edge shapes could result in substantial differences in power production with implied variations potentially around 10-30% based on typical engineering study interpretations. This highlights the importance of accurately modelling building shapes to optimise turbine performance and assess wake effects precisely.

Most of the research on HAWTs integrated into building structures has focused on blade design optimisation, including achieving high aerodynamic performance at low wind speeds and reducing aerodynamic noise. Other studies have explored the impact of design variables and roof edge shapes on wind turbine performance. The use of modelling and design optimisation techniques has led to significant improvements in

wind turbine performance. However, there is also a need to investigate wind resource assessment for building integrated wind turbines in different settings, such as urban, rural, or wind farm layouts, to further optimise the system's capacity.

2.2.1.2 Vertical-axis wind turbine (VAWT)

Vertical-axis wind turbines (VAWT) have a rotor axis oriented vertically and do not require a yawing mechanism or self-starting capability. Their generators are located on the ground, making maintenance easier, and they operate at low heights. The two main commercially available types of VAWT are Savonius and Darrieus. Figure 8(a) shows the Savonius VAWT, which uses drag to convert wind energy into mechanical rotational energy. Figure 8(b) illustrates the Darrieus VAWT, which uses the principle of lift to convert wind energy, making it more efficient than the Savonius design. The Darrieus VAWT uses aerofoil-shaped blades, producing lift and rotation as the wind passes over the blade [60].

The study will focus on the Savonius and Darrieus designs of vertical axis wind turbines (VAWT) as these are the most commonly integrated into building roof structure. VAWT operates using different aerodynamic principles to convert wind energy into power. The Savonius turbine has a simple S-shaped blade design that uses drag force to generate torque, making it cost-effective for small-scale wind energy production. Figure 9 (a) illustrates the working principle of the Savonius rotor [78]. In contrast, the Darrieus turbine employs aerofoil blades that generate lift force to spin the rotor, requiring an initial spin to reach operating speed. Figure 9 (b) demonstrates the working principle of the Darrieus rotor VAWT [79]. The Darrieus turbine is more complex and advanced than the Savonius, but its blade shape enables higher energy generation potential. The choice between the two will depend on the specific requirements and limitations of each project. In addition, other factors such as maintenance, operation, and cost should also be considered.

The integration of Savonius and Darrieus wind turbines into buildings can be achieved through various methods, depending on the specific design and requirements of the project. These turbines can be mounted on roofs, walls, or used as standalone structures. The Savonius turbine is a vertical axis turbine that can be installed vertically, whereas the Darrieus turbine is a horizontal axis turbine that requires a tall

mast or tower. Both types of turbines can generate electricity or mechanical power for building applications such as lighting, ventilation, or water pumping. Integrating wind turbines into buildings provides a renewable energy source and reduces reliance on traditional power sources, promoting sustainability and energy independence.

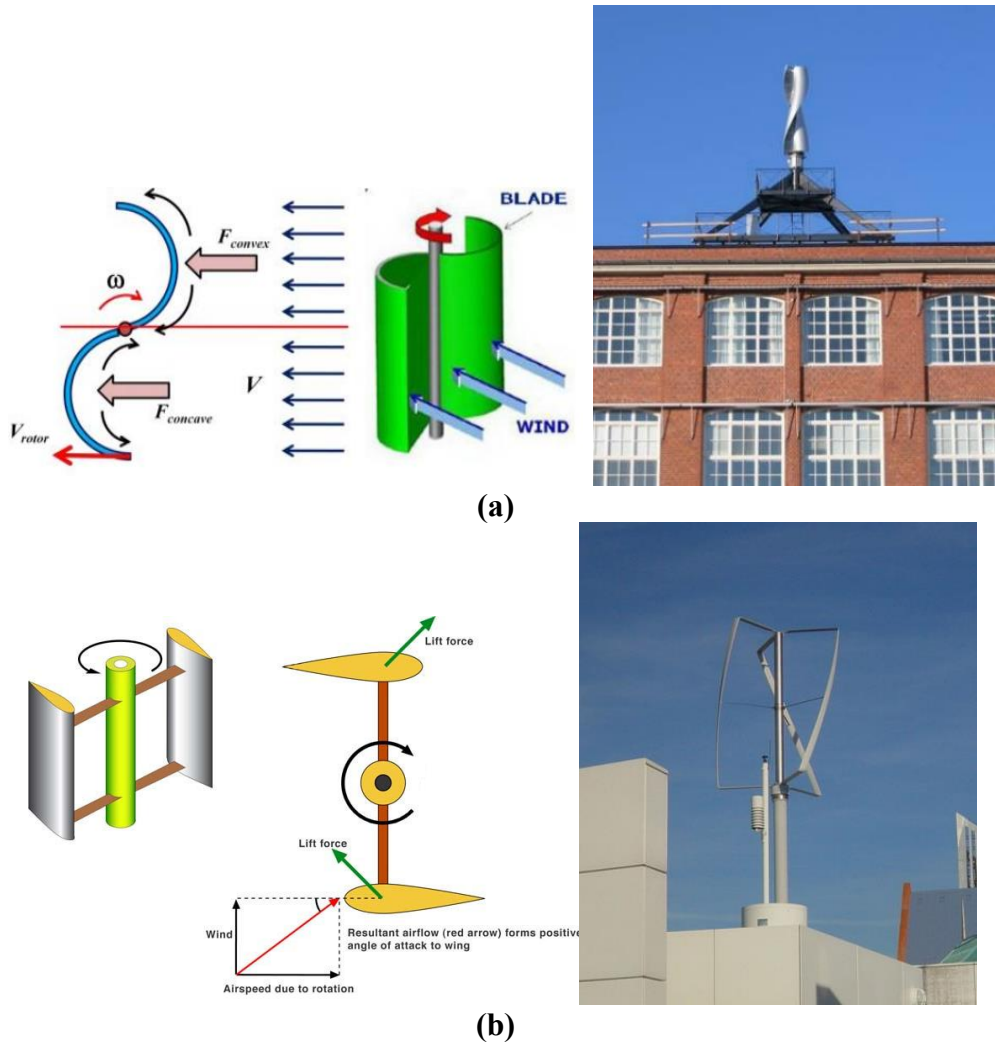


Figure 9. Principles of operation and rooftop wind turbines for buildings (a) Savonius [79] and (b) Darrieus [80-81]

Kuang et al. [82] presented a novel design called the building augmented vertical axis wind turbine (BA-VAWT), which aims to harness wind power in urban environments. The study investigated the aerodynamic performance of the turbine using numerical simulations with the NACA 0021 blade aerofoil. The wind energy utilisation coefficients of various building diffusers were evaluated at different Tip-Speed Ratios (TSR), and results indicated that the trapezium BA-VAWT had the best performance.

At an optimal TSR of 4.62, it achieved a maximum power coefficient of 1.56. In contrast, the A1 aerofoil had minimal pressure difference and negligible power generation. The torque coefficient and its variance increased with TSR, resulting in stable load fluctuation. Overall, the study concluded that the trapezium BA-VAWT had the best aerodynamic performance.

Different research of VAWT design was investigated [83]. The impact of rotor solidity and other factors on the power output of dual vertical axis wind turbines (VAWTs) in an urban setting were investigated. Twelve wind tunnel experiments were conducted to examine the effect of dual VAWT configuration on power output in different tip-speed ratio conditions. The study found that the effect of dual VAWT configuration on power output was limited at low tip-speed ratio conditions. Smaller rotor solidity was found to increase the sensitivity of power output to the spacing between the two rotors.

High-rotor solidity dual VAWTs were found to be more suitable for low wind power density areas, while low-rotor solidity dual VAWTs were better suited for high wind power density areas. This is because high-rotor solidity dual VAWTs with their increased blade area, capture more wind energy in slow-moving wind conditions, enhancing performance where wind energy is less abundant. Conversely, low-rotor solidity dual VAWTs with their reduced blade area, minimise aerodynamic drag, allowing them to operate more efficiently at higher wind speeds and higher tip-speed ratios. This balance between rotor solidity and wind conditions ensures optimal turbine performance by capturing sufficient wind energy while minimising aerodynamic losses, particularly in varied urban environments.

To achieve optimal utilisation of urban wind resources, it is necessary to consider factors such as rotor spacing, rotor solidity, high turbulence intensity, and low wind speed conditions, while combining the layout of multiple VAWTs with the rooftop and building structure. An array of multiple VAWTs can significantly improve aerodynamic performance and increase power output by improving wake interaction between VAWTs, especially in urban environments.

Whereas in the study of [84], experimental research was carried out which was focused on examining the optimal position of a roof mounted Savonius vertical axis wind turbine. The study involved two building cubes with a small VAWT of the Savonius

type placed on a circular flat plate that was rotated to simulate varying wind directions. The study examined three different wind turbine positions on the cube and varied the distance between the turbine blades and the roof of the cube. The experimental setup was based on a previous study conducted in a large-scale wind tunnel. The study found that the ideal position for a turbine was in the centre of the building for a uniform wind rose. However, for individual wind directions, the outside position was best for low turbines for winds from certain directions, and the inside position was best for others. The study recommends placing turbines in the centre of the building and as high as possible, but if there is a dominant wind direction, a specific location may be superior.

Another investigation of Savonius vertical axis wind turbines on the side of a building using numerical analysis [85]. A cylindrical building with five typical flow regions is used as a simplified model, and simulations of single and multiple turbines at different positions are conducted. The results demonstrated the viability of incorporating turbines onto buildings, with notable enhancements in energy generation observed in crosswind and tailwind zones. Despite a decrease in power coefficients as the number of turbines increased, most of the arrangements still surpassed the reference value. The overall power coefficient can be further improved by situating the forward blades of all turbines near the wall.

The study of [85] focused on the performance of a Darrieus VAWT in turbulent inflow conditions in an urban environment, using High-fidelity scale resolving Detached Eddy Simulation (DES) simulations to investigate a scaled-up, generic H-VAWT with NACA0021 aerofoil at various locations. Detached Eddy Simulation (DES) is an advanced turbulence modelling technique that blends aspects of Reynolds-averaged Navier-Stokes (RANS) and Large Eddy Simulation (LES). Its purpose is to effectively capture turbulent flows in both attached boundary layers and separated regions. By leveraging RANS near walls where flows are more predictable and transitioning to LES in turbulent or separated regions where larger eddies are significant, DES offers a balanced approach to simulating complex fluid dynamics. This method is particularly valued in fields like aerodynamics, turbomachinery, and automotive engineering for its ability to provide predictions with reduced computational costs compared to pure LES methods. Their findings show that the H-VAWT performs better at heights of 10 m and 12 m from building rooftops due to the combined influence of turbulence and

skewed angle of the flow, and that turbulence has a positive impact on the turbine's performance.

The wake of a Troposkien-shaped Darrieus wind turbine situated above a cubic building at two different locations and in varying wind flow conditions was carried out in [86]. The Troposkein-shaped Darrieus wind turbine is a type of vertical axis wind turbine featuring blades designed with a Troposkein shape, an aerodynamic curve that optimises performance by improving lift and reducing drag. This design enhances the turbine's efficiency in capturing wind from various directions without requiring orientation adjustments, while also reducing noise and potentially increasing durability. It is particularly suitable for urban and residential applications, as well as for off-grid power systems where space is limited, and performance needs to be optimised across varying wind conditions. The study utilised 3D unsteady CFD simulations, and the methodology was validated by comparing the C_p data with experimental data. The results indicate that placing the turbine above the building's corner can enhance its C_p from 0.318 to 0.549 at a tip speed ratio of 5. Moreover, the rotor wake's structure is shorter when operating in a freestream than when mixed with the surrounding accelerated flow.

Allard and Paraschivoiu [87] also conducted a study on the power coefficient performance of a vertical axis wind turbine (VAWT) at two distinct locations on a building. According to the findings, the VAWT's placement above the building led to better performance due to the rotor's position inside the accelerated flow region above the upstream edge of the building. The study also identified an even more promising location with higher flow acceleration, namely the side corners of the building.

The VAWT achieved a C_p value of 0.55. Future research could investigate the performance of this turbine across different building sizes and configurations. The study suggests that further experimental or field research should focus on placing VAWTs at the upper corners of buildings, oriented at a 45-degree angle towards the prevailing wind direction. The VAWT achieved a C_p value of 0.55, which is impressive, and further research could explore various building sizes and turbines. The study concludes that this work should encourage experimental or field studies

involving VAWTs placed above the side corners of buildings facing the main wind direction at a 45-degree angle.

The study by [88] focused on the examination of the aerodynamics of micro-wind turbines equipped with large-tip, non-twisted blades. The large tip blade chord length ratio between the blade root and tip (C_r / C_t) was set at 0.3. The study compared the performance of these large-tip blades to previously used shorter-tip blades with a chord length ratio of 0.5. Results indicated that the large-tip blades achieved better power and torque outputs at lower rotor rotational speeds, suggesting their suitability for micro-wind turbine applications.

Shorter-tip blades had a chord length ratio of 0.5. This means that the chord length at the root of the blade is 30% of the chord length at the tip for the large-tip blades, whereas for the shorter-tip blades, the chord length at the root is 50% of the chord length at the tip. This difference in chord length ratios affects the aerodynamic performance of the blades, with the large-tip blades showing better power and torque outputs at lower rotor rotational speeds compared to the shorter-tip blades.

The researchers used a wind tunnel system to investigate the relationship between C_p , TSR, (CT), while considering the effects of rotor position, rotor solidity, and blade number on rotor performance. The study utilised NACA4415 aerofoil for blade cross-section and fixed pitch angle and chord length ratio. Results indicate that positioning the rotor closer to the diffuser inlet leads to higher power output. In addition, the 60% solidity rotor performed better, and the number of blades had minimal impact on power output. Furthermore, large-tip blades outperformed short-tip blades at lower rotor speeds, making them well-suited for micro-wind turbines and providing greater flexibility for rotor-generator matching.

This is followed by another study by [89] that explored the design of an exhaust air energy recovery wind turbine generator to promote energy conservation in commercial buildings. The research concluded that integrating an energy recovery wind turbine generator with a cooling tower resulted in various benefits, including a reduction in power consumption of the fan motor, increased intake air speed, and improved performance of the VAWTs. The VAWTs showed a 7% increase in rotational speed and a 41% reduction in response time. This system has the potential to generate

supplemental power for building lighting or feed it into the electricity grid to meet energy demands in urban buildings. The consistent energy output of this system makes it easier to design downstream systems. Moreover, given the prevalence of cooling tower applications and artificial exhaust air resources worldwide, this system has significant market potential. Figure 10 illustrates the conceptual design of an exhaust air wind energy recovery turbine generator located at the outlet of a cooling tower on the rooftop of a building, as envisioned by an artist.

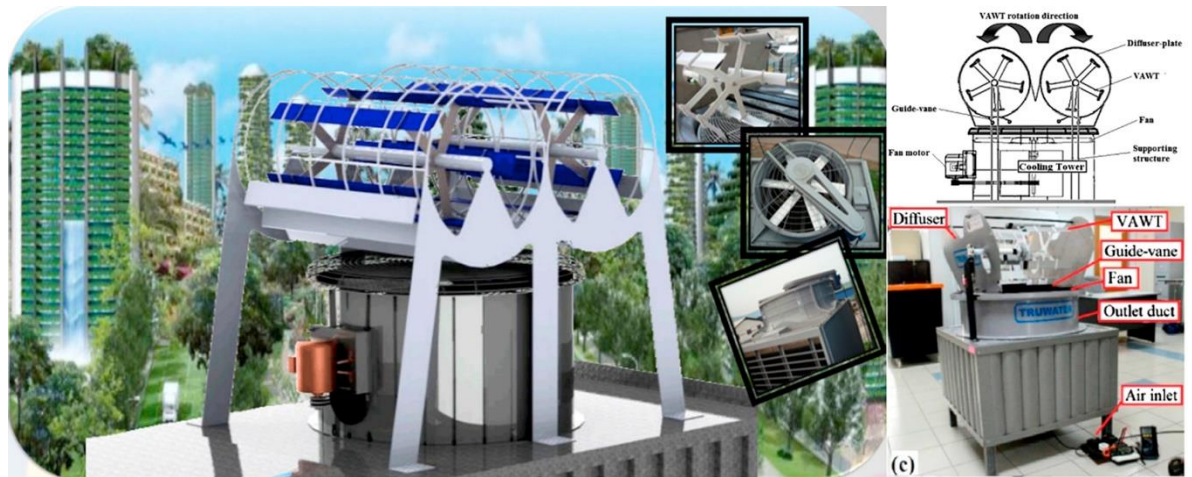


Figure 10. Test configuration for cooling tower with VAWTs and enclosure by [89]

Most studies on vertical-axis wind turbines (VAWTs) concentrate on their design and efficiency of power coefficient when incorporated into buildings. These studies analyse the design and positioning of VAWTs in urban settings, exploring different factors that influence their performance, such as rotor solidity, turbine position, and wind flow conditions.

2.2.1.3 Diffuser augmented wind turbine wind turbine

The aerodynamic performance of both horizontal and vertical axis wind turbines can be improved using a shroud or duct surrounding the rotor blades, known as diffuser augmented wind turbines. A diffuser augmented wind turbine reduces drag and enhances efficiency through a specific aerodynamic design. In this setup, the diffuser is a shroud or duct that surrounds the rotor blades, with a shape that initially narrows and then widens as it extends from the wind entry point. As the wind flows through the narrower part of the diffuser, its velocity increases due to the reduction in cross-sectional area. This accelerated wind is then directed smoothly towards the rotor

blades. The diffuser also streamlines the airflow, reducing turbulence and thereby decreasing drag on the blades. Through minimising resistance and channeling the wind more effectively, the diffuser helps the turbine capture wind energy more efficiently, resulting in increased power output. Thus, the diffuser improves overall turbine performance by enhancing wind flow dynamics and reducing aerodynamic drag [90].

In Krishnan [91] study, three-dimensional model analysis was conducted on a building-mounted vertical axis wind turbine (VAWT) equipped with a diffuser-shaped shroud using CFD. The study aims to enhance the power coefficient of the wind turbine by optimising the blade position and geometry and using a diffuser-shaped shroud. The results show a 2.5-fold increase in the coefficient of power, from 0.135 to 0.34, by incorporating the diffuser and other modifications. The study suggests that future research should focus on optimising the diffuser shape, analysing the impact of other turbine parameters, and examining the turbine's performance in different flow directions. In addition, the study identifies the optimal position and geometry of turbine blades.

Bhakare et al. [92] conducted research on the design of a convergent-divergent duct to power a household room in Nasik, India, using a diffuser augmented wind turbine on the rooftop, while considering safety, noise, and space limitations. The study used Ansys Fluent to analyse various duct designs. The results revealed that the divergent section significantly affected the velocity augmentation factor, which was optimised to achieve a value of 1.35 against the desired value of 1.4. The blade specifications were derived, and a generator was selected to produce the required power output of 100-250 W for wind speeds of 10-14 mph. The study predicted an energy generation of 1.2-2 kWh for 12 hours of operation per day at the specified wind speed, but actual results may vary due to mechanical and electrical losses. The study also suggested that increasing the divergent section's size or blade length can boost power output, but space constraints limit their sizes. The addition of a vortex generator in the duct can enhance the velocity augmentation factor by up to 15%.

A research study conducted by [93] focused on optimising the performance of ducted wind turbines and integrating them into the built environment. The study involved both numerical and experimental investigations into design methodology, atmospheric

boundary layer (ABL) profiles, and wind tunnel testing. The study found that the optimum ducted wind turbine was able to restore wind speeds lost at the rotor due to building presence and demonstrated better responsive behaviour than a test bare wind turbine. The study also utilised a new technique in the design, manufacture, and assembly of a lightweight, portable, durable, and easily accessible full-scale diffuser augmented wind turbine prototype. Fluid flow characteristics and performance parameters were analysed based on CFD results, and velocity contours for both the shroud case and the shroud and building test section were presented, with the velocity distribution observed to increase through the shroud to a maximum at the rotor where power is generated. However, the distribution of velocity along the rotor diameter was less uniform for the roof-mounted shroud than for the free-stream shroud. Figure 11 shows the velocity contours for both cases.

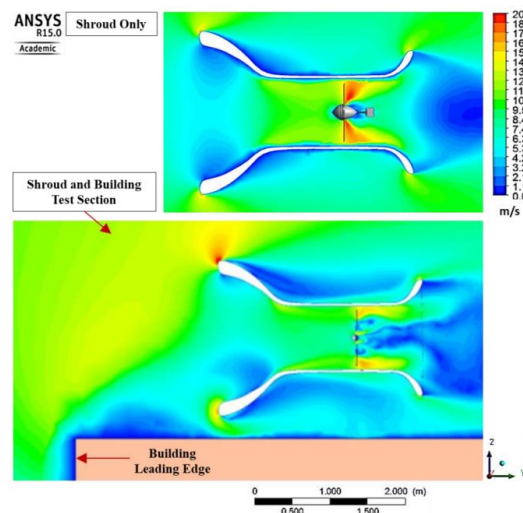


Figure 11. Velocity contours of shroud and building test section in comparison with shroud case [93]

The CFD tool was also used to investigate the airflow distribution around and inside the DAWT installed into the building structure [94]. The CFD analysis revealed that the velocity was increased by 1.52 times at the diffuser throat, which was in close agreement with the predicted value of 1.6 from the earlier design stage. The velocity was determined by comparing the mass flow average at the throat to the upstream velocity at the same height. Figure 12 (a) illustrates the flow pattern near the building with the diffuser, which is similar to that without the diffuser, but with Figure 12 (b) streamlines at the diffuser inlet indicating an acceleration of the flow. The diffuser on

the test building effectively took advantage of the local flow acceleration, as predicted during the design stage.

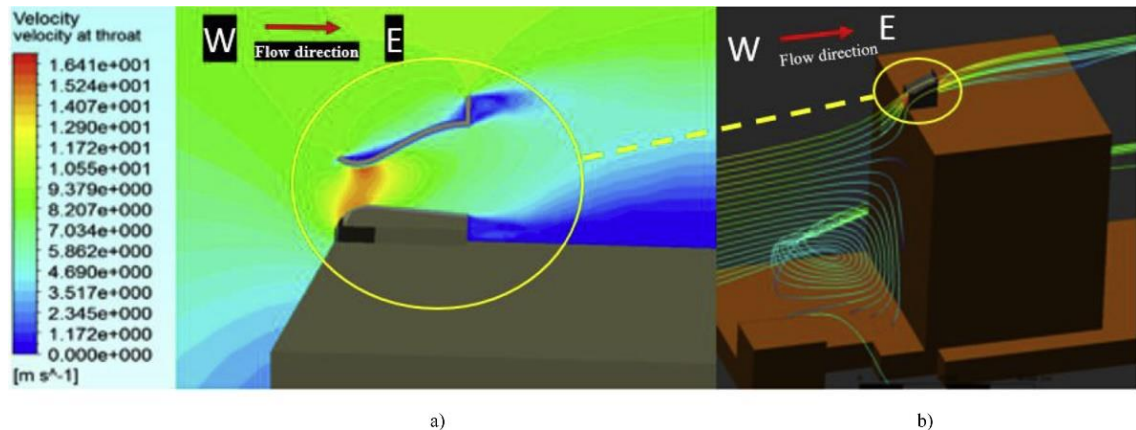


Figure 12. (a) The velocity contour at the symmetry plane of the diffuser, (b) illustrates the velocity streamlines from a perspective view of the chosen building [94]

Abu-Thuraia et al. [95] conducted a study on a novel configuration of a building-mounted Savonius turbine with seven blades enclosed inside a shroud or duct, equipped with four deflectable guide vanes at the entrance. The research involved simulations to compute the power coefficient (C_p) of the turbine for different wind orientations. It was found that the C_p value remains high for small deviations of wind but decreases by half when the wind direction reaches 45°. When guide vanes were fixed at 35°, 45°, and 55° relative to the horizontal direction, the highest C_p value was achieved at 55° with a value of 0.333 and TSR of 0.5. The guide vanes enable control over the flow through the turbine and can enhance the turbine's capacity factor. Although the turbine's performance decreases with guide vanes at TSR of 0.5, neighbouring TSR values of 0.48 indicate a C_p value of 0.336. Future studies will include the calculation of the power coefficient of the turbine at various vane angles and simulation of different wind directions with guide vanes attached.

In conclusion, studies have demonstrated the potential of shrouds and ducts in increasing the power output of building-mounted wind turbines. The use of a diffuser-shaped shroud can increase the power coefficient of a vertical axis wind turbine by up to 2.5 times, while a convergent-divergent duct can achieve a velocity augmentation factor of up to 1.35. Adding guide vanes in a ducted Savonius turbine can also improve its performance by controlling the flow through the turbine. These findings can

contribute to the development of sustainable and renewable energy sources. Further research in this area includes optimising the design of shrouds and ducts, exploring the impact of other turbine parameters, and investigating the performance of these turbines in varying flow directions.

2.2.1.4 Other types of small-scale wind energy harvesting systems

Alternative designs of small-scale wind energy harvesting systems have gained increasing interest in recent years. One such design is the cross-axis wind turbine (CAWT) proposed by [96]. This technology uses a novel cross-linked configuration of both horizontal and vertical turbine blades. As shown in Figure 13 (a), the CAWT consists of six horizontal blades and three vertical blades mounted on a supportive frame that rotates on a vertical axis. The central shaft is directly fixed to the generator, and the horizontal blades act as connectors linking the hub to the vertical blades via six connectors. Figure 13 (b) shows the CAWT installed on top of a building, while Figure 13 (c) demonstrates the CAWT CAD model.

According to [96], the CAWT has been found to produce 2.5 times more power than a conventional VAWT in the same wind conditions. However, continuous testing and development of the technology is required, and the actual energy output of the CAWT is yet to be determined. Figure 13 (d) presents the relationship between the coefficient of power (C_p) and the tip speed ratio (TSR) for different pitch angles of the horizontal blades in the CAWT. The curves demonstrate a consistent pattern where C_p increases with TSR, reaches a peak value between 0.89 and 1.16, and then decreases as TSR continues to increase. The study found that a pitch angle of 10° generates the highest C_p values, which is attributed to the optimal angle of attack and laminar flow along the blade. The results also indicate that varying the pitch angle above or below 10° significantly decreases the C_p values, emphasising the significance of the pitch angle in the CAWT's performance.

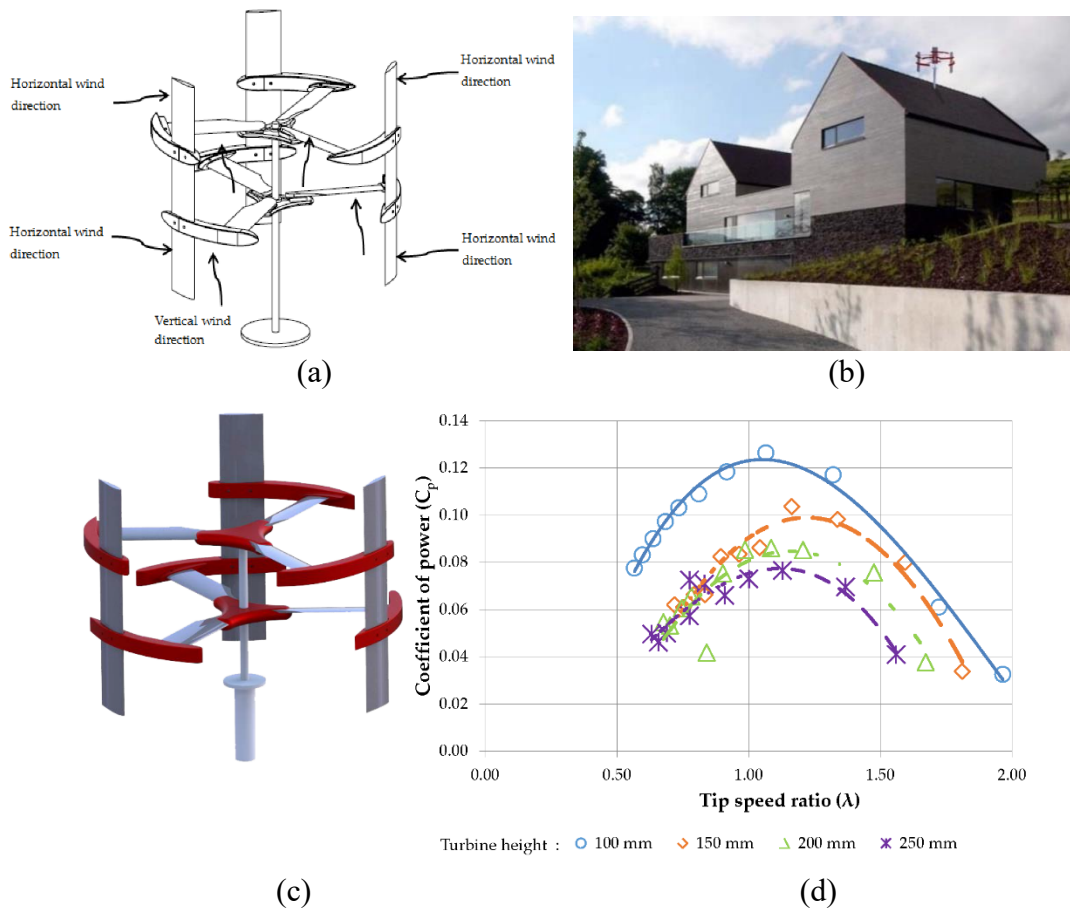


Figure 13. CAWT (a) configuration and (b) CAWT on top of the building (c) CAWT CAD Model and (d) power coefficient plotted against the tip speed ratio for various pitch angles [96].

The limitations of traditional wind turbines for building integration include the need for building modifications and limited space. To overcome these limitations, [63] proposed a novel building-integrated wind turbine system (BIWT) that generates electricity using wind pressure on the building skin, as shown in Figure 14 (a-b). The system is composed of a guide vane and an optimally shaped rotor, and its optimal configuration was determined using CFD analysis. The system's performance was evaluated through two-step experiments, and it was estimated to be capable of supplying 6.3% of the electricity needed for a residential building. Unlike other BIWT systems, this system takes advantage of wind pressure that acts on the building walls, eliminating the need for any structural reinforcement or alteration. This is because the wind pressure is already considered during the building design stage.

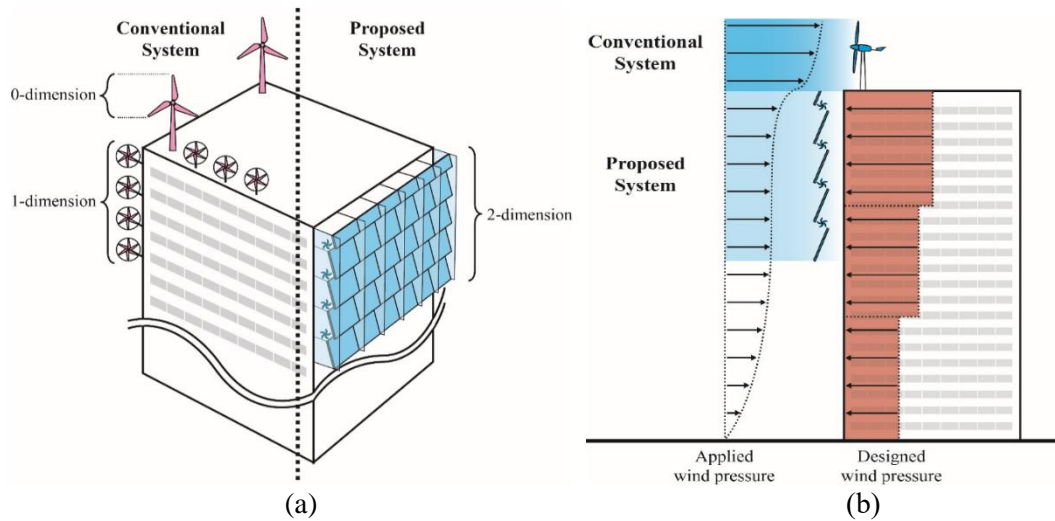
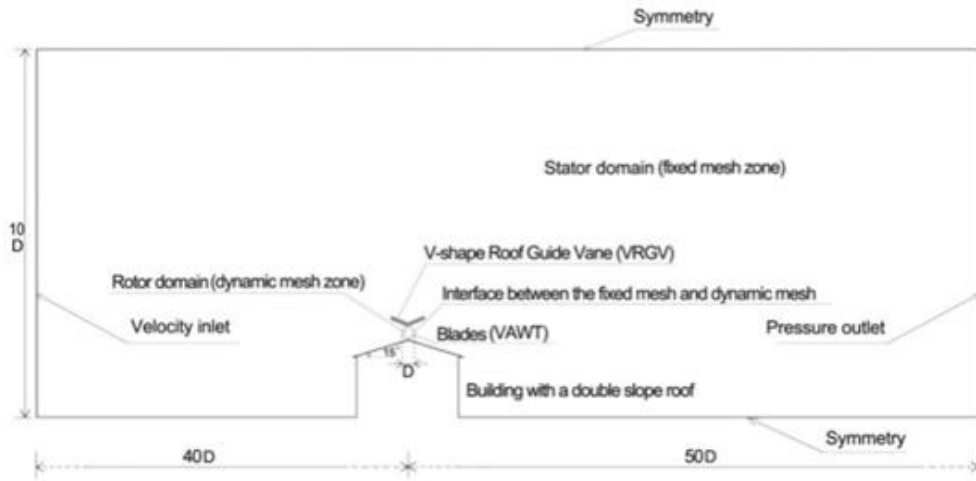


Figure 14. Comparison of the installation area between the (a) conventional BIWT and proposed system (b) structural aspect of the proposed system [63]

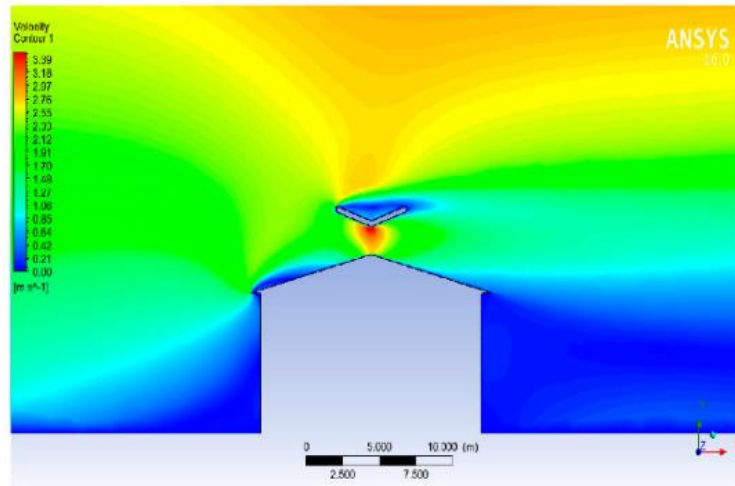
A novel VAWT system was developed by [97] to generate electricity for building usage. VAWTs were mounted between a gable roof and a V-shaped roof structure, and the Venturi effect was created by the upper V-shaped roof and gable roof, which increased wind speed and enhanced the system's performance. The experiment conducted showed a 36% increase in wind speed and an estimated energy generation of 773.16 kWh/year. The design also includes solar panels, water harvesting, a transparent roof, and ventilation vents. Figure 15 shows the (a) proposed design of VAWT with the V-shape roof guide vane (VRGV) with a solar and wind power generation system mounted on an eco-roof system, (b) boundary condition, CFD model and domain size, and (c) wind velocity contour distribution. The position of the turbines between the upper V-shaped roof and gable roof creates a concentrator and diffuser effect, enhancing the Venturi effect and resulting in improved energy generation efficiency, making the system a promising solution for building electricity generation.



(a)



(b)



(c)

Figure 15. VAWT with the VRGV (a) design and components (b) boundary condition and the domain size of the VAWT with the VRGV and (c) wind velocity contour distribution for the VRGV with pitch angle 19.5° [97]

Another design called the Wind Booster was proposed in the study [98] to improve energy generation. The study presented a methodology for selecting and optimising

the main components of the Wind Booster, using CFD and DOE techniques to design a Wind Booster for a VAWT in Mexico City. A Wind Booster is an aerodynamic structure added to a wind turbine system to enhance airflow and increase wind speed entering the turbine. It typically includes shrouds, diffusers, or other modifications designed to channel and accelerate wind towards the blades, reducing drag and funnelling more wind energy into the turbine. Figure 16 shows the (a) design of the primary function of a Wind Booster is to increase the efficiency and power output of wind turbines, particularly in areas with suboptimal wind speeds. Wind Boosters can be integrated with both Vertical-Axis Wind Turbines (VAWTs) and Horizontal-Axis Wind Turbines (HAWTs) to maximise energy generation by improving the performance of existing turbines. The results of the experiment showed a 35.23% increase in torque with the optimised Wind Booster configuration, demonstrating the potential of this methodology to improve wind turbine system performance. This proposal could be useful for researchers looking to implement the best possible wind turbine for their specific location, considering the varying wind behaviour in different cities.

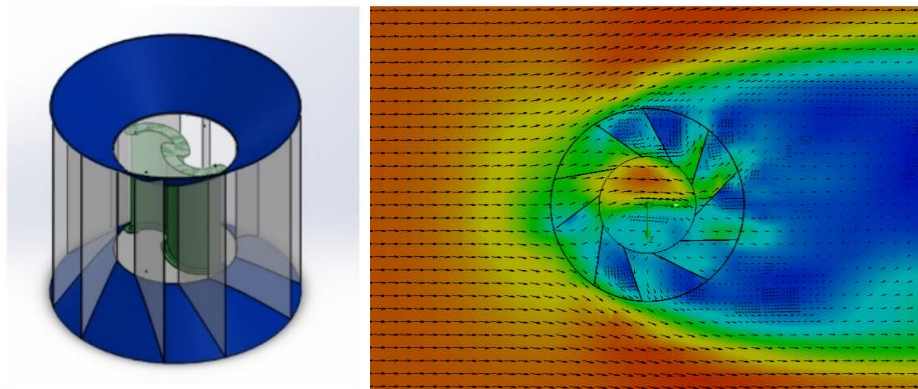


Figure 16. Wind Booster (a) 3D model and fluid analysis [98]

Overall, various studies have introduced new designs for building integrated wind energy harvesting systems, which have shown promising results for energy outputs. However, it is important to note that the design and configuration of each system have a significant impact on its power performance. Therefore, further research is necessary to determine the optimal configurations for different locations and conditions. This research can lead to the development of more efficient and effective wind energy

harvesting systems, which can ultimately contribute to reducing greenhouse gas emissions and addressing global climate change.

2.2.2 Wind-induced vibration technologies

With the rapid expansion of the internet of things (IoT) and wireless condition monitoring systems, energy harvesters that utilise ambient energy have become essential for creating energy-autonomous systems. Among these, micro/small-scale wind energy harvesters have gained significant interest due to their high-power density potential and the abundance of wind energy in various application areas, such as cities and buildings [39]. This section reviews the latest advancements in micro/small-scale wind energy harvesting systems, which encompass galloping-based, vortex-induced vibration, and flutter-based technologies. Various energy coupling mechanisms were studied, considering different designs, environmental conditions, and method analyses. Furthermore, we examined the key factors necessary for achieving high efficiency in these systems when operating at lower wind speeds.

Wen et al. [38] explored the design and key factors contributing to high efficiency in low wind speed conditions for micro/small-scale wind energy harvesting systems. These include the three different designs such as galloping, flutter, and vortex-induced vibration (VIV). The results showed that VIV-based technology had the potential to achieve optimal efficiency with the right design. However, VIV's operational wind speed range is limited due to its operating mechanism. On the other hand, aeroelastic flutter design employs a different approach and involves negative damping, causing device damage at high wind speeds. Galloping shares similar features with VIV and aeroelastic flutter, but its analytical model has not been established. The study suggests that more research is necessary to develop analytical models for galloping to improve its efficiency.

Wind-induced vibration technology employs lift and drag forces to convert wind flow energy into electrical energy, making it suitable for low wind speed deployment in the sub-centimetre range. This is unlike rotational motion, where the vibration on the body structure can be easily converted into electrical energy. Dynamic instabilities generated from the interaction of unsteady inertial, elastic, and aerodynamic forces are

observed in flutter and vortex-induced vibration (VIV)-based wind-induced vibration. Galloping-based wind-induced vibration combines the characteristics of aeroelastic flutter and VIV. These small-scale wind-induced vibration systems can operate in low wind speeds and a wide range of operational wind velocities, making them ideal for building-integrated wind energy harvesting systems. These technologies have the potential to harvest energy from the roof building structure in low wind speeds and non-uniform wind flow, thereby addressing the limitations of conventional wind turbines that are non-operational when subjected to low wind speeds [38].

2.2.2.1. Galloping-type energy harvesting

Galloping is an aeroelastic phenomenon observed in structures exposed to wind flow, characterised by large-scale, low-frequency oscillations driven by alternating lift forces generated due to the asymmetrical shape of the structure [99]. Although galloping can generate vibrations in multiple directions, it can also cause dynamic instability due to negative damping. To implement galloping technology in building structures, additional research is required to identify appropriate designs that can function in non-uniform wind flows, investigate the effects of wind acceleration on the energy harvester, and comprehend the airflow distribution around the body structure

A wind tunnel experiment conducted by [100] investigated the power and efficiency of small-scale wind-induced galloping energy harvesters with different tip cross-section shapes, including triangle D-shape, square, and rectangle. Figure 15 demonstrates the proposed galloping energy harvesting system (a) showing top and the side view and (b) experimental setup [100]. The study found that the square profile achieved a maximum power of 8.4 milliwatts. The results showed that the square profile achieved a maximum power output of 8.4 milliwatts. This achievement is attributed to the square profile's balanced aerodynamic characteristics, which minimise drag and turbulence, optimising the conversion of wind energy into mechanical oscillations necessary for galloping. The symmetrical shape of the square profile also contributes to stable and predictable oscillatory motion in response to wind flow, crucial for consistent energy generation without excessive vibration or structural fatigue. Moreover, the square shape facilitates efficient coupling with the energy

harvesting mechanism, enhancing resonance properties and enabling effective energy transfer to electrical generation components. Therefore, the study suggests that future research in this area should consider the square cross-section shape for its potential to improve the efficiency and reliability of small-scale wind-induced galloping energy harvesters. Based on this finding, the authors suggested that a square cross-section should be considered for future research in this area.

Zhao et al. [101] also examined various shapes, including funnel, triangle, and square, in a wind tunnel with a closed direct flow. Figure 17 demonstrated the design and experimental set up. The tested shapes included funnel, triangle, and square profiles, and the experiments were conducted at various wind speeds. The results showed that the funnel profile provided the highest power density of $2.34\text{mW}/\text{cm}^3$ at a wind speed of $7\text{m}/\text{s}$, followed by the triangle profile with $1.56\text{mW}/\text{cm}^3$ at a wind speed of $9\text{m}/\text{s}$, and finally, the square profile with $0.207\text{mW}/\text{cm}^3$ at a wind speed of $13\text{m}/\text{s}$. Based on these results, a wind energy harvester design was proposed that can achieve high normalised harvesting power and a broad working wind-speed range.

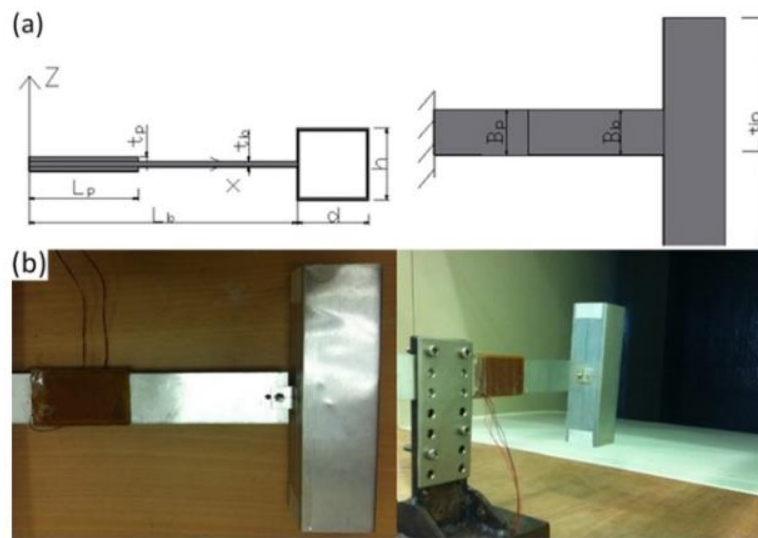


Figure 17. Proposed design of galloping energy harvesting system (a) showing top and the side view and (b) experimental setup [101]

Another design of galloping based wind energy harvester using quadruple halfbach arrays was introduced by [102]. The performance of the system was evaluated through numerical simulations and wind tunnel tests. Results showed that the electrical load resistance was influenced by the onset velocity and vibration amplitude of the harvester during galloping. The study suggested that adjusting the external load

resistance could enable the harvesting system to generate power even at low wind velocities. For example, the system was able to produce 8 mW of output power at a wind speed of 12 m/s.

In [99] developed a wind-induced energy harvesting system based on the galloping mechanism using a cut corner prism. The system created a pressure difference between the upper and lower surfaces of the prism, as shown in Figure 18. CFD simulations were used to assess the system's efficiency, and the results indicated that the cut corner design reduced shear layer reattachment and improved backflow, leading to an increased pressure difference. An experimental study was conducted to determine the impact of size on harvesting performance, and the results showed that a parallel side with a length of $0.6B$ and a windward side length of $0.4B$ could generate 47.5 milliwatts at a wind speed of 6.24 m/s, which is 261% higher than the square prism. The " $0.6B$ " is the length of the parallel side of the prism, while " $0.4B$ " indicates the length of the windward side. These dimensions are important in optimising the performance of the system by affecting the airflow and pressure distribution around the prism, which influence the efficiency of energy harvesting.

In the study by [99], the terms " $0.6B$ " and " $0.4B$ " refer to the dimensions of the cut corner prism used in their wind-induced energy harvesting system. Here, B represents a characteristic length of the prism, such as the length of one of its sides.

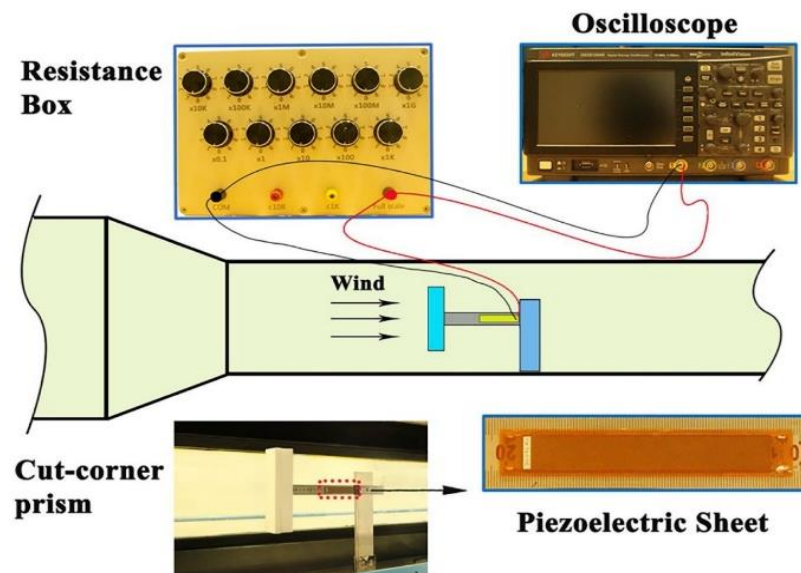


Figure 18. Design of the energy harvesting system based on galloping mechanism using cut corner prism [99]

Zhang et al. [103] proposed an electromagnetic energy harvester for extracting energy from environmental airflows to power sensors. The design aimed to improve environmental adaptability and output power, and involved a Y-shaped bluff body that induces an aeroelastic response to cut magnetic induction lines. The team constructed a theoretical model and experimentally verified their design, achieving an average power output of 2.5 mW at a wind speed of 4 m/s. This result was higher than those obtained with existing aeroelastic energy harvesters. The study also demonstrated the harvester's adaptability in air-conditioner vent conditions, offering guidance for the development of efficient electromagnetic energy harvesters for airflow power generation, with potential applications in self-powering structural health monitoring sensors for buildings and bridges.

Another design of a galloping-based wind energy harvester was proposed in [104]. The design comprises of rotatable transverse galloping piezoelectric energy harvester (EH. The study investigated three different cross-section bluff bodies (equilateral triangle, square, and D-section) in natural wind conditions. The results showed that a rotating base (RB) configuration produces a higher cut-in speed compared to a fixed base (FB) configuration, and the square bluff body is the most effective in terms of voltage production, followed by the triangular shape and then the D-section. This study is the first to use these prisms in an open environment and proposes a tuneable harvester that can adapt to varying wind directions, providing guidance for optimising bluff body shape suitable for real-world conditions.

In conclusion, recent studies on galloping-based wind-induced vibration technology have demonstrated promising results in terms of energy harvesting and power performance in laboratory or numerical simulation settings. However, there is a lack of studies exploring its integration with building structures. The technology has the potential for energy harvesting at wind speeds suitable for use on buildings or roofs and has advantages in terms of being lightweight and cost-effective compared to traditional wind turbines. Nevertheless, there is a need for more information on the costs associated with this technology, and a comprehensive analysis of its techno-economic aspects would be necessary for commercialisation viability. Further research

and development in this area could lead to the practical application of galloping-based wind-induced vibration technology in building energy systems.

2.2.2.2. Flutter-type low-energy harvesting

Flutter is another instability, involves rapid, self-excited oscillations of structures caused by the resonance between aerodynamic forces and the natural frequencies of the system. It is characterised by negative aerodynamic damping effects, particularly problematic at higher wind speeds, which potentially leads to structural damage if not properly managed. Flutter's occurrence demands precise design considerations to prevent destructive vibrations and ensure operational safety and efficiency in wind energy systems. Most previous research on flutter-based wind energy harvesters has relied on numerical analysis or wind tunnel experiments, focusing on stand-alone systems. Integrated flutter-based wind energy harvesting systems in building structures have received limited research attention [105] conducted a study on the use of a flutter-based aeroelastic belt as a device for small-scale wind energy harvesting systems integrated into urban building structures. The device was composed of electromagnetic coils, a tensioning membrane, and power conditioning device was evaluated using CFD analysis in various wind directions, wind speeds, placements, sizing, and physical parameters.

Figure 19 illustrates the dimensions and schematic of the aeroelastic belt wind energy harvesting system prototype. The aeroelastic belt used for the wind tunnel testing featured a circular casing with an outer diameter of 54 mm and an inner diameter of 12.5 mm. The casing had an outer thickness of 20 mm and an inner spacing for coil winding of 12 mm. The harvester used a 1 cm wide section of tape material, with 0.5 m of its length exposed to airflow, which was found to be effective for initiating flutter while maintaining the economical use of tape material. These dimensions were crucial to achieving optimal flutter performance and ensuring the magnets remained securely attached during testing. The study found that a roof building with an apex angle of 45 degrees achieved the highest power output of 62.4 milliwatts at an incoming wind speed of up to 6.2 m/s. The device's simplicity makes it cost-effective and easy to integrate with other technologies.

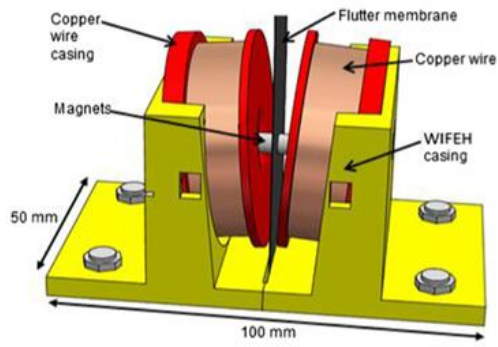


Figure 19. Dimensions and schematic of the aeroelastic belt wind energy harvesting system prototype [105]

Different design of flutter-based energy harvesting technology was presented in [106], which consisted of a cuboid chamber, a piezoelectric cantilever, and a resonant cavity. The system was capable of temperature monitoring and data transmission to a receiver. The experimental results indicated a power output of 1.59 milliwatts for a 20 k Ω resistor at a wind speed of 11.2 m/s. In addition, the self-powered wireless sensor network (WSN) operated correctly as the wind speed increased from 6 to 11.5 m/s.

Chawdhury and Morgenthal [107] investigated the use of a cantilever beam in aeroelastic instabilities and flutter phenomena for small-scale wind energy harvesting. The study employed fluid-structure interaction (FSI) simulation to evaluate the performance of the wind energy harvester. Moreover, a CFD solver based on the vortex particle method (VPM) was used to examine the susceptibility of a T-shaped cantilever beam to small-scale wind energy harvesters. A strategic optimisation study of the T-shaped wind energy harvesting system was carried out to measure the generated energy and wind speeds. The results showed that the projected energy output and wind flutter speed were consistent in various electrical resistances, and the highest power output achieved was 5.3 milliwatts at a wind speed of 8 m/s. The CFD simulations were consistent with wind tunnel test data, indicating the accuracy of the simulation.

The piezo-electric energy harvesting system presented in [108] comprises of a piezoelectric cantilever beam with a proof mass attached to its free end. The beam is fixed at its base to a mounting block that is connected to the structure being monitored. As illustrated in Figure 20, when the structure undergoes vibration, the proof mass on the cantilever beam oscillates, causing a deformation in the piezoelectric material, which generates an electrical charge. This charge is collected by electrodes attached to

the piezoelectric material and is then transmitted to a storage device, such as a battery, through a rectifying circuit. This compact and versatile system can be installed in various applications to monitor vibrations and convert them into useful electrical energy.

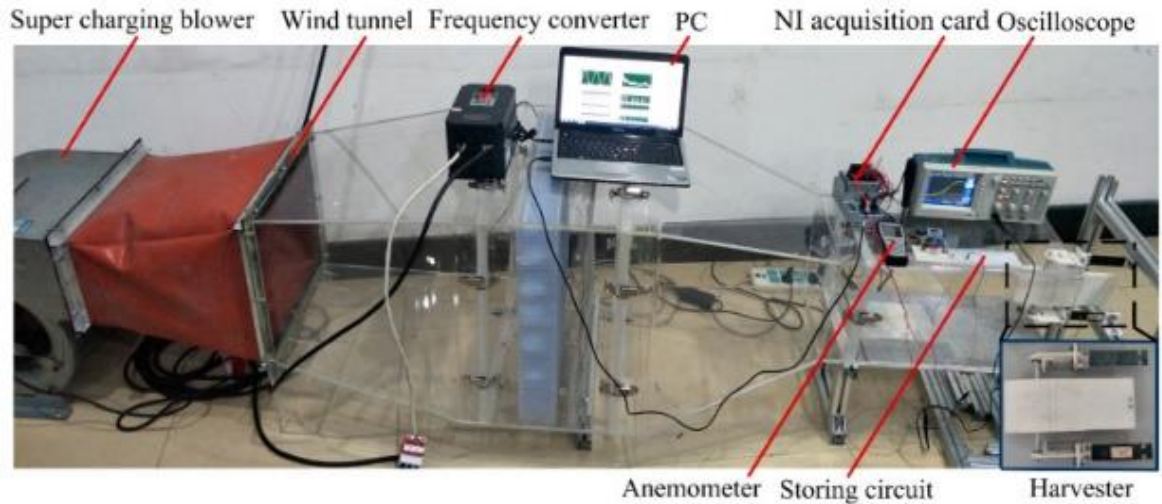


Figure 20. Schematic design of a piezo-electric energy harvesting system [108]

Bo et al. [109] proposed a bionic dipteran piezoelectric-electromagnetic composite energy harvester (BCEH) that utilises the flutter wing-flapping system of dipteran insects for ultra-low frequency vibration energy harvesting. The BCEH design is validated through finite element analysis, with parameters optimised to enhance vibration energy harvesting by reducing inherent frequency. Experimental results demonstrate that BCEH can generate an average power of 69.14 MW at 5 Hz ultra-low frequency vibration, making it a promising technology for energy extraction in low excitation.

With the research work of [110] a coupled formulation for modelling piezoelectric energy harvesters based on vortex-induced vibration (VIV) was examined. This formulation includes multiple piezoelectric materials and allows for arbitrary locations to be modelled. To validate the numerical simulations, experiments were conducted for single and two-cylinder piezoelectric energy harvesters in tandem. The model was then used to evaluate the performance of three piezoelectric energy harvesters in tandem. Results demonstrated the accuracy of the proposed model and its cost-effectiveness compared to other experimental methods.

In [111] study, a wind energy harvesting system based on aerofoil flutter was investigated using a numerical simulation that considered pitch and plunge motion degrees of freedom. The system incorporated an aerofoil section with piezoelectric coupling and pseudo-elastic hysteresis of shape memory springs to capture wind energy. The study analysed the post-flutter mechanism and found that the amplitudes of electrical and mechanical outputs increased with airflow speed for load resistance. The highest power output achieved was 120 mW for the best load resistance at 4.5 N and 14 m/s. Figure 21 displays the peak electrical power output from plunge displacement. [119] concluded that the addition of pseudo-elastic hysteresis was beneficial to the design of aerofoil flutter wind-induced energy harvesters. This design element was found to improve power performance compared to hardened steel springs.

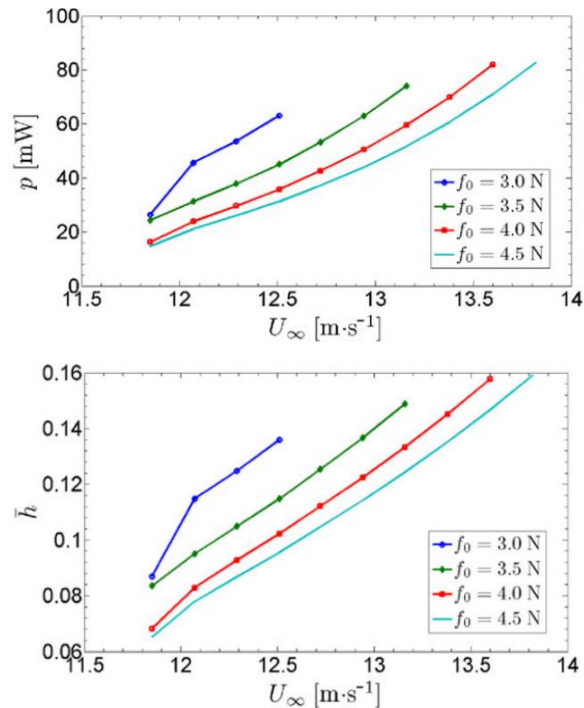


Figure 21. Maximum electrical power output obtained from the amplitude of plunge displacement was analysed and reported [111]

A different transducer was applied to the energy harvester in [112]. A novel aeroelastic flutter wind energy harvesting system was developed, incorporating an electret transducer as the energy converter. The system utilised the flutter effect, with a membrane oscillating and interacting with two flat electrodes. The electret transducer directly transformed the motion into electrical power. The study evaluated various models and demonstrated that a 2.7 cm³ prototype could generate 481 μ W (178 μ W

cm⁻³) of power at 15 m/s and 2.1 mW (782 μW cm⁻³) at 30 m/s when the electret was charged at 650V.

Whereas in [113], a hybrid nanogenerator was designed by optimising the shape and structure of a triboelectric nanogenerator (TENG) film and an electromagnetic generator (EMG) to collect wind energy and convert it into electrical energy for small electronic devices and micro sensing systems. The combined system improves energy collection and reduces charging time. A capacitor was integrated with the hybrid generator to create a self-powered system, which achieved real-time sensing detection of temperature and humidity in greenhouses and fan malfunctions. This study contributes to the development of practical wind energy harvesting devices for sensing systems.

After reviewing various studies, it was observed that only one of them investigated the energy harvesting potential of an aeroelastic belt integrated into a building's roof structure using wind-induced vibrations caused by flutter. While this study showed promise, it was limited to laboratory-scale experiments and numerical analyses through CFD simulations. The results indicated that the proposed design could be easily integrated into buildings to harvest energy from flutter-based wind-induced vibrations, while also providing advantages such as low cost, simple structure, and modularity. However, the other designs examined were standalone wind energy harvesters, not integrated into the building, and were only evaluated through laboratory or numerical simulations. Further research is needed to evaluate the performance of these technologies in real-world field test conditions and conduct techno-economic analyses.

2.2.2.3 Vortex-induced vibration-type low-energy harvesting

Vortex-induced vibration (VIV) occurs when structures interact with fluid flows, generating vortex shedding and resulting in oscillatory forces. While VIV-based designs show promise in optimising energy capture in low wind speed conditions, their practical application is constrained by the specific flow dynamics they rely upon. Managing VIV involves careful engineering to harness its benefits while mitigating potential drawbacks related to operational stability and reliability [114].

Lee et al. [114] developed a microelectromechanical wind energy harvesting device that utilised vortex induced vibration (VIV) to generate electrical energy. The device consisted of a cylindrical oscillator connected to a piezo-electric microelectromechanical system. To evaluate the harvester's power performance, a wind tunnel experiment was conducted, which showed that the harvester generated a power output in the nanowatt range. The study also found that the use of multiple cylinders increased the output compared to a single cylinder. In addition, the researchers conducted CFD simulations to examine the behaviour of vortex shedding from the cylinder and found that upstream cylinders induced high periodic transverse velocity components on the approaching wind stream facing downstream cylinders, enhancing the vortex-induced vibration response. The study concluded that the proposed model has potential for cost-effective power generation for small-scale off-grid WSNs, with a simple integration of the sensor and harvester.

In [115] study, a bionic structure to a vortex-induced vibration (VIV) model to improve the amplitude response and reduce the VIV threshold wind velocity. The study involved creating 12 prototypes using different pit sizes and hemispheric protrusions attached to a smooth cylinder. The harvester with the bionic structure outperformed the smooth cylinder in terms of energy harvesting. The bandwidth increased from 39.3% to 51.4% when the threshold wind speed decreased from 1.8 m/s to 1 m/s. The harvester with a 10mm pit and 5 columns produced the highest power output of 1.2 milliwatts with 800 k Ω resistance, which was 0.57 milliwatts more than the smooth cylinder. The hemispherical structure harvesting system had a smaller voltage than the smooth cylinder, with a maximum voltage below 15 V and a decreased bandwidth. However, the hemispheric with three columns performed better for energy harvesting, with a power output improvement from 0.48 to 0.56 milliwatts at 35 V and 800 k Ω resistance at 3.097 m/s wind speed.

A different shape of the bluff body structure was proposed by [116]. The design featured tuned mass blocks on vertical beams and drive sheets to move the first two-order resonant frequencies as required, resulting in a superior capability to widen the frequency bandwidth with two adjacent power peaks. The harvester efficiently utilised the space and energy in the flow field behind the cylinder through interaction between the beam and the other two beams. Figure 22 illustrates the (a) experimental setup and

(b) harvester design. The e-shaped piezoelectric energy harvesting system showed up to 70% improvement in efficiency and 3 times increase in power compared to traditional piezoelectric harvesting systems based on VIV. The maximum output power reached 3.35 mW at resistive load, mean fluid velocity, and scale factor of 105Ω and 1.5 m/s. The proposed design was found to be suitable for powering actuators and Micro Electro-Mechanical System (MEMS) sensors at low velocities.

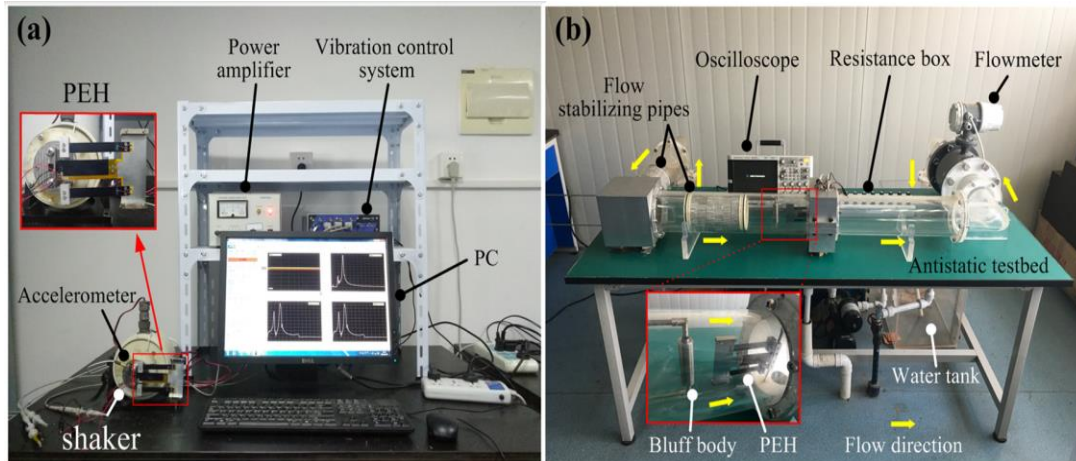


Figure 22. Actual image of (a) experimental setup (b) piezo-electric energy harvester in the circular flow arrangement [116]

Using an indirectly stimulated composite piezoelectric transducer, a novel non-contact vortex-induced vibration-based wind energy harvester is being researched to improve the dependability and environmental adaptability [99]. The study aimed to improve the harvester's dependability and environmental adaptability. Results indicated that increasing the transducer mass and reducing the shell mass led to an increase in wind speed bandwidth, vibration displacement, and output voltage as wind speed increased. An optimal load resistance of 300 k was employed to maximise output power. The highest power output of 1.438 mW was obtained from a single piezoelectric pre-bending beam, with a transducer mass of 65 g and a wind speed of 40.0 m/s. Moreover, the non-contact piezoelectric wind energy harvester could operate effectively over a wide wind speed range of 5.5 m/s to 40.0 m/s (corresponding to a wind speed bandwidth of 34.5 m/s) when an output voltage of 5 V was used as a reference value.

Zhang et al. [117] introduced a novel method for efficiently harvesting energy from low-speed wind using a triboelectric nanogenerator (TENG) based on vortex-induced vibration (VIV). The researchers constructed a theoretical model, which was validated

with experiments that revealed a lock-in region with significant vibration amplitude and output voltage. To increase the lock-in region and achieve higher power and power density, a tandem VIV-TENG model was designed. The practical application of the VIV-TENG was demonstrated by continuously powering wireless sensors, enabling self-powered wireless sensing in low wind speed environments. This study has significant implications for the development of sustainable energy sources.

The Vortex Bladeless company has developed a wind energy generator that uses vortex-induced vibration (VIV) technology to capture wind energy, as shown in Figure 23. Figure 23 shows the Vortex Bladeless (a) the configuration, (b) schematic design, and (c) VIV phenomenon in fluid dynamics [118]. The technology takes advantage of fluid mechanics by harnessing the phenomenon of vortex shedding, in which vortices are created in a cyclical pattern as wind flows past a blunt body. The VIV technology matches the frequency of these forces with the structure's frequency, causing the system to oscillate and enter resonance with the wind, resulting in up to 100 watts of power generation. This design is suitable for use in farmlands and for residential self-generation purposes, according to [119].

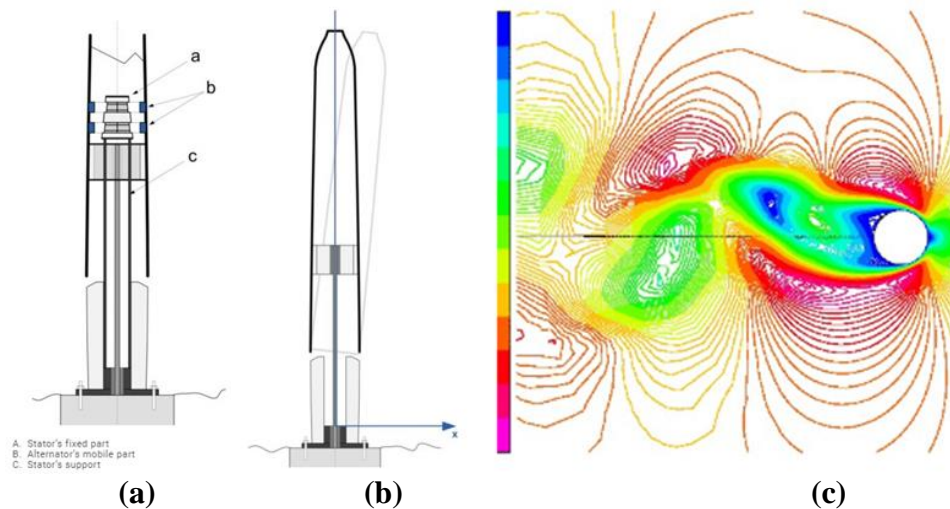


Figure 23. Vortex Bladeless (a) the configuration, (b) schematic design, and (c) VIV phenomenon in fluid dynamics [118]

Overall, it should be noted that while VIV wind-induced vibration energy harvesting has shown potential for building integration applications, none of the research conducted to date has integrated the wind energy harvester into building structures. Evaluations have mostly been conducted through wind tunnel testing or numerical

simulations. In addition, it has been shown that the technology can operate effectively at low Reynolds numbers and generate power outputs ranging from nW to mW. However, it may be possible to further improve these power output ranges by increasing the device's size and integrating it into the roof structure of pitched or curved buildings, taking advantage of the higher wind velocity in such locations.

2.3. Modelling methods for the evaluation and optimisation of wind energy harvesting systems

Although conventional wind turbines have been integrated into building structures for decades, their efficiency is highly dependent on environmental conditions and wind resources, which can be challenging to assess. To address this issue, researchers and engineers are exploring alternative and more affordable methods for wind resource assessment. Measuring wind speed, direction, and ambient turbulence is crucial for optimising energy capture and harvesting efficiency for conventional wind turbines. Cutting-edge software tools are used to create computer-generated environments that enable researchers and engineers to test their ideas and potentially disruptive technology before proceeding with development. These methods aid in evaluating wind resources and determining the potential for wind energy development. Hemida [119] highlights the importance of acknowledging these challenges and exploring alternative approaches to improve wind energy harvesting efficiency. In addition, [120-121] present different methods and software tools that aid in wind resource assessment and evaluation.

Wind-induced vibration technologies on a micro or small-scale present distinct challenges due to their smaller size and shape, often installed in confined spaces such as on buildings or in urban areas with numerous obstacles that can cause turbulence and drag. Designers must carefully choose materials that can withstand harsh weather conditions and consider the placement of the wind energy harvester to ensure its efficiency and durability.

2.3.1 Wind resource assessment tool for wind energy harvesting systems

Several methods including WAsP and CFD have been employed to evaluate wind resources in the built environment for small wind turbines. These methods are essential in understanding wind conditions, such as acceleration zones, recirculation, blocking,

and channelling, for micro-scale wind turbines. CFD is a numerical simulation method that employs mathematical models to predict wind speeds and patterns in a specific location, and it is sensitive to building height and shape, roof shape, wind direction, and turbine installation height and location. Although most CFD studies for micro-scale wind-induced vibration technologies focus on dynamic behaviour, such as vortex-induced vibration, galloping, and flutter-based mechanisms, these technologies are still in their early stages of research and development. Therefore, wind resource assessment investigations are necessary to enhance the design and increase the energy harvesting efficiency of micro-scale wind energy harvesting systems.

Calautit et al. [122] conducted a comprehensive review of recent studies on CFD simulations for micro to small wind turbines and wind turbines integrated with buildings. Their research indicates that CFD simulations can be an effective tool in predicting and optimising the performance of small-scale wind turbines, although ongoing improvements are needed to handle the complexity of turbulent flow. The review highlights the importance of CFD in reducing design costs, improving wind turbine performance, and enhancing wind power utilisation, especially in urban areas.

Whereas the study of [123], used a combination of long-term wind data analysis, weather patterns, and domain topography with CFD to improve wind power utilisation in the design of wind turbines for high-rise buildings in Hong Kong. The study found that wind power density was 1.3-5.4 times higher at 4 metres above the roof with 5-7 m/s inlet velocity. Wind power utilisation was found to be the most effective at the windward top roof in the dominant wind direction. The thickness of wind speed below 8 m/s was only 3.6 metres in these areas. The concentration effect of high-rise buildings resulted in a 4 times higher wind power enhancement for 7 m/s inlet velocity compared to 5 m/s, exceeding the expected 2.7 times enhancement based on general velocity-power models.

There are several methods available to consider the impact of orography on wind flow. One commonly used approach is the use of WasP software, which adopts a linear flow model and relies on terrain and roughness data to describe the wind climate in a particular area based on local wind observations. However, the latest version of WasP

has incorporated a CFD model to overcome the limitations of linear models in steep terrain. On the other hand, computational fluid dynamics methods use numerical techniques to solve Navier-Stokes equations that govern fluid motion. These techniques can be applied to detailed terrain models with high-resolution meshes, enabling the resolution of more complex flows at a higher computational cost [124].

A research study carried out by the University of Leeds used WasP software to assess the wind resource potential for a small-scale wind energy harvester installed on a building rooftop [42]. The study found that the harvester could generate substantial energy if installed in an optimal location with favourable wind conditions. Despite the complexity of the urban surface, the accuracy of the methodology used to identify suitable sites for small-scale turbines was reasonable. However, significant predictive errors were observed at some validation sites, possibly due to uncertainties in building height data, particularly for locations near the top of the building canopy. Minor changes in local building data can significantly affect predicted wind speeds. To improve the precision of wind speed predictions, height-based inputs such as average building heights and displacement heights need to be estimated with high precision. This may require providing a detailed description of the shapes and heights of local building roofs. Using more detailed input-building data may improve the accuracy of the model's predictions. It is worth noting that the WasP software has not been investigated for wind-induced vibration technologies such as vortex-induced vibration. Furthermore, there is no research available in the literature on flutter-based and galloping-based mechanisms using this software [42].

Bashirzadeh et al. [125] utilised a combination of CFX and WasP software to examine local micrometeorological characteristics of wind flow and the influence of complex urban topography by identifying areas of wind acceleration, recirculation, and blocking. It is important to understand the zones of wind recirculation and turbulent wakes to ensure high energy production and to protect the machine from excessive loading caused by gusts by avoiding installation in such areas. The turbulent nature of the rooftop of a tall building offers insights into the micro-siting of wind turbines. The study aimed to evaluate the effectiveness of the CFD package CFX with the wind atlas software WasP as a tool for assessing wind energy resources for small rooftop wind

turbines in a built environment. In addition, the research investigated the impact of wind power or turbulence kinetic energy on the rooftop.

In conclusion, CFD simulations have proved to be a useful tool in evaluating the potential of integrating wind turbines into buildings. The assessment of factors such as wind patterns and the influence of surrounding buildings is crucial in determining the placement of wind turbines and maximising the amount of power generated. Although there are some limitations to CFD simulations, ongoing improvements in technology and techniques have the potential to address these limitations and further enhance the accuracy of wind energy resource assessments in built environments. Overall, the use of CFD simulations in wind energy resource assessments for buildings has great potential for advancing the development of sustainable energy solutions and reducing carbon emissions.

2.3.2 Modelling of HAWT in building integration

Various CFD tools were employed to model HAWT incorporated into buildings. In [126], CFD simulations were used to model horizontal axis wind turbines (HAWT) integrated into buildings. The study aimed to identify the wind stream contours around the building with the HAWT and determine the optimal location for installing small wind turbines. Figure 24 shows the CFD modelling of a) turbine-building at 13.5 m height streamlines b) turbine-building at 21 m height streamlines [126]. Moreover, the CFD results indicated a growing wake effect on the roof of the building from the northern facade to the rear, suggesting that this location may not be suitable for installing small wind turbines. The study recommended a height of 21m above ground level for the installation of the turbines. However, the building was found to be a good site for wind projects due to the absence of structures that could interrupt the flow of wind resources in the area. The CFD simulations provided crucial information that was used to select the best place to install the turbines on the building.

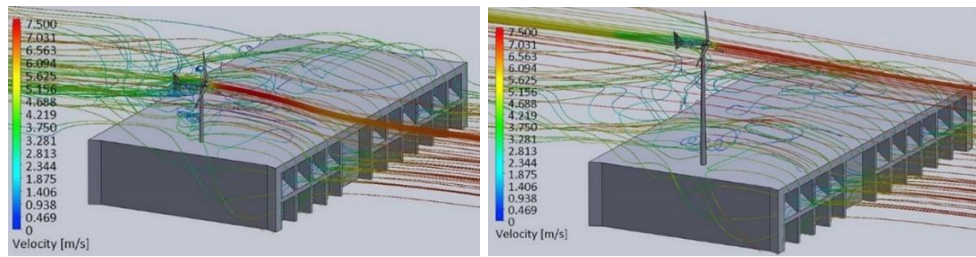


Figure 24. CFD modelling of a) turbine-building at 13.5 m height streamlines b) turbine-building at 21 m height streamlines [126]

Heo et al. [127] carried out extensive research using a CFD tool to analyse the aerodynamic characteristics of a 110-kW building augmented wind turbine (BAWT). Their 3D model investigated wind speeds and incoming flow angles of atmospheric boundary layers, showing that wind speed in the axial direction increases as it passes through buildings, due to flow separation from sharp corners. The BAWT was found to demonstrate higher aerodynamic power output than a stand-alone wind turbine of the same capacity, due to wind speed acceleration between buildings creating a concentration effect. This also allows the BAWT to achieve its designed power at lower wind speeds, providing an advantage. The buildings acted similarly to ducts or shrouds, allowing the power coefficient of the BAWT to exceed the Betz limit. The study found that the shrouded turbine achieved a power coefficient of approximately 0.65 for 4 m/s, which means it was able to convert 65% of the wind energy into mechanical energy. This value exceeds the Betz limit due to the enhancement provided by the shroud design, which improves the aerodynamic performance and increases the efficiency of the wind turbine beyond the traditional theoretical constraint.

Furthermore, the study examined the effect of incoming flow angle on flow patterns and aerodynamic power output. The flow patterns and power output were found to be asymmetric with respect to 0° of flow angle, due to the fixed rotating direction of the turbine blade and confinement of flows by the buildings. The maximum aerodynamic power occurred when the incoming flow angle was near -10° , and the aerodynamic power output of the BAWT with the incoming flow angle between -30° and $+20^\circ$ was higher than the designed power of the stand-alone wind turbine. However, when the wind direction had higher yaw angles than $\pm 30^\circ$, power output decreased sharply.

CFX tool was used in [128] to assess the accuracy of simulated flow around obstacles, a test case was performed using a rectangular structure with dimensions of 125 mm height, 100 mm width, and 150 mm length. The simulation results were then compared with CEDVAL wind tunnel data from Hamburg University, which included thorough documentation of boundary conditions and quality assurance checks during measurements. The CFX simulation domain and obstacle were set up in a similar manner to the configuration used in the CEDVAL data set, with a mesh size of 125 mm cell edge length and two inflation layers of 10 mm thickness near the walls. The wind flow in the CFX model was set to produce a Reynolds number of 37,250, and an equation was utilised to simulate the inlet velocity profile with a ground roughness of 0.007 m. The data set included values for longitudinal and vertical wind components at 603 points in the vertical plane and longitudinal and lateral wind components at 660 points in the horizontal plane. Furthermore, the flow around the structure was visualised in both horizontal and vertical planes.

In conclusion, CFD simulations have proven to be effective in modelling the aerodynamic characteristics of wind turbines integrated into buildings. Through analysing wind stream contours and wake effects, CFD tools can help determine the optimal location and height for installing small wind turbines. Furthermore, CFD simulations have demonstrated the effectiveness of building-augmented wind turbines in increasing aerodynamic power output. The accuracy of CFD simulations has also been evaluated through comparison with high-quality wind tunnel data, proving the reliability of CFD tools in modelling wind flow around obstacles. In summary, CFD simulations are a valuable tool for assessing wind turbines' aerodynamic performance in buildings, providing useful insights for optimal design and installation.

2.3.3 Modelling of VAWT in building integration

Similarly, various CFD tools were employed to model VAWT incorporated into buildings. Larin et al. [129] employed various CFD tools to model vertical axis wind turbines (VAWT) integrated into buildings. The study proposed a horizontal Savonius wind turbine configuration mounted on the upstream edge of a building to improve its low performance by utilising flow acceleration. To understand the behaviour of the turbine in low-speed urban environments, integrated simulations of both the building and the turbine were conducted, investigating the position, blade number, and

circumferential length of the turbine when mounted on a building. The CFD tool was used to solve flow fields of conventional and cup type turbines, and it was found that cup type turbines perform better in the right environment, resulting in a significant improvement in the power coefficient from 0.043 to 0.24, which is 5 times increase.

Elbakheit [130] conducted a study to optimise wing parameters for wind turbine application. The optimised wing parameters resulted in lower resistance to flow, which allowed for higher wind speeds to be harnessed. The study found that wind speed jets under the wing were suitable for Savonius turbines. While the introduction of turbine resistance lowered wind acceleration, it did not significantly affect the pressure drop, indicating that more power potential could be extracted. The optimised wing case resulted in a higher potential power output of 650.8 W/m² compared to the unoptimised case that yielded 400 W/m². The study also investigated the effect of varying turbine resistance on wind speed and pressure drop, finding no significant changes. Finally, the maximum pressure drop for more power generation was achieved by placing the turbine at 2 m behind the wing tip on the opposite windward side.

Whereas in the study of [131], a wind energy optimisation tool (WEOT) was developed which can aid architects in integrating VAWTs into high-rise building designs during the early planning phase. The tool uses CFD simulations, wind characteristics, and optimisation algorithms to provide recommendations on how to achieve the desired energy yield by utilising wind power potential at specific zones on the building's surface. Through applying WEOT to case study high-rise models, the authors demonstrated how the tool can assist architects in determining the optimal positions, numbers, and sizes of VAWTs, which can save time, reduce expenses, and improve aesthetics. One limitation of the study is that the CFD analyses were conducted on generic buildings that were not surrounded by a built context. However, the WEOT tool is flexible enough to incorporate results from any CFD analysis and can be helpful in optimising more complex building forms.

The application of CFD tools in modelling VAWT integrated into buildings has proven to be effective in enhancing turbine performance. Various studies highlighted in this section demonstrate that CFD simulations were utilised to determine the optimal location, blade number, and circumferential length of the turbine, and the wing

parameters for wind turbine application, leading to an increase in power output. CFD simulations also facilitated the development of the wind energy optimisation tool (WEOT), which architects can use to plan the integration of VAWTs in high-rise buildings. The tool recommends the positions, numbers, and sizes of VAWTs required to achieve a desired energy yield and can aid architects in determining these parameters early in the design phase.

In the study by on the feasibility of high-rise façade augmented wind turbines, the optimal locations for integrating wind energy harvesting systems into building roof structures are identified based on wind flow dynamics and building architecture. The study indicates that the [131] windward side and the edges of the flat roof building are the best locations for installing wind turbines. These positions benefit from accelerated wind flow and higher wind speeds, enhancing the turbines' power generation potential.

The research emphasises leveraging the aerodynamic effects created by the building structure to augment wind speed. Specifically, positioning turbines near the edges or corners of the flat roof building significantly increases wind power density, thereby improving the efficiency and power output of the turbines. This approach takes advantage of the natural acceleration of wind as it moves over and around the building, creating a micro-generation effect that is particularly beneficial in urban environments where wind speeds are generally lower than in open rural areas. However, it is important to note that the study primarily focused on flat roof structures and did not consider other roof shapes such as pitched and curved roofs. This exclusion leaves a gap in the research, as different roof geometries can influence wind flow patterns and potentially offer different advantages or challenges for wind energy harvesting systems integrated into building roofs

2.3.4 Modelling of DAWT in building integration

Chaudhry et al. [132] used CFD simulations to investigate the feasibility of implementing building-integrated wind turbines and how structural morphology affects wind extraction. The study compared triangular, square, and circular cross-section buildings to the Bahrain Trade Centre benchmark model to determine the power generation capacity of wind turbines. The results showed that circular cross-

sections had the highest wind stream extraction capacity, with a capacity factor of 19.9% and an estimated power production capability of 35.1 kW. The study suggests that circular cross-sections are the most suitable building orientation for regions with a dominant prevailing wind direction, as they achieved a 5% mean wind speed augmentation at the turbines. Overall, CFD simulations proved to be an effective tool in assessing the feasibility of building-integrated wind turbines and the optimal building orientation for wind extraction.

A different tool was used to examine in the study of [133]. The purpose is to investigate how the pressure drop between two buildings could increase air velocity through a duct and a turbine, and how different building geometries and wind input angles could affect power augmentation. The study used a simplified turbine model to compare the total power captured by various building configurations and an Adaptive Neuro Fuzzy Inference System (ANFIS) application. ANFIS was chosen for its ability to predict building augmented power and estimate wind, while also being computationally efficient and adaptable to complex parameters. The study found that wind power output is directly proportional to wind speed, and diffuser-augmented wind turbines could concentrate wind energy for greater power output. However, the use of architectural structures for wind augmentation is still constrained by technical and architectural limitations.

In summary, the results demonstrated that CFD simulations are a useful tool for evaluating the feasibility of building-integrated wind turbines. Circular cross-sections have been identified as the most practical building orientation in regions with a dominant prevailing wind direction, due to their ability to extract the highest amount of incoming wind streams and generate significant power. In addition, the implementation of an adaptive neuro-fuzzy application has shown potential for optimising wind turbine performance. However, technical, and architectural barriers continue to hinder the use of building structures for wind augmentation. These studies offer valuable insights into the efficient design and deployment of building-integrated wind turbines.

2.3.5 Modelling of other configurations in building integration

Toja-Silva et al. [134] used CFD simulations to determine the most appropriate type of wind turbine for different regions based on the turbulence intensity map and velocity field. Figure 25 (a) shows a diagram indicating the recommended installation height and inclination for horizontal axis wind turbines (HAWT) and vertical axis wind turbines (VAWT). For HAWTs, the suggested installation height is above $z/77 = 0.19$ upstream and $z/77 = 0.31$ downstream, with a 5° downward inclination at the upstream region below $z/77 = 0.31$. VAWTs are more suitable below these heights as they resist wind direction fluctuations better. They can be installed in a horizontal position at the central-upstream region close to the roof surface to take advantage of flow recirculation. However, the behaviour of VAWTs in highly turbulent environments requires further investigation. Figure 25 (b) demonstrates a diffuser augmented wind turbine positioned at the upstream corner of the roof, taking advantage of the pressure field. These findings can help improve wind turbine performance and inform optimal design and installation practices.

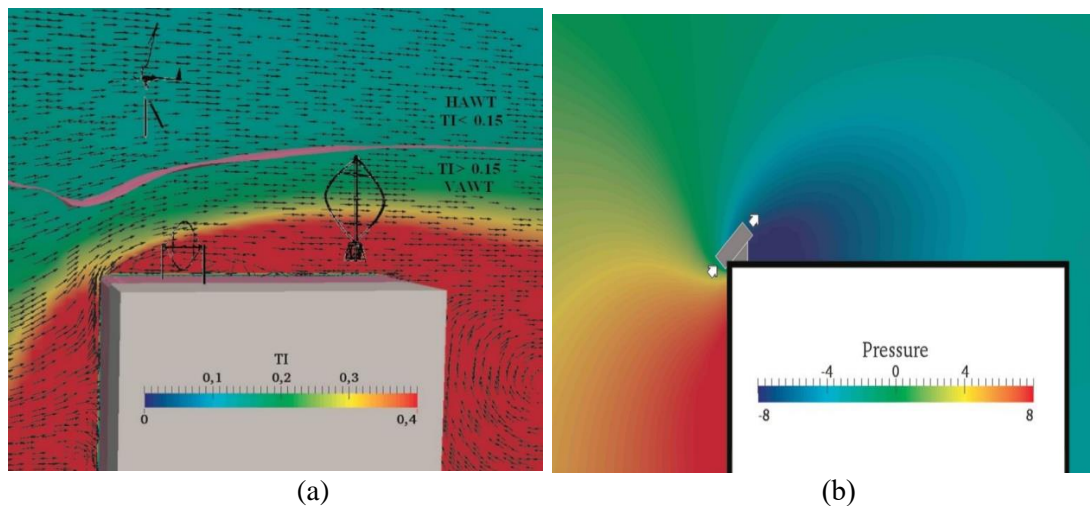


Figure 25. Wind turbine positioning. (a) most suitable wind energy exploitation systems for HAWT, VAWT, and DAWT (b) diffuser augmented wind turbine positioned at the upstream corner of the roof [134]

Wang et al. [135] utilised CFD simulations to investigate the wind energy potential of two perpendicular buildings forming a corner. The study explored various parameters, including building dimensions, corner openings, inlet angles and modes, and assessment altitudes, to identify optimal configurations for wind energy generation. The study findings include the optimal inlet direction, the effect of corner separation

and inlet mode on wind energy over the roof, and the impact of building plan area and altitude on energy production. The research provides general trends for various configurations, but further simulations and evaluations are necessary for the practical application of wind turbines in architecture. Future research will explore different building configurations and more complex models to contribute to urban planning proposals for wind energy development.

Another CFD numerical analysis of wind conditions of building integrated wind turbines was conducted by [136] to examine the effects of wind direction in a high-rise building. The computational simulations were carried out in OpenFOAM software. The aim was to identify the optimal siting of wind turbines over high-rise buildings using realistic wind profiles derived from a numerical weather prediction model. The study revealed that for a single tall building, there are wind speeds sufficient for wind power generation. In the case of twin buildings, wind turbines can be placed not only on the roof but also in between the buildings, with velocities of 2m/s achievable at a separation distance fraction of 0.2 and 2-2.8m/s achievable at a separation distance fraction of 0.5. The findings were dependent on the specific building geometry, and further research is required to optimise wind turbine siting for various building configurations.

Kono et al. [137] utilised large eddy simulations to investigate the influence of wind direction and the horizontal aspect ratio of a building on wind conditions over its roof for the installation of small wind turbines (SWTs). Various aspect ratios and wind directions were used for a scale model building. The results indicated that the wind conditions were generally unfavourable at low heights for the windward corners and midpoint of the longer edge, whereas leeward locations had better wind conditions. The most optimal locations for installing SWTs were found to be the centre and midpoints of the shorter edges. The study recommends further investigation of the impact of increasing building sides and Reynolds number on flow characteristics to enhance the understanding of SWT performance.

Nishimura et al. [138] emphasised the importance of incorporating renewable energy into smart cities and evaluated the potential energy in wind and wind turbine performance by analysing wind velocity profiles. CFD simulation was used to model

wind velocity distribution among buildings, and wind turbine power output was estimated. The research recommends installing wind turbines at the back of buildings, positioned centrally between two buildings to exploit the accelerated wind in the space between them. The study also identifies the optimal wind velocity distribution for maximising wind energy output.

In conclusion, the use of CFD simulations has provided significant contributions to the understanding of the optimal positioning and design of wind turbines for harvesting wind energy in urban environments. The studies have shown that the wind velocity profile, building configuration, and turbulence intensity all significantly impact the performance of wind turbines. The findings have provided guidelines for the recommended height and incline of HAWT, and the suitability of VAWT for different conditions. In addition, the placement of wind turbines in between buildings and at the back of buildings has been suggested as optimal locations to take advantage of the accelerated wind in the intervening space. Despite these significant contributions, further studies are needed to evaluate the practical application of these findings in urban planning proposals for wind energy development. Future research should explore the integration of wind energy into urban environments and evaluate the economic and environmental feasibility of these systems.

2.3.6 Modelling of micro scale wind induced vibration technologies

Sun [139] used CFX-ANSYS to evaluate the design and performance of micro/small-scale flapping cantilevered beams for wind energy harvesting systems. The study utilised the design optimisation feature of the ANSYS commercial package to compare and present the results of various configurations. A 3D static model, including essential components of the mechanical structure, was developed using ANSYS software to examine aeroelastic phenomena. Moreover, the research determined the minimum wind speed required for operation by analysing the lift force acting on the aerofoil. This analysis was instrumental in identifying the optimal structural design for achieving a low threshold wind speed. The wind energy harvester operates by generating oscillations in a cantilevered beam that is aligned with the direction of the airflow.

Aquino et al. [105] employed detailed CFD modelling to investigate the impact of wind speed and the location of aeroelastic belts on power generation. The findings indicate that the apex of the roof or the highest point of the building offers the best power output, and a 45-degree wind approach relative to the building is the most efficient. Intelligent placement of the aeroelastic belt prioritizes the roof and trailing edges of the building. The system can be scaled up, with the potential for an array of aeroelastic belts. The study highlights the significance of CFD analysis in determining the optimal placement of wind energy devices around buildings and provides a modelling process and data for further exploration of the integration of aeroelastic belts in urban environments.

Aljadiri [140] conducted a study on the design and modelling of electrostatic-based wind energy harvesting systems. The proposed harvester was simulated using Matlab and Simulink to investigate energy transfer during the three harvesting phases, and energy analysis was performed to examine the impact of modifying the structure of the multi-pole capacitor on the amount of harvested energy. Simulation results showed that modifying the capacitor structure could improve the amount of harvested energy, with an 8-pole variable capacitor producing 29.43 $\mu\text{J}/\text{sec}$ of energy at 10 m/s. Further improvement was achieved with an array of 10 capacitors with the same capacitance variation, producing 295 $\mu\text{J}/\text{sec}$ of energy at 10 m/s. The study suggests that installing the wind energy harvester in a building can further enhance its performance.

Wind speeds in urban areas are lower than in open areas, and wind energy harvesting systems will be subjected to complex and turbulent flows. Different studies used CFD and WasP software to assess the local micro-meteorological features of the wind flow and identify zones of wind acceleration, recirculation, and blocking for building integrated wind turbines. Moreover, the modelling of small-scale systems such as HAWT and VAWT are well established in the literature. HAWT and VAWT are increasingly being installed into building structures to harness wind energy in urban areas. CFD is a well-established modelling technique used to determine the efficiency of these wind turbines Romanic [141]. Software tools like ANSYS, SolidWorks, and MATLAB are commonly used to design and simulate small-scale wind turbines integrated into building structures. CFD simulations enable the prediction of turbine energy output and can identify areas for optimisation of blade design for maximum

energy extraction. However, there are limited modelling studies evaluating micro-scale energy harvesting installations in buildings. The modelling of wind-induced vibration technologies, in most cases, did not include the impact on the building or surrounding buildings. This is important when evaluating the performance of these devices and should be considered in future works [142].

From the reviewed studies, several works have been conducted to evaluate the design and performance of wind energy harvesting systems. CFX-ANSYS was used in [139] to examine the optimal structural design for achieving a low threshold wind speed using micro/small-scale flapping cantilevered beams. The study of wind speed and aeroelastic belt location on power generation Aquino [107] employed detailed CFD modelling, while [140] simulated electrostatic-based wind energy harvesting systems using Matlab and Simulink. The modelling of small-scale systems such as HAWT and VAWT are well established in the literature, and CFD simulations enable the prediction of turbine energy output and can identify areas for optimisation of blade design for maximum energy extraction. However, future studies should also consider the impact of wind-induced vibration technologies on the building and surrounding buildings when evaluating the performance of these devices.

2.3.7 CFD modelling of buildings and atmospheric boundary layer (ABL)

This study examines the impact of ABL inhomogeneity error on CFD simulations of tall buildings and its findings reveal that detecting this error is crucial for verifying numerical solutions and establishing confidence. The study discovered that ABL inhomogeneity can significantly affect wind loading simulations of tall buildings, and steady RANS models often fail to reproduce high-roughness terrain conditions, resulting in ABL inhomogeneity errors in pressure values on the windward surface of the building. Nonetheless, a fully horizontally homogenous atmospheric boundary layer (HHABL) can be achieved for the RNG model by using a modified wall function at the ground and a driving shear stress at the top of the domain. Monitoring base reaction values can effectively detect blockage effects caused by very short upstream domain lengths. The study provides practical recommendations for assessing ABL inhomogeneity and helps inform verification activities related to this error. However, further research is needed to comprehensively extend these findings to unsteady simulations [143].

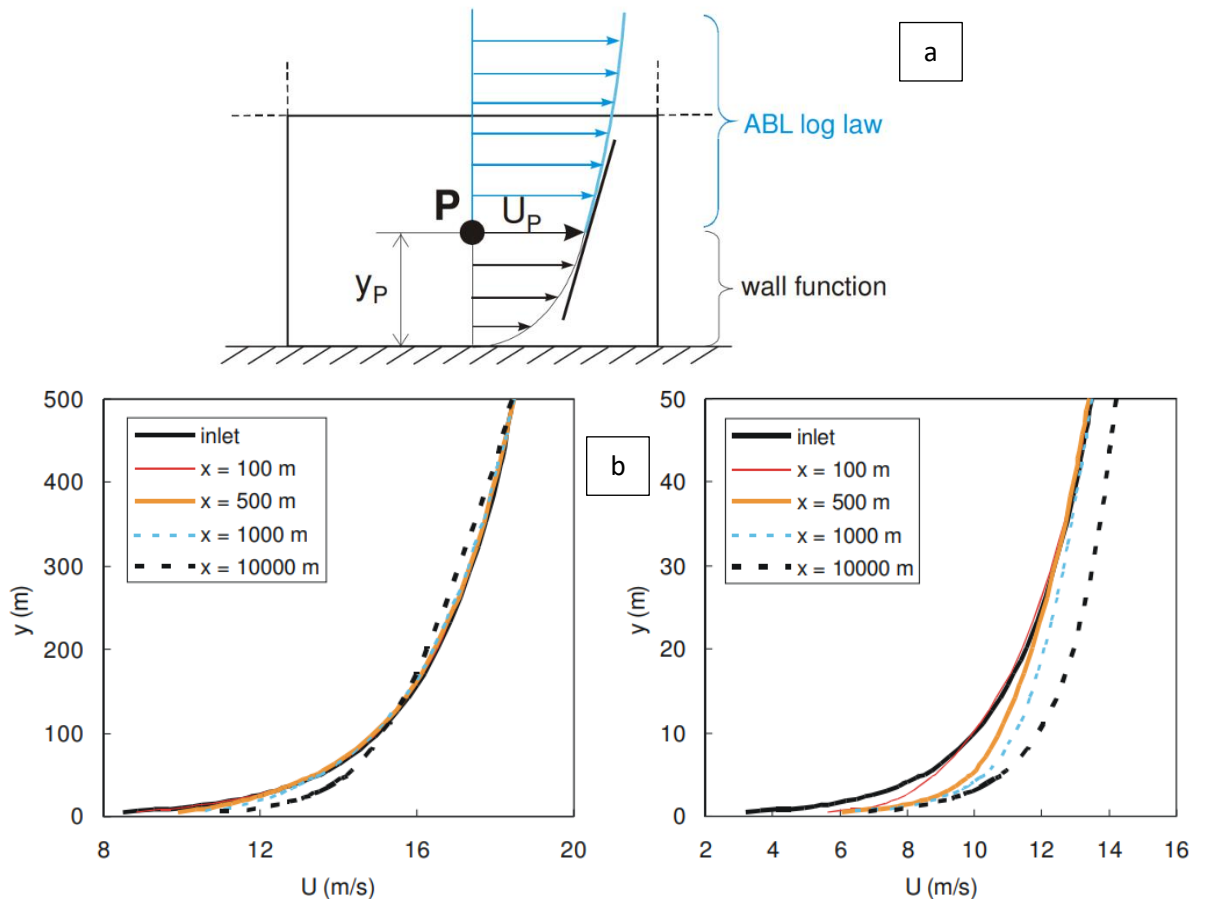
This article [144] reviews the progress made in computational evaluation of wind loads on both low- and high-rise buildings. Researchers have discussed key findings on selecting turbulence modelling techniques, boundary conditions, sizing of the computational flow domain, and the dynamics of high Reynolds number turbulent flows. High-resolution simulations of complex flows are now possible due to progress made in turbulence modelling and high-performance computing. Comparisons with wind tunnel experiments show good agreement, but discrepancies are observed in the sidewalls and leeward face due to computational mesh resolution and boundary conditions. LES and hybrid RANS/LES methods show good agreement with experimental data. Time-dependent analysis using LES is necessary for wind load estimation, especially for peak pressure values, which are essential wind load parameters in building design. However, current computational resource limitations prevent studies on peak pressures. Further research should simulate buildings with more complex shapes, interference of neighbouring buildings, and multiple wind directions to accelerate the use of these simulations as a design tool.

CFD simulations for atmospheric studies can be inaccurate when kS -type wall functions based on sand-grain roughness data are used, causing unintended changes in wind and turbulence profiles (horizontal homogeneity problem). This is due to difficulties in satisfying all four requirements for ABL flow simulations. Possible solutions include using y_0 -type wall functions or exceeding the $yP > kS$ requirement. Remedial measures may be necessary for CFD codes that do not offer these options. It is recommended to assess horizontal inhomogeneity and conduct sensitivity tests before the actual simulation, and to report both inlet and incident flow profiles for each simulation [145].

In Figure 26 (a), it demonstrates the graphical representation of fitting the mean-velocity ABL log-law inlet profile to the wall function for mean velocity. While Figure 26 (b) shows the CFD simulation results illustrating the streamwise gradients in the vertical profiles of mean wind speed, turbulent kinetic energy, turbulence dissipation rate, and turbulence intensity at different downstream distances in the empty domain. The left column shows the lowest 500 m of the boundary layer, and the right column shows the lowest 50 m. While Figure 26 shows the graphical representation of (c)

turbulent kinetic energy k ; (d) turbulence dissipation rate ε and (e) turbulence intensity [145].

Overall, these studies contribute valuable insights into the impact of ABL inhomogeneity on CFD simulations of tall buildings, wind load evaluations, and atmospheric studies. They provide practical recommendations, identify limitations, and highlight areas for further research to improve the accuracy and reliability of CFD simulations in these domains.



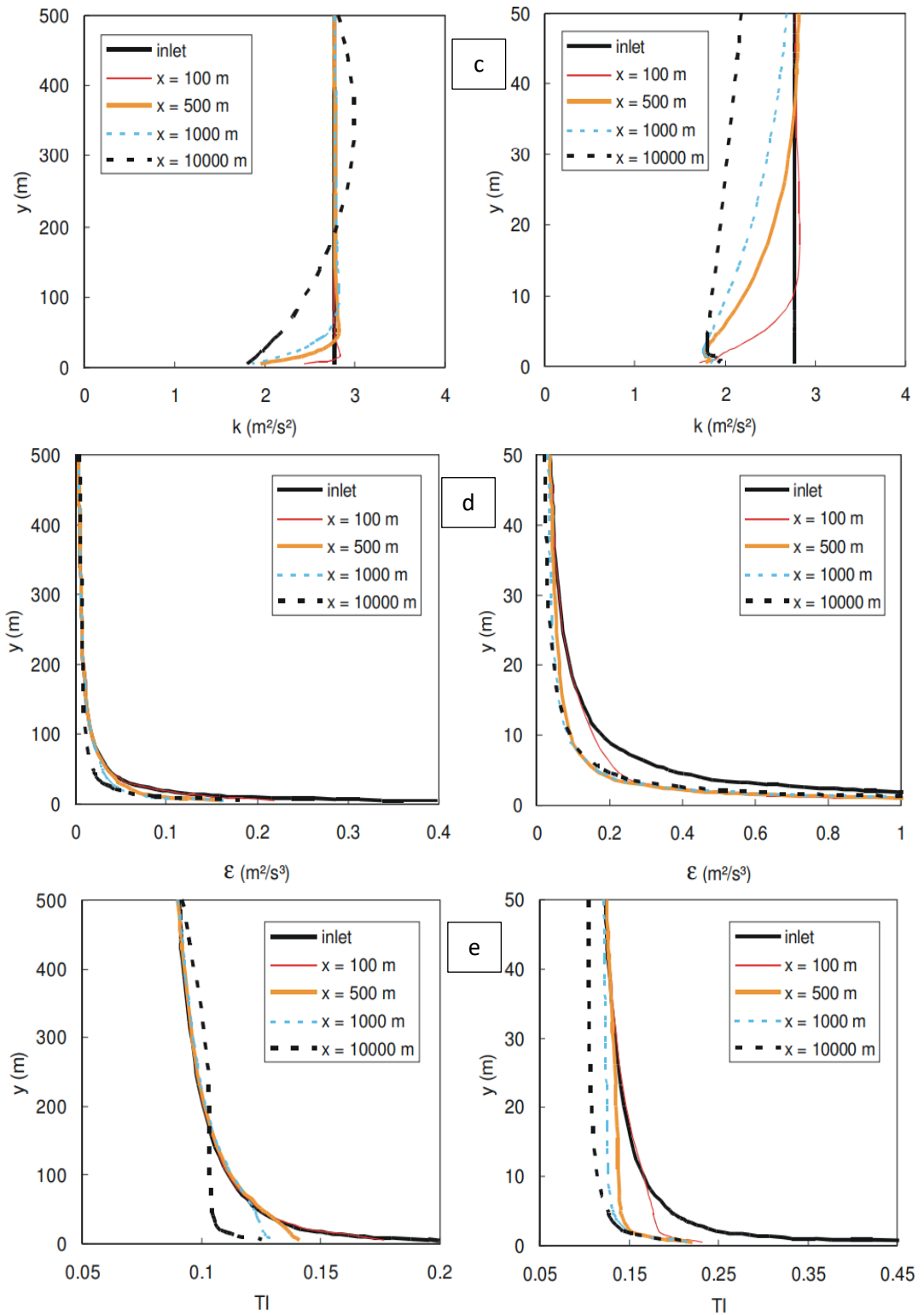


Figure 26. Graphical representation of (a) fitting the mean-velocity ABL log-law inlet profile to the wall function for mean velocity in the centre point P of the wall-adjacent cell, CFD simulation results for the streamwise gradients in the vertical profiles of (b) mean wind speed U ; (c) turbulent kinetic energy k ; (d) turbulence dissipation rate ε and (e) turbulence intensity [145]

Table 2. Summary of reviewed technical characteristics for reviewed building integrated horizontal axis wind turbine

Author(s)	Power capacity (W, kW)	Analysis		Applications/ Purpose	Key Findings
		Numerical	Experimental		
[82]	-	-	✓	Reduction of aerodynamic noise	<ul style="list-style-type: none"> • KV200-profiled blades (10% thickness) have lower sound power levels than S834-profile blades. • Tripping and trailing edge serrations can reduce noise but also reduce turbine shaft power.
[81]	Micro (1 kW), mid-range (5 kW) and mini wind turbines (20 kW+)	-	✓	Design and performance test	<ul style="list-style-type: none"> • 2-bladed rotor performed better at a pitch angle of 18°. • The 2-bladed rotor had lower cut-in wind speeds and higher power coefficients in the 3-7 m/s wind speed range compared to the baseline 3-bladed rotor. • The peak power coefficient achieved at 6 m/s wind speed was 0.29.
[146]	-	✓QBlade	-	Design and Aerodynamic assessment	<ul style="list-style-type: none"> • The optimal performance for the turbine rotor was achieved at a tip speed ratio of 7 • Power factor obtained ($C_p = 0.4742$) did not surpass the Betz limit (0.59%) and was efficient for a small wind turbine • The design of a small horizontal wind turbine with 3 blades is suitable for low wind speed areas
[83]	-	✓CFD	-	Design and Aerodynamic assessment	<ul style="list-style-type: none"> • Optimal performance improved by 64.7% for PTh and 279.9% for SR • The HAWT designed for the throat had a C_p of 0.46 • The optimal Invelox's entering mass flow rate decreased by 49.6% when the turbine wasn't rotating
[84]	-	-	✓ Wind Tunnel	Power production and wake characteristics to the roof edge shape	<ul style="list-style-type: none"> • Fence case presents the highest wake recovery and expansion rates • Smoothness of roof edges is inversely proportional to the recovery and expansion rates • As the roof edges become smoother, the wake recovery and expansion rates decrease

Table 3. Summary of reviewed technical characteristics for building integrated vertical axis wind turbine

Author(s)	Power capacity (W, kW)	Analysis		Applications/ Purpose	Key Findings
		Numerical	Experimental		
[89]	-	√CFD	-	Device for Accelerating Wind Energy Capture	<ul style="list-style-type: none"> External diffuser system has shown promising results in increasing power coefficient of VAWT at TSR=1.5 Specifically, L1/D=2 and $\theta_1=20^\circ$ resulted in a 51.73% increase in power coefficient Flange and ejector can further enhance system capabilities by increasing pressure differences and stabilizing flow fields External diffuser system has potential applications in specific urban areas Key benefits of external diffuser system for VAWT include increased power generation and improved stability of the flow field
[147]	-	-	√	Design and testing	<ul style="list-style-type: none"> Hybrid VAWT generates 63% more energy than a traditional VAWT
[148]	-	√CFD/BEM	-	Analyse the local wind flow patterns and turbulence using CFD	<ul style="list-style-type: none"> Proposed methodology offers the chance to map potential power generated by a turbine system across city regions for different mast heights This will enable the evaluation of urban wind project feasibility by mapping the capacity factor over built environments. Methodology will consider the spatial variability in both mean winds and turbulence intensities
[149]	-	√CFD	√	Impact of turbulence and ground clearance on the performance	<ul style="list-style-type: none"> Maximum efficiency is achieved when the tip speed ratio is 3 and ground clearance is 7.5c (wire length) With a ground clearance of 1.0c, 2.5c, and 4.0c, the turbine performance is reduced by 30.10%, 20.65%, and 10.65%, respectively If the ground clearance exceeds 7.5c, the turbine performance remains constant
[94]	-	√CFD	√	Optimal placement	<ul style="list-style-type: none"> Placing the turbine above the building's corner increased its C_p from 0.318 to 0.549 at a tip speed ratio of 5 The rotor wake's structure was shorter when operating in a freestream compared to when mixed with the surrounding accelerated flow

Table 4. Summary of reviewed technical characteristics for reviewed building integrated diffuser augmented wind turbine

Author(s)	Power capacity (W, kW)	Analysis		Applications/ Purpose	Key Findings
		Numerical	Experimental		
[99]	-	√CFD	-	Design and placement of blade	<ul style="list-style-type: none"> Optimised turbine blade position and geometry result in a 2.5-fold increase in the coefficient of power from 0.135 to 0.34
[100]	100-250W at 10~14 mph	√CFD	-	Design optimisation	<ul style="list-style-type: none"> Blade and generator achieved 100-250 W at 10-14 mph The expected energy generation was 1.2-2 KWh for 12 hours of operation per day at the specified wind speed, but actual results may differ due to mechanical and electrical losses
[101]	-	√CFD	✓	Design optimisation and air flow distribution	<ul style="list-style-type: none"> CFD results showed increased wind speeds through the shroud to a maximum at the rotor where power is generated Optimum DAWT was found to restore wind speeds lost at the rotor due to building presence and showed better responsive behaviour than a test bare wind turbine Velocity distribution along the rotor diameter was not as uniform for the roof-mounted shroud as it was for the free-stream shroud
[102]	-	√CFD	-	Design optimisation and air flow distribution	<ul style="list-style-type: none"> Velocity amplification of 1.52 times at the diffuser throat, close to the predicted value of 1.6 from the earlier design stage CFD
[103]	-	√CFD	-	Design optimisation, wind direction, and air flow distribution	<ul style="list-style-type: none"> Highest C_p value obtained was 0.333 with guide vanes set at 55° and TSR of 0.5.

Table 5. Summary of reviewed technical characteristics for galloping based wind induced vibration technologies

Authors	Transducer	Body shape	Power capacity (nW, μ W,mW)	Analysis		Purpose	Applications	Key Findings
				Numerical	Experimental			
[110]	Piezoelectric	Quadruple Halbach Arrays	8 mW	✓	✓	Use halbach arrays to enhance performance	Experimental and numerical study	<ul style="list-style-type: none"> External load resistance was found to have a significant impact on the galloping onset velocity and vibration amplitude of the harvester
[107]	Piezoelectric	A cut-corner prism	47.5 mW	✓	✓	Use enclosure effect to enhance performance	Experimental test	<ul style="list-style-type: none"> Optimal windward side length for the cut-corner prism energy harvester was found to be 0.4B, resulting in the highest power output. Parallel side with a length of 0.6B was able to produce 47.5 mW
[109]	Piezoelectric	Square, triangular and funnel-shaped	0.207 mW/cm, 1.56 mW/cm, and 2.34 mW/cm	✓	✓	Improve aerodynamic model to enhance performance	Experimental and numerical study	<ul style="list-style-type: none"> The maximum power achieved were 2.34 mW/cm, 1.56 mW/cm and 0.207 mW/cm at 7, 9 and 13 m/s for the 3 different shape designs
[108]	Piezoelectric	D-shape, Square, rectangle, and triangle	8.4 mW	–	✓	Improve power and harvesting performance with efficient strategy	Sensors	<ul style="list-style-type: none"> Square section showed the highest performance for a low cut-in wind speed of 2.5 m/s and achieved a peak power output of 8.4 mW
[111]	Electromagnetic	Y-shaped cross-section	2.5 mW	-	✓	Enhance energy capture efficiency	Sensors	<ul style="list-style-type: none"> Average power up to 2.5 mW at wind speed of 4 m/s

Table 6. Summary of reviewed technical characteristics flutter based wind induced vibration technologies

Authors	Transducer	Body shape	Power capacity (nW, μ W,mW)	Analysis		Purpose	Application (s)	Key Findings
				Numerical	Experimental			
[78]	Piezoelectric	Aerofoil	0.764 mW	–	✓	Examine the power and harvesting efficiency of aerofoil flutter	LED light, pedometer, and sensor,	<ul style="list-style-type: none"> 0.764 mW obtained at 17.48 V maximum power voltage during 16.32 m/s conditions.
[114]	Electromagnetic	Aeroelastic belt	62.4mW	✓ Integrated into building	✓	Analyse the power and harvesting efficiency of integrating an aeroelastic belt into the building	WSN, RF transceivers, charging devices, small-scale electronic devices	<ul style="list-style-type: none"> 62.4 mW generated from wind acceleration up to 6.2 m/s
[120]	Electrostatic	Teflon electret layers with 25 μ m-thickness	481 μ W (178 μ W/cm ³) and 2.1mW (782 μ W/cm ³)	–	✓	Enhance power and harvesting efficiency via electrets	WSN	<ul style="list-style-type: none"> Compact design generates 481μW (178μW/cm³) at 15m/s and 2.1mW (782μW/cm³) at 30m/s
[119]	Piezoelectric	Aerofoil	120 mW	✓	–	Examine power and harvesting efficiency of aerofoil flutter	WSN for aircraft health monitoring and rotorcraft structures	<ul style="list-style-type: none"> Optimal load resistance produced 120 mW power output at 14 m/s
[115]	Piezoelectric	Chamber with a cuboid shape and cantilever design	1.59 mW	–	✓	Examine the power performance of temperature sensor	WSN with self-powering capability	<ul style="list-style-type: none"> 1.59 mW power generated with 20 kΩ electrical load at 11.2 m/s

Table 7. Summary of reviewed technical characteristics VIV based wind induced vibration technologies

Authors	Transducer	Body shape	Power capacity (nW, μW,mW)	Analysis		Purpose	Application (s)	Key Findings
				Numerical	Experimental			
[123]	Piezoelectric	Bionic bluff body with 10 mm pits structure	1.21 mW	–	✓	Assess various VIV designs and their performance	Experimental study	<ul style="list-style-type: none"> Maximum power output of 1.21 mW achieved with 800 kΩ resistance, 0.57 mW higher than smooth cylinder
[122]	Piezoelectric	Cylindrical oscillator	1.6 nW 1.2 nW 0.8 nW	✓	✓	Investigate the power and energy harvesting performance of a cylindrical oscillator	MEMS	<ul style="list-style-type: none"> Cylinder-shaped harvester generated nano-watt power output and performed better when incorporated into a formation to improve power output
[124]	Piezoelectric	E-shaped piezoelectric based on vortex induced vibration	3.35 mW at 1.5 m/s	✓	–	Investigate the harvesting performance of an E-shaped piezoelectric wind energy harvester	Numerical study	<ul style="list-style-type: none"> Power output of 3.35 mW generated at 1.5 m/s through vortex excitation, while E-shaped piezoelectric system demonstrates improved performance over traditional designs in adjusting to a wider range of wind velocities
[125]	Triboelectric	Cylindrical oscillator	392.72 μW	–	✓	Design and testing	Experimental study	<ul style="list-style-type: none"> Average power generated by a wind turbine is 392.72 μW at 2.78 m/s

2.4 Recent developments with research methodology for dynamic mesh

In evaluating the application of dynamic mesh techniques and solver methods in wind energy research, several key arguments and discussions arise, particularly regarding the use of the 6 DOF solver method. This method has been used to explore the dynamics of offshore wind turbines [150]. The 6 DOF solver is known for its ability to simulate complex movements and interactions, creating reduced-order models (ROMs) that simplify the dynamic analysis. However, it is often noted that these ROMs may suffer from. The evaluation of dynamic mesh techniques and 6 DOF solver method reveals significant insights and gaps in wind energy research. The 6 DOF solver was used for offshore wind turbines to simulate complex dynamics and interactions for large amplitude movements, which is crucial for wind energy systems integrated into building structures. Despite its successful application in transient CFD simulations for turbines like Hybrid Darrieus and Savonius, there is a notable absence of research applying the 6 DOF solver to oscillating aerofoil systems on building roofs.

The six degree of freedom (DOF) solver method was used in [150] to investigate the dynamics of offshore wind turbines. This method is often applied to create reduced order models (ROMs), which can be less reliable for large amplitude movements. Similar with the research of [151], the six degrees of freedom solver method was applied in a transient computational fluid dynamics simulation to study the behaviour of the initial rotation of Hybrid Darrieus and Savonius wind turbines at various wind speeds. Based on the review of literature, it was observed that the proposed model of an oscillating aerofoil integrated into a building roof has not been investigated, particularly utilising the 6 DOF solver method. Moreover, the 6 DOF solver method under pitch rotational motion has not been used for this type of design/model and setup conditions. In the literature, this method has been mainly used for offshore wind turbines under pitch motion using a tightly coupled six-degree freedom solver in the studies of [151-154].

Ayhan et al. [155] examined three distinct CFD model scenarios of wind turbines, encompassing vertical axial Darrieus and Savonius turbines, and horizontal axial propeller integrated within urban and rural residential environments. The study affirmed its capability to assess the efficiency of wind energy harvesting technologies

in areas with optimal wind energy resources while avoiding turbulent zones. Studies of [156-157] were also focused on the wind resources assessments using CFD simulations and were of great interest to many researchers and engineers to predict and evaluate the airflow distribution around and above the building roof structures. Another study conducted by [134] involved CFD simulations to examine the airflow around a building. The objective was to qualitatively evaluate the impact of a dynamically fluctuating airflow environment on wind turbines integrated into the building roof.

Moreover, based on the results of the undertaken review, the modelling and simulation of an oscillating aerofoil energy harvester integrated into the building structure have not been explored in the literature. Many works have employed CFD to evaluate the performance of conventional wind turbines. The study of [158] used CFD with the dynamic mesh method to analyse power extraction, the dynamics of offshore wind turbines, and the behaviour of the initial rotation of a hybrid Darrieus and Savonius wind turbines at various wind speeds.

2.5 Discussion

In exploring the effectiveness of various wind energy harvesting technologies integrated into building structures, several critical arguments emerge, particularly concerning power output, efficiency, and design considerations. The comparative analysis of horizontal axis wind turbines (HAWTs) and vertical axis wind turbines (VAWTs) presents a complex discussion on their respective advantages and limitations.

One of the central arguments revolves around the efficiency of HAWTs. Studies such as [73-74] demonstrate that the type of blade profile significantly impacts both power output and noise levels, with KV200-profiled blades proving quieter and more efficient compared to S834-profile blades. The performance metrics, such as the peak power coefficient of 0.29 achieved by a 2-bladed rotor, suggest that HAWTs can be optimised for specific wind speed ranges, which offer robust performance in the 3-7 m/s range. This indicates that HAWTs are well-suited for environments where wind speeds fall within this range, potentially making them more effective in specific urban or rural settings. However, the negative impact of roof edge smoothness on wake recovery, as

reported by [76]. The study highlights a critical design consideration that can diminish overall efficiency.

In contrast, VAWTs offer a different set of advantages and challenges. The impact of external diffusers on VAWT performance, as shown by [89], with a power coefficient increase of 51.73% highlights the potential for significant performance gains through design modifications. Mohamed et al. [120] further demonstrate that hybrid VAWTs can outperform traditional designs by generating 63% more energy. This suggests that VAWTs, particularly with optimised diffusers and ground clearances, may provide a higher energy yield in certain scenarios. However, the variations in performance based on design factors such as ground clearance highlighted by [150], indicate that careful consideration of these parameters is crucial for maximising efficiency.

The discussion extends to diffuser-augmented wind turbines (DAWTs), which have shown substantial improvements in power generation. The optimisation of blade geometry and position resulting in a 2.5-fold increase in the coefficient of power, as reported by [90], argues for the efficiency of diffusers in enhancing turbine performance. CFD analyses by [92-93] also emphasise the benefit of velocity increase through diffusers, which suggest that integrating such technology can yield significant performance improvements. Nevertheless, the technical challenges and potential for increased complexity must be considered.

When evaluating galloping-based wind energy harvesting systems, the argument focuses on their current developmental stage. These systems can generate milliwatt-range power and still in the proof-of-concept phase. The need for further refinement and testing before practical application is evident, as noted in Table 5. Similarly, even though flutter-based systems show to be promising in terms of power generation proportional to wind velocity, which require more comprehensive research to assess their feasibility for integration into building structures. The highest power output of 120 milliwatts achieved by aerofoil-based piezoelectric designs indicates potential, but the limited research highlights the need for further studies to explore scaling and integration challenges.

The vortex-induced vibration (VIV) energy harvesting systems present lower power outputs compared to other technologies with outputs ranging from nano-watts to

milliwatts. Despite their ability to operate at low wind speeds, the performance of VIV systems is greatly influenced by wind flow conditions. This highlights a research gap in understanding their stability and efficiency under varying wind velocities, emphasising the need for future investigations.

The identified research gaps highlight the novelty and importance of further exploration into oscillating aerofoil systems integrated into building roofs. Through addressing the current limitations in research and applying methodologies such as the 1-degree-of-freedom dynamic mesh in rotational motion, future studies can enhance the understanding of these systems' potential and performance. This approach will provide valuable insights and contribute to advancing the field of building-integrated wind energy systems.

2.6 Summary

The literature review identified research gaps, highlighting areas where current studies are lacking and further research is needed, as outlined below:

- Predominance of studies on wind turbines integrated into buildings, with no available research on oscillating aerofoil wind energy harvesting systems for building roofs.
- Current research on aeroelastic belts in building roofs does not address oscillating aerofoil systems.
- Oscillating aerofoil systems have been proven to generate power output, but further improvements are needed to enhance their efficiency.
- There is a lack of research on installing wind-induced vibration technologies (galloping, vortex-induced vibration, flutter mechanisms) in building roof structures.
- Dynamic mesh techniques in rotational motion have been applied to floating platforms or water turbines, but not to wind induced vibration systems.

The literature review identifies key research gaps such as the lack of studies on oscillating aerofoil wind energy harvesting systems for building roofs, the absence of research on oscillating aerofoil integrated into the building roof structures, and insufficient exploration of wind-induced vibration technologies and dynamic mesh

techniques. Chapters 5-6 will address these gaps by examining oscillating aerofoils' potential for energy harvesting by exploring the oscillating aerofoil integrated into the building roof structure using CFD dynamic mesh technique.

Chapter 3

Research Methodology

This chapter will introduce the tools and methods used to investigate the proposed design and approach to analysing the dynamic behaviour, and airflow distribution around the building integrated wind energy harvesting systems (BI-WEHS). This system comprises of oscillating NACA 0012 aerofoil integrated into the building roof structure. The integrated design influences the lift principle to capture wind energy. Through oscillations in response to wind flow, the aerofoil generates lift, which is then converted into usable energy. This approach is particularly effective for building integration because it allows the system to harness wind energy without relying on large, rotating blades typical of conventional wind turbines. Instead, the system's oscillatory motion, driven by the lift generated by the aerofoil enables efficient energy capture even in urban environments where space and wind conditions may vary.

This integration of BI-WEHS into the roof structure also offers the added advantage of blending seamlessly with the building's design, making it a practical and aesthetically pleasing solution for sustainable energy generation. The ANSYS software computational fluid dynamics (CFD) tool used in this research to investigate the energy harvesting performance of the proposed design of BI-WEHS will be discussed. Different equations, models, mesh, and fluent settings will be discussed further to examine their potential in predicting the dynamic behaviour of an oscillating aerofoil integrated into the building roof structure. The degree of freedom solver in Fluent used to investigate the fluid-structure interaction in unsteady/transient simulations over different sets of time will be detailed. Furthermore, the CFD guidelines applied in this

study to developed models and run simulations will be discussed. To conclude, a summary and analysis of the research gaps will be discussed.

3.1 CFD research methodology framework

Figure 27 demonstrates the CFD research methodology which include the development of a sequential analytical methodology, evaluation process, and parametric analysis for analysing oscillating aerofoils integrated into building structures. CFD is adopted as the primary tool for evaluation against the methodology. The increasing demand for energy-efficient solutions has led to the exploration of renewable energy options, including micro-wind turbines and wind induced vibration energy harvesting devices. However, challenges in implementing micro-wind turbines have driven the investigation of alternative solutions such as oscillating aerofoils. While the fundamental mechanisms of oscillating foils have been studied [50] [159-160], their integration into buildings presents a knowledge gap. This study demonstrates the significance of CFD in analysing the fluid dynamics of oscillating aerofoils integrated into building structures and discusses the advantages offered by this approach.



Figure 27. CFD research methodology framework

To address the challenges associated with the integration of oscillating aerofoils into building structures, a sequential analytical methodology and evaluation process have been developed. CFD serves as a powerful tool to evaluate the methodology and provides insights into complex fluid dynamics phenomena. This study highlights the advantages of using CFD in the analysis of oscillating aerofoils and discusses its role in enhancing the understanding of fluid dynamics and optimising the performance of these systems. The use of CFD in analysing oscillating aerofoils integrated into building structures offers several significant advantages. CFD enables researchers to

study fluid dynamics, turbulence, and complex phenomena that are challenging to observe and measure in real-life experiments [161]. This is particularly relevant when analysing the behaviour of oscillating aerofoils in complex geometries such as building roof structures. CFD simulations provide valuable insights into aerodynamic forces, flow patterns, and energy extraction, leading to a comprehensive understanding of the fluid-structure interaction phenomena [162]. The method of dynamic mesh will be used to study the fluid-structure interaction between the wind flow and an oscillating aerofoil integrated into the building roof structure. Dynamic mesh is a technique within CFD, and it plays a crucial role in representing the changing shape and position of oscillating aerofoils during their motion. Through allowing the mesh to displace and adapt to the aerofoil's movement, precise calculations of fluid forces acting on the aerofoil can be obtained. This facilitates an in-depth analysis of the fluid-structure interaction phenomena, leading to predictions of fluid forces and their impact on the aerofoil's motion [162].

The developed sequential analytical methodology comprises several steps that enable a comprehensive understanding of oscillating aerofoils. These steps include problem formulation, mathematical modelling, solution approach, validation, and interpretation of results. CFD serves as a valuable tool in the evaluation and validation of each step, ensuring the accuracy and reliability of the methodology. This is followed by the evaluation process using CFD. The study presents the development of a coupled numerical model using CFD with a six degrees of freedom (DOF) solver constrained to 1 DOF rotational motion. The model incorporates the unsteady Reynolds-averaged Navier-Stokes equations and the k-epsilon turbulence model. Validation of the model is performed by comparing the results with experimental wind tunnel data, demonstrating the capabilities of the six DOF solver in predicting the behaviour of oscillating aerofoils.

Figure 28 shows the CFD set up and process. The CFD setup involved defining the system's geometry, generating a suitable mesh, applying boundary conditions, specifying fluid properties, selecting governing equations, choosing a solver method, adjusting solver settings and control parameters, and conducting post-processing of

the results. This comprehensive approach will provide simulation and analysis of the fluid flow, providing insights into the system's behaviour and performance characteristics.

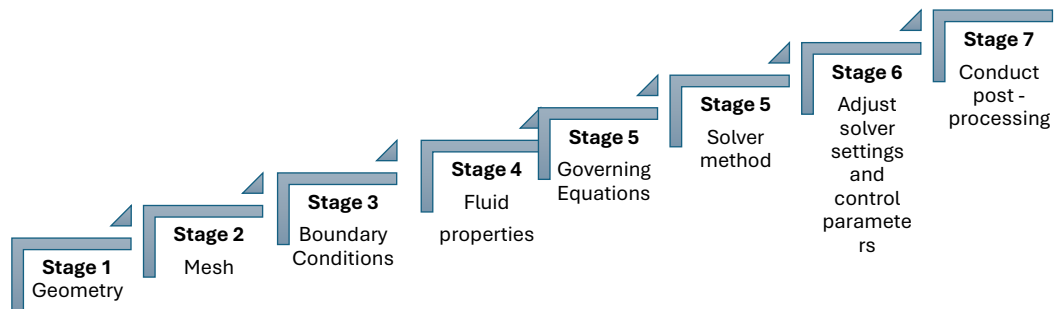


Figure 28. CFD set up and process [162]

3.2 Theory of CFD

CFD theory involves the numerical simulation and analysis of fluid flows using mathematical models and algorithms. It is based on conservation laws and the Navier-Stokes equations, which describe the behaviour of fluid properties like velocity and pressure. Discretisation methods, such as finite difference and finite volume, convert the continuous equations into algebraic ones. Numerical algorithms, including iterative and time-marching methods, solve these equations. Turbulence modelling is used to simulate turbulent flows, and validation and verification ensure accuracy. Post-processing techniques analyse and visualise results. CFD modelling is a valuable tool for engineers, enabling the study of complex flow phenomena and optimising designs in various applications [162]. The mathematics used as part of the CFD process will be discussed in this section. For more details including the derivation of these equations see the references [163-166].

3.2.1 CFD Equations

The main equations used in Computational Fluid Dynamics (CFD) are the Navier-Stokes equations, which describe the conservation of mass, momentum, and energy for fluid flow. These equations are written in (3.1 – 3.3)

Conservation of Mass

$$(3.1) \frac{\partial \rho}{\partial t} + \nabla \cdot (\rho \mathbf{V}) = 0$$

Conservation of Momentum

$$(3.2) \frac{\partial (\rho \mathbf{V})}{\partial t} + \nabla \cdot (\rho \mathbf{V} \mathbf{V}) = -\nabla P + \nabla \cdot \boldsymbol{\tau} + \rho \mathbf{g}$$

Conservation of Energy

$$\frac{\partial (\rho E)}{\partial t} + \nabla \cdot (\rho \mathbf{V} E) = -\nabla \cdot (P \mathbf{V}) + \nabla \cdot (k \nabla T) + \rho \mathbf{g} \cdot \mathbf{V} \quad (1.4)$$

In these equations, ρ represents the fluid density, t denotes time, \mathbf{V} is the fluid velocity vector, P is the pressure, $\boldsymbol{\tau}$ is the stress tensor, \mathbf{g} is the gravitational acceleration vector, E is the total energy per unit mass (including internal and kinetic energy), k is the thermal conductivity, and T is the fluid temperature. These equations are partial differential equations (PDEs) and need to be solved numerically to obtain the flow field in each domain. In addition to the Navier-Stokes equations, specialized equations and models can be included in CFD simulations to account for specific phenomena, such as turbulence modelling using the Reynolds-Averaged Navier-Stokes (RANS) equations [162].

CFD uses numerical techniques and a computer to solve fluid flow problems, specifically the Navier-Stokes (N-S) equations, which can be given in different forms. Equation 3.4 was used to describe the motion of any Newtonian fluid

$$(3.4) \quad \frac{\partial u}{\partial t} + \frac{\partial v}{\partial y} + \frac{\partial w}{\partial z} = 0$$

This is a simplified form of the continuity equation, also known as the incompressibility condition, for fluid flow in three dimensions. It represents the conservation of mass in the fluid. The equations can be found in (3.5-3.7)

u , v , and w represent the velocity components in the x , y , and z directions, respectively. $\partial u / \partial t$ represents the rate of change of velocity component u with respect to time.

$\partial v / \partial y$ represents the rate of change of velocity component v with respect to the y -coordinate.

$\partial w / \partial z$ represents the rate of change of velocity component w with respect to the z -coordinate.

The equation states that the sum of the rates of change of the velocity components in each direction (x, y, z) is equal to zero. This implies that the net change in the fluid's velocity over time, as well as in the y and z directions, is balanced and does not contribute to any net flow of mass. In addition, this equation is fundamental in fluid dynamics, particularly when dealing with incompressible flows, where the fluid's density remains constant. It is often used as a simplification or assumption in the study and analysis of fluid flow problems.

Represents the conservation of momentum in the x direction:

$$(3.5) \quad \frac{\partial(\rho u)}{\partial t} + \frac{\partial(\rho u^2)}{\partial x} + \frac{\partial(\rho uv)}{\partial y} + \frac{\partial(\rho uw)}{\partial z} = -\frac{\partial p}{\partial x} + \frac{\partial \tau_{xx}}{\partial x} + \frac{\partial \tau_{xy}}{\partial y} + \frac{\partial \tau_{xz}}{\partial z} + \rho f_x$$

Represents the conservation of momentum in the y direction:

$$(3.6) \quad \frac{\partial(\rho v)}{\partial t} + \frac{\partial(\rho uv)}{\partial x} + \frac{\partial(\rho v^2)}{\partial y} + \frac{\partial(\rho vw)}{\partial z} = -\frac{\partial p}{\partial y} + \frac{\partial \tau_{yx}}{\partial x} + \frac{\partial \tau_{yy}}{\partial y} + \frac{\partial \tau_{yz}}{\partial z} + \rho f_y$$

Represents the conservation of momentum in the z direction:

$$(3.7) \quad \frac{\partial(\rho w)}{\partial t} + \frac{\partial(\rho uw)}{\partial x} + \frac{\partial(\rho vw)}{\partial y} + \frac{\partial(\rho w^2)}{\partial z} = -\frac{\partial p}{\partial z} + \frac{\partial \tau_{zx}}{\partial x} + \frac{\partial \tau_{zy}}{\partial y} + \frac{\partial \tau_{zz}}{\partial z} + \rho f_z$$

Where x, y,z is the Cartesian coordinate system, u, v, w is the Cartesian velocity system, t is time, ρ is density, p is the pressure, μ is the viscosity and $f=(f_x, f_y, f_z)$ for body force per unit volume in the x, y, and z directions.

3.2.2 Transient modelling

Transient modelling in CFD is used to simulate time in transient modelling with dynamic mesh, which is essential for studying dependent or unsteady flow phenomena, particularly in the case of an oscillating aerofoil with one degree of freedom (1-DOF) rotational motion. This type of motion involves periodic or non-periodic rotation of the aerofoil, requiring the mesh to adapt and deform accordingly to represent the changing flow field.

To model the transient behaviour of an oscillating aerofoil with dynamic mesh, several steps are involved. Initially, a suitable mesh is generated that represents the geometry of the aerofoil and the fluid domain. The aerofoil's rotational motion is defined using appropriate equations, and the mesh must deform and adapt as the aerofoil moves. Mesh deformation techniques, time integration schemes, and proper boundary

conditions are employed to ensure accurate simulations. The transient simulation is considered converged when the solution no longer changes with successive time steps. This convergence is determined based on criteria such as residual tolerances or stability criteria. Through employing transient modelling with dynamic mesh and considering the 1-DOF rotational motion, engineers can accurately capture the time-varying flow behaviour, including lift and drag forces, vortex shedding, and flow separation.

This approach enables the evaluation of the oscillating aerofoil's performance, stability, and control mechanisms, which are crucial for efficient power and energy extraction in building roof structures. Through studying the transient behaviour and accurately capturing the flow phenomena, engineers can optimise the design and operation of wind energy harvesters integrated into building roofs, leading to enhanced energy efficiency and power extraction.

3.2.3 Turbulence models

ANSYS Fluent was selected for this study due to its advanced Unsteady Reynolds-Averaged Navier-Stokes (URANS) capabilities, which are particularly suited to capturing the unsteady behaviour of turbulent flows around oscillating aerofoils. The dynamic mesh technique in ANSYS Fluent enables the mesh to adapt to the aerofoil's motion, ensuring resolution of boundary layers and wake regions. This adaptability is crucial for modelling the complex interactions between the fluid and the moving aerofoil, which are essential for computing dynamic responses such as torque and angular velocity.

The k-epsilon model was chosen for its stability across various flow conditions. While methods like Large Eddy Simulation (LES) and Direct Numerical Simulation (DNS) offer higher fidelity by resolving more scales of turbulence, these models require significantly greater computational resources. The k-epsilon model coupled with URANS offers a practical solution for engineering applications by effectively managing the trade-off between computational demands and the quality of results. Its robustness in handling mesh deformation without causing significant numerical instabilities makes it suitable for simulations involving dynamic meshes. This

reliability ensures that the complex interactions between fluid and the moving aerofoil are captured, providing valuable insights into dynamic responses such as torque and angular velocity.

This study's methodology, employing the k-epsilon model with dynamic mesh techniques in ANSYS Fluent lays the groundwork for more complex analyses in future research phases. While the current approach provides a reliable method for capturing dynamic responses, the foundation it establishes will facilitate the incorporation of more advanced turbulence models or techniques such as LES or hybrid RANS-LES, as research progresses. The choice of ANSYS Fluent and the k-epsilon model ensures that the study can achieve a balance of robustness, computational efficiency, and suitability for the specific problem, ultimately advancing the understanding of unsteady turbulent flows around oscillating aerofoils [165].

The decision to use the standard k-epsilon model instead of the RNG k-epsilon model for URANS transient simulations of an oscillating aerofoil integrated into a building roof structure was based on several key factors. The standard k-epsilon model is widely applied for aerodynamic scenarios including oscillating aerofoils and provides reliable results across a broad range of flow conditions. Furthermore, it is less computationally intensive than the RNG variant, which makes it more suitable for large-scale simulations involving complex structures like a building roof with integrated aerofoils, where time and resource efficiency are critical.

Another important consideration was the model's performance in dynamic mesh simulations, especially with rotational motion. The standard k-epsilon model is more robust and less sensitive to mesh quality issues compared to the RNG k-epsilon model, which is crucial for maintaining numerical stability in simulations involving significant geometrical changes. While the RNG k-epsilon model offers improved predictions in scenarios with rapid strain and high turbulence intensities, such enhancements were not necessary for this particular application, where the primary focus was on overall aerodynamic performance and robustness in handling dynamic mesh distortions. Thus, the standard k-epsilon model was chosen as the most appropriate and efficient option for this simulation. While the $k-\epsilon$ turbulence model is widely used in computational fluid dynamics (CFD) simulations has limitations that

are particularly relevant when studying the dynamic behaviour of an oscillating aerofoil, especially in the context of fluid-structure interaction (FSI) and for advanced research.

While the limitations of $k-\epsilon$ model include the struggle with capturing complex flow phenomena such as separated flows and vortex shedding, which are crucial in understanding the aerodynamic forces acting on an oscillating aerofoil. These limitations can lead to inaccuracies in predicting the forces and moments exerted on the aerofoil during oscillation, potentially affecting the fidelity of FSI simulations. Moreover, for aiming to explore one-way FSI, where the aerofoil motion influences the fluid flow but not vice versa, the $k-\epsilon$ model's inherent assumptions about isotropic turbulence and neglect of specific flow characteristics may not adequately capture the transient and unsteady flow behaviours induced by the aerofoil's oscillations.

Future work involving sensitivity analyses of more advanced turbulence models such as unsteady $k-\omega$, SST (Shear Stress Transport), RNG (Re-Normalization Group), LES (Large Eddy Simulation), and DES (Detached Eddy Simulation) would be essential. These models offer improved capabilities to handle unsteady flows, resolve turbulent structures, and better predict phenomena like flow separation and vortex shedding, which are critical in simulating the aerodynamic responses of oscillating aerofoils under varying conditions.

Therefore, while the $k-\epsilon$ model serves as a starting point for initial studies, especially in understanding basic flow behaviour and boundary layer characteristics, advancing to more sophisticated turbulence models are necessary for aiming to explore dynamic behaviours and FSI effects. This progression would enable deeper insights into the complex interactions between the oscillating aerofoil and the surrounding flow, essential for advancing knowledge and optimising design in aerodynamic applications

Through incorporating the standard k -epsilon turbulence model and standard wall functions in CFD simulations, the flow dynamics around an oscillating aerofoil integrated into a building roof structure can be efficiently modelled. This approach captures key turbulence characteristics including eddy formation, flow separation, reattachment, and boundary layer behaviour. These insights are important for

predicting lift, drag, and overall aerodynamic performance, which makes it an effective method for understanding the aerofoil's impact on the surrounding flow field.

In ANSYS Fluent, the standard k-epsilon turbulence model for unsteady Reynolds-Averaged Navier-Stokes (URANS) simulations can be described by the following equations:

Turbulent Kinetic Energy (k) Equation

$$(3.8) \quad \frac{\partial(\rho k)}{\partial t} + \frac{\partial(\rho u k)}{\partial x_i} = \frac{\partial}{\partial x_i} [\mu + \mu_t/\sigma_k] \frac{\partial k}{\partial x_i} + G_k - \rho \epsilon$$

Equation (3.8) represents the conservation of turbulent kinetic energy. It describes the time rate of change of turbulent kinetic energy, the advection of turbulent kinetic energy, the diffusion of turbulent kinetic energy, production of turbulent kinetic energy due to mean velocity gradients (G_k), and turbulent kinetic energy dissipation rate (ϵ).

Turbulent Dissipation Rate (ϵ) Equation

$$(3.9) \quad \frac{\partial(\rho \epsilon)}{\partial t} + \frac{\partial(\rho u \epsilon)}{\partial x_i} = \frac{\partial}{\partial x_i} [\mu + \mu_t/\sigma_\epsilon] \frac{\partial \epsilon}{\partial x_i} + C_{1\epsilon} \epsilon/k G_k - C_{2\epsilon} \rho \epsilon^2/k$$

Equation (3.9) represents the conservation of turbulent dissipation rate. It describes the time rate of change of turbulent dissipation rate, the advection of turbulent dissipation rate, the diffusion of turbulent dissipation rate, production of turbulent dissipation rate due to mean velocity gradients, and turbulent dissipation rate through the dissipation mechanism. In these equations, ρ is the density of the fluid, t is time, u is the velocity vector, x_i represents the coordinate directions, μ is the dynamic viscosity, μ_t is the turbulent viscosity, σ_k and σ_ϵ are the turbulence model constants, G_k is the turbulence kinetic energy generation term, ϵ is the turbulent dissipation rate, and $C_{1\epsilon}$ and $C_{2\epsilon}$ are the turbulence model constants. These equations, along with appropriate boundary conditions, form the basis for solving the URANS simulations using the standard k-epsilon turbulence model in ANSYS Fluent.

3.2.4 SIMPLE Algorithm

To solve the pressure-velocity coupling equation in computational fluid dynamics (CFD) simulations, specific numerical procedures known as solution algorithms are employed. These algorithms are designed to iteratively solve the governing equations and enforce the coupling between pressure and velocity fields. In this study, the SIMPLE algorithm was employed as the chosen solution algorithm. SIMPLE stands for Semi-Implicit Method for Pressure-Linked Equations and is a widely used and well-established technique in CFD simulations. It is known for its effectiveness in handling the pressure-velocity coupling in an iterative manner [162].

The Semi-Implicit Method for Pressure Linked Equations (SIMPLE) is a technique widely utilised in solving the Navier-Stokes equations. Researchers extensively employ this method to address various fluid flow problems. Specifically, it focuses on two-dimensional laminar steady flow equations in Cartesian coordinates. The fundamental concept behind this approach involves making an initial guess for the pressure field (p^*) to solve the discretised momentum equations, which subsequently yield the velocity components u^* and v^* . In addition, the correction pressure (p') is introduced as the disparity between the guessed pressure (p^*) and the actual pressure (p). Therefore, this method enables the determination of the velocity field (u and v), ensuring that continuity is maintained [166].

In summary, a simple algorithm was used for analysing an oscillating aerofoil integrated into a building roof structure due to its computational efficiency, ability to provide conceptual understanding, usefulness as a baseline for comparison, and suitability for proof of concept and educational purposes. Simple algorithms require fewer computational steps, aid in interpreting results, facilitate comparisons with advanced methods, validate feasibility, and enhance learning. However, it's important to recognise that simple algorithms may not capture all complexities, and as the problem complexity increases, more advanced algorithms may be required for accurate and detailed results.

3.2.5 Residuals monitoring and convergence

Figure 29 shows the residuals 3500 iterations. In the CFD simulation of an oscillating aerofoil with a dynamic mesh, residuals for continuity, momentum, and turbulence quantities were monitored to evaluate convergence. The residuals provide insight into the numerical stability and accuracy of the simulation. The findings revealed oscillations in the continuity residuals, which remained around 1×10^{-2} , while epsilon residuals varied from 1×10^{-3} to 1×10^{-4} . The turbulence kinetic energy (k) residuals stabilized around 1×10^{-5} , and the residuals for X, Y, and Z velocities ranged between 1×10^{-5} and 1×10^{-4} . The oscillations in the continuity residuals at 1×10^{-2} are common in unsteady simulations involving dynamic meshes. This pattern suggests that the solver is effectively managing the continual changes in the mesh and flow field. Although lower residuals are generally preferable, the periodic behaviour of the continuity residuals indicates that the simulation has achieved a reasonable level of convergence, suitable for the dynamic nature of the problem.

While for epsilon residuals, which fall within the range of 1×10^{-3} to 1×10^{-4} , are acceptable for capturing the turbulence dissipation rate. The relative stability of these residuals suggests that the turbulence model is functioning as expected and providing reliable results. Similarly, the low residuals for turbulence kinetic energy (k), around 1×10^{-5} , demonstrate effective resolution of the turbulence energy, further supporting the reliability of the simulation.

Residuals for momentum equations, specifically the X, Y, and Z velocities, ranging from 1×10^{-5} to 1×10^{-4} , indicate that the solver is successfully capturing the momentum transfer in all directions. Despite the dynamic motion of the aerofoil, these values suggest that the solver's performance is adequate for the unsteady flow conditions. Overall, while some residuals are higher than ideal, particularly for continuity, the stability of other residuals supports the simulation's convergence and reliability for further analysis.

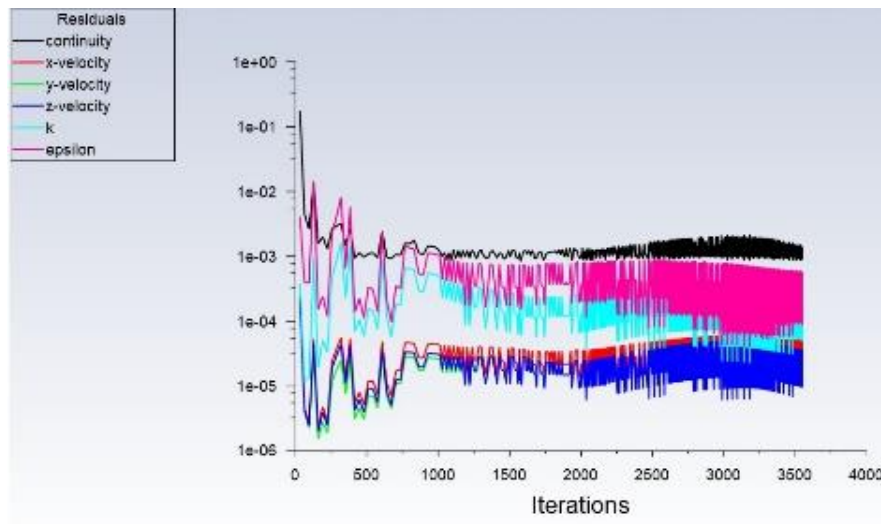


Figure 29. Monitoring of residuals

3.3 Dynamic mesh

ANSYS CFD software has been a useful tool to simulate the airflow patterns over and around buildings. This facilitates the examination of optimal designs and placement of wind energy harvesting systems both above and around buildings to optimise performance. As computing capacity has increased, CFD modelling has become a crucial tool for numerical analysis, particularly regarding wind conditions and various environmental settings. Recent advancements in wind energy harvesting systems using CFD simulations demonstrated developments from wind flow modelling around aerofoil to atmospheric boundary layer (ABL) through arrangements of wind farms or turbines [122].

The use of high-fidelity CFD method in combination with one degree of freedom simulations has certain benefits over using engineering models. 1 DOF simulations can provide a more accurate solution by only requiring the geometry and mass specifications of the CFD model, although the method is computationally more expensive [167]. The dynamic mesh method allows for modelling fluid flows in situations where the computational domain shape undergoes changes over time due to movement along the domain boundaries. Through integrating a 1 DOF solver, this method can determine the trajectory of a moving object, based on the aerodynamic forces present in the surrounding flow field [159]. Several studies on 1 DOF and CFD solvers have been developed for simulating offshore oil platform dynamics, as

referenced in studies [168-170]. However, it is worth noting that these solvers use proprietary or closed-source software to calculate the 1 to 6-DOF equations of motion and Navier–Stokes equations in a coupled approach [168-170].

Based on the review of relevant research findings, it can be implied that the suggested model of integrating an oscillating aerofoil into the structure of a building roof has not been explored. Moreover, the CFD combined with one to six degrees of freedom simulations are usually used for offshore wind turbine simulations [162] [168-170]. The literature lacks exploration of the interaction between fluid (wind flow) and solid (wind energy harvester integrated into the building roof structure), especially regarding the utilisation of dynamic mesh and DOF methods.

To model the 1 DOF rotational motion, specifically the pitch oscillation, of an object with a dynamic mesh in the y-axis direction, The equation of motion can be deduced by applying Newton's second law, and it can be expressed in (3.10 and 3.11) [162].

$$(3.10) \quad I \cdot \frac{d^2\theta}{dt^2} + c \cdot \frac{d\theta}{dt} + k \cdot \theta = M(t)$$

$$(3.11) \quad 0.4 \cdot \frac{d^2\theta}{dt^2} + 850 \cdot \frac{d\theta}{dt} + k \cdot \theta = M(t)$$

where: θ represents the angular displacement of the object (pitch angle) in radians.

t represents time in seconds. I represent the object's moment of inertia around the pitch axis, measured in $\text{kg}\cdot\text{m}^2$. c stands for the damping coefficient, measured in $\text{N}\cdot\text{m}\cdot\text{s}/\text{rad}$. k is the stiffness coefficient in $\text{N}\cdot\text{m}/\text{rad}$. $M(t)$ is the external moment acting on the object due to aerodynamic forces or other applied loads in $\text{N}\cdot\text{m}$.

The stiffness coefficient (k) was not provided. The stiffness coefficient depends on the specific system and is typically determined by the structural properties of the object. Equation (3.11) represents the dynamic behaviour of the object undergoing pitch oscillation in the y-axis direction. The external moment, $M(t)$, will depend on the specific conditions, forces, or loads acting on the object. To simulate this system using a dynamic mesh in ANSYS Fluent DOF solver with a 1 DOF constraint, additional equations and modifications would be required within the software to enforce the constraint and incorporate the dynamic mesh capability. Further discussions and equations may be required to analyse the impact of parameters such as the aerofoil

stiffness coefficient (k) on system behaviour, particularly in scenarios involving different types of motion such as heave motion. The stiffness coefficient directly influences how the aerofoil responds to external forces, affecting its deformation and dynamic response. Higher stiffness results in less deformation and a more rigid response, while lower stiffness allows for greater flexibility and deformation. Dynamic mesh considerations become crucial in such cases, enabling adaptation of the computational mesh to accommodate the changing geometry of the aerofoil as it deforms during motion. This ensures accurate representation of the flow field and pressure distribution around the aerofoil throughout its motion.

In addition, sensitivity analyses were conducted to ensure the most suitable spring constant values for the proposed system, focusing on an oscillating aerofoil integrated into a building roof structure. These analyses showed that a spring constant of constant 850 (n-m/rad) was the most effective for our specific application. This choice was predicated on the observation that pitch oscillations maintained a continuous and stable pattern in this spring constant.

The sensitivity analyses conducted for the oscillating aerofoil integrated into the building roof structure aimed to identify the most effective spring constant values for various wind speeds. These analyses were crucial for achieving stable and efficient pitch oscillations, which significantly impact the mechanical power output and overall reliability of the system.

Figure 30 (a) demonstrates for a wind speed of 3 m/s, three spring constants were tested: 750 Nm/rad, 850 Nm/rad, and 950 Nm/rad. Among these, a spring constant of 850 Nm/rad emerged as the optimal choice. This value provided the most stable and continuous pitch oscillations, avoiding the chaotic behaviour observed with the other constants. The stability achieved with 850 Nm/rad was essential for preventing inefficiencies in mechanical power generation, making it the preferred option for this wind speed. While in Figure 30 (b) shows at a higher wind speed of 6 m/s, the spring constants tested were 550 Nm/rad, 650 Nm/rad, and 750 Nm/rad. The analysis revealed that 650 Nm/rad was the most effective spring constant. It offered the best balance between stability and efficiency, minimising chaotic oscillations that could adversely affect the system's mechanical power output. This choice ensured that the

aerofoil's oscillatory behaviour remained manageable and efficient under increased wind speeds.

For higher wind speed of 9 m/s, Figure 30 (c) demonstrates the tested spring constants with 350 Nm/rad, 450 Nm/rad, and 550 Nm/rad. The spring constant of 450 Nm/rad was found to be the most suitable for this condition. It provided stable pitch oscillations and avoided the excessive oscillatory behaviour seen with higher constants. This selection was crucial for maintaining efficiency and preventing issues related to chaotic movement.

In conclusion, the selected spring constants include 850 Nm/rad for 3 m/s, 650 Nm/rad for 6 m/s, and 450 Nm/rad for 9 m/s were chosen based on their ability to ensure stable and continuous oscillatory behaviour. This selection was fundamental for achieving reliable simulation results and optimising mechanical power output across different wind speeds.

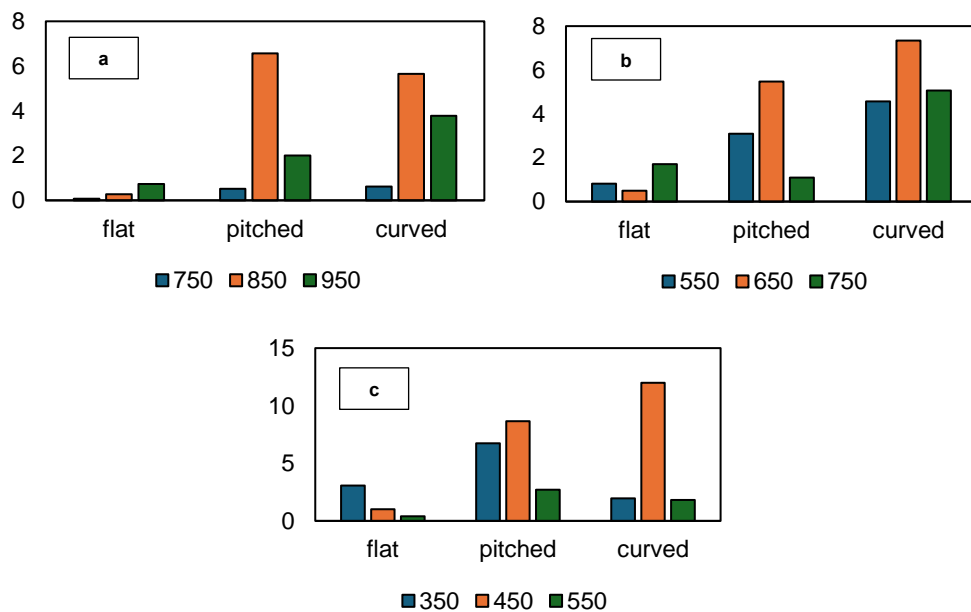


Figure 30. Sensitivity analyses of spring constant values for different parameters in (a) 3 m/s (b) 6 m/s, and 9 m/s wind speeds

3.4 CFD geometry and domain

The geometry features a domain that encompasses the aerofoil and building roof structure. The NACA 0012 aerofoil was chosen for baseline for this research since it has been previously utilised in different research on oscillating aerofoils in low Reynolds number and have been proven to be effective in these conditions. The

aerodynamic characteristics of NACA 0012 profile are well known and there is abundance of published research data available. In addition, the SD7003 aerofoil was also considered for the purpose of comparison with NACA 0012 in terms of wind energy harvesting performance.

3.4.1 Aerofoil wind energy harvester – NACA 0012

In the study, a 3D model of a NACA 0012 aerofoil was created using DesignModeler in Ansys. The NACA 0012 aerofoil is a widely recognised aerofoil shape, known for its specific contour defined by the National Advisory Committee for Aeronautics (NACA). The purpose of developing this aerofoil model was to investigate its energy and power extraction capabilities.

Beyond its role as a reference, the NACA 0012 is also noted for its effectiveness in various aerodynamic applications. Particularly in scenarios involving pitch oscillating NACA 0012 aerofoil demonstrates stable performance due to its balanced lift-to-drag ratio. Its symmetrical shape maintains aerodynamic stability under dynamic conditions, which is essential for power extraction in fluctuating wind environments. This combination of historical significance and practical applicability highlights the NACA 0012's ongoing relevance in [48] [171].

Figure 31 shows the study of [171] which investigated the effect of different Reynolds numbers (Re) on the aerofoil performance of the baseline aerofoil, the lift coefficient (C_l) and drag coefficient (C_d) obtained from wind tunnel experiments were analysed. Numerical results at $Re = 20,000$ and $40,000$ were validated against experimental data. The experimental results showed that at higher Re ($43,200$ and $60,000$), C_l trends remained consistent across all angles of attack, whereas at lower Re ($10,000$ and $20,000$), C_l values decreased, specifically at $Re = 10,000$ where the peak C_l at $\alpha = 10^\circ$ started to reduce. While the C_d values increased with the angle of attack regardless of Re , but rapid increases between $\alpha = 10^\circ$ and 12° due to stall were observed only at $Re = 43,200$ and $60,000$.

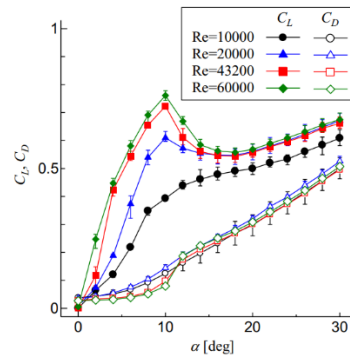


Figure 31. C_l and C_d for NACA 0012 [171]

Table 8 displays the specifications of the symmetrical NACA 0012 aerofoil with PVC foam material. These parameters included dimensions such as length, width, and thickness, which define the physical size and geometry of the aerofoil. In addition, the table also specified the mass, moment of inertia, centre of rotation, and centre of gravity of the aerofoil. These parameters play a vital role in analysing the forces, stability, and dynamic behaviour of the aerofoil during fluid flow simulations. Through considering these parameters, the study aimed to investigate the energy and power extraction potential of the NACA 0012 aerofoil in various flow conditions. Table 8 demonstrates the parameters of the oscillating NACA 0012 aerofoil applied in the CFD simulations.

Figure 32 illustrates the symmetrical aerofoil with a rod mounted at 0.25 m chord length. The rod has 15 mm length, which serves as a support, allowing the aerofoil to oscillate in the pitch direction. The rod acts as a support for oscillatory motion, has a length of 0.015 m, as shown in Figure 32. This design choice is based on previous work by [48] and aligns with theoretical principles and practical considerations. Placing the rod at the quarter-chord length optimises aerodynamic balance, enhances energy harvesting efficiency, minimises structural stresses induced by aerodynamic forces, and improves device durability and integrity. This approach also enhances stability and controllability, ensuring smoother and more predictable motion for effective energy harvesting. Previous studies and simulations provide empirical evidence supporting the favourable aerodynamic performance considerations of this approach [48] [171]. While the centre of gravity of the aerofoil is located at 0.42 metres

along the chord length, measured from the leading edge towards the centre of gravity of the aerofoil.

Table 8. Parameters of the oscillating NACA 0012 aerofoil applied in the CFD simulations

Aerofoil profile	Dimension (m)	Mass (kg)	Moment of inertia (kg-m ²)	Centre of rotation (m)	Centre of gravity location (m)
Symmetrical NACA 0012	1 metre span and 1 metre chord length	3.2	0.4	X - 0.25 Y - 0 Z - 0	X - 0.4182 Y - 0 Z - 0

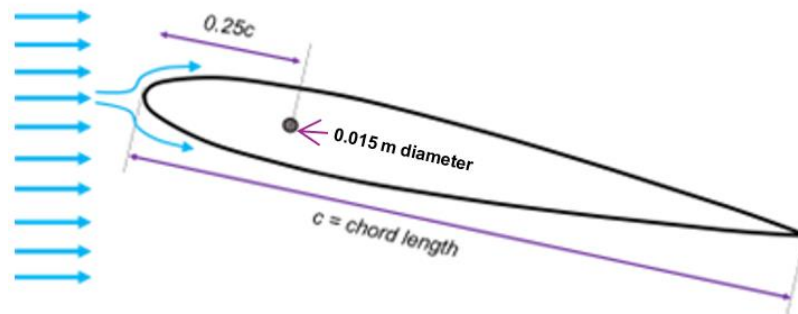


Figure 32. Aerofoil centre of rotation

3.4.2 Aerofoil wind energy harvester – SD7003

The SD7003 aerofoil has also been used for the study due to its proven performance in pitch oscillating motions, making it suitable for dynamic applications such as flapping wings and oscillating aerofoils [172-174]. Its effectiveness in these conditions is supported by number of research in the literature, which provides foundation for investigating its aerodynamic efficiency. This extensive literature not only offers a reliable baseline but also allows researchers to build on existing knowledge, facilitating further advancements in the design and application of oscillating aerofoils.

In addition to its dynamic performance, the SD7003 is recognised for its high lift characteristics compared to the symmetrical NACA 0012. This high lift capability is particularly beneficial for wind energy harvesting systems, where maximizing lift can enhance efficiency and power output. In wind energy harvesting systems, the SD7003's ability to capture and utilise wind energy more effectively can lead to

improved operational performance. Through focusing on high lift and demonstrating effective performance in pitch oscillations, the SD7003 shows to be good option for advancing wind energy technologies and optimising aerodynamic efficiency in practical applications [172-174].

The SD7003 aerofoil in Figure 33, the angle of attack at which the non-linear lift increase becomes smaller as the Reynolds number increases, and the C_l max increases. The drag curve exhibits a significant Reynolds number dependence, especially at positive angles of attack. The C_l against the angle of attack showed peak of 1 for SD7003. While C_d was 0.25 at its peak.

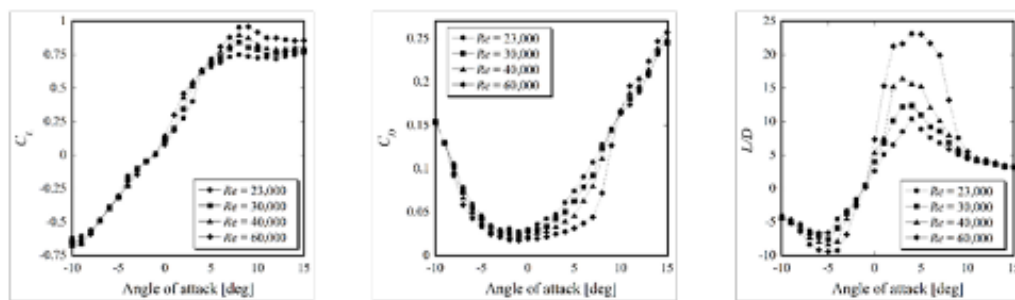


Figure 33. Reynolds number dependence on aerodynamic characteristics of SD7003 aerofoil (a) C_l , (b) C_d , (c) L/D [174]

3.4.3 Building model

This study involved developing 3D model for the pitched roof building structure was based on the study of [175]. The roof shape was represented by its unique characteristics and dimensions in Figure 34. The pitched roof design featured a sloping surface, often seen in residential and traditional houses. The dimensions provided in Figure 27 provide analysis of the roofs' size, shape, and sections. The study aimed to examine the fluid flow behaviour, aerodynamics, and structural performance of this roof type, considering factors such as energy efficiency and wind resistance. The simulations and assessments were facilitated by the detailed 3D models, providing valuable insights into the performance of these building roof structures in different flow conditions and environmental factors.

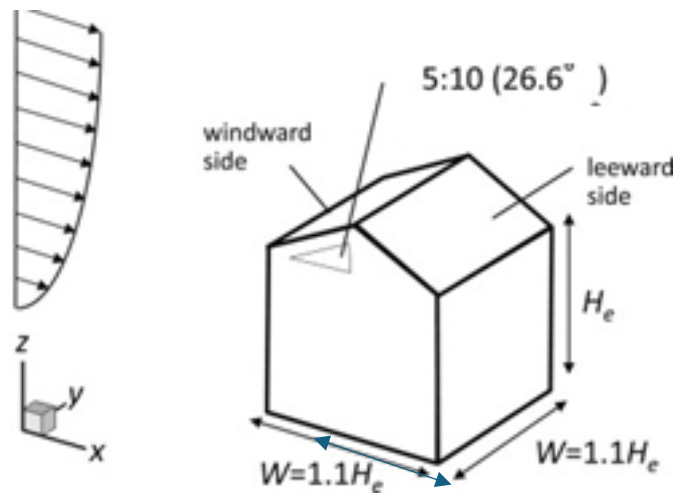


Figure 34. 3D pitched roof building structure [175]

3.4.4 Building integrated wind energy harvesting system

The integration of the 3D model of the NACA 0012 aerofoil and the building roof structure aimed to improve the efficiency and performance of an oscillating aerofoil. Through incorporating wind energy harvesting technologies into the building roofs, the study aimed to optimise the extraction of energy and power. Past designs of building integrated wind energy systems [20-21] [135] have demonstrated that installing wind energy harvesters into the roof can enhance energy extraction. This is due to the roof's favourable shape, which can either accelerate wind speeds or channel the wind in a beneficial manner.

Figure 35 shows the 3D model of the integrated design of an oscillating aerofoil and pitched roof building structure with the dimensions. The integration of the 3D models enabled a thorough examination of the interaction between the oscillating aerofoil and the specific roof shapes. Through considering the aerodynamic behaviour and flow characteristics of the wind around the roof structures, the study aimed to identify the best positions and orientations for installing wind energy harvesters. The use of CFD tools enabled researchers in wind energy technologies to investigate and optimise the performance of building-integrated wind energy harvesting systems. Through analysing flow patterns, velocity distributions, and pressure gradients around the aerofoil and the building roofs, valuable insights were gained regarding how the roof

shape influences wind flow and enhances the efficiency of the oscillating aerofoil system.

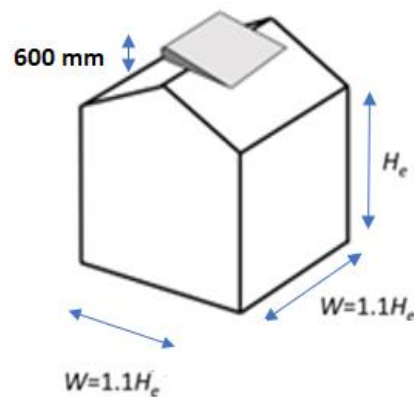


Figure 35. 3D building integrated wind energy harvesting system [175]

In summary, the integration of the NACA 0012 aerofoil model and the building roof structures aimed to harness the advantageous roof shapes to improve the energy and power extraction of the oscillating aerofoil. This approach employed computational simulations and analysis to optimise the installation and configuration of wind energy harvesters within the roofs, capitalising on the accelerated wind speeds or wind channelling effects generated by the roof shapes.

3.5 Computational domain generation

Figure 36 demonstrates the computational domain generation in CFD, which involves defining the system's geometry, generating a mesh to discretise the domain, ensuring mesh quality and refinement, setting boundary conditions, considering domain size and symmetry, and conducting a grid independence study. This illustrates the computational domain, whereas the building with the dimensions of 6m x 6.6m x 6m is located. A 1m span and 1m chord length were chosen for the aerofoil size. The dimensions of the building roof were according to the research of [175]. The specifications and parameters were applied to validate the current computational fluid dynamics model for the curved and pitched roof building. It is a crucial step that directly impacts the reliability of CFD simulations. Through representing the physical space and flow properties, computational domain generation enables engineers to obtain reliable results for fluid flow analysis.

In this study, the selection of the computational domain size was guided by the Architectural Institute of Japan (AIJ) guidelines for practical applications of CFD to pedestrian wind environments around buildings [177]. The choice of guidelines was influenced by the goal of conducting a CFD case study in the Philippines, which requires consideration of the region's specific geographic, climatic, and urban characteristics. The AIJ (Architectural Institute of Japan) guidelines are particularly well-suited for this context due to their detailed focus on urban aerodynamics and complex building interactions, which align with the dense urban configurations typical of Philippine cities. Moreover, the AIJ guidelines are a relevant choice due to Japan's climatic and geographic similarities to the Philippines particularly in terms of wind patterns influenced by monsoons and typhoons.

These guidelines provide a robust framework for analysing wind flow around buildings and optimising building-integrated wind energy systems. Their detailed recommendations are designed to ensure accurate and reliable results in such contexts. The AIJ guidelines' effectiveness is further supported by studies such as that by [178] employed these guidelines to develop a CFD model for fluid-structure interaction (FSI) and energy generation in roof-mounted renewable energy systems, addressing challenges related to extreme weather and typhoon resilience in the Philippines. Pantua [178] also referenced Tominaga's study, which used the AIJ guidelines and FLUENT software to analyse airflow around gabled roof buildings with different pitches, demonstrating effective CFD simulation validated against wind tunnel data, despite some deviations.

While the European COST (Cooperation in Science and Technology) guidelines offer a framework applicable to various environments including both urban and rural settings, their broader scope might not address the specific urban complexities and climatic differences of the Philippines as effectively as the AIJ guidelines. However, incorporating elements from both AIJ and COST guidelines could enhance the research's robustness and applicability, especially if the study covers diverse settings.

According to these guidelines: the lateral and top boundaries of the domain were set to be at least 5 times the height ($5H$) of the target building. This distance is critical to minimise boundary effects on the airflow and to replicate an open environment. The

inlet boundary was positioned to correspond to the upwind area covered by a smooth floor in wind tunnel tests, effectively replicating the approach flow conditions. The outflow boundary was placed at least $10H$ behind the building, ensuring that the wake region was adequately captured and did not influence the inflow conditions. Through adhering to these guidelines, the aim was to ensure that the computational domain adequately represents the real-world conditions while minimising the impact of boundary conditions on the flow field around the building. This approach is essential for accurately capturing the pedestrian-level wind environment in the vicinity of the building. Also, a detailed description of the domain size selection process, explicitly mentioning the adherence to the AIJ guidelines and the rationale behind each boundary placement relative to the building [177].

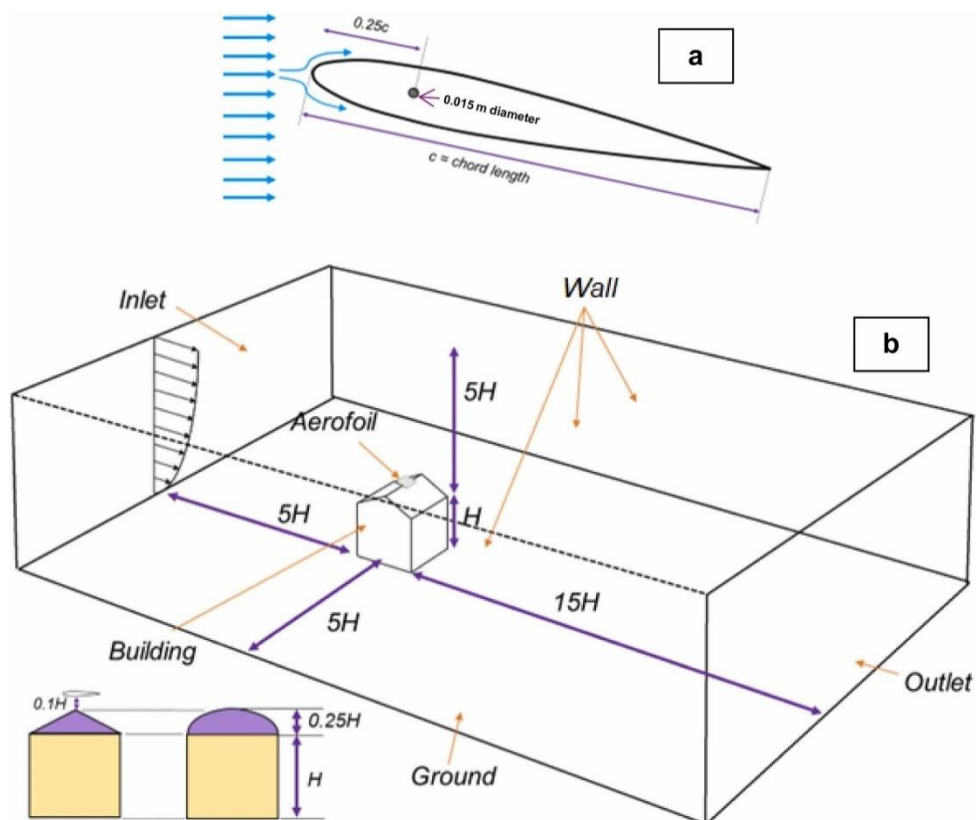


Figure 36. 3D CFD model computational building and domain

3.6 Computational mesh and verification

Figure 37 shows the mesh of the (a) computational domain of the building with the oscillating 3D NACA 0012 aerofoil integrated into the pitched roof (b) 2D view of the

mesh for BI-WEHS model (c) surface mesh around the oscillating aerofoil. The number of elements and nodes are shown in Table 9. The complexity of the model required the use of tetrahedral elements. The mesh analysis examined skewness, orthogonality, and aspect ratio criteria to ensure an appropriate mesh was generated. The maximum skewness value obtained was 0.7, which is within the acceptable range for highly skewed faces and cells [162]. The minimum orthogonality quality achieved was 0.5 and the minimum aspect ratio mesh quality was 1.16.

It is noted that the importance of mesh quality in ensuring accurate CFD simulations. Given the values obtained for skewness, orthogonality, and aspect ratio, the mesh was refined to improve the results. Through refining the mesh, the integrity of the simulations and achieve more reliable predictions of fluid flow behaviour can be improved

In summary, the selected mesh quality criteria and simulation setup appear well-suited for studying the fluid dynamics around an oscillating aerofoil integrated into a building roof structure. Through ensuring appropriate mesh quality and utilising a suitable turbulence model in transient conditions, the simulations can provide valuable insights into the aerodynamic behaviour and structural interactions, facilitating informed design decisions.

3.6.1 Mesh generation for BI-WEHS model

A sensitivity analysis of the computational grid was implemented by carrying out supplementary simulations with identical computational domains and boundary conditions but varying grid sizes. Grid refinement was conducted in alignment with critical zones of interest within the simulation of the integrated design involving an aerofoil and building roof structure. The mesh size was systematically adjusted to precisely capture regions with high gradients, as shown in Figure 37. This iterative process led to an augmentation in the number of elements, transitioning from coarse to fine resolution. This was between the medium and fine mesh. Therefore, a reiteration of the CFD model with a fine mesh did not result in a significant change in the results.

Ensuring a dependable mesh is crucial for obtaining precise outcomes. To ensure the robustness of the results, a sensitivity analysis for meshing was conducted. Figures 37 (a-c) illustrate the mesh configurations employed for the BI-WEHS model with the specified parameters: Three different meshes were assessed including coarse, medium, and fine. Ensuring mesh independence requires the convergence of results to approximately equal values. Table 9 provides details on mesh sizes for the three parameters. In regions proximate to walls, high solution gradients require precise calculations, which are crucial for the success of the simulation. Given the criticality of forces on the aerofoils in simulations, the approach to near-wall treatment is vital. This involves addressing the viscous sublayer to achieve a y^+ value of approximately 1 at the initial grid cell near the wall. As demonstrated in Figures 37 (a-c), mesh refinement is strategically implemented around the aerofoil and rod to ensure a $y^+ < 1$ all through the whole simulations.

The reliability of the CFD method was analysed based on previous studies. In summarising the mentioned studies, mesh sensitivity analyses were conducted to evaluate the impact of varying mesh resolutions (fine, medium, and coarse) on accuracy and computational efficiency. The fine mesh offered high detail and accuracy but demanded substantial computational resources, while the medium mesh achieved a balance between accuracy and efficiency, capturing essential aerodynamic features. The utilisation of a coarse mesh aimed to enhance computational efficiency, although at the cost of losing certain levels of detail. While the first study [180] specifically detailed both mesh and time step sensitivity analyses, the others incorporated mesh sensitivity to accurately capture aerodynamic forces in varying rotor geometries and predict aerodynamic damping and vortex-induced vibrations. However, these were not clearly outlined in the respective papers [180-184] presenting variations in the level of detail and emphasis on sensitivity analyses across the studies.

The set up and criteria used for the CFD model and simulations include the following:

- The mesh near the walls or boundaries was refined to capture the boundary layer dynamics accurately. For this setup, an initial cell height was chosen to ensure a low Y^+ value, specifically targeting $Y^+ < 1$ for URANS (Unsteady Reynolds-Averaged Navier-Stokes) with wall functions. This careful selection

of cell height was crucial for achieving accurate simulation results in the near-wall regions.

- The expansion ratio was set to range between 1.1 and 1.3, meaning each cell was 10% to 30% larger than the previous one. This gradual increase in cell size ensured a smooth transition from the fine mesh near the wall to the coarser mesh further away, maintaining gradient capture. The controlled expansion ratio played a key role in balancing computational efficiency with the need for detailed resolution in critical areas.
- The overall growth of the mesh was carefully controlled to avoid sudden changes in cell size, which could lead to numerical inaccuracies. A smooth transition in cell size was maintained to capture gradients and ensure the stability of the simulation. This approach ensured that the dynamics of the oscillating aerofoil were precisely captured, leading to reliable and precise simulation results.
- These adjustments in the boundary expansion ratios have been successfully integrated into the dynamic mesh setup for the oscillating aerofoil, ensuring that the simulation represents the physical phenomena involved. The detailed attention to mesh refinement, expansion ratios, and overall growth control has resulted in a robust and effective simulation framework for this complex engineering problem. The inlet condition was set to a constant velocity of 3 m/s, 6 m/s, and 9 m/s to ensure initial stability, the wind flow within the domain becomes dynamic due to interactions with the building structures and the oscillating aerofoil. As the wind encounters these elements, it undergoes significant changes, creating varying flow patterns, velocity, and pressure distributions. The oscillating aerofoil introduces additional complexities by generating vortices and wake regions, which further alter the flow characteristics over time. This evolving flow behaviour is crucial for accurately capturing the aerodynamic effects and overall impact of the wind on the structures.

Table 9. Mesh size details for three parameters

NACA 0012 integrated into the flat roof building			NACA 0012 integrated into the pitched roof building			NACA 0012 integrated into the curved roof building		
Mesh	Nodes	Elements	Mesh	Nodes	Elements	Mesh	Nodes	Elements
Fine	368587	1996799	Fine	369663	2002791	Fine	375320	2033751
Medium	255271	1371146	Medium	256458	1377991	Medium	261897	1406820
Coarse	190737	1023838	Coarse	192319	1033189	Coarse	190737	1023838

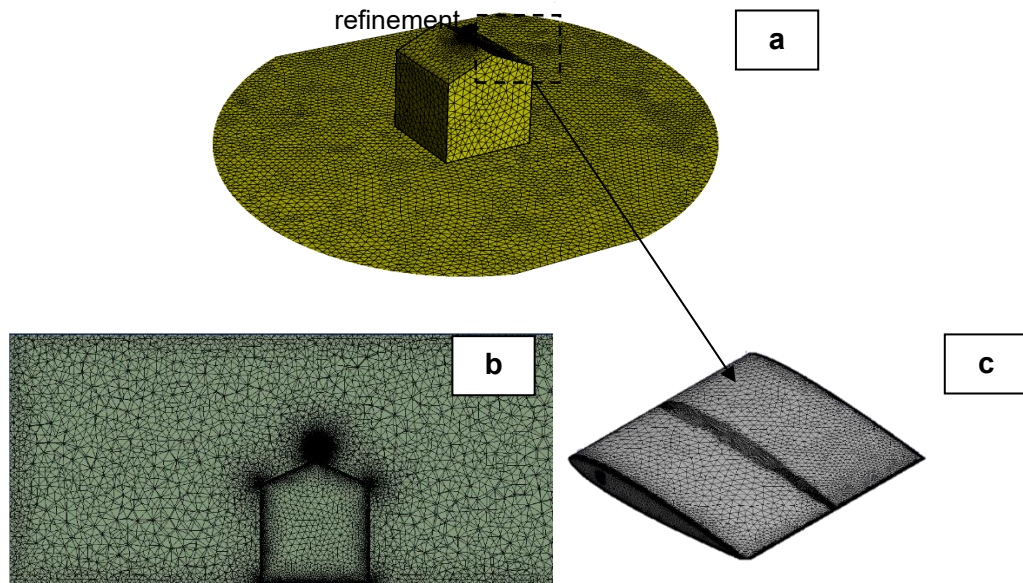


Figure 37. Mesh of the (a) computational domain of the building with the oscillating 3D NACA 0012 aerofoil integrated into the pitched roof (b) 2D view of the mesh for BI-WEHS model (c) surface mesh around the oscillating aerofoil

To evaluate the dynamic mesh behaviour, the mesh distribution can be sampled at specific locations along the aerofoil surface at different instances during the simulation. At each angle of attack, the mesh distribution can be examined at key positions, such as the leading edge, mid-chord, and trailing edge of the aerofoil. These samples can provide insights into how the mesh displaces or oscillates and adapts to capture the changing flow conditions around the aerofoil throughout the pitching motion. As shown in Figure 38 (a-d), areas of high mesh density near the leading edge and trailing edge of the aerofoil indicate regions of intense flow separation or vorticity formation, potentially influencing lift and drag characteristics. Conversely, regions of lower mesh density, particularly downstream of the aerofoil, may suggest smoother

flow conditions with reduced aerodynamic effects. In addition, observing how the mesh evolves over time during dynamic simulations can reveal the transient behaviour of lift and drag forces, highlighting fluctuations or oscillations in aerodynamic performance as the aerofoil moves through different angles of attack. Overall, analysing mesh distribution provides valuable diagnostic information for understanding the complex relationship between flow dynamics, mesh behaviour, and aerodynamic forces acting on the aerofoil.

Moreover, in near-wall regions where solution gradients are particularly high, ensuring accurate calculations is imperative for the success of the simulation. Given the critical role of forces on the aerofoil, near-wall treatment becomes essential. Resolving the viscous sublayer and employing mesh inflation around the aerofoil and rod ensures a smooth transition in mesh resolution, guaranteeing accuracy throughout all simulations. Through addressing these complexities in mesh refinement and near-wall treatment, the simulation framework maintains fidelity in capturing aerodynamic phenomena, ultimately enhancing the reliability and trustworthiness of the computational results.

Figure 38 shows the samples of results of mesh distribution at various positions of the aerofoil for dynamic mesh behaviour in different angles (a) 0 degree (b) 5 degrees (c) -10 degrees (d) 10 degrees. These offers valuable insights into the dynamic behaviour of the mesh, particularly concerning lift and drag forces acting on the aerofoil. Through analysing the mesh distribution, one can observe how the mesh adapts and deforms in response to changes in the flow field around the aerofoil. Specifically, variations in mesh density and structure can provide indications of regions where the flow is highly complex or where significant aerodynamic forces are exerted.

The use of four mesh samples to illustrate the mesh deformation at different time steps is justified by the need to capture the dynamic changes in aerodynamic forces during the upward and downward movements of the aerofoil. The higher cell density at the nose (leading edge) and trailing edge is crucial for resolving the pressure gradients, boundary layer adjustments, and flow separation/reattachment phenomena. This dynamic adaptation ensures accurate and reliable simulation results, which essential for understanding the aerofoil's aerodynamic performance. The four samples provide

a clear and concise representation of how the mesh deforms over time, which help to understand the dynamic behaviour of the mesh and its interaction with the aerofoil's movement. Emphasising the nose and trailing edge regions with more cells is justified due to their importance in capturing key aerodynamic phenomena.

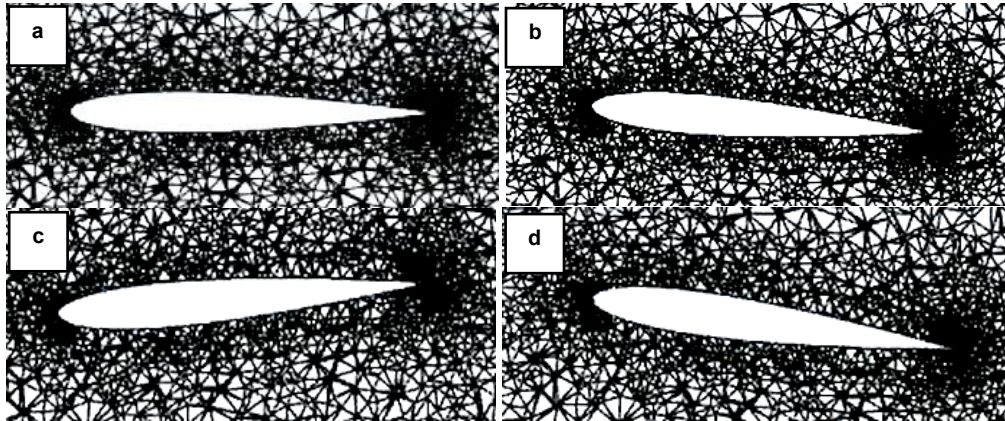


Figure 38. Samples of results of mesh distribution at different positions of the aerofoil for dynamic mesh behaviour in different angles (a) 0 degree (b) 5 degrees (c) -10 degrees (d) 10 degrees

3.6.2 Mesh sensitivity analysis

To validate the dynamic mesh behaviour, it is imperative to analyse the mesh distribution at various positions of the aerofoil throughout the simulation. Figure 39 shows the aerofoil response to pitching motions at freestream velocities of 3 m/s, alongside different angles of attack (0° , 5° , 10° , and 15°). Employing a comprehensive meshing approach in dynamic mesh simulations ensures efficient capture of flow dynamics while upholding computational accuracy. Tetrahedral meshing around the aerofoil provides effective boundary layer resolution and robust turbulence modeling, supporting grid independence for a reliable representation of aerodynamic behaviour. A mesh sensitivity study was conducted, varying the mesh size, and assessing the scheme convergence. This sensitivity analysis encompassed three parameters, including the NACA 0012 aerofoil integrated into three distinct roof configurations including flat, pitched, and curved structures. It is crucial for the mesh sensitivity test to consider lift coefficients of the aerofoil at specific angles of attack (e.g., 10°).

Figure 39 demonstrates the investigation which evaluates various mesh resolutions including fine, medium, and coarse for three different design parameters including

NACA 0012 integrated into the (a) flat, (b) pitched, and (c) curved roof building and their effects on result precision and computational expenses within the simulation framework. Fine meshes are known for their complex detail and precision, offer an understanding of the studied phenomena. However, this advantage accompanies significantly higher computational resource requirements. Conversely, coarse meshes prioritise computational efficiency by sacrificing some detail, yet they offer broader insights into overall system behaviour.

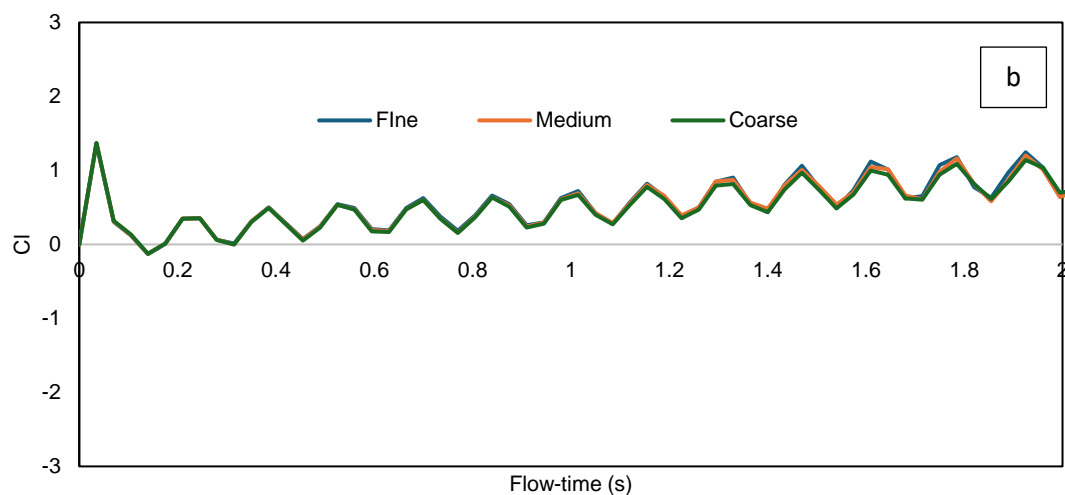
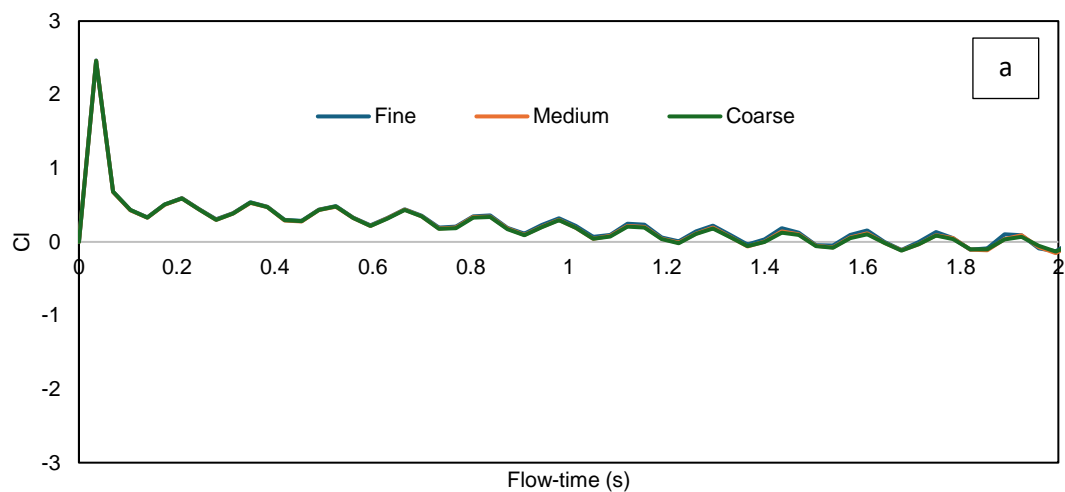
The aim of the study was to evaluate how different mesh resolutions including coarse, medium, and fine affect the accuracy of transient simulations of an oscillating aerofoil. To achieve this, plotting C_l against flow-time is crucial as it directly captures how lift varies over time during dynamic conditions. This approach allows for a detailed assessment of the dynamic response of the aerofoil, including its ability to simulate oscillations and unsteady flow effects. Through analysing how each mesh resolution impacts these time-dependent variations, the study can determine the accuracy and reliability of the simulation results in representing transient aerodynamic behaviour.

In contrast, plotting C_l against the angle of attack is more appropriate for steady-state analyses, where the focus is on how lift changes with different angles of attack rather than with time. While such plots provide valuable insights into aerodynamic performance at various operational angles, these simulations do not address the time-dependent aspects that are central to transient simulations. Therefore, for the sensitivity analysis aimed at evaluating dynamic accuracy, examining C_l over flow-time is the most relevant method. This approach ensures a comprehensive understanding of how mesh resolution affects the simulation of transient phenomena.

Moreover, these results provide a fundamental role in this analysis, providing a comparative assessment of the aerofoil C_l across different mesh resolutions and parameters. Also, the results reveal a consistent evolution in wind energy capture technology with medium and fine meshes, indicating accurate capture of system dynamics. However, disparities emerge with coarse meshes, suggesting inadequate representation of airflow complexities around the aerofoil. Furthermore, the evolution of results with mesh refinement, as shown in s Figure 32 highlights the importance of

attaining optimal mesh resolution in numerical simulations. While mesh refinement enhances accuracy, it also escalates computational costs. In this context, the medium mesh, offering identical results to the fine mesh but with lower computational burden, was chosen for all simulations. This decision ensures a balance between accuracy and computational efficiency, maximising the utility of computational resources.

Considering computational expenditure, employing a fine mesh entails a significant time investment for simulation completion. Thus, the medium mesh was selected to strike a balance, delivering satisfactory CFD quality without overburdening computational resources. Specifically, the fine mesh required 20 hours, the medium mesh 12 hours, and the coarse mesh 9 hours of processing time on a PC equipped with a 6-core processor.



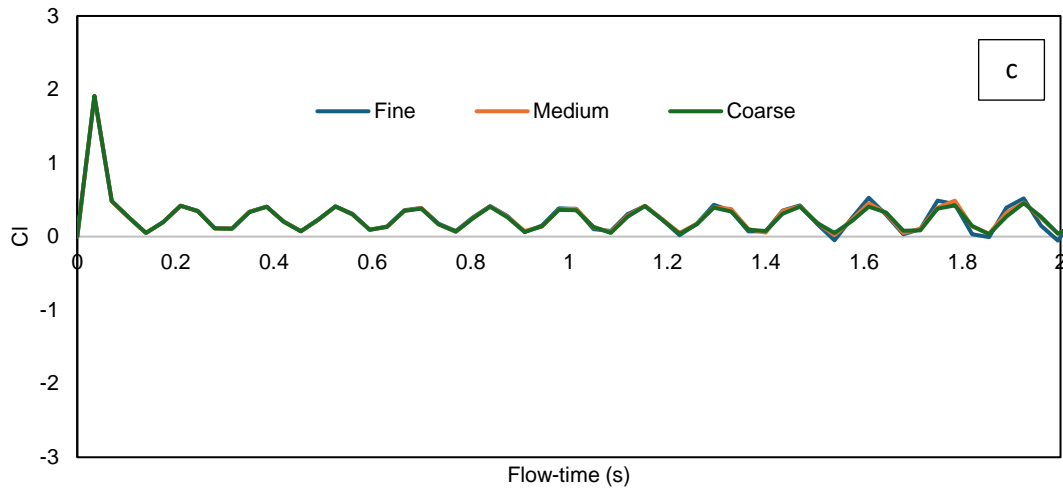


Figure 39. Mesh grid sensitivity analysis for the lift coefficient of NACA 0012 integrated into the (a) flat (b) pitched, and (c) curved roof building

3.6.3 Time sensitivity analysis

The time sensitivity assessment was carried out to examine the effect of time step variations on transient simulations that studied the velocity magnitude at the leading edge of a NACA 0012 aerofoil. The analysis was performed within the context of three different building roof shapes: flat, pitched, and curved. Two-time step sizes (0.035s and 0.03s) were used, aiming to maintain a Courant–Friedrichs–Lewy (CFL) number below 1. As shown in Figure 40 (a-c), the sensitivity analysis provided valuable insights into how variations in input parameters, specifically time steps, influenced the output, facilitating the identification of the optimal parameter value. In essence, reaching numerical stability at almost 1(t) s flow time in CFD simulations for the two parameters at 0.035 s and 0.03 s time steps, which signify efficient convergence, suitable numerical methods, and time step sizes, indicating the physical significance of the results. Table 10 provides a summary of the parameters investigated in the time sensitivity analysis conducted for this study. This not only enhances computational efficiency and emphasises parameter sensitivity but also highlights the importance of validating results against real-world data to ensure their accuracy and applicability to the studied physical system. Consequently, a time step of 0.035s was adopted for subsequent simulations, yielding computational cost and time savings.

The CFL number is a dimensionless parameter used to determine the stability of numerical simulations, particularly in fluid dynamics. It is calculated as the product of the time step size (Δt), the velocity of the flow (V), and the reciprocal of the characteristic length scale (L), divided by the kinematic viscosity (ν). The equation (3.13) [162] for CFL number (CFL) is:

$$(3.13) \quad CFL = \frac{V \cdot \Delta t}{L \nu}$$

The CFL number was calculated for each time step using the formula: $CFL = (\text{velocity} \times \text{time step}) / \text{grid spacing}$. Table 10 shows the analysis of how changing the time step affects the CFL number, which is critical for ensuring numerical stability and accuracy in simulations. Also, it shows the sensitivity analysis of time steps for two different values including 0.035 and 0.03 with a constant velocity of 3 m/s.

Table 10. Time steps sensitivity analysis

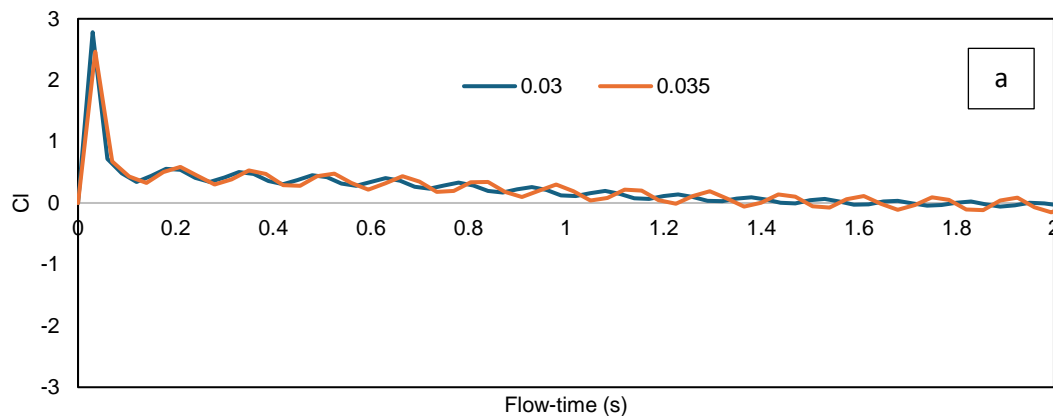
Time step (s)	Velocity (m/s)	Grid Spacing (m) for CFL =1
0.035	3	0.105
0.03	3	0.09

In the current CFD study, both mesh and time step sensitivity analyses are essential for optimising accuracy and efficiency. The mesh sensitivity analysis ensures that the simulations accurately represent complex flow interactions around an aerofoil and various building roof structures. It aids in determining the ideal mesh resolution, striking a balance between computational efficiency and result precision. Similarly, the time step sensitivity analysis is essential for maintaining simulation stability during transient behaviour, crucial in capturing the evolving flow patterns. It enables the selection of appropriate time steps that neither sacrifice accuracy nor overstrain computational resources. Overall, these sensitivity analyses are fundamental in guiding parameter choices and ensuring dependable insights into aerofoil behaviour in different roof shapes, enhancing the overall quality and success of the study.

The choice of time step in the sensitivity analysis not only affects computational efficiency but also has implications for the accuracy of aerodynamic parameters such as C_l of the aerofoil. Figure 40 shows the comparative analysis for the two cases of time steps including 0.03 and 0.035 for different parameters including NACA 0012

integrated into the (a) flat, (b) pitched, and (c) curved roof building. In the context of the study, the selection of a time step directly impacts the temporal resolution of the simulation, influencing how well the aerodynamic forces acting on the aerofoil are captured over time. A finer time step, such as 0.03, allows for more frequent updates of the flow field and aerodynamic forces acting on the aerofoil throughout the simulation. This finer resolution can potentially result in more reliable predictions of the lift coefficients, especially in capturing transient phenomena or rapid changes in flow conditions. However, this increased temporal resolution comes at the cost of higher computational demands. On the other hand, a coarser time step, such as 0.035, provides less frequent updates of the flow field and aerodynamic forces. While this may lead to slightly reduced accuracy in capturing rapid changes, it also reduces computational time, making it a more efficient choice for simulations where computational resources are limited.

Overall, this approach integrates multiple analyses to make informed decisions about simulation parameters. Through carefully considering how variations in time step affect aerodynamic parameters and coordinating this with the findings of the mesh sensitivity analysis, the confidence with selecting the optimal time step that balances accuracy, reliability, and computational efficiency in predicting the lift coefficients of the aerofoil.



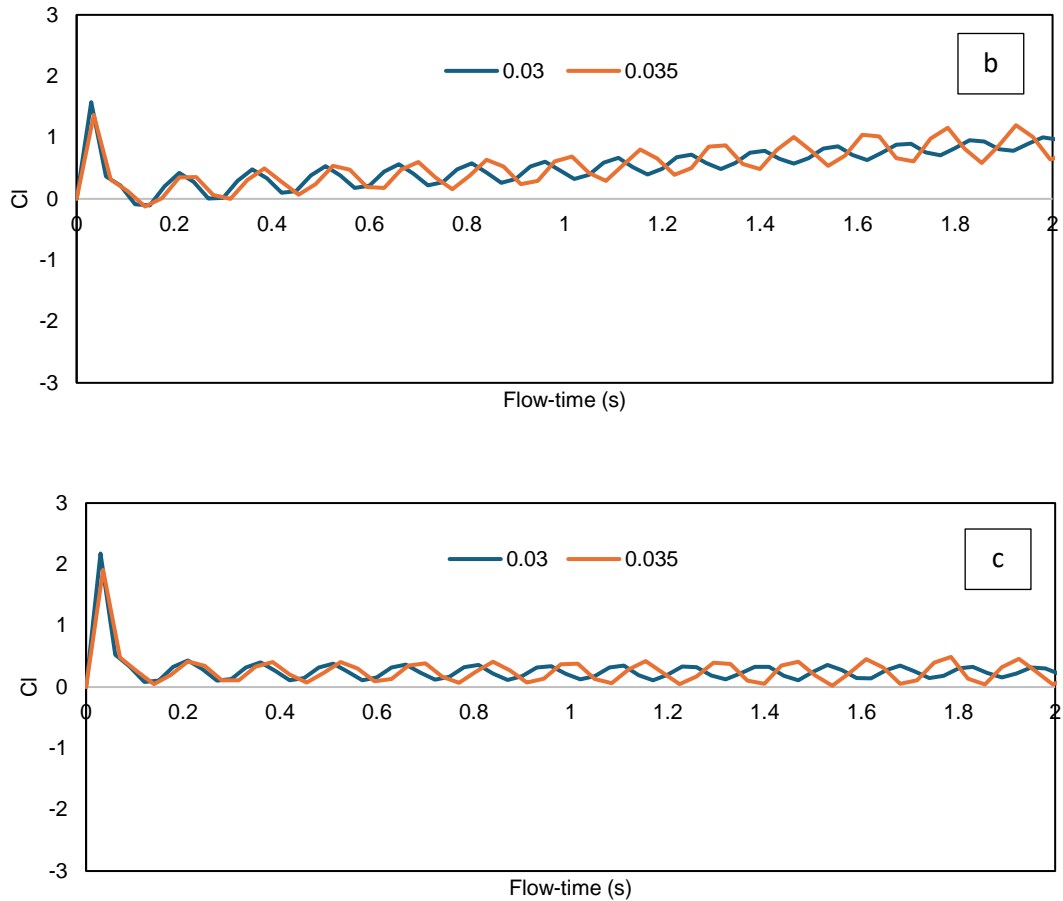


Figure 40. Time sensitivity analysis for the lift coefficient of NACA 0012 installed into the (a) flat (b) pitched, and (c) curved roof structure

3.7 CFD setup and boundary conditions

The simulation used a 3D unsteady Reynolds-averaged Navier-Stokes (URANS) equation model along with momentum and continuity equations to analyse the dynamic behaviour of the proposed Building-Integrated Wind Energy Harvesting System (BI-WEHS). In Table 11, it demonstrates the CFD model set up and boundary conditions for analysing the dynamic behaviour of the proposed design of BI-WEHS. The inlet velocities were set to 3, 6, and 9 m/s with wall boundary conditions on the top boundary. While for the pressure-based, the transient model was used for this simulation while considering the gravitational forces. For an oscillating aerofoil with constant 850 (n-m/rad) at 1 degree of freedom (1-DOF) rotational rigid body motion in ANSYS Fluent, it means that the simulation is modelling the aerofoil motion in a fluid flow environment where the aerofoil is subjected to rotational oscillations around a fixed axis. The spring constant represents the stiffness of the rotational spring system,

indicating how resistant the system is to rotational displacement. The selection of a constant 850 (n-m/rad) is supported by relevant studies [182-187] investigating various aspects of oscillating aerofoil systems. These studies indicate that this specific spring constant optimises stability, controls oscillations effectively, and regulates dynamic response. Its importance lies in providing predictable and controlled aerofoil movements, preventing undesirable oscillations, and contributing to enhanced aerodynamic performance, stability, and control different flow conditions.

For the freedom of movement of the aerofoil in this simulation, the axis of the rod was positioned at 0.25 metres from the leading edge along the chord length. Remeshing-smoothing commands were implemented in the simulations. To analyse pitch motion, a one-degree of freedom (1-DOF) rotation solver with a centre at 0.25 and along the z-axis was utilised, with a mass of 3.27 kg and a moment of inertia of 0.4 kg.m². The centre of gravity was situated at 0.41 metres along the chord length, with these values derived from the material properties of PVC foam as shown in the DesignModeler CAD model of the NACA 0012 aerofoil profile.

Table 11. CFD model set up and boundary conditions

Turbulence model	Standard k-epsilon
Algorithm	SIMPLE
Time	Unsteady state
Solver type	Pressure based
Discretisation Scheme	First order upwind
Turbulence model	Standard k-epsilon
Wall boundaries	Standard wall functions
Wall (Sides)	Wall (zero normal velocity and zero gradients)
Wall (Top)	Wall (zero normal velocity and zero gradients)
Fluid	Air
Inlet velocity (m/s) at UH	3 m/s, 6 m/s, and 9 m/s
Pressure outlet	0 Pa
Gravity (m/s ²)	-9.81

The application of constant 850 (n-m/rad) m spring constant in the simulation of oscillating aerofoil systems, supported by studies in the field, ensures enhanced stability, precise control of oscillations, and regulation of dynamic response. This specific spring constant has been chosen to provide predictable and controlled aerofoil movements, effectively preventing undesired oscillations. Moreover, the utilisation of a 1-degree-of-freedom setup, focusing on rotational motion typically around the pitch axis, simplifies the simulation while enabling a comprehensive analysis of the aerofoil behaviour in varying fluid forces. The incorporation of a dynamic mesh approach further enhances accuracy by facilitating detailed examination of aerofoil deformations and forces such as lift and drag. This methodology, combined with a 1-DOF solver and rigorous grid quality assessment techniques, contributes to improved stability, control, and accuracy in aerodynamic simulations, thereby advancing the optimisation of aerofoil design and performance.

The 1-DOF setup, focusing on rotational motion typically around the pitch axis, simplifies the simulation while enabling a comprehensive analysis of the aerofoil behaviour in different fluid forces. In addition, the dynamic mesh approach enhances accuracy by facilitating detailed examination of aerofoil deformations, lift, and drag forces. This methodology, combined with rigorous grid quality assessment techniques, contributes to improved stability, control, and accuracy in aerodynamic simulations, advancing aerofoil performance. Moreover, the unsteady CFD, determining convergence poses unique challenges due to time-varying solutions. In this study, the CFD results utilised the monitors, flow patterns, and residuals to assess convergence. Monitors track variations in outputs over time, ensuring expected behaviour or stabilisation of convergence. While the flow patterns were qualitatively assessed in terms of simulation sensibility, identifying irregularities. The residuals monitor iterative solution progress, with decreasing trends indicating convergence toward a periodic solution. In conclusion, navigating convergence in unsteady CFD simulations requires adaptability and a combination of specialised tools to ensure reliable results.

Moreover, the k-epsilon turbulence model and a 1 degree of freedom (1-DOF) dynamic mesh approach were applied for these simulations. The choice of wall treatment and corresponding y^+ values become crucial for capturing the near-wall flow behaviour.

The k- ϵ models with enhanced near-wall treatment were used. These models directly resolve the viscous sublayer and capture the complex flow patterns occurring near the wall. For the oscillating NACA 0012 integrated into the building roof cases where the dimensionless wall distance y^+ is less than 1, low Reynolds number models were employed to ensure reliable representation of laminar or transitional flow phenomena near the wall. The model offered comprehensive understanding of flow behaviour in critical regions, enabling detailed analyses of aerofoil and building aerodynamic characteristics. This range is advised to ensure precise predictions of near-wall turbulence effects. Through adhering to this range, the model can effectively capture the complex dynamics occurring close to the wall, thereby enhancing the accuracy of the predictions in computational fluid dynamics simulations. However, in simulations involving dynamic mesh motion, such as oscillating aerofoils, the near-wall flow behaviour can be highly complex and dynamic, requiring finer resolution near the wall. In such cases, especially when employing specific wall treatment models that demand very fine mesh resolution near the wall, y^+ values below 1 may be necessary to accurately capture the turbulent structures and shear effects close to the surface. This finer mesh resolution helps in better resolving the boundary layer and turbulent flow structures, which is essential for predicting the aerodynamic forces acting on the oscillating aerofoil.

The selection of a 1-metres chord length and 1-metres span for an oscillating aerofoil integrated into a building roof structure is supported by findings from various studies focusing on wind energy harvesting systems. Roothaan et al. [187] emphasise the importance of design parameters such as chord length and span in maximising energy capture while minimising the impact on surrounding structures and aesthetics, aligning with the concept of compact design for compatibility with urban environments. Similarly, [188] explore blade dimensions to balance performance and structural integrity, suggesting that smaller chord lengths and spans optimise aerodynamic efficiency while maintaining stability. Hernandez-Estrada et al., [189] provides insights into considerations for wind turbine tower design, potentially discussing optimal dimensions to withstand wind loads and ensure stability. Finally, [171] offer a review of wind energy research, including discussions on chord length and span optimisation, supporting the use of a 1-metre chord length and 1-metre span for

efficient energy capture. Overall, these studies provide a solid foundation for the selection of compact dimensions in wind energy systems, aligning with established principles and findings in the field.

3.8 Solver methods and control

The 3D URANS equation with a combination of turbulence models was resolved using ANSYS Fluent 21 R2, and all computational simulations were carried out on a remote desktop at the University of Strathclyde in Glasgow, UK. The SIMPLE algorithm was used for velocity pressure coupling, and the governing equations were discretized. The transient formulations employed a first-order implicit method, with a time step size of $\Delta t = 0.035$ s (calculated as the typical element size divided by the characteristic flow mean wind velocity). To ensure continuity, convergence was achieved when all residuals were scaled and levelled off, reaching a minimum of 10^{-5} and 10^{-6} for x, y, and z momentum. The residuals were monitored over an extended period to confirm that the assumed values were attained.

3.9 Computational method, analysis, and visualisation

In this section, the CFD computational method, analysis, and visualisation will be discussed for a single NACA aerofoil wind energy harvesting system and when integrated into the building roof structure. The analyses will focus on the wind speed acceleration, wind flow characteristics, and the dynamic behaviour of the oscillating aerofoil in terms of aerodynamic characteristics, torque and angular velocity will be presented. Moreover, the results will provide the analyses and visualisation of the gathered CFD results and data to gain insights into the performance and behaviour of the system.

3.9.1 Airflow characteristics and speed acceleration for isolated standalone NACA 0012 aerofoil

Unsteady state CFD simulations, employing the URANS turbulence model, were employed to examine the aerodynamic traits of the NACA 0012 aerofoil. In Fluent, lift and drag coefficients for NACA 0012 aerofoil profile were derived from pressure and shear forces integrated over the surface, normalised by dynamic pressure and reference

area. Fluent's monitoring capabilities facilitated the real-time assessment of these coefficients.

Concurrently, visualisation of velocity magnitude and static pressure contours provided valuable insights into airflow patterns and pressure distribution. The velocity magnitude can provide information regarding the airflow distribution and wind speed acceleration at different angle of attack, while the presence of airflow separation at the trailing edge indicated potential performance limitations affecting efficiency and stability. For a standard aerofoil, managing separation at the trailing edge can help mitigate flow detachment and reduce drag. Uncontrolled or premature separation can lead to significant performance drawbacks. To achieve the desired separation characteristics, several approaches can be utilised. Adjusting the angle of attack allows for control over the timing and location of separation, improving aerodynamic efficiency. Moreover, flow control techniques such as leading-edge modifications, or boundary layer suction can be employed to manage and delay separation, thereby enhancing performance.

Moreover, the CFD method allowed for investigation of wind speed acceleration, crucial for applications such as wind energy harvesting by quantifying the percentage increase in wind speed and thus assessing the aerofoil's capability to enhance energy conversion or propulsion. Visualisation of velocity magnitude and static pressure contours, as depicted in Figure 41 for the NACA 0012 at 3 m/s with a 0-degree angle of attack provides insights into airflow distribution and pressure variations.

Through integrating analysis of these parameters, engineers can refine the aerofoil designs for optimal aerodynamic efficiency and stability across diverse applications. Ultimately, these observations deepen understanding of the aerofoil's aerodynamic behaviour, offering insights into its potential for applications such as wind energy harvesting and propulsion systems.

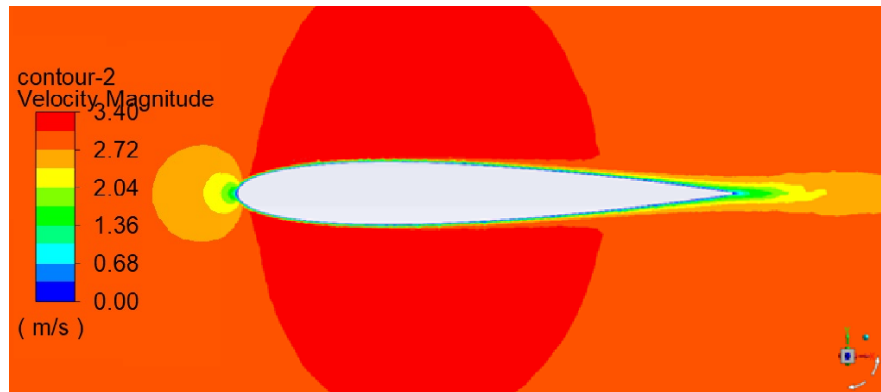
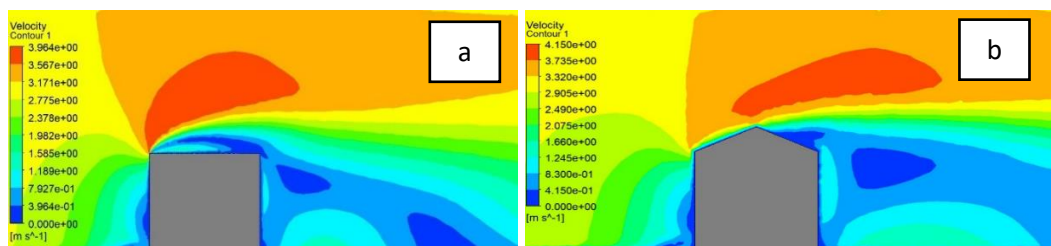


Figure 41. Velocity magnitude contour of NACA 0012 at 3 m/s with 0 angle of attack

3.9.2 Airflow characteristics and speed acceleration for building roof structure

The modelling approaches for assessing the potential acceleration of flow on flat, pitched, and curved roof structures involve 3D CFD simulations, which utilise advanced numerical methods to solve the Navier-Stokes equations within the defined geometry of the roofs. These simulations consider complex flow patterns, boundary layer interactions, and potential flow acceleration effects, such as vortex shedding and wind shear, depending on the specific roof geometry. The analysis was focused on demonstrating distinct wind flow dynamics and evaluating the potential for renewable energy integration, particularly by examining wind speed acceleration for different roof shapes to assess the feasibility of integrating an oscillating aerofoil and identifying optimal placements. Figure 42 shows the velocity magnitude for the (a) flat, (b) pitched, and (c) curved roof building structure. Velocity magnitude was measured and monitored in ANSYS Fluent, with post-processing conducted through contours and plots from various points surrounding the aerofoil and building roof structure to provide insights into flow behaviour and inform design decisions.



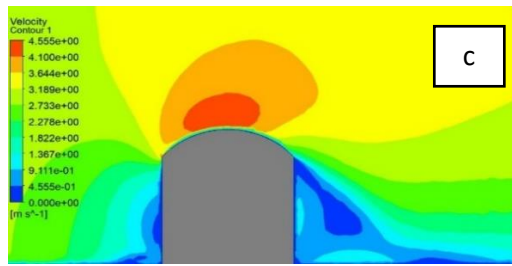


Figure 42. Velocity magnitude contours of (a) flat (b) pitched (c) curved roof building

3.9.3 Atmospheric boundary layer velocity profile

This study will also investigate the influence of atmospheric boundary layer (ABL) data on the integrated design of an oscillating aerofoil with a building's roof structure, using data sourced from the [190]. Figure 43 (a) shows the ABL velocity profile [190] imported to the CFD simulations and Basilan, Phillipines map gathered from [191]. The research includes a comprehensive analysis based on hourly wind data for 24 hours on January 1, 2021, centered around a rural location in Basilan, Philippines, characterised by its low wind speeds. This location has wind speeds ranging from 0 to 7 m/s and an average speed of 3.5 m/s over a 24-hour period, which provides an ideal environment to assess the performance of a wind energy harvesting system embedded in the roof of a building. Figure 43 (b) shows a far view of the Basilan map sourced from [191], while Figure 43 (c) presents a closer view obtained from [192].

Basilan, Philippines was chosen for exploring rural electrification opportunities due to its known scarcity of electricity and poor community infrastructure, which makes it challenging for many residents to afford or access consistent electrical power. Through targeting areas such as Basilan, the proposed design can potentially provide direct power to low-powered devices such as mobile phones, sensors, and LED lights without relying on the grid. Basilan experiences varying wind conditions throughout the year with average wind speeds ranging from 5.9 km/h to 8.9 km/h [193]. While these wind conditions are not consistently high enough to rely solely on wind energy, these may be adequate for certain wind energy harvesting technologies designed for lower wind speeds.

Pitched residential roofs are common in Basilan and best represent the typical building structure in the area. These roofs can accommodate oscillating aerofoil systems,

making them suitable for harnessing wind energy in a practical and efficient manner. Through leveraging local conditions and integrating innovative wind energy technologies, it is possible to complement solar power and enhance the overall energy supply for rural areas like Basilan, contributing to improved electrification and quality of life for its residents.

Moreover, the study will use CFD simulations to evaluate the behavior of a NACA 0012 aerofoil positioned on three different roof types including flat, pitched, and curved. The simulations were standardised by using the same dimensions for the aerofoil, the roof structure, and the computational domain across all models. In addition, the selection of a rural area for this study was due to the wind behaviour which has smoother and less turbulent wind flows common to such areas to optimise the stability and efficiency of wind energy harvesting technologies. This integration is also beneficial for remote or off-grid locations, enhancing their energy security and ecological footprint.

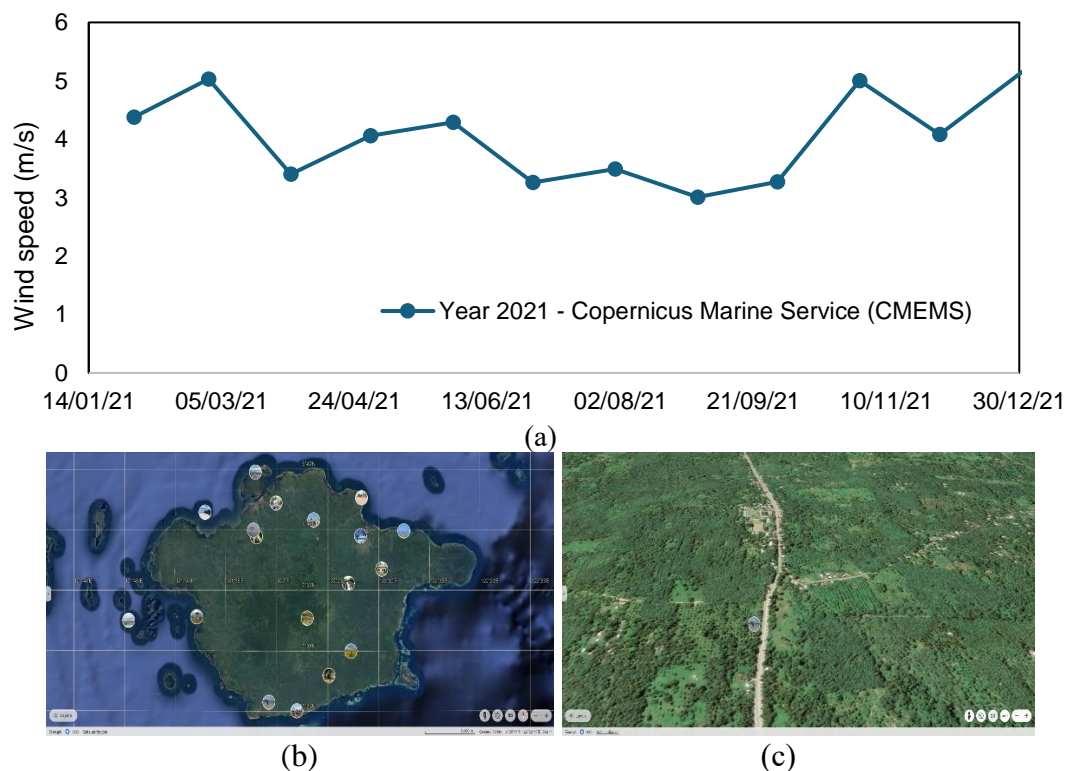


Figure 43. Basilan Philippines (a) ABL velocity profile data imported to the CFD simulations using data from the [190] and (b) Map data: Google, Data SIO, NOAA, U.S. Navy, NGA, GEBCO, Maxar Technologies, Airbus [191] and (c) Map data: Google, Maxar Technologies, Data SIO, NOAA, U.S. Navy, NGA, GEBCO, TerraMetrics, Landsat / Copernicus [192]

3.10 Dynamic behaviour

The dynamic behaviour of a single stand-alone oscillating aerofoil wind energy harvesting system, including the standalone and when incorporated into the building's roof structure will be examined. The research method used was the 1 Degree of Freedom (DOF) solver and CFD transient analysis in ANSYS Fluent. At the same time, it will predict the average mechanical power output by analysing the dynamic behaviour of an oscillating aerofoil, both stand-alone oscillating aerofoil and when integrated into the building roof structure.

For one study, a constant inlet velocity was used to simplify the boundary conditions. In this setup, the inlet velocity was specified directly as a constant value such as 3 m/s, 6 m/s, and 9 m/s in the velocity inlet boundary condition panel. This method ensures that the focus remains on the transient effects introduced by the dynamic behavior of the oscillating airfoil itself, without additional complexities from varying inlet conditions.

In another study, the inlet velocity and velocity profile were defined using a power law with height instead of using an average velocity. This approach allows for a more precise representation of how velocity changes with altitude, which is critical for capturing the dynamics of the flow in the specific context of the study area. Through considering the variation in velocity with height, the simulation can be more accurately reflect the real-world conditions and provide more reliable results.

These methodologies highlight the importance of tailoring the setup of inlet conditions to the specific requirements and goals of the CFD analysis. Whether using a constant velocity or a height-dependent velocity profile, the key is to ensure that the inlet conditions are represented to achieve meaningful and applicable results from the transient analysis.

3.10.1 Dynamic behaviour of the oscillating aerofoil energy harvester

The dynamic behaviour of the single stand-alone oscillating aerofoil will be examined by analysing various parameters such as pitch oscillation, torque exerted on the aerofoil, angular velocity, and expected mechanical power output. The response of the aerofoil to wind gusts or steady wind conditions will be simulated, recording the time-dependent variations of these parameters.

When an oscillating aerofoil is integrated into a building and positioned too close to the roof or other obstructions, several critical issues can arise. One major concern is aerodynamic interference, where the movement of the aerofoil generates varying aerodynamic forces that can disrupt airflow patterns around it. This disruption can alter the intended oscillatory motion, leading to unpredictable behavior or reduced efficiency of the system. Moreover, mechanical constraints can cause problems if the aerofoil encounters physical obstructions, such as the building's roof, during its oscillations. This can result in the aerofoil becoming stuck or unable to return to its neutral position, compromising both the functionality and safety of the system.

To address these risks, careful design considerations are necessary. Engineers must ensure that the placement and clearance of the oscillating aerofoil are adequately planned to allow for its full range of motion without encountering obstructions. Using CFD simulations and physical testing can provide valuable insights into the aerodynamic forces and airflow patterns affecting the aerofoil, helping to optimise the design and minimise interference.

The pitch oscillation, torque, and angular velocity as a function of time to understand the aerofoil's response to different wind condition were observed. Through analysing the expected power output, the energy harvesting potential of the oscillating aerofoil and its dependence on wind characteristics will be assessed. The torque values can demonstrate the aerofoil's ability to convert the kinetic energy of the wind into rotational motion. To further assess the performance of the aerofoil, it would be beneficial to compare these torque values with other relevant parameters, such as the aerofoil's lift and drag coefficients, power output or efficiency. In addition, conducting similar analyses at different wind speeds or aerofoil configurations can provide a comprehensive understanding of the aerofoil's behaviour and its potential for energy

harvesting applications. Overall, the torque analysis of the oscillating NACA 0012 aerofoil provides valuable insights into its performance characteristics, enabling engineers and designers to assess its effectiveness in various applications and make informed decisions regarding its use for wind energy conversion.

While the angular velocity (ω) is a measure of how quickly the position angle of an object changes over time. It is defined as the ratio of the change in position angle (θ) to the elapsed time (t). Mathematically, angular velocity can be expressed as $\omega = \frac{d\theta}{dt}$ where ω represents the angular velocity, $d\theta$ represents the position angle, and dt represents the elapsed time. This equation demonstrates that angular velocity provides information about the rate at which an object rotates or changes its position angle relative to time.

The angular velocity of an oscillating aerofoil is a crucial parameter as it directly relates to the power output and performance of the system. Higher angular velocities generally indicate higher power generation potential. Therefore, a higher maximum angular velocity suggests that the aerofoil can achieve faster rotation and higher power output during its oscillation in the given wind speed. Whereas the negative average angular velocity suggests that on average, the aerofoil is rotating in the opposite direction compared to the reference frame. This information is valuable for understanding the behaviour of the aerofoil and its interaction with the wind flow.

To further assess the performance of the aerofoil, it would be beneficial to analyse other relevant parameters, such as the generated torque, lift and drag coefficients, power output, or efficiency. In addition, conducting similar analyses at different wind speeds or aerofoil configurations can provide a comprehensive understanding of the aerofoil's behaviour and its potential for energy harvesting applications.

In summary, the analysis of the average and maximum angular velocity achieved by the oscillating aerofoil provides insights into its rotational behaviour and performance characteristics. These parameters are essential for assessing the aerofoil's effectiveness

in converting wind energy into rotational motion and can assist engineers and designers in optimising its design for efficient energy harvesting.

3.10.2 Dynamic behaviour of the roof-integrated oscillating aerofoil energy harvester

To improve the wind energy harvesting performance, the oscillating aerofoil will be integrated into the building roof structure. In this section, the single aerofoil will be installed into the pitched roof building structure to investigate the wind speed acceleration and relation to the torque, angular velocity, and potential power output. This will provide a fundamental understanding of the dynamic behaviour and effects on the power extraction performance of the proposed model of an oscillating NACA 0012 aerofoil incorporated into the building roof.

The integration of the oscillating aerofoil into the building structure to analyse its dynamic behaviour and potential structural implications will be investigated. This involved assessing the interaction between the aerofoil and the building in different wind conditions. The response of the integrated system and analysed parameters such as pitch oscillation, torque, and angular velocity of the oscillating aerofoil installed into the building structure will be simulated. Through visualising these results, it will provide insights into the dynamic behaviour and structural impact of the oscillating aerofoil within the building context.

When an oscillating aerofoil is integrated into a building and positioned too close to the roof or other obstructions, several critical issues can arise. One major concern is aerodynamic interference where the movement of the aerofoil generates varying aerodynamic forces that can disrupt airflow patterns around it. This disruption can alter the intended oscillatory motion, which can lead to unpredictable behaviour or reduced efficiency of the system. Furthermore, mechanical constraints can cause problems if the aerofoil encounters physical obstructions, such as the building's roof during its oscillations. This can result in the aerofoil becoming stuck or unable to return to its neutral position, compromising both the functionality and safety of the system.

To address these risks, careful design considerations are necessary. Engineers must ensure that the placement and clearance of the oscillating aerofoil are adequately planned to allow for its full range of motion without encountering obstructions. Using computational fluid dynamics (CFD) simulations and physical testing can provide valuable insights into the aerodynamic forces and airflow patterns affecting the aerofoil, helping to optimise the design and minimise interference.

Overall, the computational results analysis and visualisation provided valuable insights into the wind speed acceleration, wind flow characteristics, and dynamic behaviour of the oscillating aerofoil. These findings contribute to a comprehensive understanding of the system's performance and inform future design considerations and optimisation strategies.

3.10.3 Mechanical power output

To calculate the potential power output of the wind energy harvesting technology, the mechanical power equation was utilised. This equation enables the calculation of power by considering the dynamic behaviour of an oscillating aerofoil integrated with a roof building structure. In mechanical systems, power arises from the interaction between forces and motion. Specifically, power can be determined by multiplying a force acting on an object by the object's velocity. Alternatively, power can also be obtained by multiplying a torque applied to a shaft by the shaft's angular velocity. Another perspective on mechanical power is viewing it as the rate of change of work.

In the field of mechanics, the work performed by a force F on an object moving along a curve C can be determined using a line integral. This line integral accounts for the force exerted by the object and the path it traverses, as shown in (3.14).

$$(3.14) \quad W_C = \int_C \mathbf{F} \cdot v \, dt = \int_C \mathbf{F} \cdot dx,$$

where x denotes the path C that the object follows, while v represents the velocity along this path.

When the force \mathbf{F} can be derived from a potential function (which implies a conservative force), the gradient formula can be applied. Through force that is the negative gradient of potential energy, the following expression is represented in (3.15).

$$(3.15) W_C = U(A) - U(B)$$

where A and B represent the starting and ending points of the path along which the work was performed.

The use of potential energy is pivotal for calculating the work done by aerodynamic forces on the oscillating aerofoil. The work done by these forces can be determined using the change in potential energy as the aerofoil moves through its oscillatory path. According to equation (3.15), W_C presents the work done by the aerodynamic forces as the aerofoil moves from point B to point A, where $U(A)$ and $U(B)$ are the potential energies at these respective positions.

In the CFD simulations with a dynamic mesh, potential energy helps quantify the impact of the aerofoil's oscillatory motion on the energy harvesting process. Through analysing how potential energy changes with the aerofoil's movement, the efficiency of energy conversion and optimise the design for maximum power output can be assessed. The dynamic mesh in CFD Fluent captures the aerofoil's motion and the corresponding variations in potential energy, enabling precise calculation of work done and overall system performance. This approach helps in refining the design of the aerofoil and its integration with the building structure to enhance energy harvesting capabilities. At any given point along the curve C, the power can be determined as the time derivative, as shown in (3.16)

$$P(t) = \frac{dW}{dt} = \mathbf{F} \cdot \mathbf{v} = - \frac{dU}{dt}$$

In a simplified one-dimensional context, this relationship can be expressed in (3.17). For rotational systems, power is the result of multiplying the torque τ by the angular velocity ω .

$$(3.17) P(t) = \tau \cdot \omega$$

τ is torque is a measure of the rotational force applied to an object, causing it to rotate around an axis. It quantifies the tendency of a force to rotate an object about a specific

point or axis. In the context of rotational systems, power $P(t)$ is calculated as the product of torque τ and angular velocity ω .

3.10.4 Torque

A comparative analysis will be performed to examine the differences in torque behaviour between a single oscillating NACA 0012 aerofoil and one integrated with various building roof structures. This analysis will consider variations in roof shapes, wind speeds, wind directions, aerofoil configurations, scale, and placement. In addition, the study will include the effects of atmospheric boundary layer (ABL) conditions using hourly data, along with the impact of an additional support arm on the oscillating NACA 0012 aerofoil.

3.10.5 Angular velocity

Further analysis will be conducted to compare the angular velocities of a single NACA 0012 aerofoil and the same aerofoil installed into a building roof structure. The angular velocity (ω) was determined by calculating the rate of angular displacement divided by the change in time, as expressed in (3.18)

$$(3.18) \quad \omega = \frac{\Delta\theta}{\Delta t}$$

3.11 Summary of methodology

The research methodology employed a Computational Fluid Dynamics (CFD) approach using ANSYS Fluent for its Unsteady Reynolds-Averaged Navier-Stokes (URANS) capabilities, which is suitable for capturing the unsteady behaviour of wind flows around oscillating aerofoils. This section details the methodological steps taken to ensure robustness and reliability in the simulation process.

- ANSYS Fluent was utilised due to its ability to manage the dynamic mesh technique, essential for modelling the interactions between fluid and the moving aerofoil. This capability is crucial for computing dynamic responses such as torque and angular velocity.

- A sensitivity analysis was conducted to determine the optimal mesh density and time step sizes, balancing accuracy and computational efficiency. The analysis ensured that the chosen parameters represented the flow characteristics without oversimplifying the model.
- The computational mesh was designed with a finer resolution around the aerofoil and a coarser mesh further away to manage computational resources efficiently. Verification and validation steps were included to ensure numerical accuracy and stability, enhancing the credibility of the simulation outcomes.
- The dynamic mesh technique was employed to adapt to the aerofoil's oscillating motion, crucial for modelling fluid-structure interactions. This technique enabled precise resolution of boundary layers and wake regions, essential for capturing complex interactions.
- Simulating the rotational motion using the dynamic mesh technique provided insights into potential mechanical power output. The simulation considered assumptions and their impact on results, which demonstrate the practical implications of the methodology.
- The k-epsilon turbulence model was selected for its suitability with the current model and computational efficiency. While acknowledging its limitations in predicting complex turbulent flows, the model was chosen for its ability to handle mesh deformation without significant numerical instabilities.

Through a thorough understanding of its CFD concept, setup, development, and application, the dynamic mesh technique will be utilised in Chapter 5. This involves creating a CFD model and running simulation results to analyse the dynamic behaviour of the proposed design, which integrates an oscillating aerofoil into the building roof structure.

Chapter 4

Model validation

This chapter focuses on the verification/calibration and validation processes conducted for CFD simulations including several key aspects. These include comparing CFD results with the aerodynamic characteristics of the NACA 0012 aerofoil, the dynamic behaviour of an oscillating aerofoil in terms of frequency, and the velocity profiles of building roof structures obtained from experimental data.

The primary objective is to evaluate the accuracy of the CFD results by comparing them with relevant experimental data available in the literature. The ANSYS Fluent software will be utilised for conducting the CFD analyses, while various experiments from the literature are selected as baselines for validation. In the first section of this chapter, the aerodynamic characteristics of the symmetrical NACA 0012 aerofoil are examined at two different Reynolds numbers: $Re = 10,000$ and $Re = 20,000$. The CFD results are compared against published experimental data from the literature to establish confidence in the CFD model. This is followed by validating the frequency of an oscillating aerofoil under pitch motion by comparing the CFD results with experimental data. The objective is to assess the agreement between the two and verify the capability of the CFD model in capturing the dynamic behaviour of the oscillating aerofoil.

Moreover, the current CFD results of velocity profile surrounding the three different roof shapes will be compared with the experimental data. In addition, the comparative analysis includes the examination of the averaged stream-wise velocity around the curved and pitched roof buildings, providing insights into the agreement between the

CFD results and experimental data. Finally, this chapter concludes with a summary of the findings obtained from the verification/calibration and validation processes for the different cases examined. It will also acknowledge the limitations encountered during the model verification/calibration and validation, highlighting areas for further improvement and exploration.

4.1 Structure of the verification/ calibration and validation

The section will start with replicating the wind tunnel and NACA 0012 aerofoil profile within a 3D CFD model, as shown in the validation framework diagram (Figure 44). The CFD results will be validated against experimental data from the literature to assess the agreement in terms of aerodynamic characteristics, specifically C_l and C_d . In addition, another 3D CFD model will be developed, integrating the NACA 0012 aerofoil with a support rod to investigate the frequency at 6 m/s, 8 m/s, and 12 m/s. The validation process will include comparing the current CFD results against experimental data, focusing on the frequency parameters. Lastly, the section will involve the development of three different roof shapes including the flat, pitched, and curved roof building structures. These structures will be integrated into a 3D CFD model, and the simulation results will be compared with experimental data available in the literature.

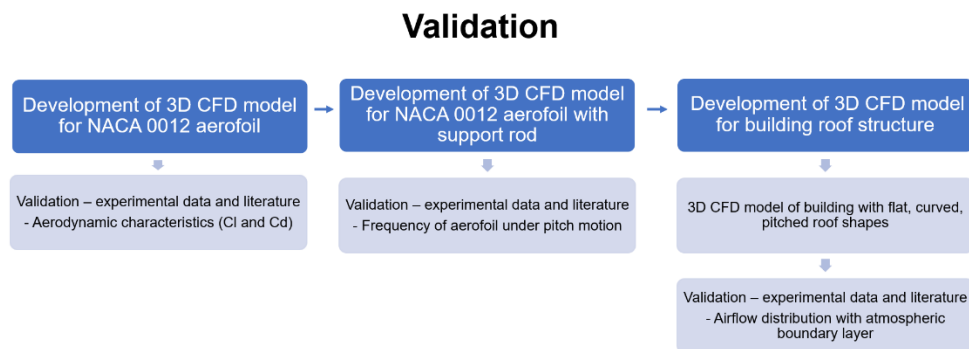


Figure 44. A diagram of validation framework

The standard k-epsilon turbulence model was chosen for these simulations as it is based on its widespread use and extensive validation in the field of computational fluid dynamics (CFD). In addition, the model has been proven to be reliable for a wide range of engineering applications. When validating CFD results against experimental data, the standard k-epsilon model is often employed since the experimental data itself

assumes the presence of turbulence. Moreover, the standard k-epsilon model strikes a balance between accuracy and computational efficiency, making it a practical choice for various simulations. It provides reasonable predictions while being computationally efficient compared to more complex turbulence models. This makes it suitable for routine engineering calculations and simulations where a good level of reliability is desired without excessive computational cost. The model's acceptance and comparison in the literature make it easier to benchmark CFD results against existing data. In using the same turbulence model employed from previous studies, it promotes consistency and facilitates the understanding of the accuracy and limitations of the simulations. This allows for meaningful comparisons and enhances the confidence in the CFD results. However, it is important to note that the choice of the turbulence model should be based on specific flow conditions, geometry, and desired accuracy.

In the simulations conducted using ANSYS Fluent R21, the Unsteady Reynolds-averaged Navier-Stokes (URANS) equations were solved using the standard k-epsilon turbulence model and the turbulent dissipation rate. Fluent employs a control-volume-based technique to discretise and solve the governing flow equations numerically. The choice of a double-precision version is made to represent the geometry with disparate length scales, requiring a dense mesh around the aerofoil and ground and a coarser mesh near the top of the domain. Furthermore, the pressure-based solver in Fluent is selected as it is commonly used for incompressible flows. The first-order Upwind scheme is applied for the interpolation of velocities, providing a good balance between accuracy and numerical stability. The pressure-velocity coupling is achieved using the SIMPLE algorithm, which iteratively solves for the pressure and velocity fields until convergence is reached. Overall, the selection of the standard k-epsilon turbulence model and its implementation in ANSYS Fluent R21 allow for reliable simulations of turbulent flow phenomena, providing valuable insights into the aerodynamic characteristics under investigation.

4.2 Verification and validation for aerodynamic characteristics

The validation process is crucial for establishing the accuracy and reliability of CFD simulations in predicting the aerodynamic characteristics and efficiency of aerofoil

profiles. Through comparing the CFD results with published experimental data from the literature, the study aims to verify the consistency and capability of the CFD models and methodologies used.

The validation process involves analysing key aerodynamic parameters such as lift coefficient and drag coefficient. These parameters provide important insights into the performance and efficiency of the aerofoil profile. Through comparing the CFD results with established tools, the study ensures that the simulations accurately capture the aerodynamic behaviour of the aerofoil profile.

The comparative analysis can identify any discrepancies between the CFD results and the published experimental data. This analysis provides a basis for understanding the accuracy and limitations of the CFD simulations. It allows for a comprehensive investigation of the aerofoil profile and their aerodynamic characteristics, contributing to a deeper understanding of their performance at low Reynolds numbers. Through validating the CFD results against established tools, the study aims to provide reliable data on the aerodynamic characteristics of the investigated aerofoil profile. This validation process adds credibility to the CFD work and ensures that the obtained results are reliable. It also enhances confidence in the predictive capabilities of the CFD simulations, enabling their application in practical engineering scenarios. Overall, the validation process serves to establish the accuracy and reliability of the CFD simulations, providing valuable insights into the aerodynamic characteristics and efficiency of NACA 0012 aerofoil profiles. It contributes to the advancement of knowledge in the field and enables the use of CFD as a reliable tool for aerodynamic analysis and design. In this section, there are different parameters that will be considered in investigating the aerodynamic characteristics. These include the Reynolds number, lift and drag coefficient.

4.2.1 Lift coefficient

The lift coefficient is also a crucial parameter utilised by engineers to capture the complex dependencies of shape, inclination, and various flow conditions on lift. It can be derived by rearranging the lift equation to solve for the lift coefficient in terms of other variables. Specifically, the C_l is determined by dividing the lift force (L) by the

product of the dynamic pressure (q), which is defined as one-half the density (ρ) times the velocity (V) squared, and the wing area (A), as shown in (4.2)

$$(4.2) C_l = L / (q * A)$$

In this equation, the lift coefficient represents the ratio of the lift force to the product of the dynamic pressure and the wing area. Through expressing the lift coefficient in this manner, engineers can quantitatively analyse the relationship between lift, dynamic pressure, and wing area, thereby facilitating a comprehensive understanding of the aerodynamic performance of a given system.

4.2.2 Drag coefficient

The drag coefficient is also an essential parameter employed by engineers to account for the complex dependencies of shape and flow conditions on aerofoil drag. It can be derived by rearranging the drag equation to solve for the drag coefficient in terms of other variables. Specifically, the drag coefficient (C_d) is calculated by dividing the drag force (D) by the product of the dynamic pressure (q), which is defined as one-half the density (ρ) times the velocity (V) squared, and the reference area (A), as shown in (4.3)

$$(4.3) C_d = D / (q * A)$$

In this equation, the C_d represents the ratio of the drag force to the force generated by the dynamic pressure multiplied by the reference area. Through expressing the C_d in this manner, engineers can quantitatively analyse the relationship between drag, dynamic pressure, and reference area, enabling a comprehensive understanding of the aerodynamic performance and drag characteristics of an aerofoil.

4.2.3 Effects of Reynolds number on lift and drag coefficient

Investigating the Reynolds number is essential for analysing and optimising the performance of an oscillating wind energy harvesting system by understanding and predicting the flow regime around the system, which directly impacts energy capture efficiency. The Reynolds number compares inertial and viscous forces in fluid flow, provides information about the flow regime and guides design decisions. The Reynolds Number is calculated in (4.1).

$$(4.1) Re = \frac{\rho u L}{\mu}$$

Factors such as the size and shape of the aerofoil and airflow velocity determine the Reynolds number, which indicates whether the flow around the aerofoil is laminar or turbulent. This is essential for understanding the aerofoil's aerodynamic performance as the Reynolds number helps predict flow regimes and aerodynamic behaviour. Additional factors such as pressure distribution, turbulence models, and real-world testing are also critical for achieving efficient energy extraction and power generation.

The study examined Reynolds numbers of 10,000 and 20,000 for the NACA 0012 aerofoil profile to directly assess its aerodynamic characteristics and efficiency. This analysis is particularly important for predicting the transition from laminar to turbulent flow, which significantly influences C_l and C_d characteristics, stall behaviour, and overall efficiency. Understanding these factors enables informed design choices to enhance performance.

Through the analysis of flow conditions, engineers can determine the optimal oscillation frequency and amplitude to maximise energy extraction while maintaining stability. However, further studies should consider power capture efficiency in future analyses of oscillating aerofoils. This topic will be explored in the final section, where the validation of CFD results for an oscillating NACA aerofoil is compared against experimental data. The comprehensive analysis will cover the aerofoil's material properties, mass, moment of inertia, and rotational motion.

In this chapter 4, the Reynolds number used were only used for the validation, which C_l and C_d were compared with CFD results against experimental data reported in the study of [189].

The equation $Re = \frac{\rho u L}{\mu}$ with the following variables:

For $Re = 10,000$

Wind speed – 2.69 m/s

Density – 1.225 kg/m³

Viscosity - 1.7894 x 10⁻⁵ kg/(m.s)

Chord length – 54.1947mm

For calculating the $Re = 20,000$, I used the following variables.

For $Re = 20,000$

Wind speed – 5.32 m/s

Density – 1.225 kg/m^3

Viscosity - $1.7894 \times 10^{-5} \text{ kg/(m.s)}$

Chord length – 54.1947mm

4.2.4 Validation - Experimental and CFD set up

The aerodynamic characteristics, such as the lift coefficient and drag coefficient, obtained from the current CFD simulations were validated by comparing them with the experimental data reported in the literature [171]. The experimental measurements were conducted at the University of Shiga Prefecture using an Eiffel-type wind tunnel, and the aerofoil model used in the experiments is shown in Figure 4. The baseline profile utilised in the experiments was NACA0012 with a chord length of 55 mm and a span length of 110 mm. The wind tunnel's test section dimensions were 500 mm in width, 500 mm in height, and 1000 mm in length, as shown in the Figure 45 (a). The lift forces (L) and drag forces (D) were measured using load cells installed in the wind tunnel, as described by [171]. The CFD simulations were designed to replicate the experimental setup, including the aerofoil profile, dimensions, domain, and Reynolds number.

The numerical simulations of the uniform flow past the aerofoil were performed using the ANSYS Fluent software to investigate the flow characteristics around the aerofoil. In these simulations, the steady, incompressible Navier-Stokes equations were solved using the finite volume method. The RANS simulation approach was adopted, employing the SIMPLE method for pressure-linked equations and a turbulence model based on scale modelling. This combination aimed to capture the turbulence flow structures surrounding the aerofoil. The RANS simulation, with the chosen turbulence model and solution method, aimed to provide a numerical representation of the flow behaviour and predict the effects of turbulence on the aerodynamic performance of the aerofoil. Figure 45 (b) demonstrates the computational mesh and domain utilised in the simulation. The computational domain had dimensions of 2000 mm in the

streamwise direction, 1000 mm in the vertical direction, and 110 mm in the spanwise direction. A polyhedral mesh with a base size of 110 mm was generated in the computational domain, with a finer mesh introduced near the aerofoil that included 15 layers to ensure computational accuracy. The first cell height in the layer mesh from the aerofoil surface was set to 0.5% of the base mesh size, and the wall y^+ values were kept below 0.85. The grid size around the wing in the spanwise direction remained the same as that in other directions. Various boundary conditions were implemented, including a uniform flow velocity condition at the inlet boundary, a pressure exit condition at the outlet boundary, free slip wall conditions at the top and bottom boundaries, and periodic boundary conditions at the left and right boundaries.

Figure 45 (a) shows the NACA 0012 aerofoil profile [194] The symmetrical NACA 0012 aerofoil, investigated in this study, has a maximum thickness of 12%, a camber of 0%. For validation, the aerodynamic characteristics of NACA 0012 were examined using the published experimental data in the literature and CFD tools [171].

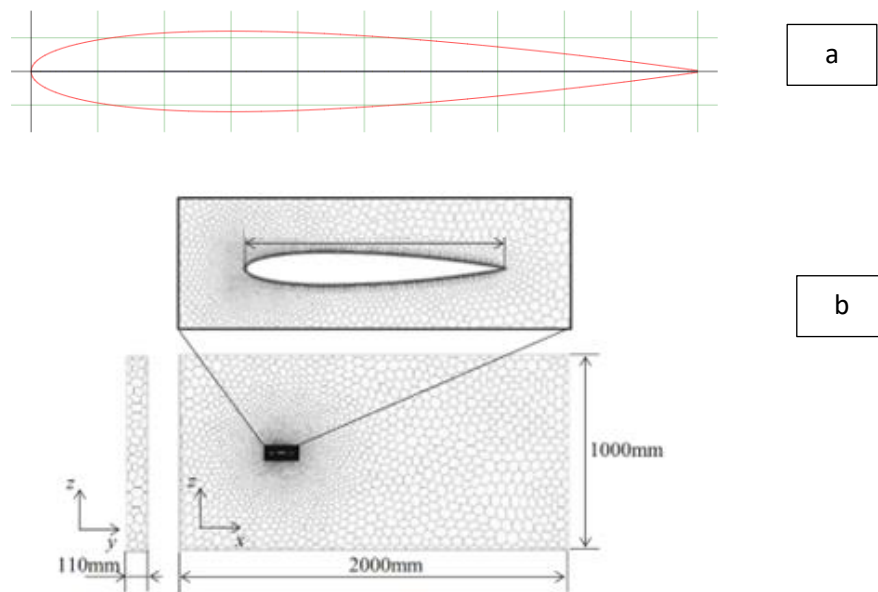


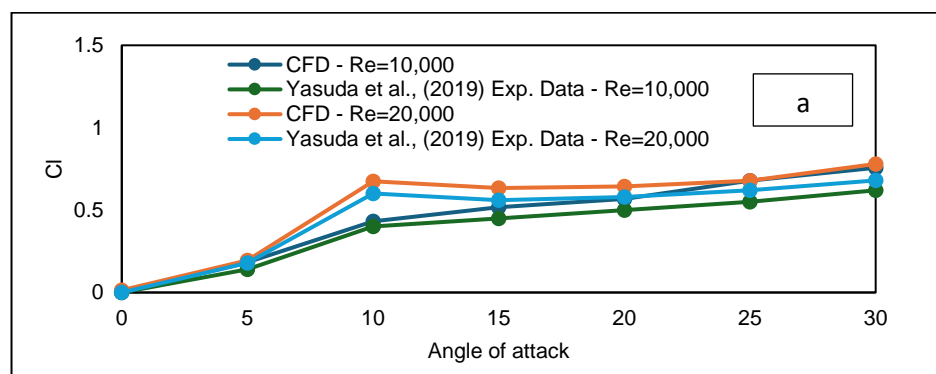
Figure 45. Design of (a) NACA 0012 aerofoil profile [175] and (b) computational mesh and domain [171]

A comparative analysis of the current CFD results against the experimental data in the literature [189] were conducted to validate the aerodynamic characteristics of lift

coefficient and drag coefficient at $Re=10,000$ and $Re=20,000$. As shown in Figure 46, it compares the CFD results with the experimental data in the literature [171].

The simulations were conducted for cases at angles of 0° , 5° , 10° , 15° , 20° , 25° , and 30° with a Reynolds number of 10,000 and 20,000 as these cases yielded significant results in the experimental investigation, as shown in Figure 46. The results demonstrate a low percentage difference and consistent trends which indicate good agreement in terms of C_l and C_d . The difference can be attributed to several factors that require detailed scientific analysis. One contributing factor is the presence of turbulent flows. Turbulence introduces additional complexities to the flow field around the aerofoil. Since the turbulence models used in the simulations are time-averaged, these may not have adequately captured the intricate turbulent behaviour, leading to difference in value for predicting the lift forces.

Furthermore, there may be discrepancies between the experimental setup and the CFD simulations in terms of configurations and boundary conditions. Even small differences in geometry, boundary layer treatment, or turbulence modelling can affect the flow behaviour and subsequently impact the predicted lift coefficient. The time-averaged nature of the turbulence models in the CFD simulations could be a key factor in these observed discrepancies, suggesting the need for more advanced modelling techniques or higher-fidelity simulations to better capture the complex flow dynamics around the aerofoil.



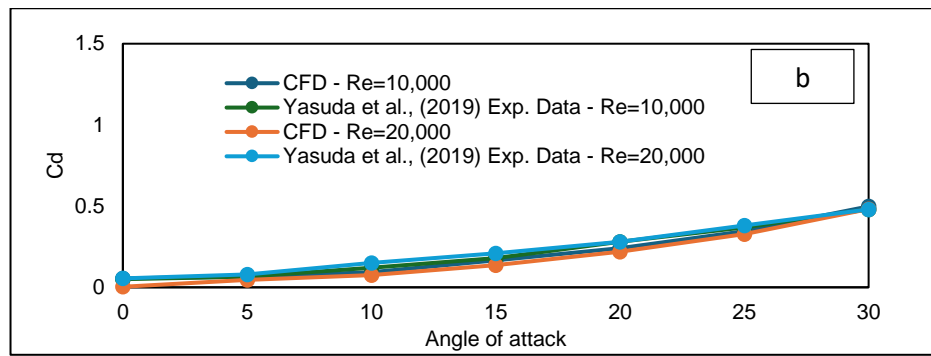


Figure 46. Aerodynamics characteristics – (a) C_l and (b) C_d – $Re=10,000$ and $Re=20,000$

Table 12 shows the percentage difference for C_l and C_d for $Re=10,000$ and $Re=20,000$. The analysis of the C_l and C_d from CFD and experimental data reveals a low percentage difference, indicating agreement between the two methods. For C_l at a Reynolds number (Re) of 10,000, the percentage differences range from 0% to 8%, demonstrating that the CFD results closely follow the experimental data. At $Re=20,000$, the differences are even lower, primarily between 1.4% to 5.58%, further validating the accuracy of the CFD model. Similarly, the C_d analysis at $Re=20,000$ shows percentage differences mostly within 4% to 3%, with a few higher differences up to 6% in another data set, but still within a reasonable range. These low percentage differences, consistently below 10%, indicate that the CFD model reliably predicts both C_l and C_d , affirming the model's accuracy and alignment with experimental results.

Table 12. Summary of percentage difference of CFD results against experimental data for (a) C_l and (b) C_d at $Re= 10,000$ and (b) $Re=20,000$

$C_l = 10,000$			$C_l = 20,000$		
CFD	Experimental data	Percentage difference (%)	CFD	Experimental data	Percentage difference (%)
0	0	0%	0.01	0	1%
0.18	0.14	4%	0.19	0.18	1%
0.43	0.4	3%	0.65	0.62	3%
0.5	0.45	5%	0.61	0.55	6%
0.57	0.5	7%	0.63	0.58	5%
0.63	0.55	8%	0.65	0.6	5%
0.69	0.62	7%	0.7	0.65	5%

(a)

Cd =20,000			Cd =20,000		
CFD	Experimental data	Percentage difference (%)	CFD	Experimental data	Percentage difference (%)
0.06	0.05	1%	0.035	0.055	2%
0.07	0.07	0%	0.058	0.08	2%
0.09	0.12	3%	0.12	0.15	3%
0.17	0.18	1%	0.15	0.21	6%
0.24	0.28	4%	0.22	0.28	6%
0.35	0.37	2%	0.327	0.38	5%
0.5	0.48	2%	0.482	0.48	0%

(b)

In addition to the aforementioned factors, another crucial aspect that may contribute to the disparity between CFD simulations and experimental data is the occurrence of stall. Stall refers to the separation of airflow over the aerofoil, causing a substantial decrease in lift and an increase in drag. Predicting stall is challenging for CFD simulations. While CFD models rely on solving the Navier-Stokes equations to simulate airflow, capturing the complex flow behaviour during stall, including separation and vortex shedding, presents difficulties. CFD models often struggle to predict the sudden changes in lift and drag that occur during stall. In contrast, wind tunnel experiments directly observe and measure the effects of stall on the aerofoil, enabling visual observations and direct quantification of the changes in lift and drag as the angle of attack approaches and surpasses the stall angle. Therefore, the lack of precise stall prediction in CFD simulations can contribute to the higher value overestimation of the lift coefficient compared to experimental data. The inability to accurately capture flow separation and the associated changes in lift and drag during stall limits the accuracy of CFD simulations in this specific regime. Overall, the comparison between the CFD results and experimental data from the literature reveals a notable agreement in terms of the observed trends for C_l and C_d . The CFD simulations and experimental measurements display consistent patterns, suggesting that both methods effectively capture the overall behaviour of the aerodynamic characteristics of the aerofoil.

4.3 Validation for oscillating NACA 0012 aerofoil

The selection of the NACA 0012 aerofoil profile to predict the energy and power extraction performance through an oscillating aerofoil is a rational choice for several reasons. Figure 47 shows the centre of rotation at $C=0.04$ centre and z axis [48]. The NACA 0012 profile has been extensively investigated and widely used in the field of wind energy harvesting. Moreover, one of the key advantages of the NACA 0012 profile is its adaptability in generating lift and providing stability. The symmetrical shape of the aerofoil allows for balanced lift distribution at different angles of attack, making it suitable for oscillatory motion. This characteristic is particularly important for energy harvesting systems that rely on the aerofoil's ability to generate lift during both the upstroke and downstroke phases. Moreover, the NACA 0012 profile shows predictable and well-documented aerodynamic characteristics. Its performance has been extensively studied, enabling engineers and researchers to estimate its lift, drag, and moment coefficients at various operating conditions. This great amount of knowledge makes it a reliable baseline for designing new building-integrated wind energy harvesting systems.

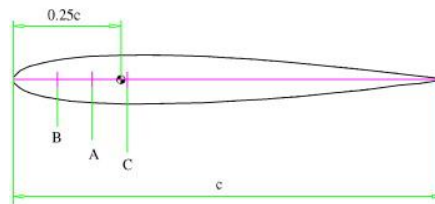


Figure 47. Centre of rotation at $C=0.04$ centre and z axis [48]

Furthermore, the NACA 0012 profile has demonstrated favourable performance in low Reynolds number flows, which are typically encountered in urban and built-up environments. This makes it well-suited for building-integrated wind energy harvesting, where low-speed and turbulent airflow conditions are common. With NACA 0012 aerofoil profile as a baseline, researchers can compare the performance of new proposed designs for building-integrated wind energy systems. This allows for a more systematic evaluation of the effectiveness and efficiency of alternative designs and can lead to improvements in energy extraction and power generation.

4.3.1 Experimental and CFD set up for aerofoil

For the oscillating aerofoil, the current CFD results were compared against the study of [48]. Figure 48 shows the aerofoil test section and investigation of self-sustained oscillations of an oscillating aerofoil under pitch motion through wind tunnel experiments in the research. The design was replicated as a three-dimensional CFD model using the ANSYS Designmodeler to generate the computational grid. The aerofoil has a chord length of 0.156 m and a span length of 0.61 m, positioned within the tunnel with 7 mm between the wingtip and the top and bottom plates. In addition, a support rod with a diameter of 15 mm, located approximately one-quarter chord length ($0.1c$) from the leading edge, facilitates both pitch and heave motion of the aerofoil. The geometry comprises a wind tunnel domain with dimensions of 0.624 m (width) \times 0.91 m (height) \times 1.56 m (length), housing an aerofoil featuring a NACA 0012 aerofoil cross-section.

In the CFD study, the geometry was meshed in Ansys Meshing software using tetrahedral elements, resulting in 1,378,924 elements and 307,083 nodes in the computational domain. A dynamic mesh approach was employed for the aerofoil dynamic motion, with automatic mesh reconstruction using Remeshing and Smoothing commands to maintain mesh quality during updates. Grid quality assessment based on skewness, orthogonality, and aspect ratio yielded metrics indicating uniform element shapes (skewness of 0.30), reasonable alignment of grid lines with flow direction (orthogonality of 0.50), and moderately elongated elements (aspect ratio of 1.18), meeting criteria for reliable CFD simulations.

This is followed by running CFD simulations by using dynamic mesh in one degree of freedom (1-DOF) solver. The aerofoil's mass and moment of inertia based on experimental data from the study of [41] were also entered. For addressing the pitch rotational motion, one Degree of Freedom (1-DOF) solver was employed to examine the dynamic behaviour of an oscillating aerofoil. The aerofoil comprises of a mass of 0.771 kg, a moment of inertia of 0.00135 kg.m², a chord length of 0.156 metres, and a span of 0.61 metres. In addition, the wind tunnel solid blockage ratio, including the

wing, rods, and plates, was maintained at 5% to minimize interference with the airflow during experimentation.

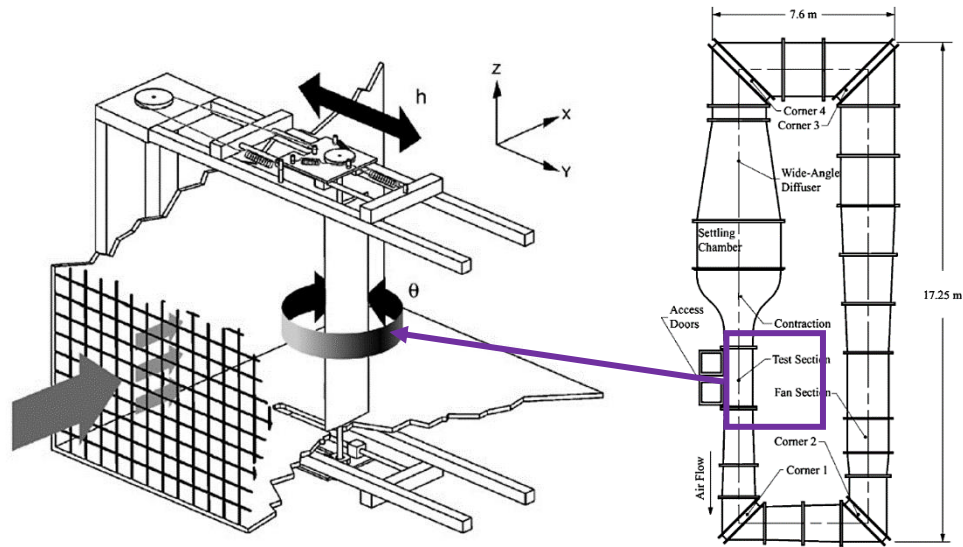


Figure 48. Representation of the aeroelastic oscillating NACA0012 device in the wind tunnel [48]

The study primarily aimed to investigate the aerodynamic performance of the aerofoil in varying conditions of pitch oscillation frequencies, as detailed in [48]. Consequently, our analysis primarily focused on quantifying pitch oscillation frequencies in different wind speeds rather than temporal variations. This approach aligns with similar methodologies employed in other studies within our field. The current CFD approach of employing transient 1-DOF dynamic mesh CFD simulation with moving mesh aligns with the transient analyses conducted in several related studies. Alrawashdeh and Stathopoulos [196] utilised transient simulations to assess wind loads on solar panels mounted on flat roofs, focusing on the effect of geometric scale. While in the study of [197], a transient analysis was conducted to study slamming wave loads on offshore wind turbine foundations generated by different types of breaking waves, emphasising dynamic loading conditions. For the study of Abdessemed [198] the morphing aerofoils analysis using dynamic meshing, demonstrating the importance of adapting computational methods to capture complex aerodynamic phenomena over time. Despite differences in specific research objectives, the use of transient analyses in these studies reflects a shared emphasis on capturing dynamic behaviours and interactions with fluid flow. Therefore, the current study of using transient 1-DOF dynamic mesh CFD simulation with moving mesh is

in alignment with similar methodologies employed in other studies within the field, emphasising the importance of investigating aerodynamic performance in transient conditions.

The first-order upwind scheme is commonly utilised for the (k) turbulence kinetic energy and, correspondingly, (ε) turbulence dissipation rate in CFD simulations due to its inherent numerical stability and robustness. This scheme employs a simple differencing approach that prioritises stability over accuracy, making it well-suited for scenarios involving turbulent flows and dynamic mesh simulations where stability is paramount. Regarding the level of numerical diffusion involved, the first-order upwind scheme is characterised by a moderate level of numerical diffusion. While it sacrifices some accuracy compared to higher-order schemes, such as first-order upwind or central differencing, the first-order upwind scheme introduces a moderate amount of numerical diffusion to ensure stability, particularly in cases with rapidly changing flow conditions or mesh deformations. This numerical diffusion aids in damping out oscillations and maintaining stability, even though at the expense of slightly smoothing out sharp gradients in the solution. Overall, the use of the first-order upwind scheme strikes a balance between stability, robustness, and computational efficiency, making it a practical choice for turbulence modelling in CFD simulations, especially in scenarios involving dynamic mesh motion and turbulent flows.

4.3.2 Validation of the oscillating aerofoil frequency

Figure 49 (a) presents the CFD results show the frequency oscillation at wind speeds of 6 m/s, 8 m/s, and 12 m/s over time. The highest frequency value, approximately 4 Hz was observed at the 12 m/s wind speed condition, while the lowest frequency, around 1.5 Hz occurred at the 6 m/s wind speed. Figure 49 (b) displays a plot diagram gathered from the study by [48], illustrating frequency oscillation data obtained from experimental measurements. Figure 49 (c) provides a comparative analysis between the frequency oscillation results from our numerical study and the experimental data sourced from [48]. Notably, the frequency values obtained from our CFD study closely match those reported in the experimental study. This consistency across different wind speeds indicates a low margin of error in our simulations compared to the experimental findings. Specifically, we observed a 2.6% error for the 6 m/s wind speed, a 4.3% error

for the 8 m/s wind speed, and a 4.7% error for the 12 m/s wind speed, highlighting the reliability of our simulation results.

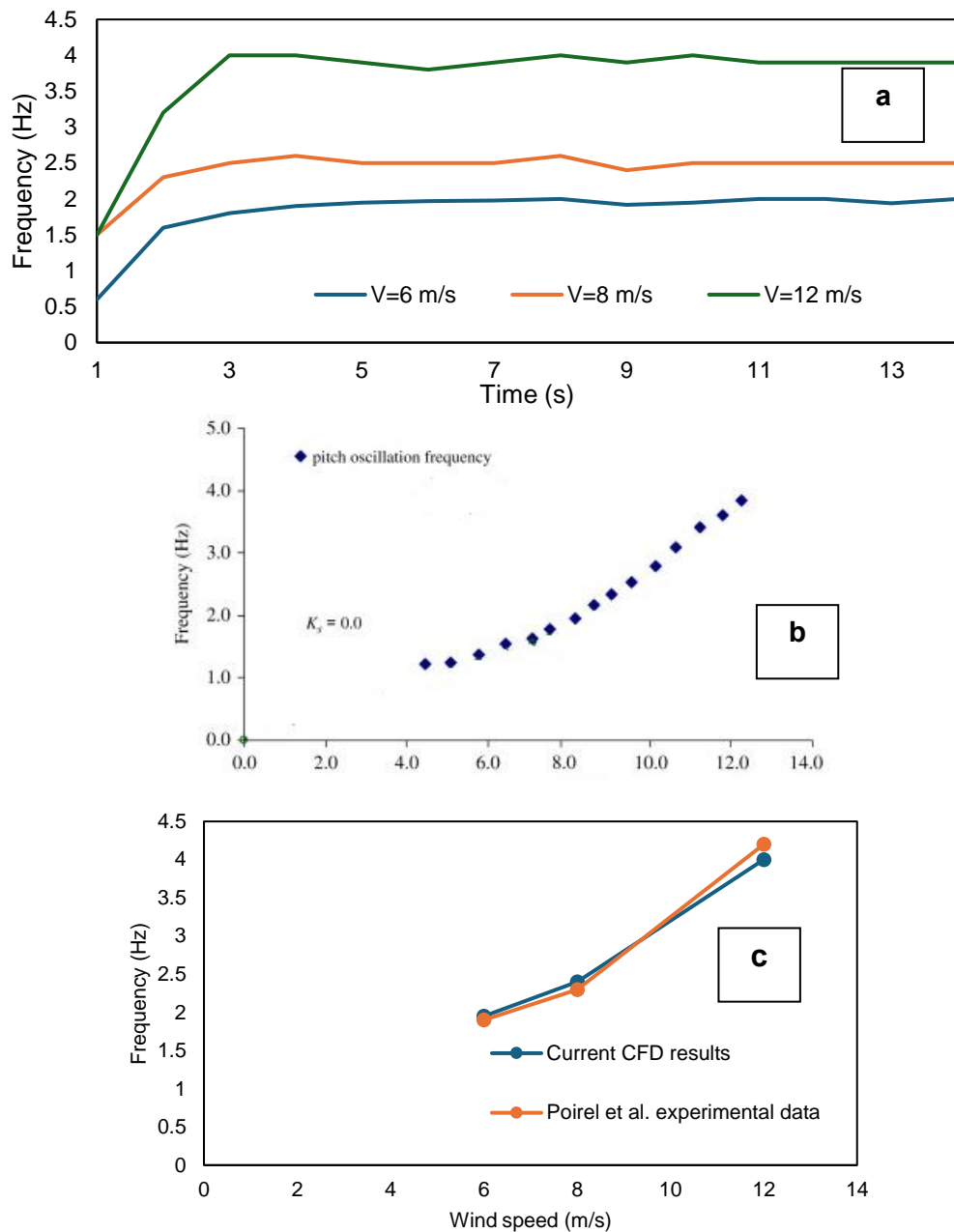


Figure 49. Validation of (a) CFD results of frequency oscillation (b) plot diagram of frequency oscillation from the study of [10], (c) comparative analysis of current CFD results against experimental data from the research of [48]

4.4 Validation of the airflow around pitched, curved and flat roof building structure

This section will discuss the validation process of the velocity profile pertaining to the building roof, drawing from insights gleaned from the study by [21]. Moreover, the

experimental and CFD setups, along with the validation procedures for airflow patterns and the atmospheric boundary layer velocity profile. Through this discussion, the aim is to provide a comprehensive understanding of the reliability and accuracy of the velocity profile data obtained for the building roof.

4.4.1 Experimental and CFD set up for building roof structure

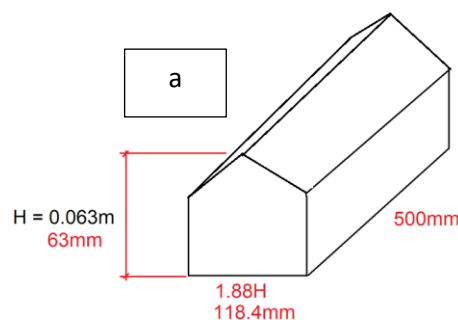
Figure 50 shows the 3D CFD model of (a) pitched roof building with (b) dimensions of computational domain (c-d) mesh generation and 3D model of (e) curved roof building with (f) computational domain, (g-h) computational domain [21], and mesh generation. The geometry was initially designed using Ansys Design Modeler software and subsequently implemented in Ansys Meshing software to generate the computational grid. The geometry comprises a wind tunnel domain with dimensions of 0.5 m (width) \times 0.5 m (height) \times 6.91 m (length), housing a curved roof building. The curved roof building has a length of 0.5 m \times 0.01184 m \times 0.063 m. Similar dimensions were used for the width, height, and length for the pitched and flat roof building. The working section of the wind tunnel, which was 0.6 m long, was covered by a transparent glass window measuring 0.8 m in length. This window facilitated the measurement of velocity and velocity fluctuations using a 2D Laser Doppler Anemometer (LDA) from Dantec Dynamics A/S, located in Skovlunde, DK. The airflow in the wind tunnel was generated by a variable speed air exhaust fan, creating negative pressure. The inlet design of the wind tunnel ensured a uniform velocity distribution for validation of the numerical simulation results. Further details can be found in the study of [21].

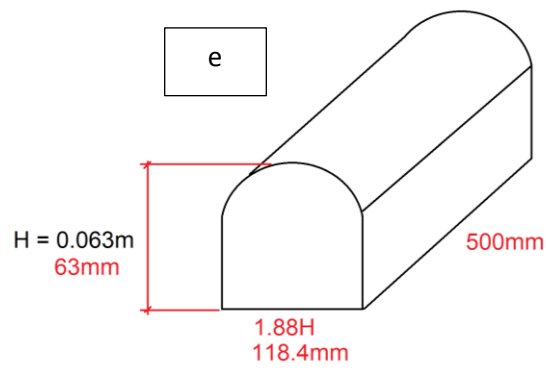
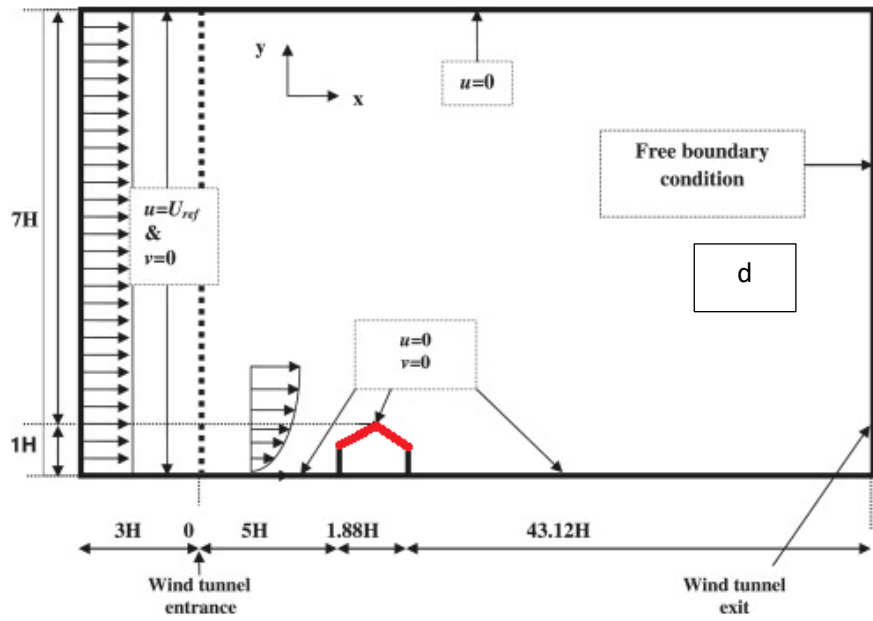
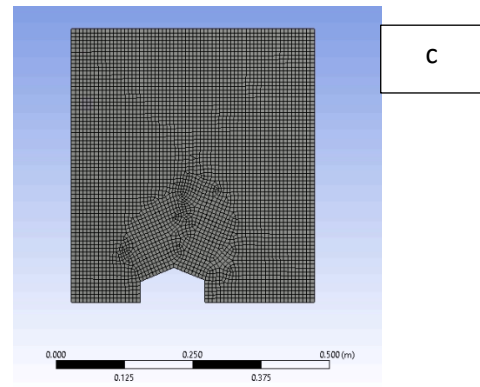
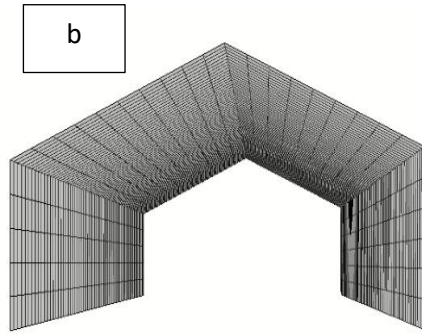
The 3D CFD models were created using Ansys Design Modeler software and meshed with tetrahedral elements in Ansys Meshing software, resulting in a mesh comprising 10,000 elements and 42,000 nodes within the wind tunnel domain, accommodating a curved roof building. Mesh quality evaluation, including skewness, orthogonality, and aspect ratio, met the required standards for precise CFD simulations. To adapt to the dynamic motion of the aerofoil, a dynamic mesh approach was employed, utilising commands such as Remeshing and Smoothing to uphold mesh quality during updates. In the absence of experimental data, validation of time steps was conducted through

complementary analyses, including grid convergence, temporal convergence, and stability analysis. These analyses systematically varied mesh resolution and time step sizes to assess solution sensitivity and transient behaviour, respectively. The stability analysis, crucial for ensuring numerical stability, evaluated criteria such as the Courant–Friedrichs–Lewy (CFL) condition to maintain stability while representing the underlying physics. Despite the lack of wind tunnel experimental data, these computational techniques provided a robust framework for validating time steps, bolstering confidence in the reliability and accuracy of the CFD simulations.

To examine the velocity profiles before the working section, two mean wind velocities of 0.32 m/s and 0.50 m/s were chosen within the wind tunnel. The working section itself started 1.82 m downstream from the wind tunnel inlet to ensure that the wind characteristics were not affected by the tunnel entrance. Prior to introducing any obstacles inside the wind tunnel, tests were conducted to confirm that the air velocity matched the desired average value of 0.32 m/s at the obstacle height. The turbulent intensity value was measured to be 0.36, and the turbulent kinetic energy value was determined to be 0.11.

The experimental data of [21] for airflow distribution around the pitched and curved roof building structures will be compared with the current CFD results for validation. Similar dimensions and roof shapes from [21] were created in ANSYS Designmodeler. The airflow distribution above and around the pitched and curved roof building structures was compared to validate the current CFD model with the experimental data.





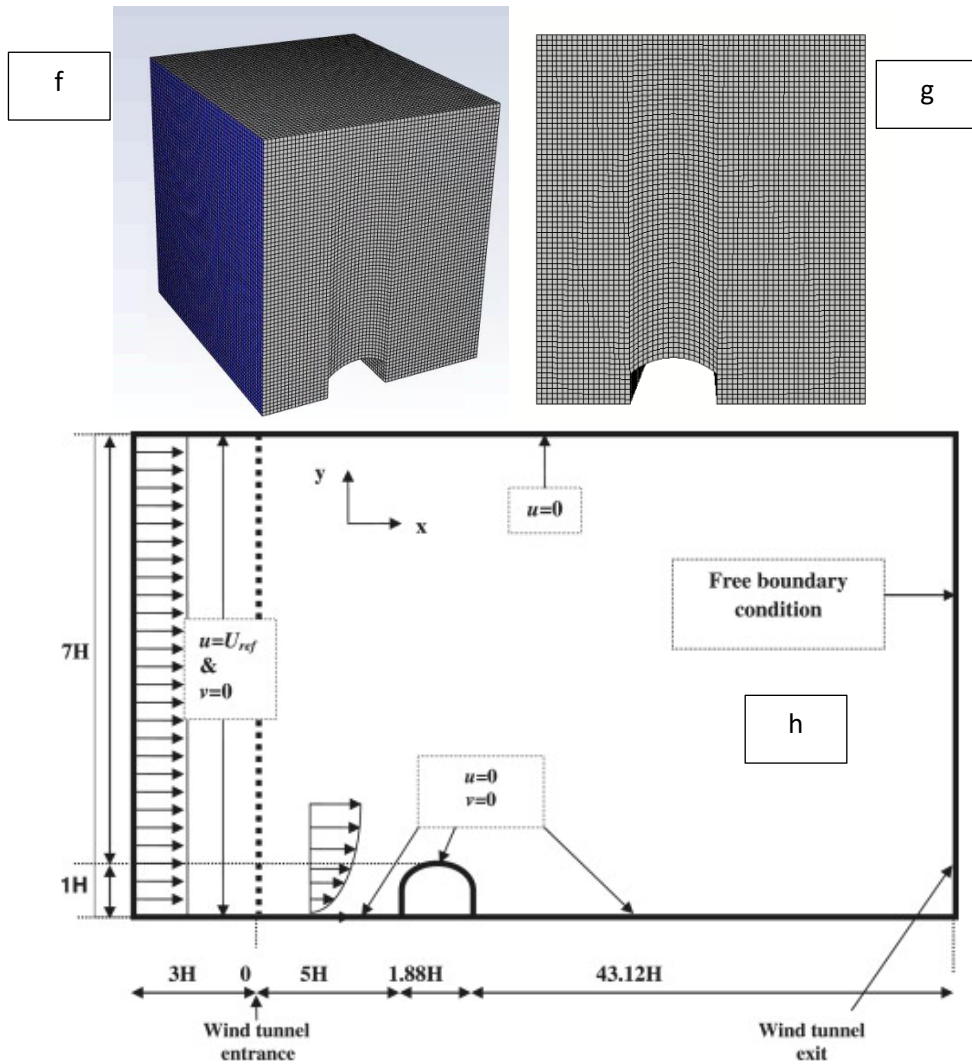


Figure 50. 3D CFD model of (a) pitched roof building with (b-c) mesh generation, (d) dimensions of computational domain and 3D model of (e) curved roof building with (f-g) mesh generation, (h) computational domain [21]

Another experimental data in the literature were used to compare the current CFD results for the airflow patterns in an atmospheric boundary layer conditions for flat roof building structure. The experimental findings presented by [199] were employed to validate the results obtained from the CFD simulation. The experiment involved conducting a comprehensive analysis of the flow characteristics surrounding a square prism with a 2:1:1 aspect ratio (height x width x depth) placed within a turbulent boundary layer. In this turbulent boundary layer, the vertical profile of average wind velocity displayed a power law behaviour with an approximate exponent of 0.27 (as shown in Figure 51. To measure the wind velocity, a split film probe was utilised, enabling the determination of average wind velocities in each direction within the

three-dimensional space, as well as the standard deviation of fluctuating wind velocities. The dimensions of the model prism were 0.08 m in both width (b) and depth (d), while the height (h) of the prism reached 0.16 m.

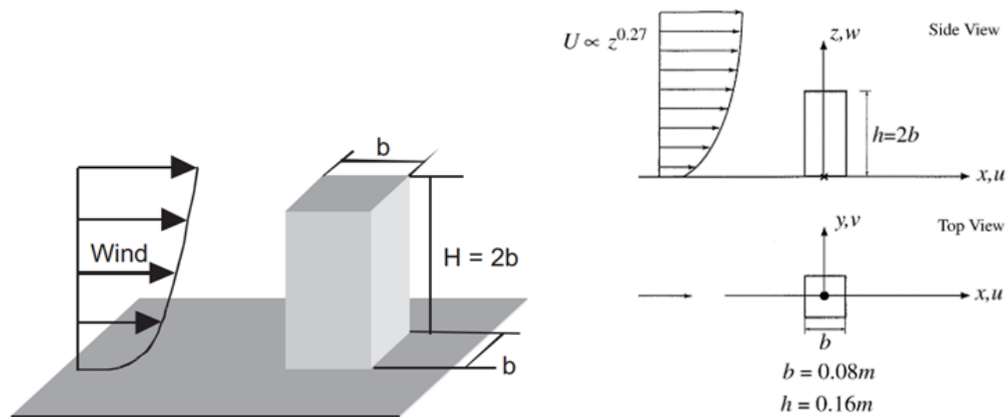


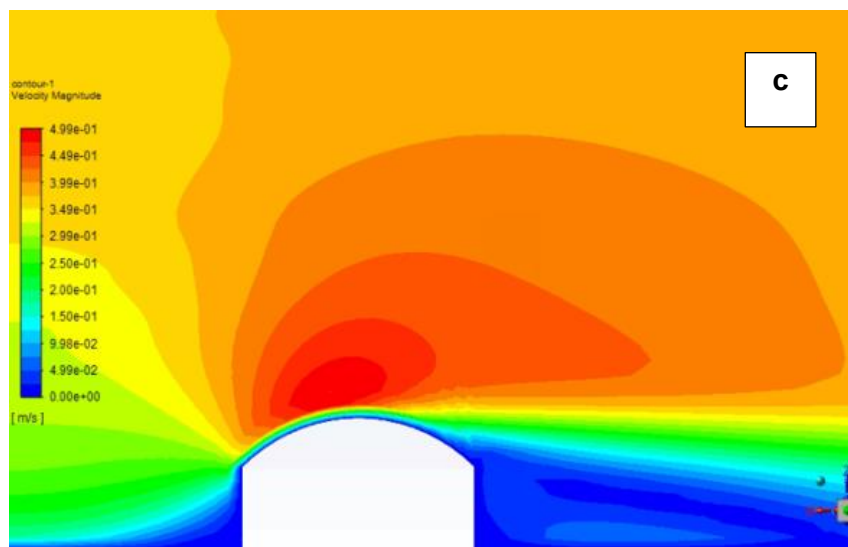
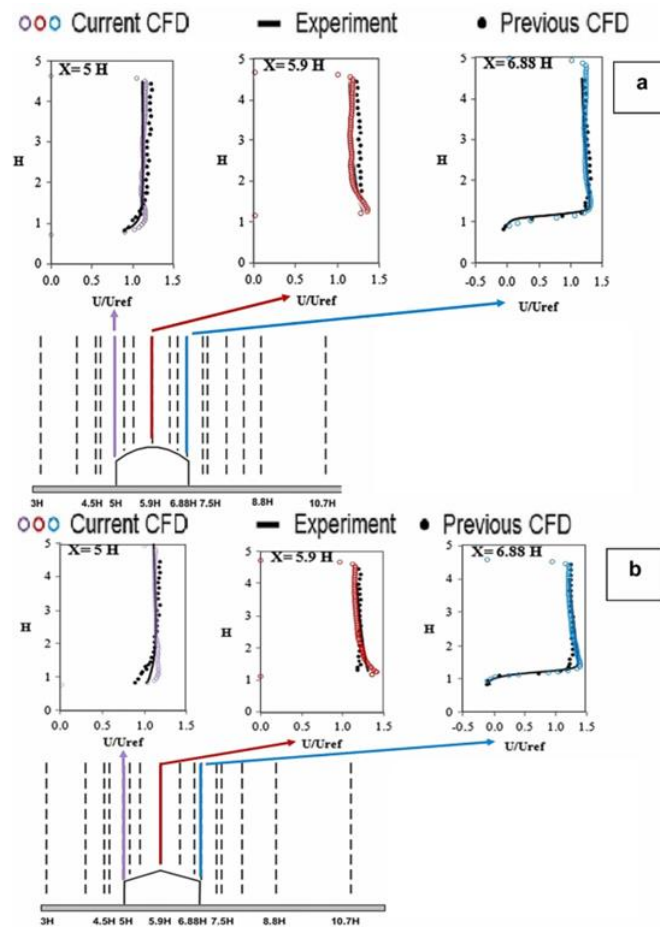
Figure 51. Set up of experimental model [198]

4.4.2 Validation of the airflow patterns for pitched, curved and flat roof building structure

For the boundary condition at the solid walls, a linear or 1/7 power-law distribution of instantaneous velocity was used [200]. This condition is based on an explicit power-law approximation to the log-law outside interfaced with the linear profile inside the viscous sub-layer. It was confirmed that most of first grid points adjacent to the wall boundary were in the viscous sub-layer in this computation. This means that no-slip boundary condition was applied to most of the solid surfaces.

The numerical model utilised in the investigation produces results of velocities and streamlines, illustrate the patterns of airflow. Figure 52 demonstrated the black line for the experiment, while the purple, red, blue was for current CFD results, and black dots are the previous CFD results in [21]. The results indicate that the variation among the current CFD results, experimental data, and previous CFD from the research of [21] were showing a minimal error. Overall, the computational results were in good agreement with the current numerical and experimental data for both Figure 52 (a) curved roof and Figure 52 (b) pitched roof building. Moreover, the acceleration rates of the wind velocity magnitude above and around the building structure were investigated for different roof shapes including the pitched and curved roof building

structures which were gathered from the validated CFD model. Figure 52 (c) shows the wind speed accelerated created for curved roof with an inlet wind velocity of 3m/s. While in Figure 52 (d) shows the wind speed acceleration created for pitched roof building structure with an inlet wind velocity of 3m/s



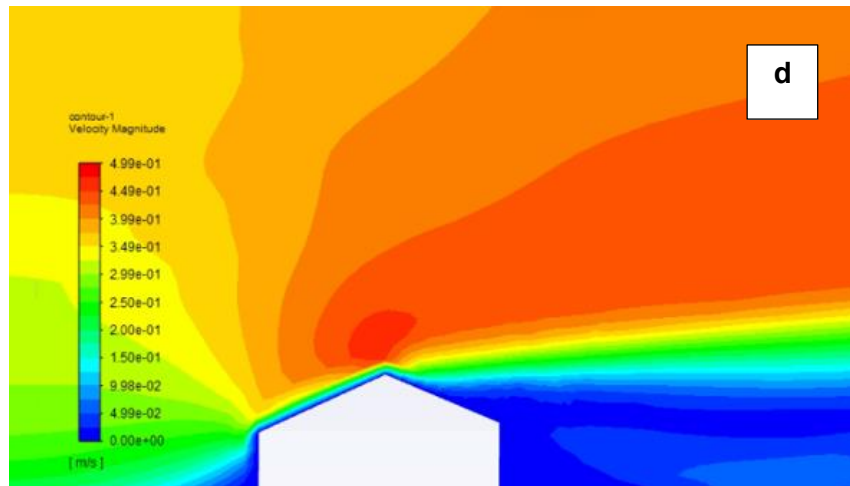


Figure 52. Comparative analysis of CFD results, experimental data, and previous CFD results [21] for (a) curved and (b) pitched roof building, and averaged steam-wise velocity around the (c) curved and (d) pitched roof building

For the validation of velocity profile for flat roof building structure. The investigation utilised a numerical model to generate results showing velocities and streamlines, effectively illustrating airflow patterns Figure 53 (a) shows the configuration of experimental model and Figure 53 (b) contours for velocity magnitude for flat roof building structure with the ABL conditions used from the experimental results data in [201-202]. As shown in Figure 53 (a) shows the black dots to represent the experiment, while red lines represented the results obtained from the CFD analysis study of [199]. While the current CFD results are in green, grey, and purple. The findings indicated a minimal deviation between the CFD results and experimental data, suggesting a high level of agreement. Overall, the computational results aligned with both numerical and experimental data. Moreover, the study examined the wind velocity acceleration above and around flat roof shape using the validated CFD model, as shown in Figure 53 (b).

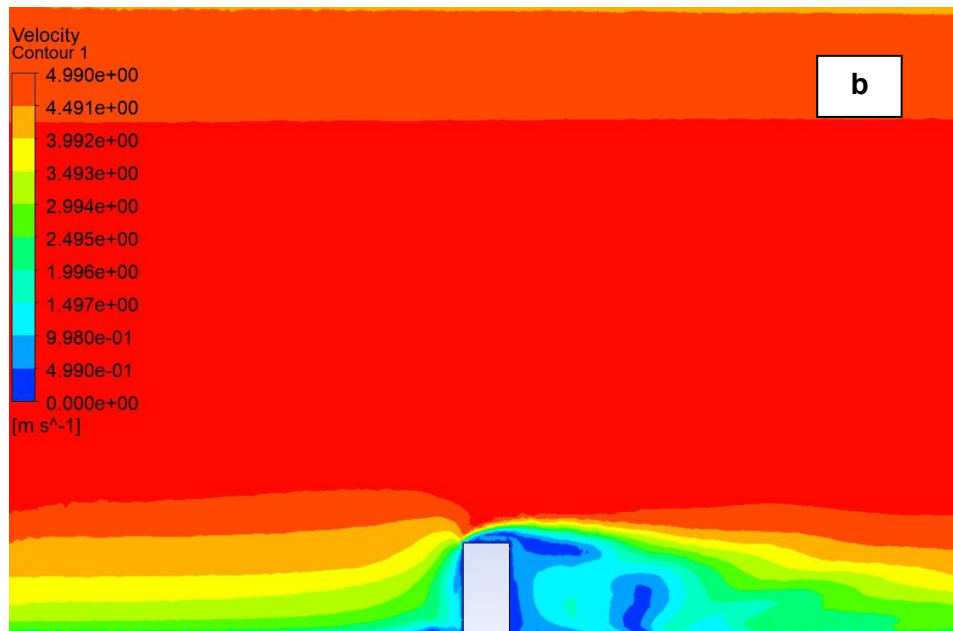
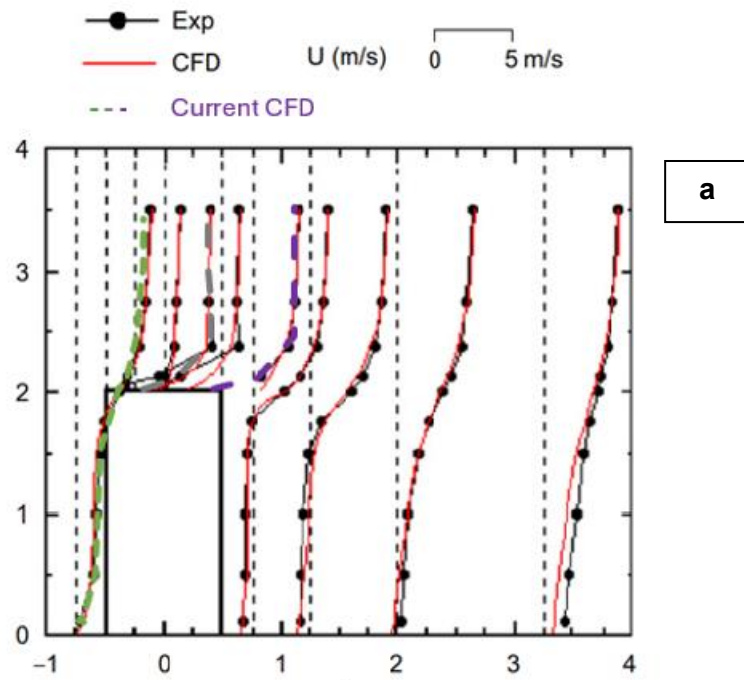


Figure 53. Comparative analysis of (a) experimental data, previous CFD results [199], and current CFD results for averaged steam-wise velocity around the flat roof building. The (b) velocity magnitude contours for the current CFD result

4.5 Summary

This section presents the validation setup, comparative analysis, and results for the aerodynamic characteristics, frequency, airflow patterns, and velocity profile from

wind tunnel experiments. The study aims to assess the reliability of the CFD model by comparing results with experimental data from the literature.

- The CFD model showed agreement with experimental data, with percentage differences in C_l ranging from 0% to 8% at $Re=10,000$ and 1.4% to 5.58% at $Re=20,000$. While C_d differences were mostly within 4% to 3% at $Re=20,000$, with some differences up to 6%.
- The validation of the CFD results for the frequency of an oscillating NACA 0012 aerofoil against experimental data demonstrated the model's capability to predict the frequency response, while the airflow patterns and atmospheric boundary layer conditions also showed agreement between experimental data and CFD simulations.
- These investigations enhance the understanding of the aerodynamic behaviour of different roof structures and provide confidence in using the validated CFD model for predicting lift and drag coefficients, frequency response, airflow patterns, and atmospheric conditions, guiding future research and optimising roof design and performance in engineering applications.

The validation of the CFD model demonstrated through predictions of aerodynamic characteristics, frequency response, and airflow patterns, provides a solid foundation for applying the proposed design and methodology in the practical CFD simulations discussed in Chapters 5 and 6.

Chapter 5

Dynamic behaviour of BI-WEHS

This chapter presents the analysis of the complex dynamics associated with a new design comprising of single oscillating aerofoil and its interaction with diverse building roof structures in the context of wind energy harvesting. The study is organised into key components, which covers dynamic behaviour, fluid-structure interaction in wind flow, and the integrated design of the oscillating aerofoil and building roof structure. It predicts mechanical power output, torque, angular velocity, and wind speed acceleration, which accounts for factors like wind speed, wind direction, wind shadow, and the Atmospheric Boundary Layer (ABL) velocity profile in rural areas.

Beginning with an in-depth examination of the dynamic behaviour of a single NACA 0012 aerofoil, the analysis expands to consider various building roof structures, recognising their fundamental role in understanding wind flow patterns and energy generation. The integration of aerofoils, particularly the NACA 0012 profile into building roof structures was explored, assessing critical parameters like torque, angular velocity, and pitch oscillations to understand their impact on power output. The study delves into the complex realm of fluid-structure interaction, examining how the relationship between the aerofoil, airflow, and building roof shapes influences the dynamics of the wind energy conversion system. This exploration is fundamental for understanding how wind speed is influenced by roof architecture, especially in the context of the Building Integrated Wind Energy Harvesting System (BI-WEHS). The analysis also rigorously evaluates the influence of environmental factors, including wind speed, wind direction, ABL velocity profile, wind shadow phenomena, PSD vs

frequency, and impact of aerofoil shape on performance. These studies provide valuable insights into the complex dynamics of wind energy harvesting systems.

The utilisation of ANSYS CFD modelling and transient analysis simulations in predicting the fluid-structure interaction and dynamic behaviour of an integrated oscillating aerofoil within a building's roof structure yields significant advantages and contributes substantially to scientific knowledge. Employing this approach enhances understanding of FSI, allowing exploration of phenomena such as vortex shedding, lift and drag forces, and dynamic responses of the aerofoil and building structure. This knowledge informs the development of more efficient and secure designs. The research also holds practical implications for optimising building design by evaluating the impact of integrating oscillating aerofoils on aerodynamic performance, which leads to increased energy efficiency and decreased wind-induced structural loads. Moreover, the study is relevant to renewable energy applications by providing insights into harnessing wind energy from building structures and contributing to sustainable energy solutions.

5.1 Isolated standalone oscillating NACA 0012 aerofoil

In this section, the aerodynamics, dynamic behaviour, and predicted mechanical power output will be examined to evaluate its potential for energy extraction in different wind speeds. A symmetrical NACA 0012 aerofoil was used as the profile has proven to work for power extraction under flapping motions, and its aerodynamic characteristics is well known in the literature. While the choice of using rigid aerofoils for wind energy converters is primarily influenced by the typical wind speeds experienced in urban and rural environments. These wind speeds are not typically high enough to induce significant deformation or elasticity in the aerofoil. This rigidity allows the aerofoils to maintain their shape and efficiently capture wind energy for power generation. Moreover, the preference for rotational motion in wind energy converters is supported by the results of a CFD investigation using dynamic mesh in ANSYS Fluent. Rotational motion tends to produce more complex and turbulent flow patterns compared to translational motion [162] [203-205]. This increased turbulence enhances the fluid's kinetic energy, contributing to higher mechanical power. Factors such as

angular velocity, torque, and the leverage effect of the rotating object play significant roles in achieving higher mechanical power in rotational motion. In addition, the pitch oscillations which may be observed in the study, can impact energy conversion efficiency and lead to fluctuations in mechanical power. Lastly, the choice of rotational motion is context-specific and depends on the system's design and intended application.

In the initial stages of designing and optimising an oscillating aerofoil integrated into a building's roof structure, an understanding of lift and drag forces is needed for wind energy harvesting, particularly in the examination of aerofoil pitch oscillation using CFD with dynamic mesh solver. The NACA 0012 aerofoil profile was chosen as it has been established to work as an oscillating aerofoil for wind energy converter in studies of [48] [206-207]. Effective aerodynamics has a direct impact on the conversion of wind energy into electrical power, thereby enhancing the capability of an energy harvesting system to maximise power output and leading to increased energy production. Moreover, this understanding allows for precise control of pitch angles to maintain the performance of the aerofoil wind energy harvester guarantees structural integrity in the face of changing loads and enables adaptability to wind changes.

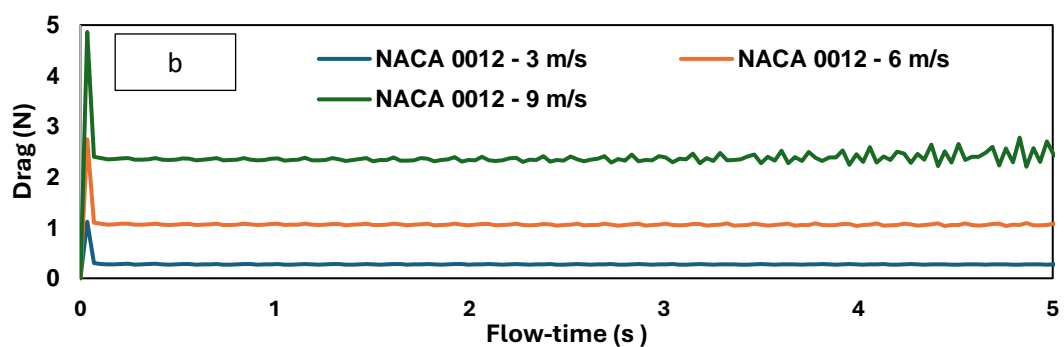
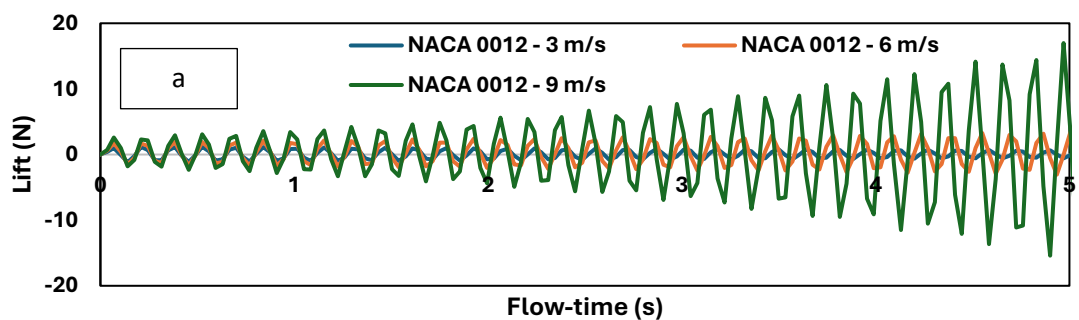
5.1.1 CFD results for lift and drag forces

Figures 54 (a-c) show the CFD results on the prediction of lift and drag forces. In the specific context of a pitch oscillating aerofoil deployed in wind energy harvesting applications, the assessment of lift and drag forces, alongside the evaluation of the lift-to-drag ratio offers insights into the aerofoil's aerodynamic performance. The CFD simulations for lift and drag forces were conducted in transient mode, which accounts for the time-dependent variations and dynamic behaviour of the aerofoils. Figure 54 (a) shows the lift force created through pressure disparities between the aerofoil's upper and lower surfaces and acting perpendicular to the incoming airflow.

As wind speed increases from 3 m/s to 6 m/s to 9 m/s, the lift force on an oscillating aerofoil wind energy harvester integrated into a building roof structure increases exponentially, which improve energy capture efficiency. This scalability is due to the lift force being proportional to the square of the wind speed, which allow for substantial increases in potential energy output. However, higher wind speeds also

induce greater oscillations in the aerofoil, which can disrupt aerodynamic stability and efficiency if not managed properly. To maintain optimal efficiency, robust design solutions such as using fatigue-resistant materials, implementing damping systems to mitigate oscillations, and optimising aerodynamic profiles are essential. These measures ensure that the harvester can harness maximum energy from varying wind speeds while maintaining structural integrity and longevity.

While in Figure 54 (b), it shows the drag force which is aligned with the incoming airflow, signifies the resistance opposing the aerofoil's movement through the air, with the minimisation of drag being important to optimise energy conversion efficiency by allowing a larger share of the wind's energy to be harnessed for power generation. In Figure 54 (c) demonstrates the lift-to-drag ratio which quantifies the aerofoil's efficiency in generating lift relative to drag, with a higher ratio denoting a more efficient aerofoil design, resulting in superior energy conversion efficiency and overall performance for the wind energy harvester.



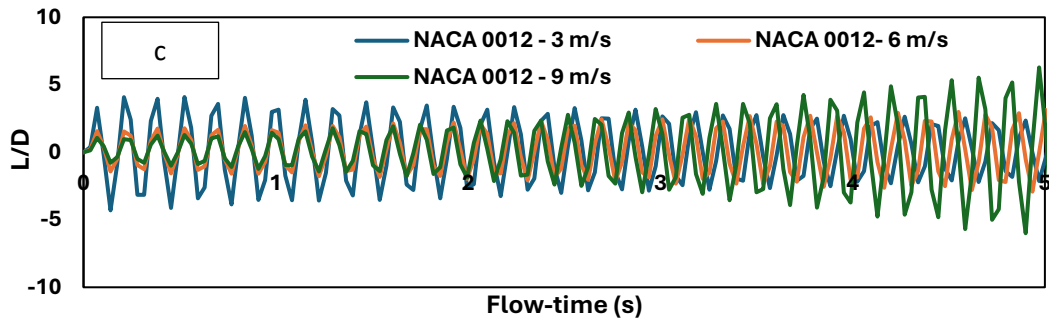


Figure 54. Diagram for (a) lift force, (b) drag force, and (c) lift-to-drag ratio under transient pitch oscillations in three different wind speeds

5.1.2 Torque and angular velocity of standalone oscillating NACA 0012

Figure 55 (a-b) show the behaviour of torque and angular velocity. From these elements, the mechanical power output can be predicted for an oscillating aerofoil, as shown in Figure 55 (c). According to the results in Figure 55 (a), the oscillating NACA 0012 at 9 m/s wind speed achieved the highest torque, while the lowest performance can be observed for lower wind speed of 3 m/s/ This clearly indicated that wind speed directly affects the efficiency of the oscillating aerofoil for wind energy harvesting. Similar behaviour can be observed for angular velocity, the highest wind speed achieved the highest value, as shown in Figure 55 (b). From the results of torque in transient conditions, the mechanical power output was calculated. The observed results demonstrate that higher wind speeds result in higher torque and angular velocity are related to the principle that power is proportional to the cube of wind speed. Increased wind speed enhances the aerodynamic forces on the aerofoil, leading to greater torque and angular velocity, and thus more effective energy harvesting.

Figure 55 illustrates the predicted average mechanical power output of isolated standalone oscillating NACA 0012 aerofoil undergoing pitch rotational motion. The CFD results reveal a rise in power output with increasing wind speed. Specifically, the power output at 3 m/s is recorded as 0.006 watts, escalating to 0.079 watts at 6 m/s, and reaching a higher power output of 0.13 watts at 9 m/s. Overall, the CFD results have proven that the average power output through pitch oscillation did not provide a useful power output. Therefore, in this study, a novel design of an oscillating energy

harvesting system integrated into the building roof structure is introduced. The efficiency of the proposed design will be investigated in section 5.3.

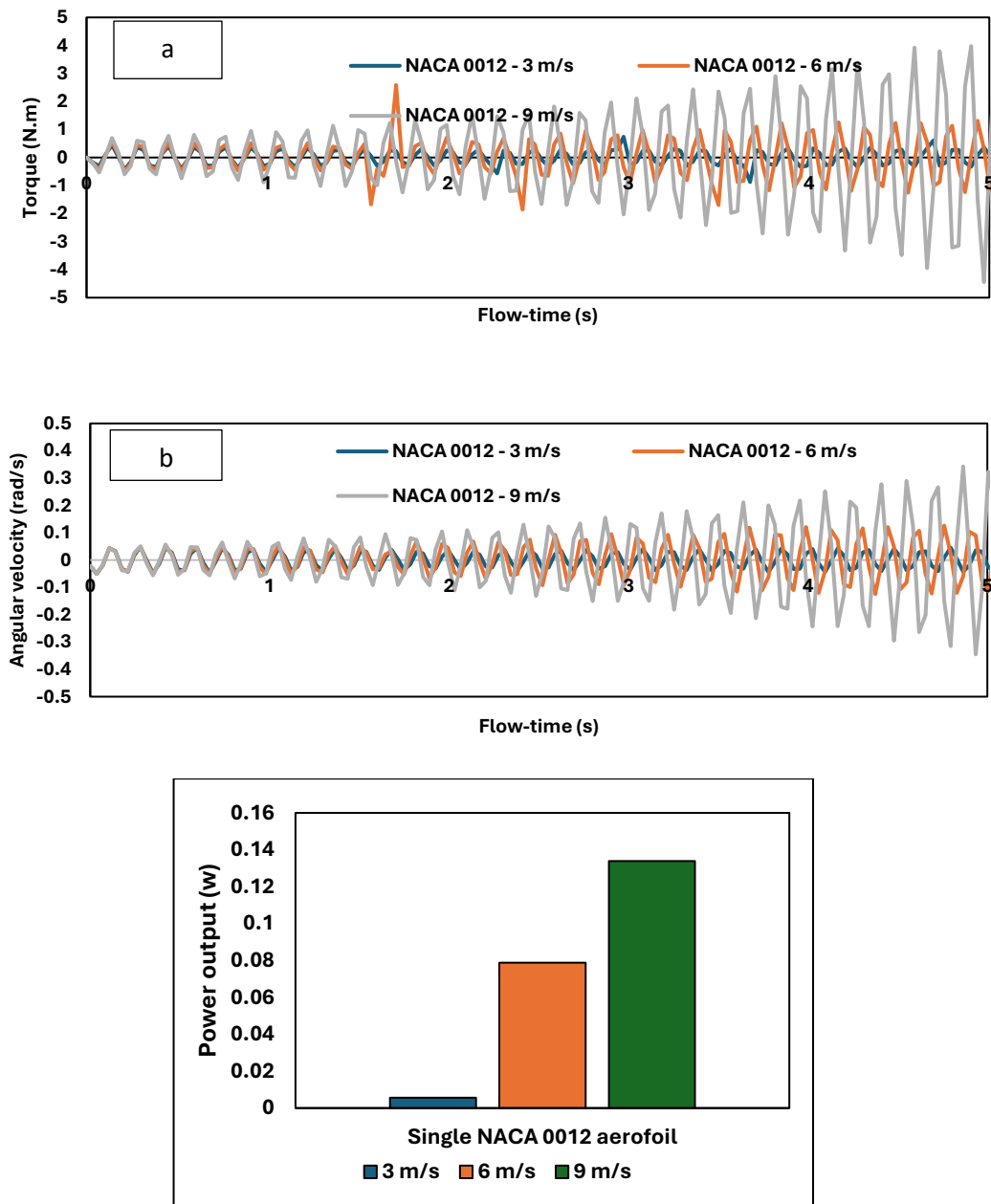


Figure 55. Isolated standalone NACA 0012 aerofoil in three different wind speeds

5.2 Evaluating the influence of building roof structures on accelerating wind flow

The investigation focused on studying the airflow patterns above and around buildings with flat, pitched, and curved roofs in different wind speeds including 3 m/s, 6 m/s, and 9 m/s. The study will explore wind speed acceleration, wind shear effects,

stagnation points, recirculation of wind flow, and separation points around the building and its rooftop. Moreover, the CFD results are expected to provide clear insights into the optimal placement of an oscillating aerofoil on the rooftop.

An investigation into the airflow distribution around buildings and their rooftops, examining factors such as the percentage increase in wind speed acceleration, recirculation phenomena, separation bubbles, and the attachment of wind flow to the roof structure. The anticipated outcomes aim to reveal the complex relationship between wind patterns and rooftops, allowing for the identification of dead zones and strategic placement of a wind energy harvesting system. The research encompasses diverse roof shapes including flat, pitched, and curved structures. At the same time, the study explores their performance at different wind speeds ranging from 3 m/s, 6 m/s, and 9 m/s. This comprehensive analysis is essential for optimising the performance of an oscillating aerofoil within wind energy converters, with the goal of enhancing efficiency in converting wind energy into usable power. The findings contribute to the understanding of the aerofoil's performance in varied conditions and inform the design and placement of wind energy harvesting systems for maximum effectiveness.

Table 13 provides a summary of wind speed acceleration for three different roof shapes at wind speeds of 3 m/s, 6 m/s, and 9 m/s. Notably, the curved roof demonstrated the highest wind speed acceleration that reached 52% at 9 m/s. In comparison, the pitched roof demonstrated a lower wind speed acceleration of 38%, while the flat roof demonstrated the least performance with an acceleration of 32%. Figure 56 shows the velocity magnitude for different roof shapes provides valuable insights into wind shear, wind speed acceleration, and recirculation of wind flow. In this Figure 56, the wind speed acceleration velocity magnitude contours are shown for the case of flat roof at (a) 3 m/s (b) 6 m/s, (c) 9 m/s, pitched roof (d) 3 m/s, (e) 6 m/s, (f) 9 m/s, and (g) curved roof (h) 3 m/s, (i) 6 m/s, and (j) 9 m/s.

The results highlight the superior performance of the curved roof, which showed the most promising outcomes in terms of wind speed acceleration and effective attachment of wind flow. This suggests strategic placements of wind energy harvesters on both the

windward and leeward sides of curved roof buildings. In contrast, the flat roof demonstrates suboptimal performance due to the wind shear effect, directing wind flow upwards.

The non-linear behaviour of lift force with increasing wind speed where the curved roof building performs better compared to flat and pitched roofs that can be attributed to the aerodynamic efficiency of the roof shapes. The curved roof smoothly redirects airflow, which minimise turbulence and flow separation and enhances lift force and overall aerodynamic performance especially at higher wind speeds. In contrast, flat roofs experience significant flow disruption and turbulence, whereas pitched roofs still face some turbulence and less optimal airflow compared to curved designs.

The exponential increase in lift force with wind speed was due to the dynamic pressure's non-linear relationship with velocity, where lift force rises more rapidly as wind speed increases. This non-linearity is reflected on the y-axis of the lift force plot, showing greater increase at higher wind speeds. The curved roof's design effectively leverages this relationship, resulting in a more efficient and better performance with increasing wind speeds compared to flat and pitched roofs.

Future considerations may involve alternative placements of wind energy harvesters at the windward edge of flat roofs for improved efficiency. The pitched roof shows wind speed acceleration on the windward side but intensified recirculation on the leeward side, which indicate that wind energy harvesters may be most effective when installed on the windward side for optimal energy capture.

Table 13. Wind speed acceleration percentage increase

Roof shape	Flat			Pitched			Curved		
Inlet velocity	3 m/s	6 m/s	9 m/s	3 m/s	6 m/s	9 m/s	3 m/s	6 m/s	9 m/s
Wind speed acceleration	3 m/s to 3.96 m/s	6 m/s to 7.93 m/s	9 m/s to 11.89 m/s	3 m/s to 4.15 m/s	6 m/s to 8.30 m/s	9 m/s to 12.50 m/s	3 m/s to 4.56 m/s	6 m/s to 9.13 m/s	9 m/s to 13.7 m/s
Percentage increase (%)	32%	32%	32.11%	38.33%	38.33%	38.89%	52%	52.17%	52.22%

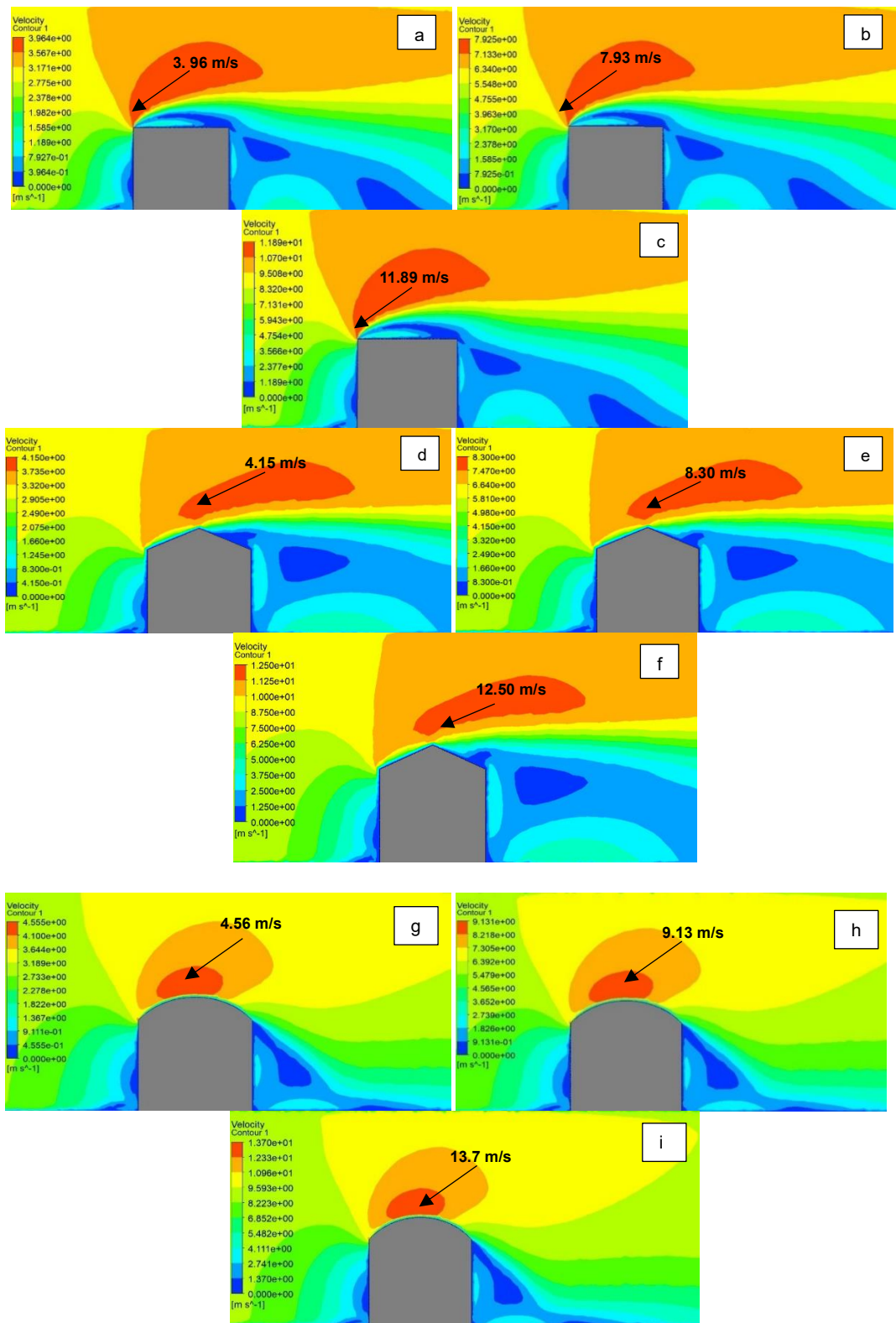


Figure 56. Wind speed acceleration velocity magnitude contours for flat roof at (a) 3 m/s (b) 6 m/s, (c) 9 m/s, pitched roof (d) 3 m/s, (e) 6 m/s, (f) 9 m/s, and (g) curved roof (h) 3 m/s, (i) 6 m/s, and (j) 9 m/s

5.3 Building integrated wind energy harvesting system (BI-WEHS)

A 3D model of an oscillating NACA 0012 aerofoil integrated into three different building roof shapes including flat, pitched, and curved roof building were developed. The purpose of the study is to examine the dynamic behaviour, predicted mechanical power output, and fluid interaction of an integrated design of an oscillating aerofoil integrated into the building roof. The important factors of wind speed, wind direction, wind shadow, and atmospheric boundary layer velocity profile in rural areas will be investigated.

To investigate the impacts of force and static pressure on self-induced oscillations of a pitching aerofoil, the study involves an examination of velocity magnitude and pressure contours obtained from Unsteady Reynolds-Averaged Navier-Stokes (URANS) simulations at various wind velocities including 3 m/s, 6 m/s, and 9 m/s. The aim is to assess the potential of the NACA 0012 oscillating aerofoil integrated into building roof for wind energy capture. This assessment involves the application of the dynamic mesh method in ANSYS Fluent employing consistent boundary conditions and dynamic mesh settings across three distinct scenarios: the installation of the NACA 0012 aerofoil on flat pitched and curved building roof structures. In addition, the investigation employs different wind speeds to assess the influence of installing the oscillating aerofoil on these varying roof shapes.

5.3.1 Velocity magnitude and static pressure distribution

This section presents the contours for velocity magnitude and static for the integrated design of an oscillating aerofoil installed into the flat, pitched, and curved roof buildings. These results are obtained at wind speeds of 3, 6, and 9 m/s. The results will demonstrate the variations in airflow distribution, torque behaviour, and angular velocity caused by installing the aerofoil into different roof shapes.

5.3.1.1 Oscillating NACA 0012 aerofoil energy harvester on a flat roof building

Figures 57-64 demonstrate the velocity magnitude and static pressure contours at a transient simulation with a time step of 0.035 at 0 seconds ($t=0s$), where the initial inlet velocities were set at 3, 6, and 9 m/s. However, given that the aerofoil is described as oscillating or moving due to the dynamic mesh or moving mesh, the contours at this

specific moment ($t=0s$) may not explicitly show the aerofoil in motion. The initial contours will show the velocity magnitude distribution across the domain set for the initial parameters with inlet velocities of 3 m/s, 6 m/s, and 9 m/s. Based on the geometry and boundary conditions created, it can be observed how the fluid begins to interact with the static or initial position of the aerofoil and how velocity is distributed around it.

In fluid flow simulations with transient time steps, the start at "0 seconds" marks the initiation of the simulation where the system is introduced to transient conditions and begins evolving dynamically. This point is where transient analysis commences, and the system starts responding to specified conditions and interactions involving fluid flow, movement of solids, and their interaction. "0 seconds" signifies the start time for the simulation, and subsequent analysis considers the dynamic evolution of the system over time. Although the system might start from a stable state, it can quickly transition into dynamic behaviour reflecting fluid-structure interactions. Recording at 0 seconds is crucial for capturing the initial conditions and early fluid-structure interactions, establishing a baseline to track the system's evolution and providing essential insights into initial transient behaviour for thorough analysis and benchmarking.

Recording from 0 seconds allows for observing the dynamic behaviour of the fluid and the oscillating aerofoil, including immediate responses and initial turbulence as the system starts to oscillate. This early-stage data is vital for understanding the system's complete dynamics and identifying phenomena that might be missed if recording begins after the system stabilises. The different times (0, 5, 20, and 30 seconds) shown in Figure 57 represent various stages of the simulation, illustrating the transient behaviour of the oscillating aerofoil with the NACA 0012 profile integrated into a flat roof building at a wind speed of 3 m/s. These intervals were chosen to capture the flow field's dynamic response and evolution over time, which showed how velocity magnitude and static pressure change as the system evolves, thus confirming the model's stability by consistent flow patterns over the simulated time.

The selection of a 1-metre chord length and 1-metre span for an oscillating aerofoil integrated into a building roof structure aligns with research findings on wind energy

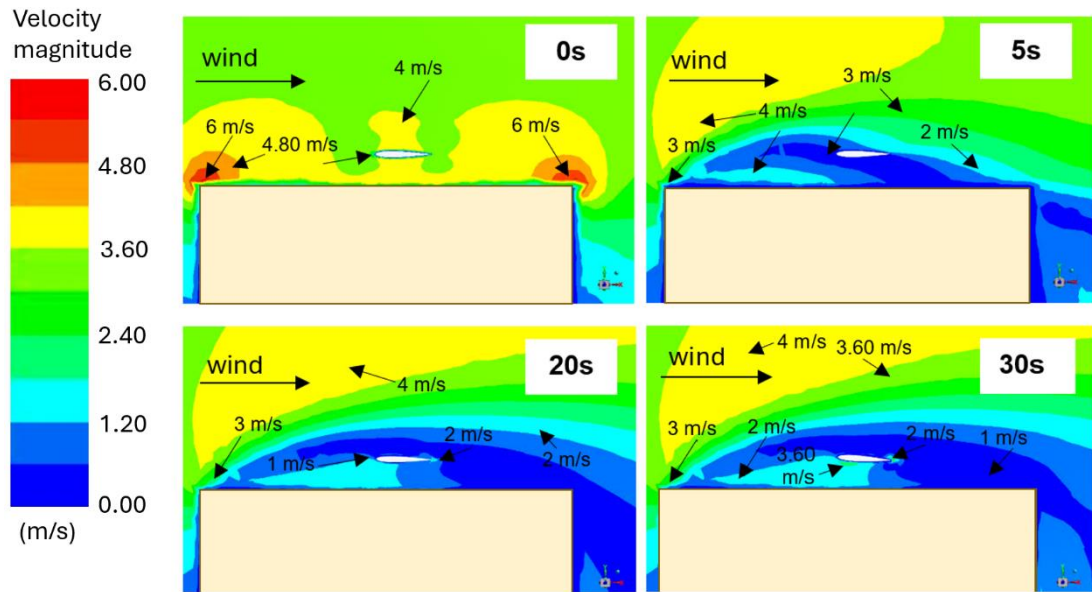
harvesting systems. Studies by [187-189] [195] indicate that shorter blade lengths with 1 to 2 metres are more efficient in urban environments due to space constraints and turbulence effects. [195] research on blade design optimisation shows improved aerodynamic performance with smaller blades in turbulent urban conditions. [195] explored blade dimensions to balance performance and structural integrity, suggesting that smaller chord lengths and spans optimise aerodynamic efficiency while maintaining stability.

To visualise the aerofoil's motion, the simulation extends beyond $t=0s$ to encompass subsequent time steps, which allows the dynamic mesh or moving mesh to exert influence on the aerofoil's position and consequently, the velocity field surrounding it. As the simulation advances, the contours dynamically display alterations in velocity magnitudes and patterns resulting from the aerofoil's oscillations or movements in accordance with the simulation's configuration.

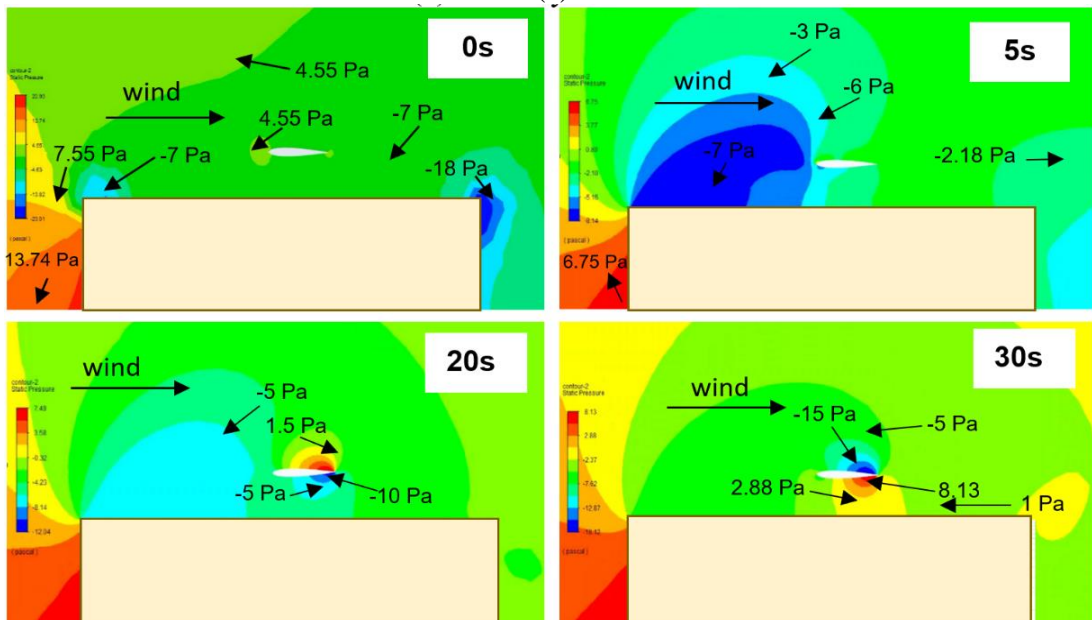
The velocity magnitude contours are observed over a 0-30 second period to examine how the velocity field around the aerofoil evolves over time. This extended timeframe allows the capture of transient phenomena such as flow separation reattachment and the development of the wake behind the aerofoil. Through analysing the flow dynamics over a longer duration, one gains insights into long-term trends and patterns including how the velocity field stabilizes and how different phases of the flow interact. This comprehensive view is crucial for understanding the broader aerodynamic behavior and performance of the aerofoil while ensuring that no transient events or flow instabilities are missed. In contrast torque and angular velocity were analysed over a shorter 0-12 second period to focus on rapid variations and high-frequency oscillations. This shorter duration was chosen to capture the immediate and detailed changes in these parameters which are vital for evaluating the aerofoil's performance under dynamic flow conditions. The detailed examination of these rapid oscillations provides insights into the aerofoil's stability and response to varying flow conditions. Together the different timeframes for these analyses offer a complete understanding of the aerofoil's aerodynamic characteristics with the longer timeframe capturing overall flow dynamics and the shorter one focusing on precise variations.

In Figure 57 (a), an oscillating aerofoil positioned at the central upper section of the flat roof showed the influence on fluid velocity magnitude, which was limited because of the low wind speed. The building structure with flat roof shape was unable to yield substantial advantages in terms of augmenting wind velocity based on its design, which requires the use of a spring constant of 850 N.m rad within the dynamic mesh for sustaining oscillations in pitch motion.

The findings presented in Figure 57 emphasise that a flat roof building is not the most suitable choice for the incorporation of an oscillating NACA 0012 aerofoil aimed at energy capture and power generation with the current design, boundary condition, and placement. In Figure 57 (b), the static pressure distribution is demonstrated for the aerofoil integrated into the flat roof structure at various time points (0, 5, 20, and 30 seconds). Notably, at 5 t(s), a decrease in static pressure is noticed on the side of the building roof facing the wind, which signifies the initiation of momentum generation that becomes evident at the aerofoil's leading edge, which results in lift force production. A reduction in static pressure under the aerofoil's surface and an increase above it trigger drag force at 20 t(s). With the aerofoil initiating pitch oscillations at 30 t(s), static pressure increases below the aerofoil's surface and diminishes above it, which leads to lift force generation. Consequently, the aerofoil persists in its oscillatory motion and undergoes vertical displacement. Video 1 visually shows the airflow distribution above and around the oscillating aerofoil with the NACA 0012 profile integrated into a building's roof.

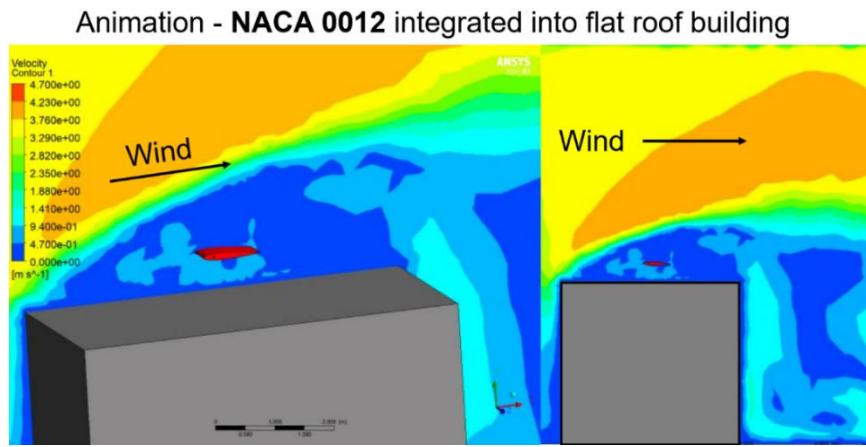


(a)



(b)

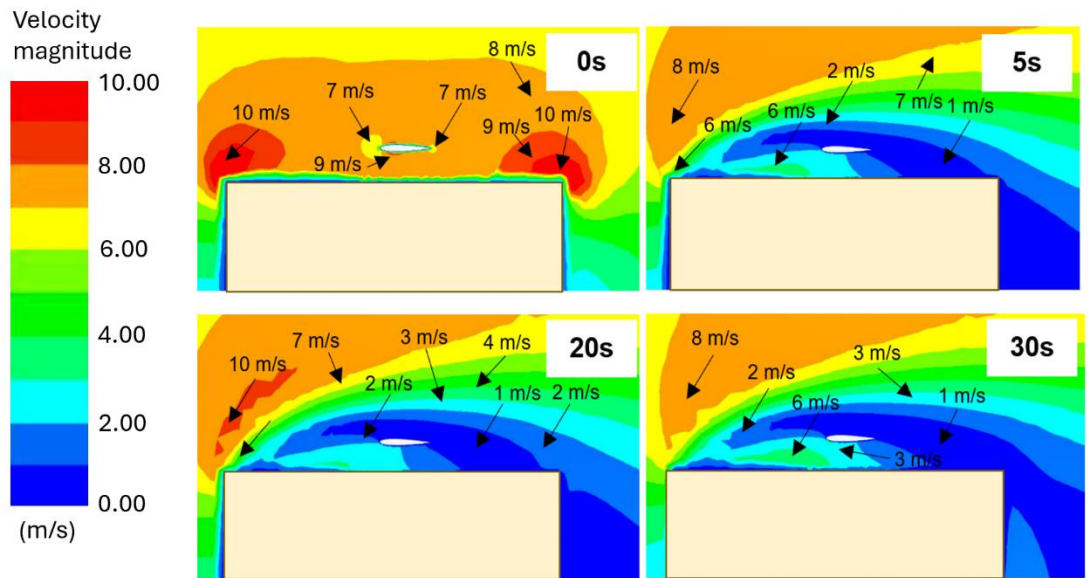
Figure 57. Contours representing (a) velocity magnitude and (b) static pressure for an oscillating aerofoil with the NACA 0012 profile integrated into flat roof building at 3 m/s for time intervals of 0, 5, 20, and 30 seconds



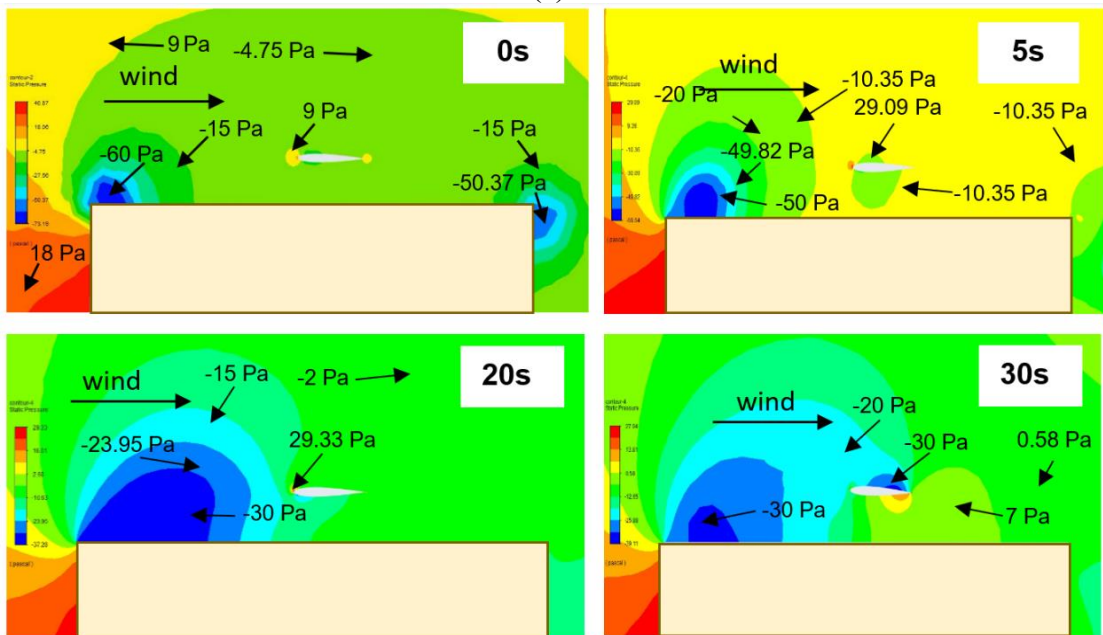
Video 1. Air flow distribution above and around oscillating aerofoil with the NACA 0012 profile integrated into flat roof building (*the playable video is available in the Appendix*) Video 1 - Flat roof.mp4

Figures 58 (a-b) shows the airflow distribution, (a) velocity magnitude and (b) static pressure for an oscillating aerofoil with the NACA 0012 profile integrated into flat roof building at 6 m/s for time intervals of 0, 5, 20, and 30 seconds. In Figure 58 (a), the wind velocity at 0 t(s), is distributed at the flat roof building and the stagnation point can be noticed at the leading edge of the aerofoil. While on 5 t(s), a low velocity magnitude can be observed at the rooftop, and force and momentum have started. This is followed by a lift force at 20 t(s) and a drag force at 30 t(s), which resulted in pitch oscillations over time.

In Figure 58 (b), a stagnation point of static pressure at the aerofoil's leading edge with a 0-degree angle of attack (AOA) can be noticed at 0 t(s). Consequently, at this angle of attack (AOA), there is no evident pressure disparity with the lower and upper surfaces of the aerofoil, attributed to the symmetrical profile of the aerofoil. Starting from 5 t(s), the aerofoil initiates momentum, leading to an augmented lift at a 4-degree AOA. While at 20 t(s), a region of low-pressure forms on the upper surface of the aerofoil, marked by elevated pressure at the leading edge and reduced pressure on the upper surface. At an increased angle of attack, the stagnation points shift toward the aerofoil's trailing edge. This alteration results to increase in drag and reduced in lift, as evident at 30 t(s).



(a)



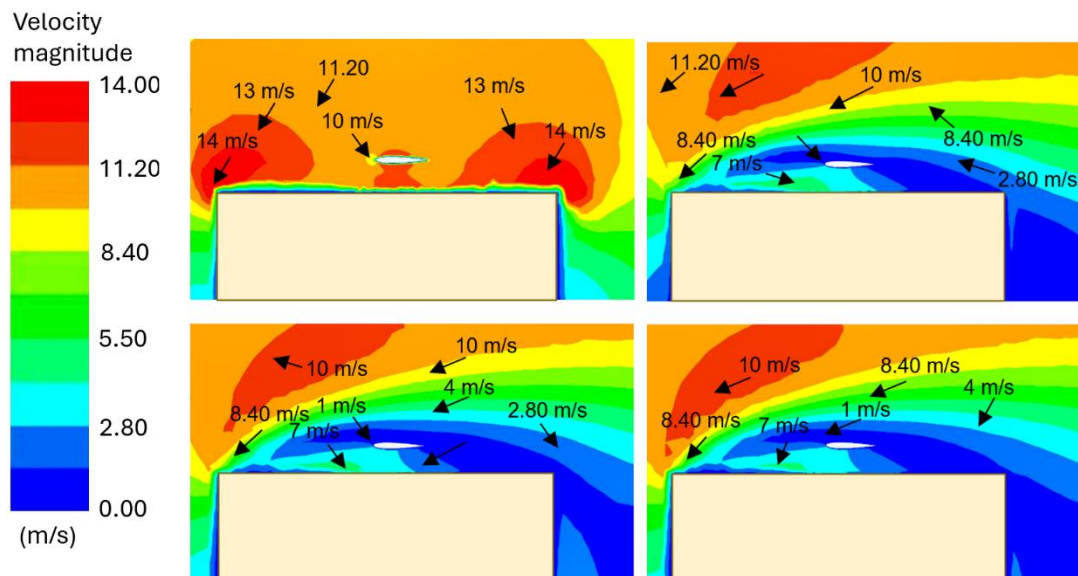
(b)

Figure 58. Contours representing (a) velocity magnitude and (b) static pressure for an oscillating aerofoil with the NACA 0012 profile integrated into flat roof building at 6 m/s for time intervals of 0, 5, 20, and 30 seconds

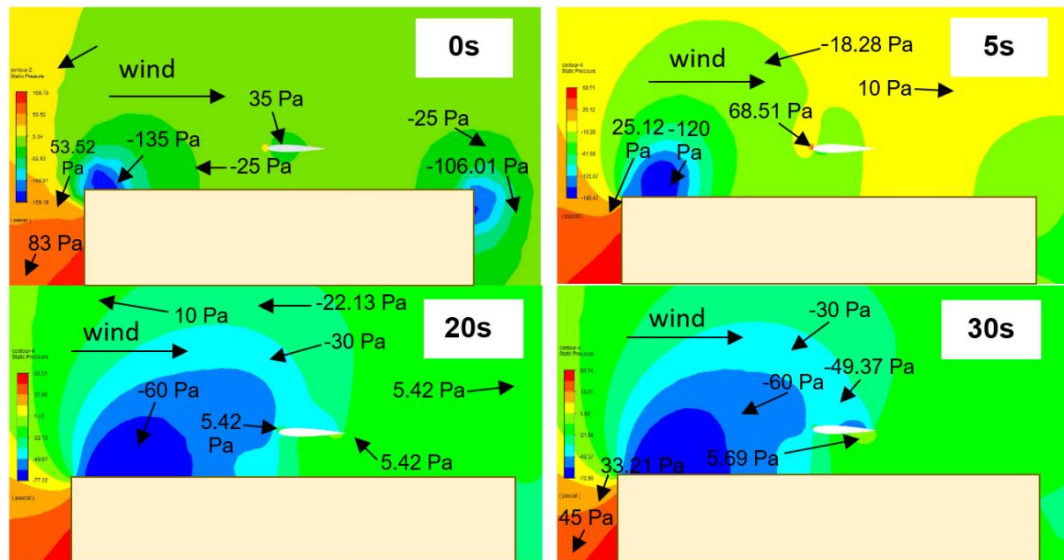
Figures 59 (a-b) demonstrate the case for an oscillating aerofoil with the NACA 0012 profile integrated into flat roof building at 9 m/s for time intervals of 0, 5, 20, and 30 seconds. The oscillating aerofoil is positioned at the at the central upper section of the flat roof. In Figure 59 (a), it shows that the airflow at 0 t(s) is distributed above the flat roof and around the aerofoil. While low-velocity magnitude at the upper section of the flat roof building structure can be observed, and a high wind velocity can be observed

at the front edge of the flat roof building from 5 t(s). A recirculation region is shown on the rooftop. Due to the spring applied into the dynamic setting, it created the lift force in 20 t(s). As shown in the contours, the accelerated wind velocity is not that much as compared to the other roof shapes investigated in this study.

As shown in Figure 59 (b), a stagnation point in pressure becomes evident at the aerofoil's leading edge can be observed at 0 t(s). This is followed by the aerofoil, initiating a momentum building phase, leading to increased pressure at the leading edge and reduced pressure on the aerofoil's lower surface. Consequently, the generation of lift force becomes apparent at 20 t(s), while drag force at 30 t(s).



(a)



(b)

Figure 59. Contours representing (a) velocity magnitude and (b) static pressure for an oscillating aerofoil with the NACA 0012 profile integrated into flat roof building at 9 m/s for time intervals of 0, 5, 20, and 30 seconds

5.3.1.2 Oscillating NACA 0012 aerofoil energy harvester on a pitched roof building

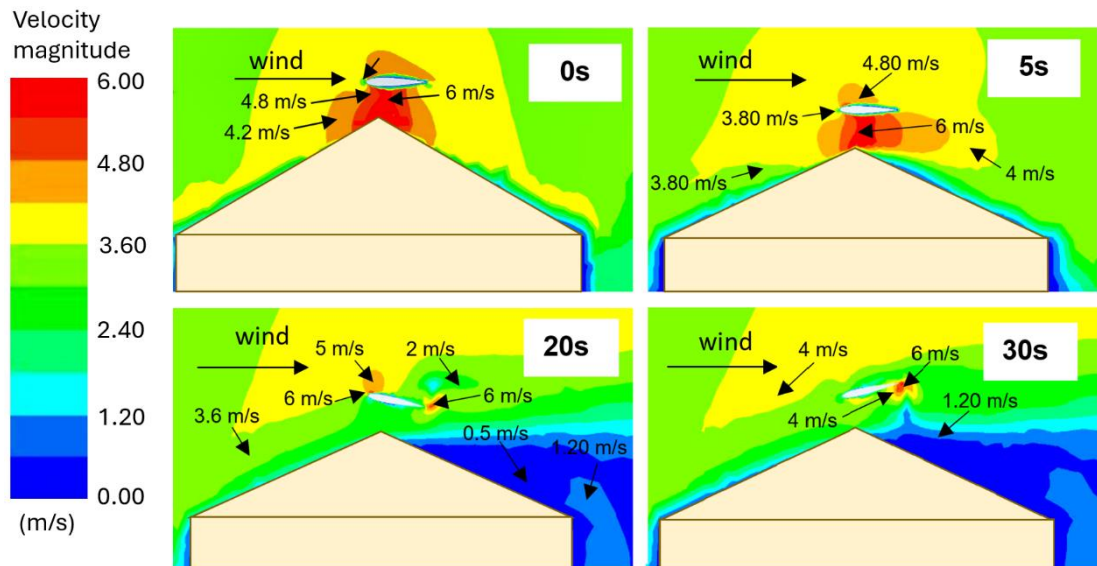
The oscillating aerofoil is positioned 6.25 metres above the roof peak, which combines the building height of 6 metres and an additional 0.25 metres above the roof. This height is chosen to ensure the aerofoil is exposed to higher wind speeds and less turbulence compared to placements closer to the roof surface. This setup influences the natural wind acceleration that occurs over roof peaks, specifically in buildings with pitched and curved roofs to enhance the aerofoil's performance. While for the direction of V , the analysis models the incoming wind direction as flowing from the left side to the right side of the building roof. This configuration allows for a detailed study of how wind flows across the building roof and interacts with the aerofoil. Through examining wind velocity from this direction, it aids to understand the wind speed profiles and their effects on the aerofoil's energy harvesting capabilities.

With the optimal position, the research indicates that the highest wind speed acceleration occurs at the ridge or mid-centre of pitched and curved roofs. Positioning the oscillating aerofoil at these locations takes advantage of this natural wind speed

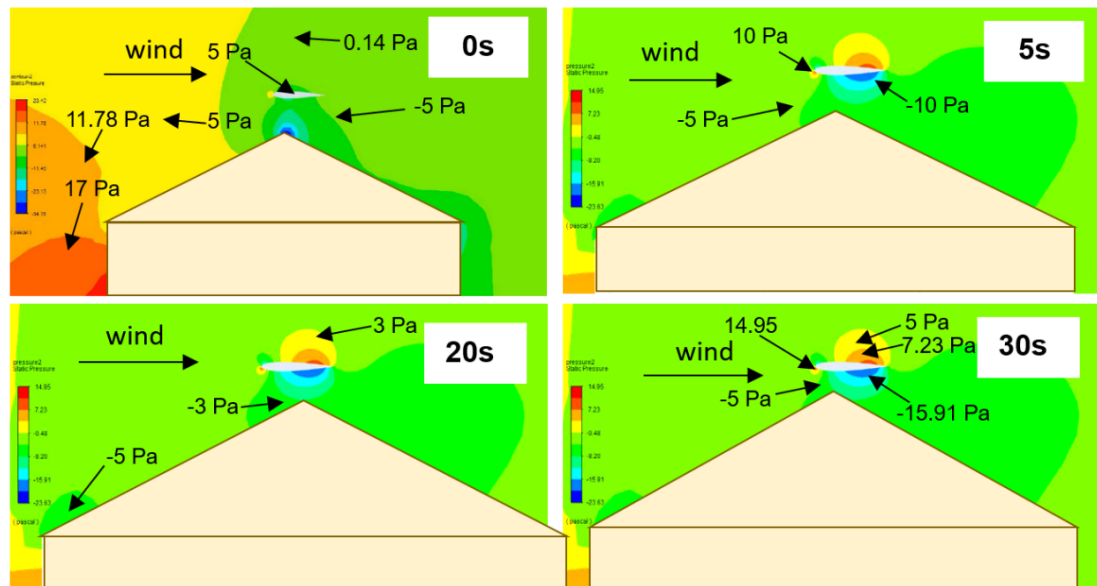
increase. The height of 6.25 metres above the roof ensures optimal wind exposure, maximising energy capture efficiency. This placement strategy minimises turbulence effects and optimises the aerofoil's performance by influencing the accelerated wind zones over the roof structure.

Figures 60 (a-b) demonstrate the airflow distribution, (a) velocity magnitude and (b) static pressure for an oscillating aerofoil with the NACA 0012 profile integrated into pitched roof building, at times of 0, 5, 20, and 30 seconds in three different wind speeds including 3, 6, and 9 m/s. For the velocity magnitude, Figure 60 (a) illustrates the distribution of airflow over the upper surface of the pitched roof at 3 m/s. Furthermore, the concentration of velocity magnitude can be noticed at the top ridge of the pitched roof, and the incoming wind is approaching the roof building structure and flow separation can be seen at the windward corner. Also, a large separation of airflow was observed from 20 t(s) and 30 t(s) at the leeward side located after the roof ridge and resulting in the occurrence of a recirculation region. Moreover, the flow separation over the roof ridge caused a reversed flow further away after the building which results in the recirculation behind the building. The recirculation zone developed at the leeward side grows larger and spreads up. Video 2 shows the motion of the air flow distribution above and around the moving oscillating aerofoil integrated into a pitched roof.

At 0 t(s), the static pressure was distributed at the pitched roof, as shown in Figure 60 (b). Through examining the CFD contours of static pressure on the flat roof, it is evident that there is a noticeable difference in pressure between the side of the roof facing the oncoming wind (windward side) and the side sheltered from the wind (leeward side). While at 5 t (s), positive static pressure is noticeable on the lower side located at the leading edge and on the upper side close to the trailing edge of the aerofoil. At 20 t(s), a positive surface area can be noticed between the pitched roof and the aerofoil when the lift force was generated from the static pressure on the lower surface area.



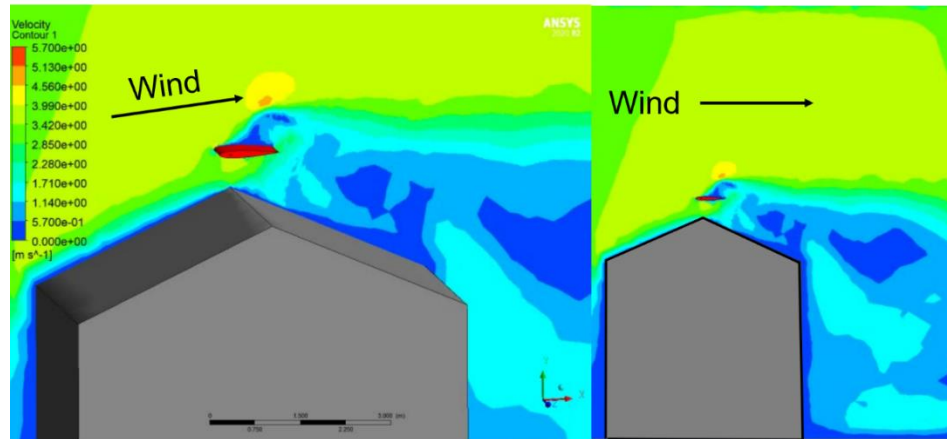
(a)



(b)

Figure 60. Contours representing (a) velocity magnitude and (b) static pressure for an oscillating aerofoil with the NACA 0012 profile integrated into pitched roof building at 3 m/s for time intervals of 0, 5, 20, and 30 seconds

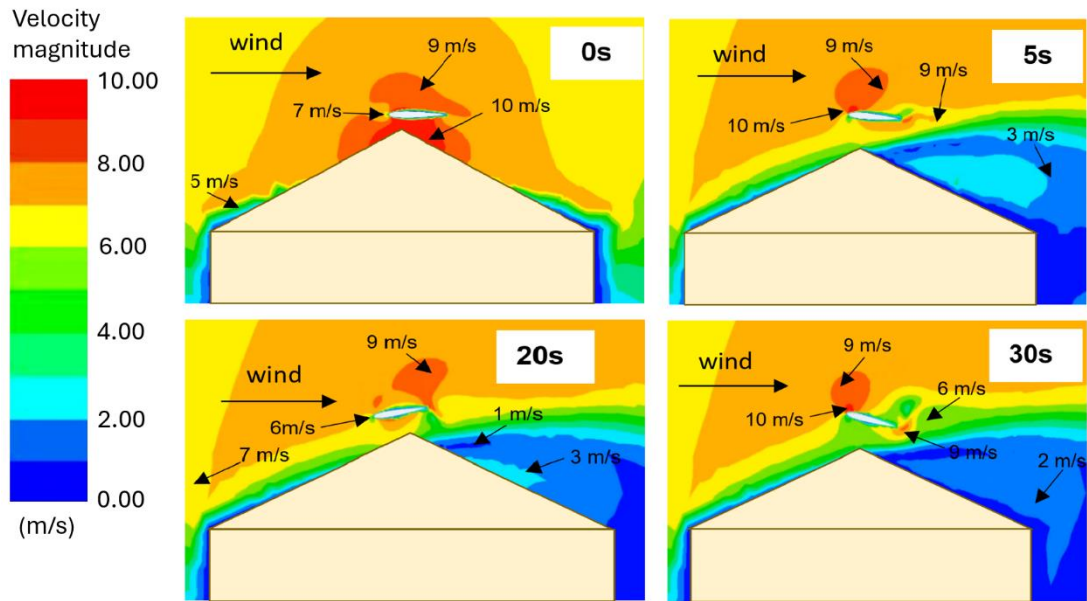
Animation - **NACA 0012** integrated into pitched roof building



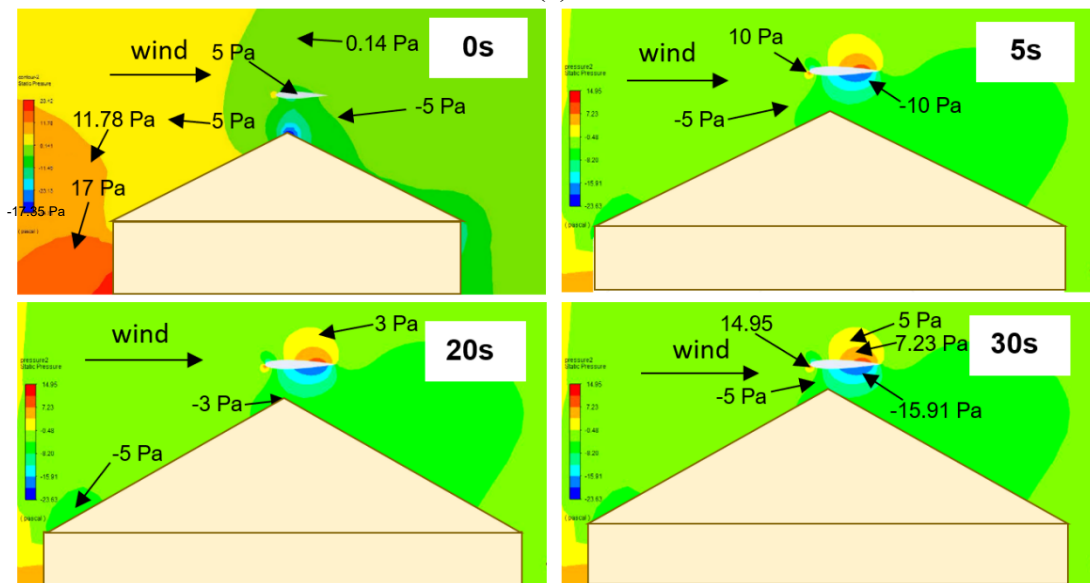
Video 2. Air flow distribution above and around the oscillating aerofoil with the NACA 0012 profile integrated into pitched roof building (*the playable video is available in the Appendix*) Video 2 - Pitched roof.mp4

Figure 61 demonstrates the airflow distribution, (a) velocity magnitude and (b) static pressure for an oscillating aerofoil with the NACA 0012 profile integrated into pitched roof building, at times of 0, 5, 20, and 30 seconds at 6 m/s. As shown in Figure 61 (a), the air flow at 0 t(s) is distributed above and around the rooftop of the pitched roof building structure. While a lift force is generated at 5 t(s), and development of separation and recirculation of wind flow at the leeward area of the pitched roof building structure. At 20 t(s), a drag force is created and a lift force at 30 t(s). This resulted in pitched oscillations with an upward and downward motion. At 0 t(s), static pressure difference at the windward and leeward regions can be observed at the pitched roof building structure.

In Figure 61 (b), the static pressure at 5 t(s) demonstrates the pressure difference between the aerofoil's pressure and suction regions, contributing to the generation of lift force. In addition, a stagnation point can be observed at the aerofoil's leading edge, accompanied by high static pressure on the upper surface at both 20 t(s) and 30 t(s). The elevated static pressure on the upper surface during these intervals indicates an accumulation of pressure in this region. In the field of wind energy capture, this pressure differential can be harnessed to generate lift force and, subsequently, convert it into usable energy. This phenomenon highlights the effective capture and utilisation of kinetic energy from the airflow by the aerofoil to produce lift force, demonstrating its potential for energy conversion.



(a)



(b)

Figure 61. Contours representing (a) velocity magnitude and (b) static pressure for an oscillating aerofoil with the NACA 0012 profile integrated into pitched roof building at 6 m/s for time intervals of 0, 5, 20, and 30 seconds

Figure 62 (a) illustrates the velocity magnitude at 9 m/s. At 0 t(s), the airflow is distributed at the pitched rooftop and the concentration of velocity magnitude is located at the ridge of the pitched roof. While at 5 t(s), a stagnation point can be noticed at the leading edge of the aerofoil and starts to create momentum. As a result, a lift force is generated at 20 t(s), and there is noticeable flow separation and recirculation on the downwind face of the pitched roof building. Subsequently, a drag force is

evident at 30 t(s), coinciding with a low velocity magnitude on the leeward side of the pitched roof building.

In Figure 62 (b), negative static pressure at 0 t(s) can be seen at the ridge of the pitched roof. While positive static pressure is noticeable beneath the aerofoil's leading edge, negative static pressure is shown above the leading-edge top at a distance of 0.1 m from the chord length. As a result, it created a lift force from 5 t(s) to 20 t(s), and a drag force at 30 t(s). This was followed by pitch oscillations.

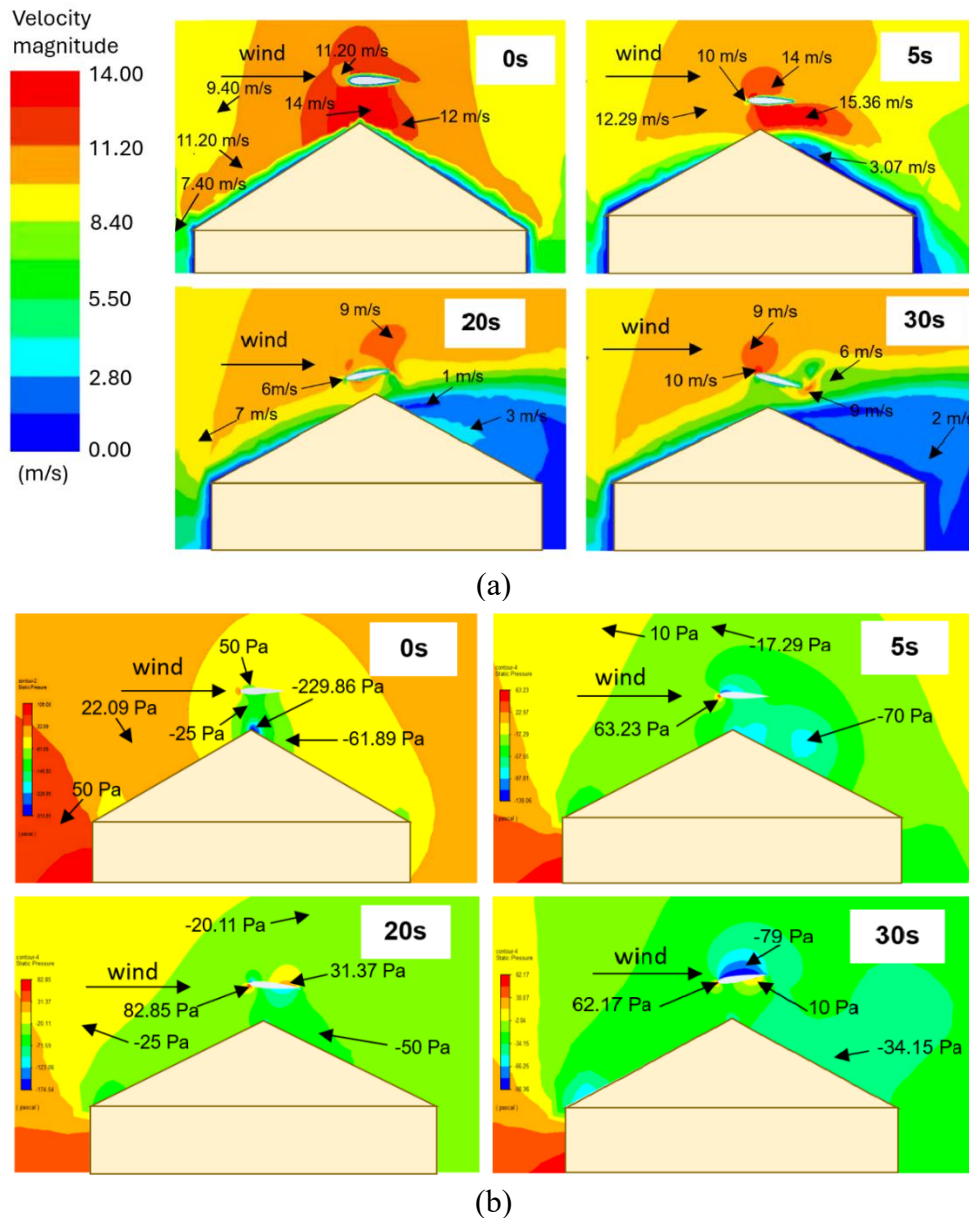
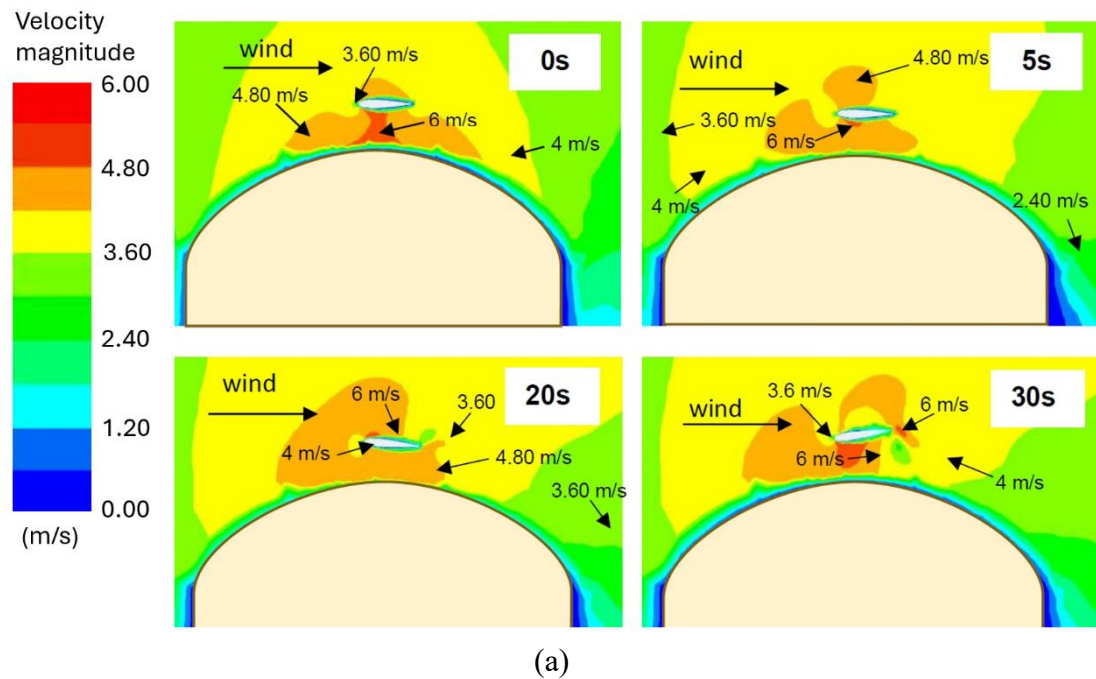


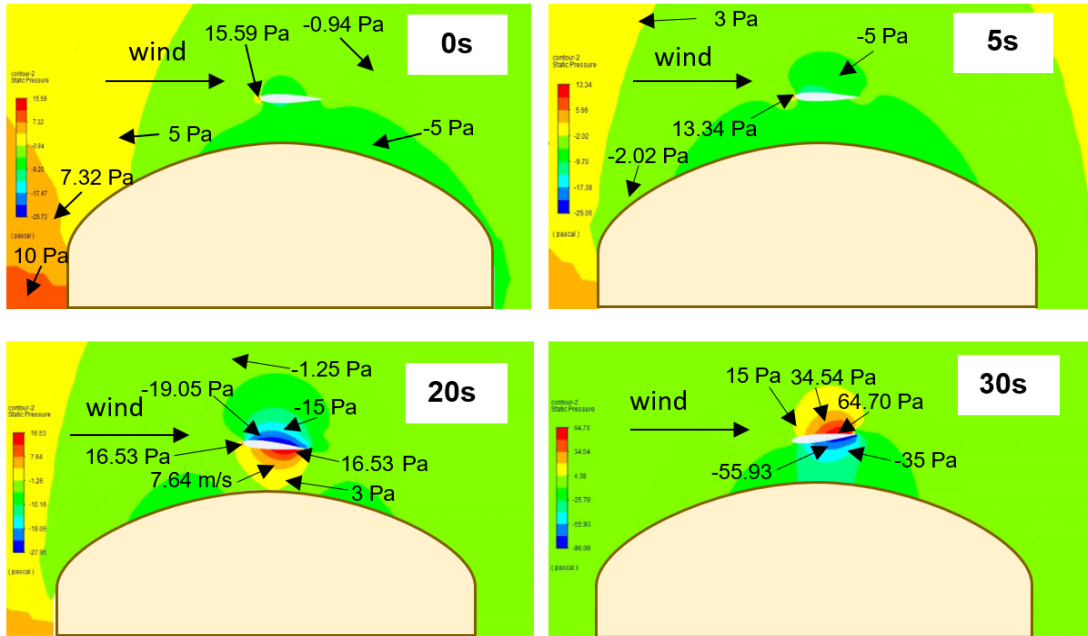
Figure 62. Contours representing (a) velocity magnitude and (b) static pressure for an oscillating aerofoil with the NACA 0012 profile integrated into pitched roof building at 9 m/s for time intervals of 0, 5, 20, and 30 seconds

5.3.1.3 Oscillating NACA 0012 aerofoil energy harvester on a curved roof building

Figure 63 (a) illustrates that the airflow adhered firmly to the curved roof, and no recirculation zones were developed at the rooftop. It can also be seen in the case of a curved roof, a high streamwise velocity occurs at the top of the roof. These results show great potential for energy harvesting systems. At 0 t(s), it can be observed an accelerated wind velocity from an inlet velocity of 3 m/s to 6 m/s, and high-velocity magnitude can be noticed at the ridge of the curved roof. As a result, the aerofoil starts to create momentum at 5 t(s). At 20 t(s) it started to generate the lift force and drag force at 30 t(s), and this continued with pitch oscillations over time. Video 3 shows the motion of the air flow distribution above and around the moving oscillating aerofoil integrated into a curved roof.

In Figure 63 (b), the static pressure difference can be seen around the aerofoil and above the curved roof as the wind flow passed it at 0 t(s). Similar to the case of the flat and pitched roof, it started its momentum force at 5 t(s). Low static pressure can be observed at the upper surface of the aerofoil at 20 t(s), and high pressure at 30 t(s). As a result, it generated a lift and drag force, and translated into pitch oscillations over time

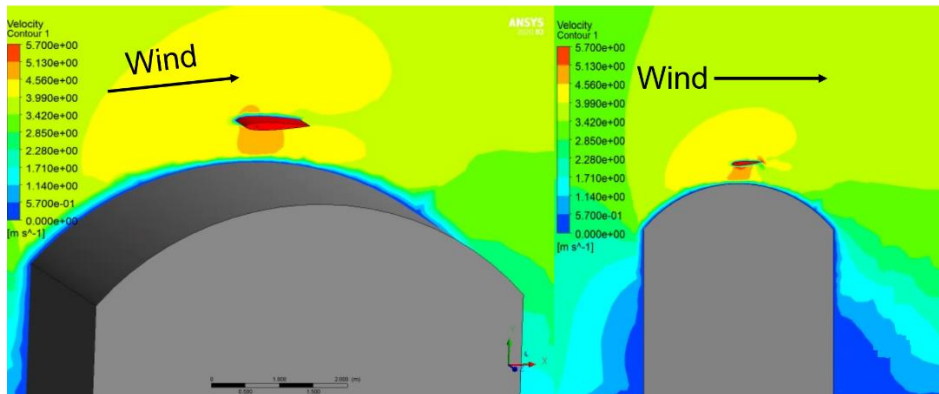




(b)

Figure 63. Contours representing (a) velocity magnitude and (b) static pressure for an oscillating aerofoil with the NACA 0012 profile integrated into curved roof building at 3 m/s for time intervals of 0, 5, 20, and 30 seconds

Animation - **NACA 0012** integrated into curved roof building

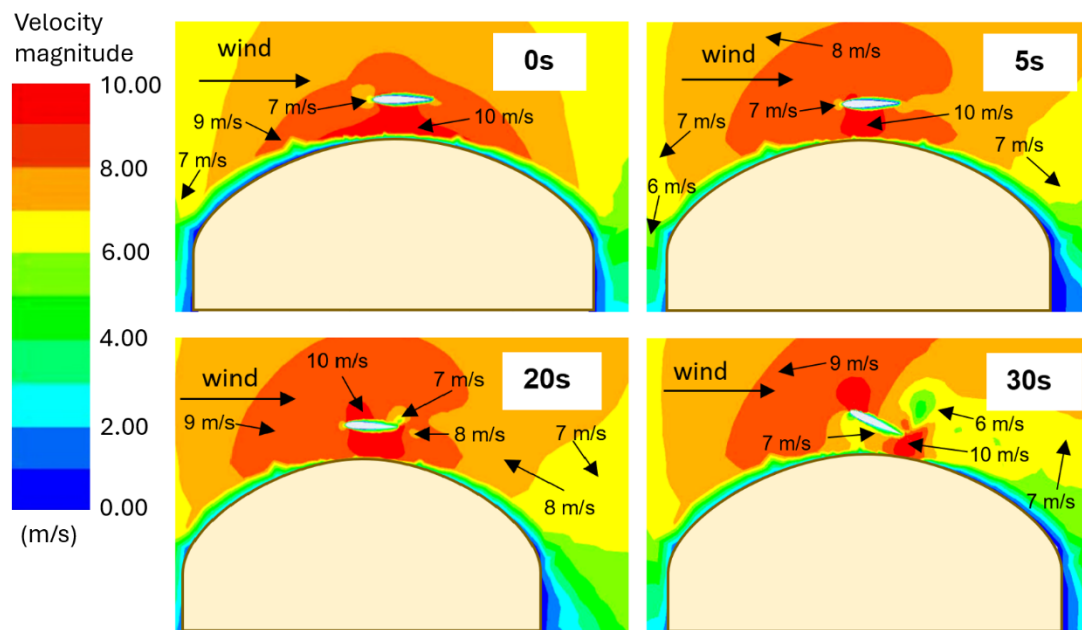


Video 3. Air flow distribution above and around the oscillating aerofoil with the NACA 0012 profile integrated into curved roof building (*the playable video is available in the Appendix*) Video 3 - Curved roof.mp4

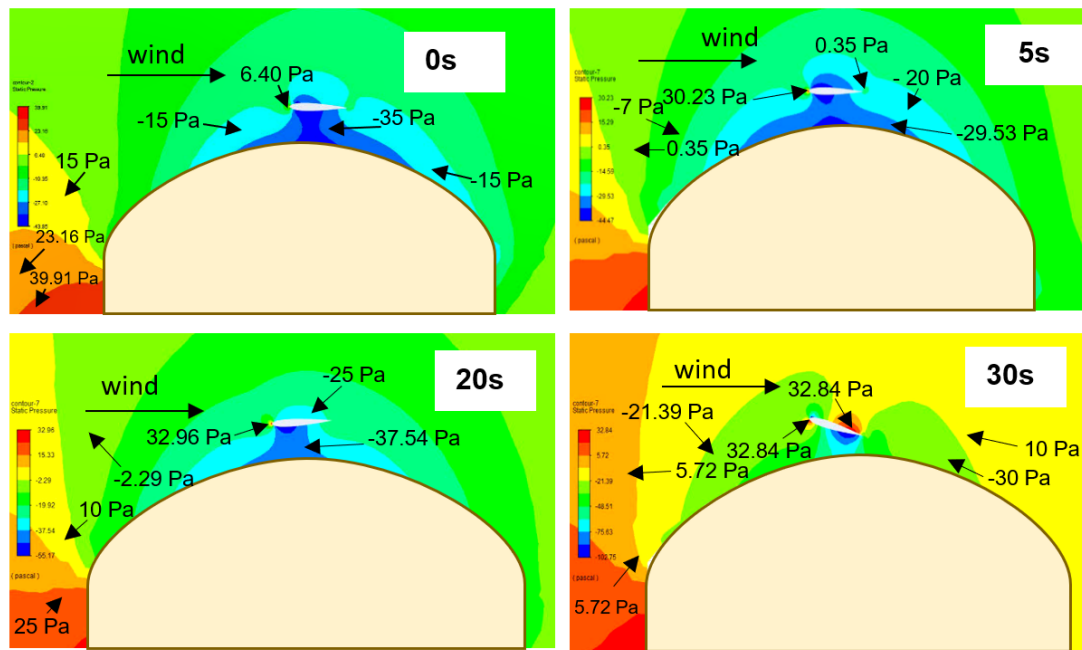
Figure 64 demonstrates the airflow distribution, (a) velocity magnitude and (b) static pressure for an oscillating aerofoil with the NACA 0012 profile integrate into curved roof building at 6 m/s for time intervals of 0, 5, 20, and 30 seconds. As shown in Figure 64 (a), it illustrates the airflow adhered significantly to the curved roof, and no regions of recirculation were developed at the rooftop at 0 t(s). It can also be seen in the case of a curved roof, a high streamwise velocity occurs at the top of the roof. At 5 t(s), it

starts to create momentum with high-velocity magnitude around the aerofoil, and slowly reduces at the trailing edge. As a result, the aerofoil's trailing edge started to develop vortices and bubbles, which are shown in 20 t(s). At 30 t(s) of velocity contour, a high magnitude of velocity is evident at the aerofoil's upper leading edge. Also, a high-velocity magnitude can be seen upper leading edge of the aerofoil, and it shows that the oscillating aerofoil can nearly hit the roof structure. The findings suggest that at 6 m/s wind speed, adjustments in the stiffness constant, particularly for pitch oscillations should be considered in future works. This analysis highlights the importance of optimising the system's performance for different wind conditions to harness its full energy harvesting capabilities.

In Figure 64 (b), the static pressure at 0 t(s) is distributed above the curved roof building structure, with a stagnation point apparent at the leading edge of the aerofoil at a 0-degree AOA. Commencing from 5 t(s), region of reduced pressure forms on the aerofoil's upper surface, creating lift as air is propelled from an area of higher pressure to a lower-pressure region, resulting in an upward motion of the aerofoil. This lift is translated into drag force at 20 t(s). Lastly, a higher lift force can be noticed at 30 t(s).



(a)



(b)

Figure 64. Contours representing (a) velocity magnitude and (b) static pressure for an oscillating aerofoil with the NACA 0012 profile integrated into curved roof building at 6 m/s for time intervals of 0, 5, 20, and 30 seconds

Figure 65 demonstrates the airflow distribution, (a) velocity magnitude and (b) static pressure for an oscillating aerofoil with the NACA 0012 profile integrated into curved roof building at 9 m/s for time intervals of 0, 5, 20, and 30 seconds. As shown in Figure 65 (a), the airflow is greatly attached to the curved roof, and no recirculation regions were produced at the rooftop. It can also be seen in the case of a curved roof, a high streamwise velocity occurs at the top of the roof. At 0 t(s), the high-velocity magnitude can be noticed at the ridge of the curved roof as shown. As a result, the aerofoil starts to create momentum at 5 t(s). At 20 t(s) it started to generate the drag force at 20 t(s) and lift force at 30 t(s), and this continued with pitch oscillations over time.

From the 0 t(s), the static pressure is distributed around the curved roof, as demonstrated in Figure 65 (b). High static pressure can be seen at the windward region of the curved rooftop, while low static pressure can be noticed. At 5 t(s), the stagnation point can be observed at the leading edge of the aerofoil and starts to create lift force. While at 20 t(s), a decreased pressure area on the aerofoil's upper surface that leads to lift generation as air transitions from a higher-pressure area to a lower pressure region,

causing the aerofoil to ascend. Consequently, drag force is produced at 30 t(s) persisting in its oscillatory pattern.

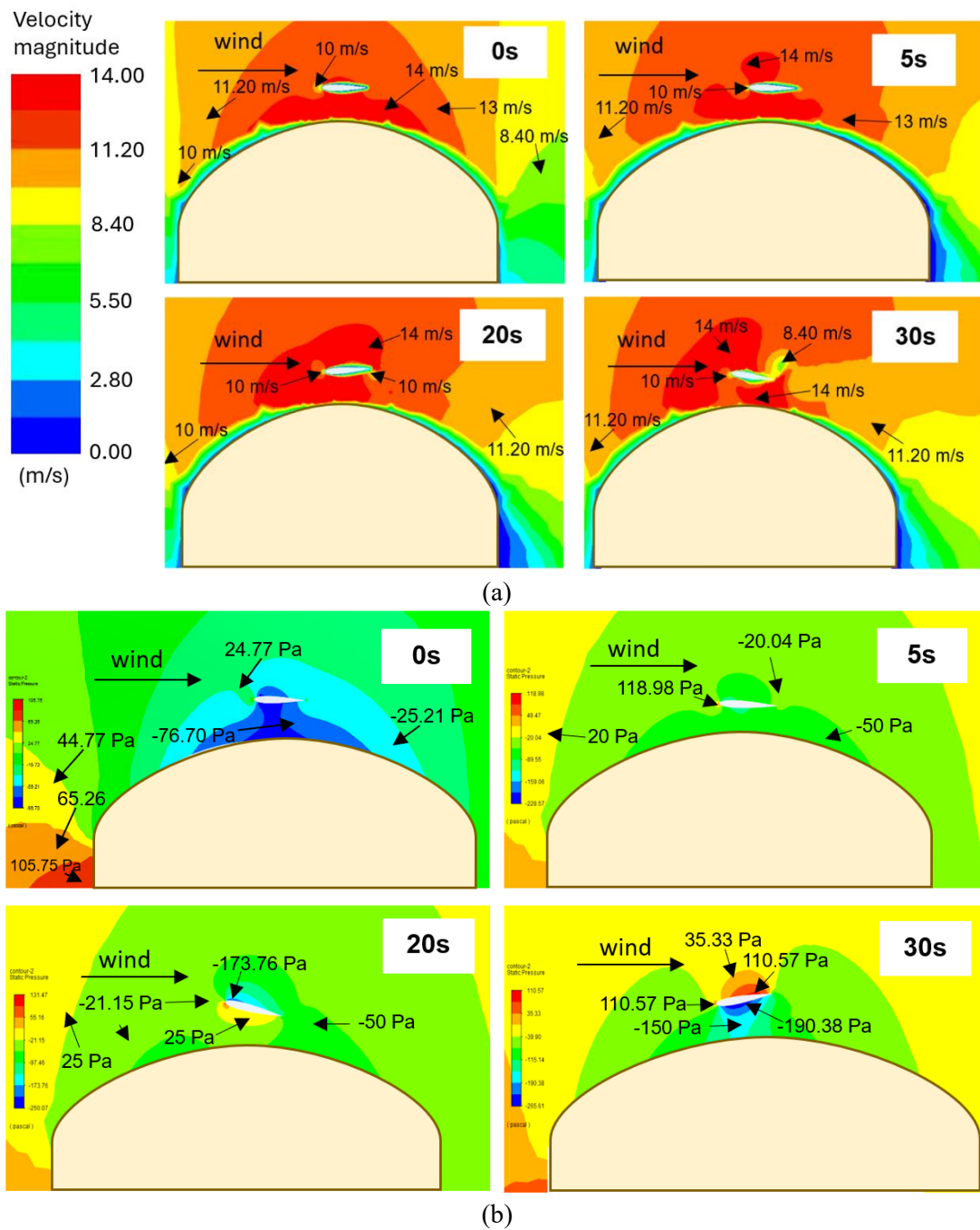


Figure 65. Contours representing (a) velocity magnitude and (b) static pressure for an oscillating aerofoil with the NACA 0012 profile integrated into curved roof building at 9 m/s for time intervals of 0, 5, 20, and 30 seconds

According to the study on the airflow above and around the three different parameters including flat, pitched, and curved roof building structure, it clearly showed that curved roof building provided the most promising results for energy harvesting

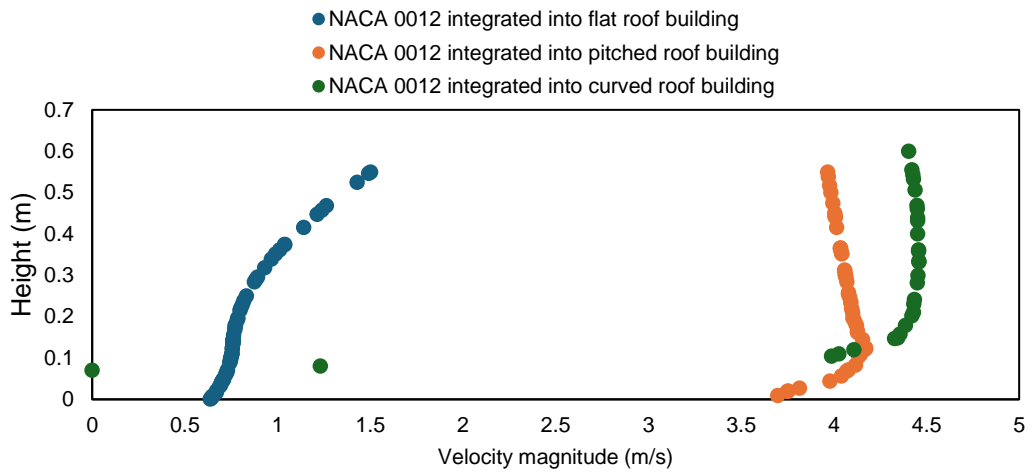
efficiency as compared to the other two roof shapes. At the same time, the dynamic response of a NACA 0012 aerofoil in oscillation when integrated into the building's roof showed the lift and drag force, and pitch oscillations over time. Moreover, sensitivity analysis of different constant damping values for different wind speeds and roof shapes should be investigated for optimisation.

5.3.2 Velocity profile surrounding the aerofoil integrated into the flat, pitched, and roof building

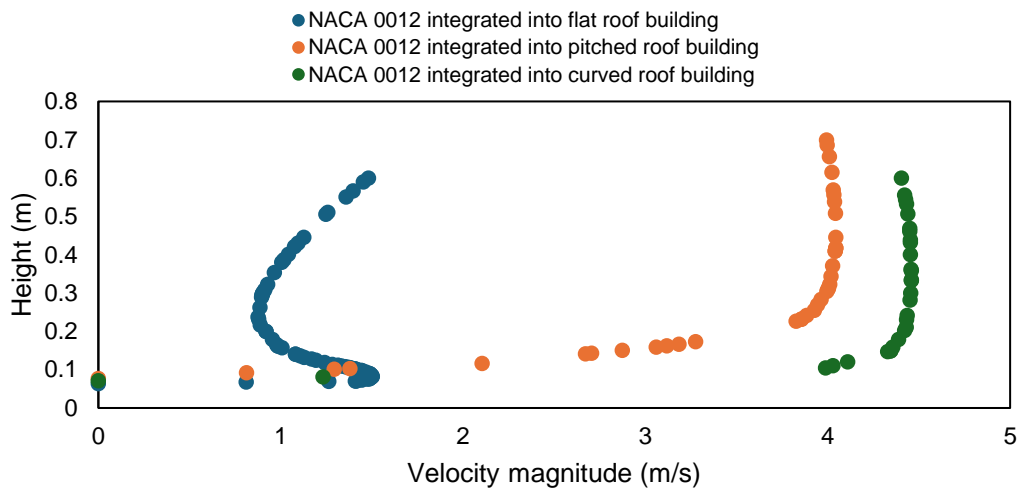
Figures 66 (a-b) show the velocity profiles surrounding the aerofoil at a 10-degree angle of attack when integrated into flat, pitched, and curved roof buildings. Figure 66 (a) illustrates notable differences between the integration of the NACA 0012 aerofoil into flat and pitched roof structures. In the case of the flat roof building, wind speed acceleration was not observed due to wind shear, despite the aerofoil ideal placement. Instead, wind flow recirculation occurred around the aerofoil, resulting in an initial wind speed of 3 m/s decreasing to 1.7 m/s.

Conversely, integrating the NACA 0012 aerofoil into pitched and curved roof buildings led to wind speed enhancements, reaching 4.3 m/s for pitched roofs and 4.45 m/s at a 10-degree angle. Figure 66 (b), focusing on the velocity profile at the mid span of the aerofoil, reveals similar trends across cases. Notably, lower wind speeds are observed for the integration into flat roofs compared to pitched and curved roofs. Wind speed acceleration occurs significantly at the leading edge of the aerofoil in flat roof settings, while a decrease in acceleration is evident at the mid span due to roof shape and aerofoil placement.

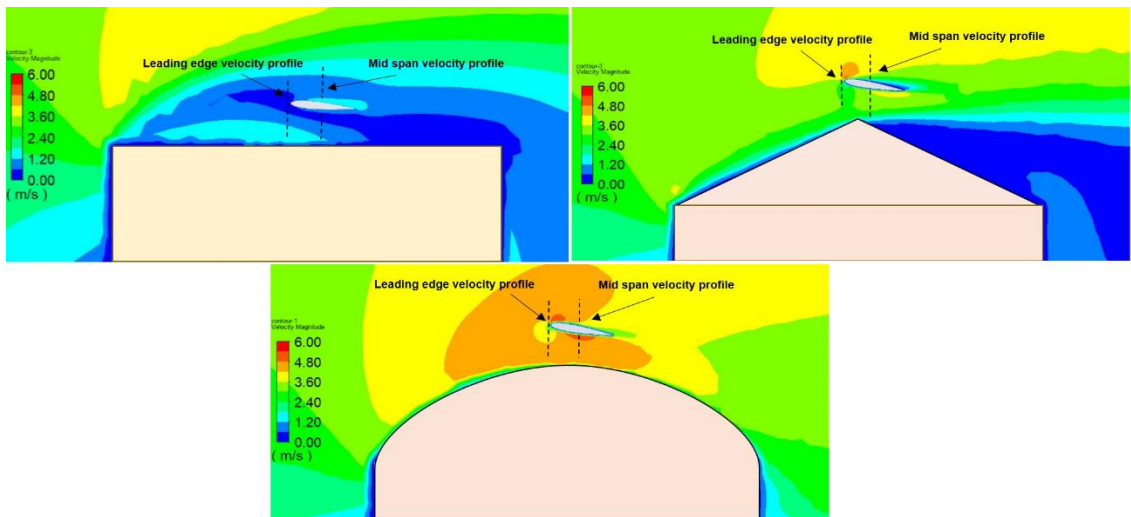
In pitched roof configurations, wind speed acceleration is prominent on the windward side of the building, with wind flow detachment observed on the leeward side. Similar wind speed enhancements are observed for NACA 0012 integration into curved roof buildings, attributed to the shape of the roof and strong wind flow attachment. These findings align with studies in the literature [20-21] [135] which emphasise the significant influence of roof geometry on wind flow patterns and the effectiveness of aerofoil integration in enhancing wind speeds in certain configurations.



(a)



(b)



(c)

Figure 66. Velocity profile located at the (a) leading edge (b) mid span of the aerofoil (c) velocity profile points location for the three design parameters

5.3.3 Dynamic behaviour of the roof-integrated oscillating aerofoil energy harvester

This section examines the dynamic behaviour of an oscillating aerofoil wind energy harvesting system integrated into three different roof shapes, focusing on pitch angle, torque, and angular velocity to predict potential power output. A sensitivity analysis was conducted to assess the impacts of various factors such as wind speed, roof shapes, wind direction, and power spectral density across different frequencies.

5.3.3.1 Impact of wind speed

The influence of wind speed and building roof shape on the dynamic behaviour of pitch angle, torque, angular velocity, and power output performance will be examined through a comparative analysis. Three different wind velocities including 3 m/s, 6 m/s, and 9 m/s will be investigated for three different models including the NACA 0012 aerofoil that is integrated into the flat, pitched, and curved roof building. Spring constant value of 850 (n-m/rad) was applied to the 1 degree-of-freedom (DOF) solver.

5.3.3.1.1 Aerofoil pitch angle

The dynamic variations of pitch angles for the NACA 0012 aerofoil integrated into flat, pitched, and curved roof buildings at different wind speeds (3 m/s, 6 m/s, and 9 m/s) are shown in Figures 67 (a-c). In Figure 67 (a), it is evident that the NACA 0012 integrated into the curved roof building showed the highest pitch angle, peaking at 1.5 degrees at 10 seconds at 3 m/s wind speed. Conversely, the lowest pitch angle, approximately 0.5 degrees, was observed for the flat roof integration. This discrepancy is attributed to wind flow recirculation around the aerofoil due to the building roof shape and wind shear generated at the flat roof edge. In addition, the 1-degree pitch angle observed for the pitched roof integration results from aerodynamic forces induced by the roof geometry.

At a wind speed of 6 m/s (Figure 67 b), the NACA 0012 integrated into the curved roof building achieved the highest pitch angle of 6 degrees at 6 seconds, while the pitched roof integration attained approximately 4 degrees. Conversely, the flat roof integration demonstrated the lowest pitch angle of 0.3 degrees. In conditions of higher

wind speeds, such as 9 m/s, lower pitch angles are observed due to a reduced spring constant of constant 450 (N·m/rad) and increased oscillation frequency over time compared to lower wind speed scenarios, as shown in in (Figure 67 c). Despite this, the NACA 0012 integrated into the curved roof building still achieved the highest pitch angle, reaching 4 degrees, followed by the pitched roof integration at 3.5 degrees. As anticipated, the flat roof integration yielded the lowest pitch angle, influenced by the roof shape and placement of the aerofoil within the flat roof structure.

The observation of varying pitch angle at different wind speeds highlights the effect of roof shapes and wind speed. The NACA 0012 aerofoil integrated into the building roof exhibited uneven pitch oscillation patterns. During the initial flow time (0 to 3 seconds), the oscillations were similar to those observed with NACA 0012 on flat and pitched roofs. However, as wind speed increased, the airflow attachment to the building roof caused significant displacement, which leads to oscillations that initially slowed down and then increased again. This difference is attributed to the complex interaction between the wind flow and the building structure, which affects the aerofoil's performance and underscores the need for further investigation into optimising pitch oscillations for enhanced efficiency.

Also, the need for precise tuning of the spring constant in the oscillating aerofoil system. For a wind speed of 9 m/s, the spring constant was adjusted to 450 N·m/rad to optimise performance, compared to 850 N·m/rad at 3 m/s and 650 N·m/rad at 6 m/s. This adjustment illustrates the significant impact of the spring constant on pitch oscillations and emphasises the necessity for future studies to fine-tune these parameters to achieve optimal performance in wind energy harvesting systems integrated into building roof structures.

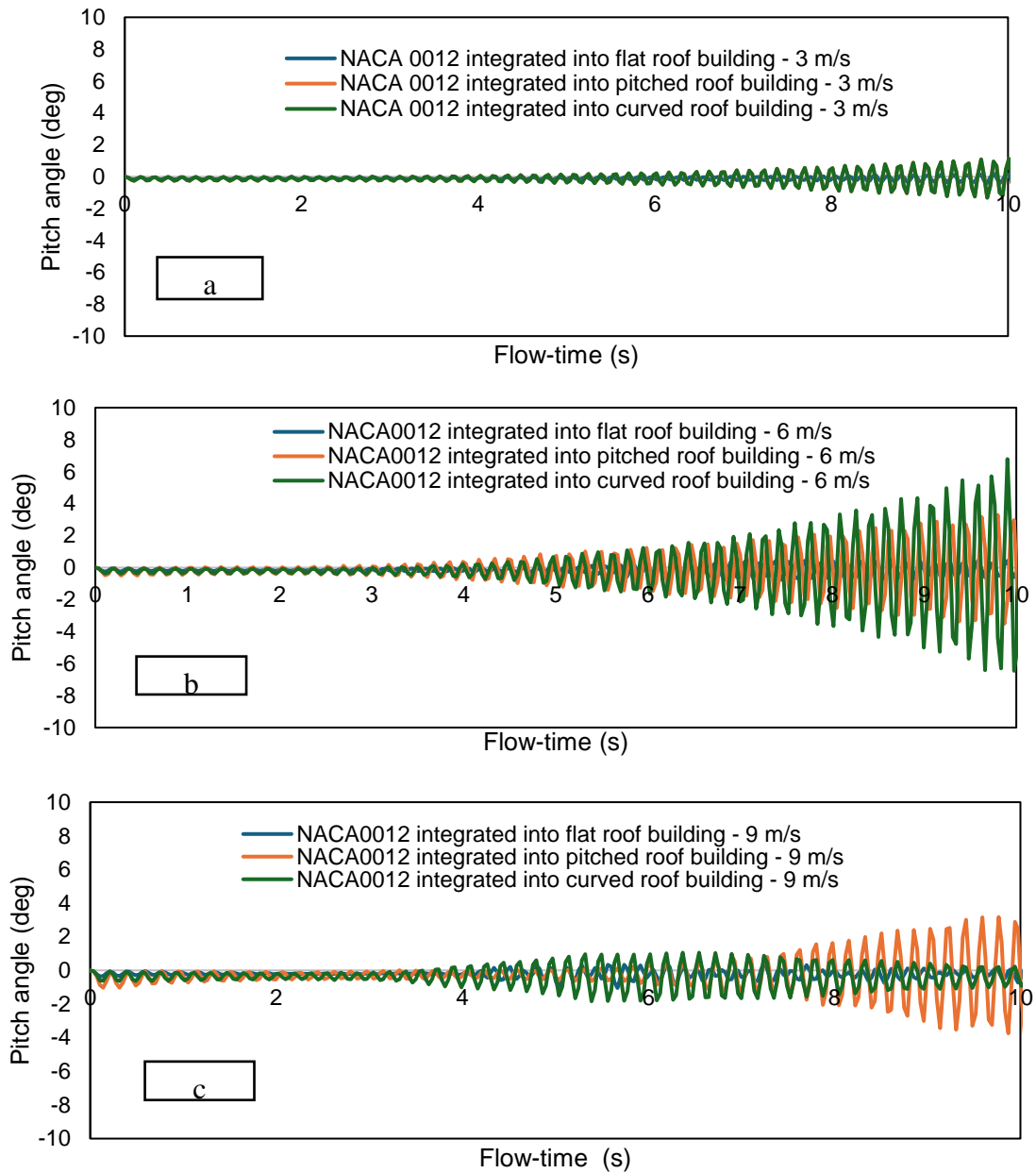


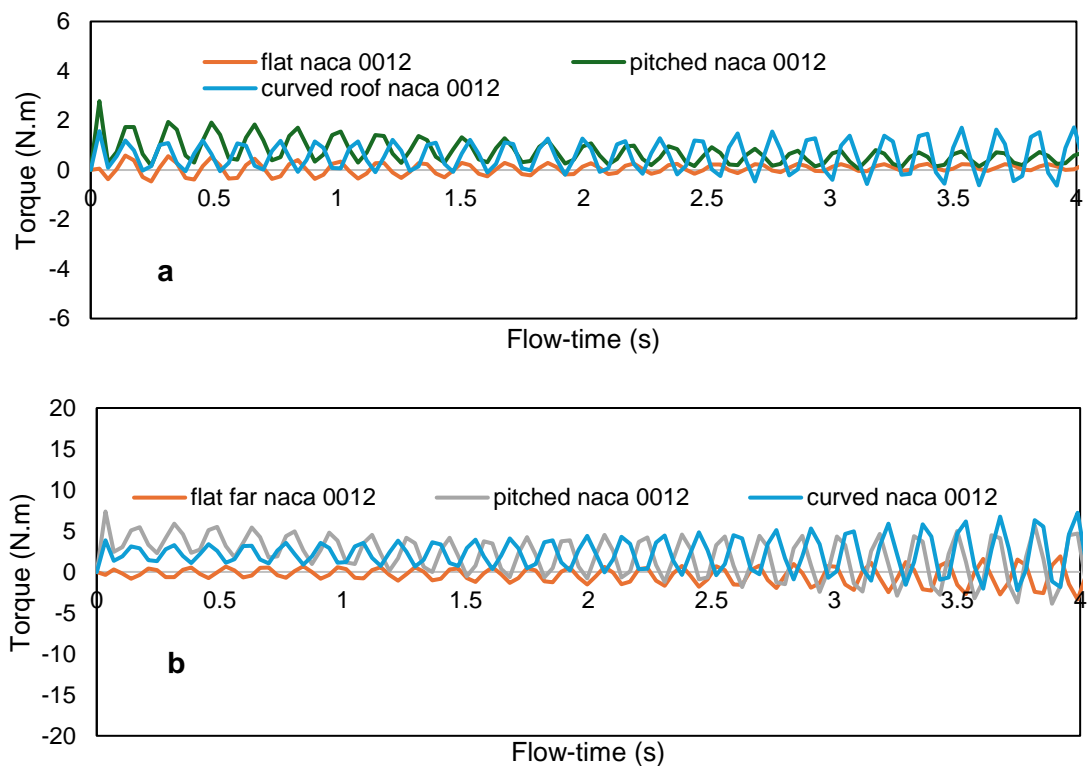
Figure 67. Comparison of pitch angle for an oscillating aerofoil with the NACA 0012 profile integrated into (a) flat, (b) pitched, and (c) curved roof building at 3 m/s, 6 m/s, and 9 m/s

5.3.3.1.2 Torque and angular velocity of NACA 0012 integrated into the building roof

Figure 68 (a) demonstrates the torque behaviour between an oscillating aerofoil with the NACA 0012 profile integrated into a flat, pitched, and curved roof at 3 m/s. From the results, it can clearly be observed that roof shapes can affect the torque behaviour in the same wind speed. The aerofoil integrated into the curved roof building achieved

the highest torque values, while the least values were seen from NACA 0012 installed into the flat roof building. While in Figure 68 (b), the three different parameters were also simulated but in a higher wind speed, which was at 6 m/s. The findings suggest that installing the oscillating aerofoil with the NACA 0012 profile integrated into pitched and curved roof buildings also increases torque values in the same conditions and settings. The integration of an oscillating NACA 0012 on a curved and pitched roof structure demonstrated improved performance compared to a flat roof structure. These results indicate that the roof shape affects the performance of the oscillating aerofoil.

At an increased wind speed of 9 m/s, as shown in Figure 68 (c), it demonstrates the torque values increased as compared to a lower wind speed of 6 m/s. The NACA 0012 integrated into flat roof showed low performance as compared to pitched and curved roof. The maximum torque value achieved by the oscillating aerofoil with the NACA 0012 profile integrated into pitched roof building was 53 N.m in an average of 3 N.m. While the oscillating NACA 0012 aerofoil integrated into the curved roof building demonstrated a maximum torque value of 70 N.m in an average of 5 N.m.



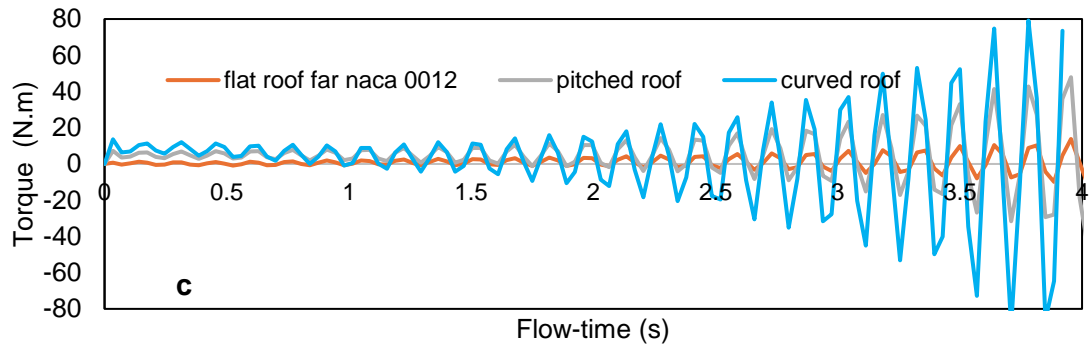


Figure 68. Comparison of the torque between an oscillating aerofoil integrated into flat, pitched, and curved roof at (a) 3, (b) 6, and (c) 9 m/s

The angular velocity graph shows that the curved roof NACA 0012 achieved the highest value in different wind speed such as 3, 6, and 9 m/s. The reason for this was the roof shape, the curved roof is known to have a higher acceleration rate of velocity magnitude as compared to the flat and pitched roof building. The angular velocity (ω) was calculated at the rate of angular displacement divided by the change in time, as shown in (5.1). Figure 69 demonstrates the comparison of angular velocity between different parameters including NACA 0012 installed into flat, pitched, and curved roof building structures in Figure 69 (a) 3 m/s, (b) 6 m/s, and (c) 9 m/s.

A comparison of the values demonstrates a considerable variation between the flat and curved roof structures integrated with an oscillating aerofoil. This difference arises from the fluctuations in the pitch oscillation pattern over time. The pitch oscillations observed for the aerofoil integrated into a flat roof structure were comparatively lower than those experienced on a curved roof structure integrating an oscillating NACA 0012 aerofoil. This difference is attributed to the flat roof building not encountering the same level of increased wind speed as the curved roof structure.

$$(5.1) \quad \omega = \frac{\Delta\theta}{\Delta t}$$

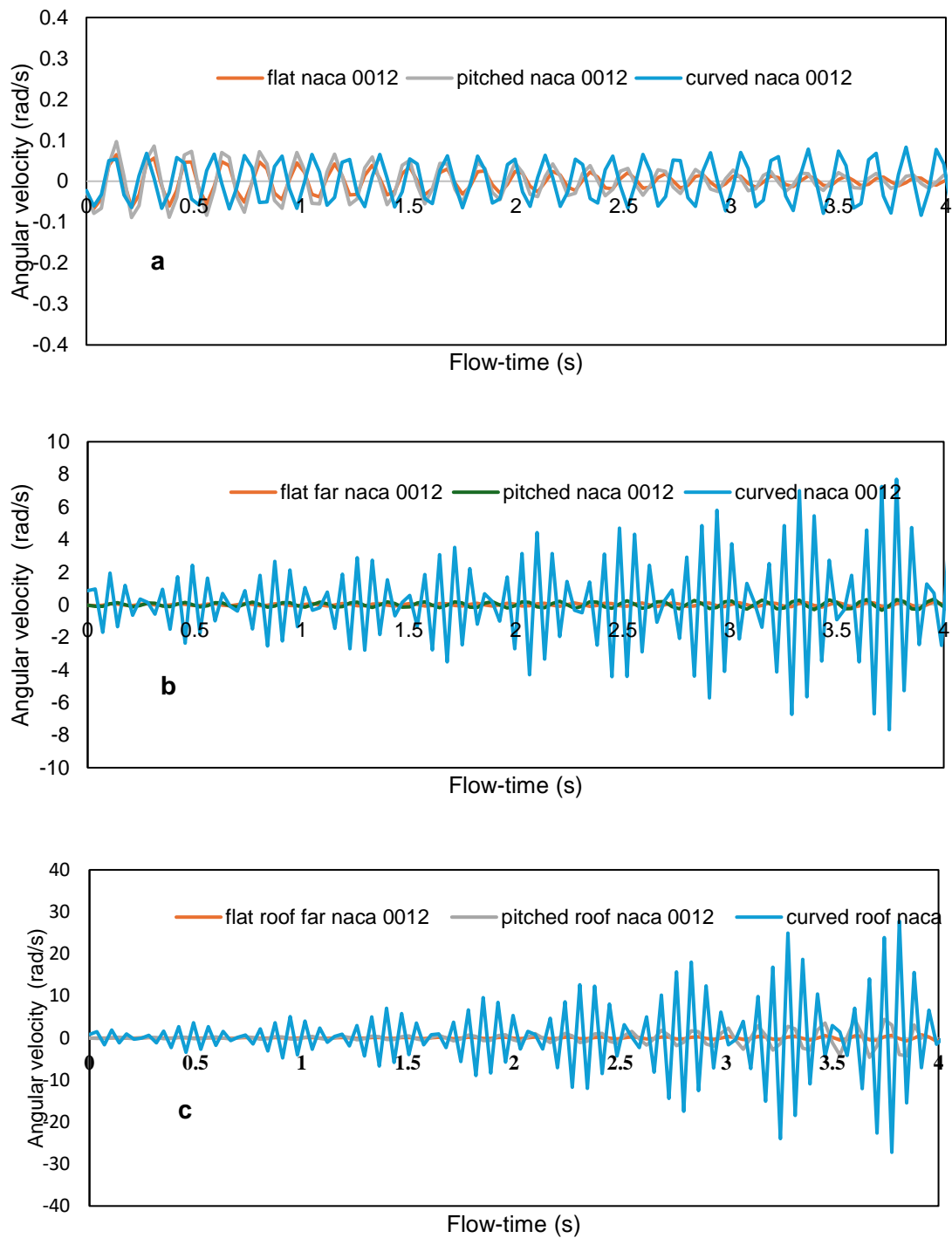


Figure 69. Comparison of the angular velocity between an oscillating aerofoil integrated into flat, pitched, and curved roof at (a) 3, (b) 6, and (c) 9 m/s

5.3.3.1.3 Effects on mechanical power output of NACA 0012 integrated into the building roof

Figure 70 (a) illustrates the average power output for three different parameters including oscillating NACA 0012 aerofoil with 1 metre chord length and span

integrated into flat, pitched, and curved roof structures at 3, 6, and 9 m/s. While Figure 70 (b) demonstrates the average output for three different models in different wind directions. The stabilisation of power calculation in wind energy systems signifies the point where power output levels off, reaching a consistent and steady value with minimal fluctuation. This stabilisation coincides with a similar steadying of wind speed, indicating a consistent state of power generation. The recorded period, commencing from the initiation of the first oscillation and extending from 0.035 to 20 flow time, encapsulates wind speed variations and their impact on power generation within this timeframe. Analysing power output during this recorded period provides valuable insights into how wind speed fluctuations influence power generation and reveals the point at which power stabilises within the specified flow time. Understanding this stabilisation concerning wind speed fluctuations is important for evaluating wind energy harvesting system performance, ensuring safe and efficient operation, and optimising energy production within wind energy systems.

Figure 70 (a) illustrates the impact of wind speed on the mechanical power output performance of an oscillating aerofoil wind energy harvesting system integrated into the building roof structure. From the results, it demonstrates the curved roof configuration, integrated with the oscillating NACA 0012 aerofoil, yielded the highest average mechanical power output across three different speeds. Specifically, the integration of the oscillating aerofoil into the curved roof structure demonstrated the most substantial average power output, reaching 12 W, contrasting with the lowest values observed for the oscillating NACA 0012 aerofoil integrated into the flat roof (1.02 W) and the NACA 0012 installed on a pitched roof (8.64 W) in higher wind speed of 9 m/s. These findings highlight the significant impact of wind speed, roof shape and aerofoil placement on the power efficiency of the proposed design. This translates to an increase of approximately 12 times increase in power output when comparing the curved roof to the flat roof.

Conversely, comparing the power output between the pitched roof configuration and the curved roof configuration at the same wind speed, the pitched roof generated 8.64 watts, whereas the curved roof produced 12 watts. This indicates a notable increase of

approximately 1.5 times increase in power output for the curved roof compared to the pitched roof. These comparisons emphasise the significant advantage of utilising a curved roof configuration with the oscillating NACA 0012 aerofoil for wind energy harvesting. The curved roof demonstrates substantial advantage over both flat and pitched roof configurations in terms of power extraction efficiency at 9 m/s, highlighting the importance of design optimisation for maximising energy output in wind energy systems.

Overall, the observed increase in power output between flat, pitched, and curved roof configurations are due to different factors including changes in wind speed, recirculation phenomena, wind shear effects, roof shape, and the placement of the aerofoil within the building roof structure. From low to higher wind speeds, these factors show differently across roof configurations. In flat roof setups, recirculation of wind flow around the oscillating aerofoil and wind shear at the roof edge hinder energy harvesting efficiency. Similarly, pitched roof structures experienced wind speed acceleration at the windward side of the roof, but they also exhibit wind flow loss and recirculation, which are unfavourable to efficient energy extraction. In contrast, the aerodynamic design of curved roofs facilitates smoother wind flow attachment, minimising recirculation, and optimising wind energy utilisation. This streamlined flow enhances the performance of the oscillating aerofoil, resulting in significantly higher power output compared to flat and pitched roofs. The placement of the aerofoil within the building roof further influences aerodynamic performance, highlighting the critical role of wind speed, roof shape and aerofoil positioning in maximising wind energy extraction efficiency.

5.4 Impact of wind directions

As shown in Figure 70 (b), an examination was conducted to assess how various wind directions affect the power output of an oscillating aerofoil with the NACA 0012 profile integrated into building's roof. A sensitivity analysis was performed on the power output, considering three parameters: the NACA 0012 profile, installed in three distinct roof shapes including flat, pitched, and curved. Simulations were conducted for four different wind directions (0 degrees, 10 degrees, 15 degrees, and 25 degrees) at 3 m/s. The study aimed to explore the effect of changes in wind direction on the power output efficiency of the NACA 0012 aerofoil in diverse roof structures,

including flat, pitched, and curved designs. The findings offer valuable insights into the aerodynamic behaviour and potential for power generation. Notably, critical observations highlight the impact of wind direction in determining power output. Specifically, a decline in power output was observed starting at 15 degrees and persisting up to 25 degrees of wind direction, highlighting the significance of the angle of wind incidence on power generation.

The mechanical power output of an oscillating aerofoil integrated into a flat roof structure varies significantly with changes in wind direction. At a wind direction of 0 degrees, the flat roof configuration generates a power output of 0.2 watts. However, as the wind direction shifts to 10 degrees, the power output decreases to 0.1 watt. Further changes in wind direction to 15 degrees result in a power output of 0.05 watt, and at 25 degrees, the output drops dramatically to 0.0001 watts. This steep decline indicates a substantial sensitivity to wind direction, with optimal performance occurring when the wind is perpendicular to the roof surface.

While for the NACA 0012 integrated into the pitched roof building, it demonstrated higher mechanical power output as compared to the flat roof but also exhibits a pronounced decrease with changing wind direction. At 0 degrees, the power output is 6.2 watts, which drops to 3 watts at 10 degrees. At 15 degrees, the power output drops to 0.001 watt, and at 25 degrees, it further reduces to 0.0001 watts. This significant drop at higher angles suggests that the pitched roof configuration is highly efficient at optimal wind alignment but loses effectiveness rapidly as the wind direction deviates.

In the case of the NACA 0012 integrated into the curved roof building, it demonstrates the highest mechanical power output and maintains better performance across varying wind directions. At 0 degrees, the curved roof generates 6.8 watts. When the wind direction changes to 10 degrees, the output decreases to 3.8 watts, and at 15 degrees, it further reduces to 0.002 watts. At 25 degrees, the power output is 0.0002 watts. Although there is a decline in power output with increasing wind angle, the curved roof configuration retains a relatively higher efficiency compared to the flat and pitched roofs, indicating its superior adaptability to varying wind directions.

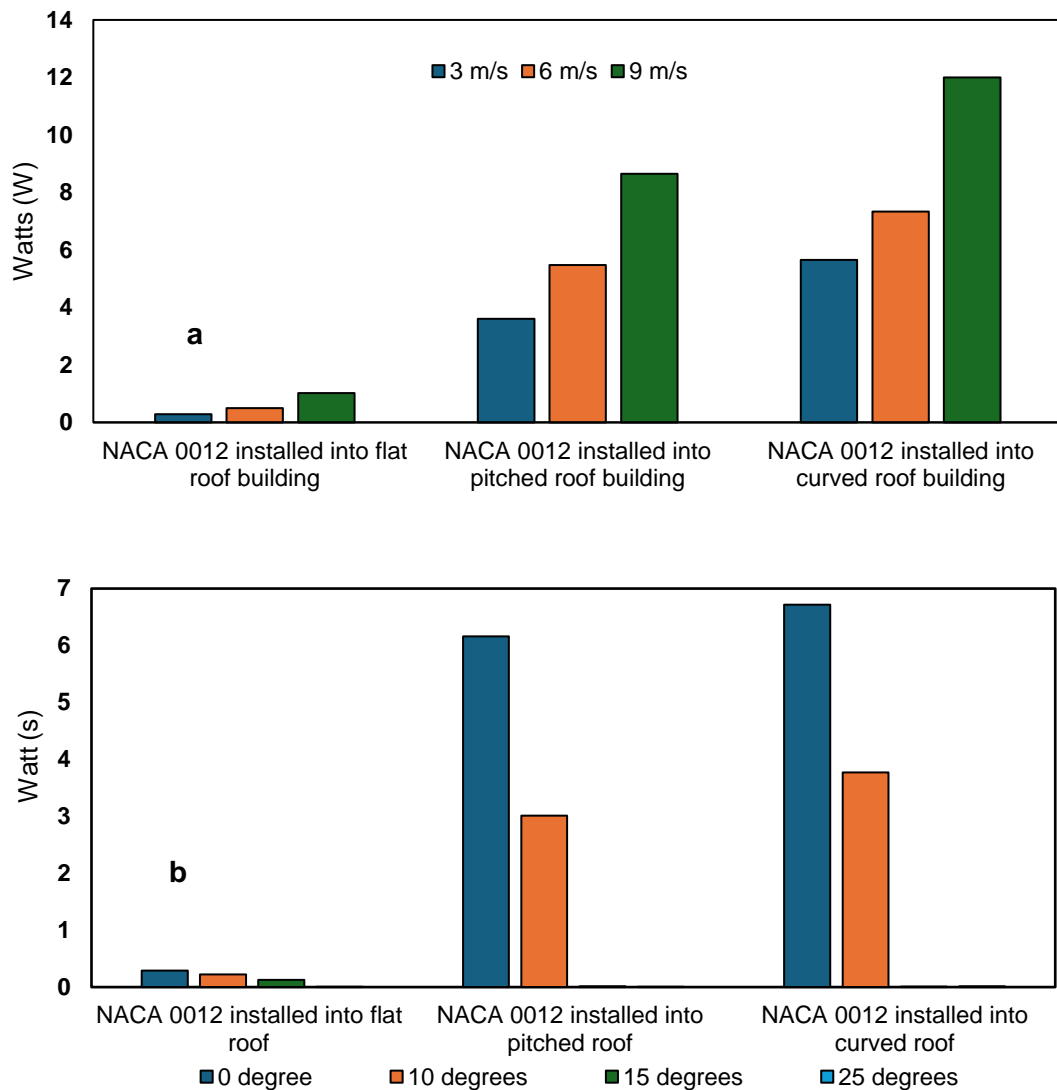


Figure 70. Average power output for three different models at different (a) wind speeds and (b) wind directions

Overall, the mechanical power output of the oscillating aerofoil was highest when integrated with curved roof structures and affected by changes in wind direction across all roof types. Flat roofs show the least power output and highest sensitivity to wind direction changes, while pitched roofs have better initial performance but suffer steep declines at off-optimal wind angles. Curved roofs, although also affected by wind direction demonstrate the most stable performance across varying angles that makes them the most effective design for maintaining mechanical power output in diverse wind conditions.

This understanding is crucial for optimising the placement and orientation of an oscillating aerofoil wind energy harvesting system on various roof structures, ultimately enhancing overall power efficiency. The results obtained from various roof structures, specifically the contrasting performance between flat, pitched, and curved roofs, highlight the critical role of a building's architecture in wind energy generation. Flat roofs show inefficiencies due to wind recirculation and shear effects, emphasising the need for strategic placement to mitigate these drawbacks. In contrast, pitched and curved roofs demonstrate improved power output, capitalising on wind speed acceleration facilitated by their design. This highlights the potential for enhancing wind energy utilisation by aligning the oscillating aerofoil wind energy harvesting design and placement with the building's structure. Furthermore, the positioning and angle of attack of integrated aerofoils relative to wind direction significantly influence system performance.

5.5 Impact of adjacent building

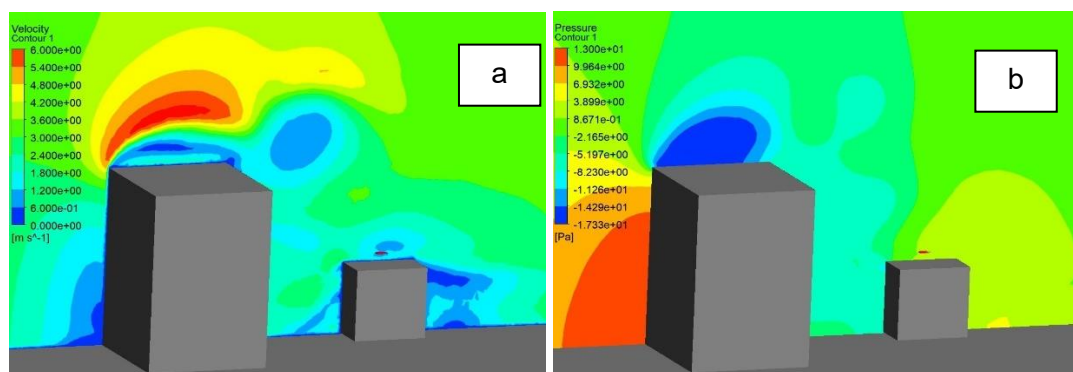
This section investigates the wind flow behaviour that examines the velocity magnitude and static pressure through contour representations for different building configurations. These configurations include flat, pitched, and curved roofs, each accompanied by an adjacent building structure. The objective is to gain insights into how adjacent building structure influence airflow patterns.

Figure 71 shows velocity magnitude contours for adjacent building and (a) flat, (c) pitched, and (e) curved roof building and static pressure contours for (b) flat (d) pitched, and (f) curved roof building structure at 3 m/s. In Figure 71 (a, c, e) a significant recirculation from the taller building can be observed, which extends towards the oscillating aerofoil integrated into the flat roof building. This phenomenon adversely affects the efficiency of the oscillating wind energy harvesting system. For Figure 71 (b, d, f) demonstrates the static pressure contours. It shows the significant recirculation patterns induced by adjacent buildings, which adversely affecting airflow dynamics, and consequently reducing the efficiency of wind energy harvesting systems integrated into these structures. In the scenario where an oscillating aerofoil is integrated into the pitched roof building, similar wind shear patterns are observed due

to the presence of the adjacent building. The airflow remains somewhat attached to the windward side but loses attachment on the leeward side of the pitched roof building.

The static pressure variations illustrate in Figure 71 (b, d, f) airflow detachment on the leeward side was influenced by the presence of neighbouring structures. This detachment leads to decreased static pressure and potential inefficiencies in wind energy harvesting, particularly where airflow separation occurs. Similarly, when an oscillating aerofoil is integrated into the curved roof building, comparable behaviour to the pitched roof scenario was observed. However, in this case, the wind flow remains significantly attached to both the windward and leeward sides of the building.

The presence of the adjacent building influences the airflow behaviour, resulting in a detrimental effect on wind energy harvesting, which is known as the wind shadow effect. In addition, the static pressure analysis for curved roof buildings shows more favourable airflow attachment characteristics, with airflow remaining attached on both the windward and leeward sides of the building. Despite the influence of neighbouring structures, the curved roof configuration demonstrates more promising static pressure distributions, potentially enhancing the efficiency of wind energy systems integrated into the building design. Among the analysed cases, the integration of the oscillating aerofoil into the curved roof building shows more favourable wind flow characteristics for wind energy harvesting compared to the other configurations.



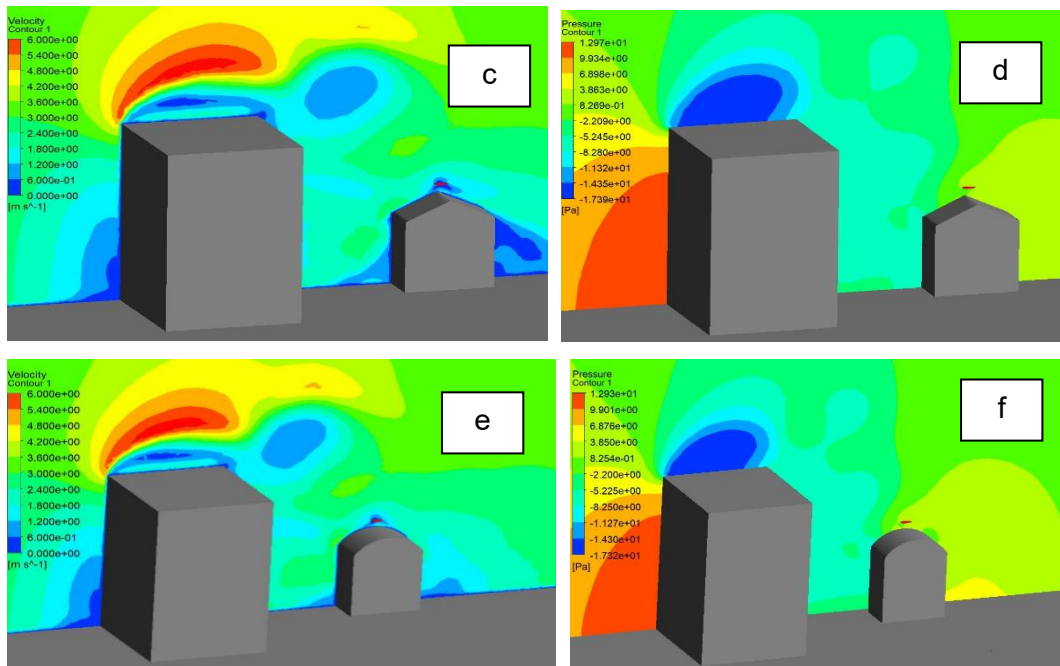


Figure 71. Velocity magnitude contours for adjacent building and (a) flat, (c) pitched, and (e) curved roof building and static pressure contours for (b) flat (d) pitched, and (f) curved roof building structure

Figure 72 shows the average mechanical power output for scenarios with the oscillating NACA 0012 aerofoil integrated into flat, pitched, and curved roof with and without an adjacent building at a wind speed of 3 m/s. The results indicate that the presence of a wind shadow significantly affects the performance of the aerofoil wind energy harvesting system and the building roof structure. The mechanical power output is generally low with the highest power reaching only 0.004 watts. However, when the NACA 0012 is integrated into curved and pitched roof buildings without an adjacent building, it produces useful power. Specifically, the curved roof design generated 5.6 watts, while the pitched roof design achieved 3.6 watts. In contrast, the flat roof design underperformed, yielding only 0.28 watts that was attributed to the incorrect placement of the aerofoil on the flat roof.

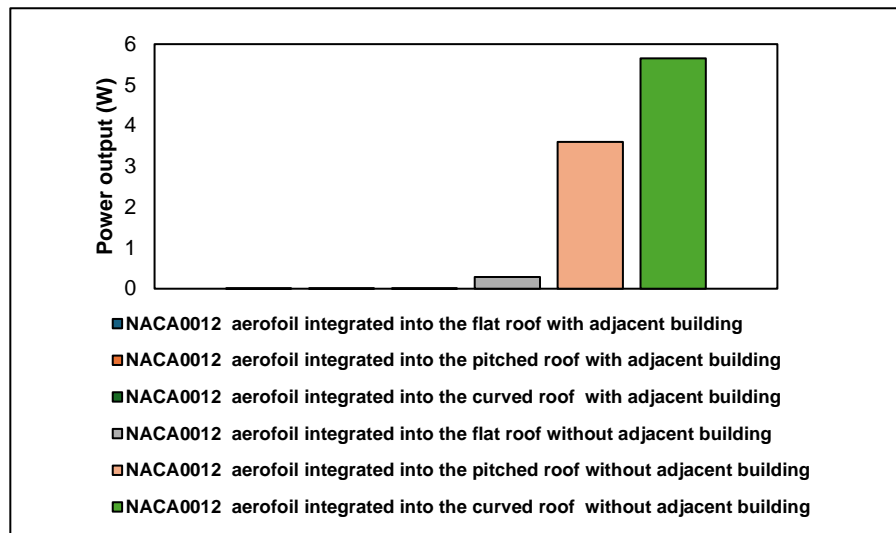


Figure 72. Comparison of average predicted power output for a NACA 0012 aerofoil integrated into two different roof shapes with and without the presence of an adjacent building.

5.6 Case study for Basilan - Philippines

The study conducted an in-depth analysis using hourly wind data from the Copernicus Marine Service (CMEMS) [188] for January 1, 2021, focusing on a rural area in Basilan, Philippines. This location is characterised by low wind speeds, served as an optimal setting to evaluate the effectiveness of a wind energy harvesting system integrated into a building's roof. The wind data pertains to a rural setting in the Philippines, featuring low wind speeds including the range of 0 to 7 m/s. The average wind speed for a 24-hour period stands at 3.53 m/s. Employing CFD simulations, the investigation examined the behaviour of an oscillating NACA 0012 aerofoil across three distinct roof shapes, including flat, pitched, and curved. The CFD model maintained consistency by employing identical dimensions for the aerofoil, building roof structure, and the computational domain.

The choice of a rural area was driven by smoother wind flows with reduced turbulence, which is primarily due to the absence of large obstructions and complex topography enhance the stability and performance of wind energy harvesting technologies. Moreover, the topography does play a significant role in determining wind flow characteristics. In rural areas, the landscape is often more uniform and less developed,

leading to less interference with wind flow. This lack of obstructions, such as dense urban infrastructure allows wind to flow more freely and consistently, which results in smoother wind conditions.

Figure 73 demonstrates the predicted power output from oscillating aerofoils in different roof shapes reveals significant trends. The curved roof design demonstrated the highest power output, reaching nearly 10 watts at 4:00 am, which aligns with earlier observations of higher static pressure at its windward edges. In contrast, the flat roof showed the lowest power output, attributed to challenges such as wind shear and recirculation around the aerofoil. The temporal aspect introduces a dynamic element, emphasising the need to optimise energy capture by aligning system performance with fluctuating wind conditions throughout the day. Another rise of power output was observed at around 13:00 to 14:00, which achieved apparently because of the higher wind speed observed from 6:00 to 12:00. Overall, the Figure 73 provides a comprehensive understanding of how roof geometry, aerodynamics, and temporal dynamics collectively influence the predicted power output of oscillating aerofoil wind energy conversion systems in a rural setting.

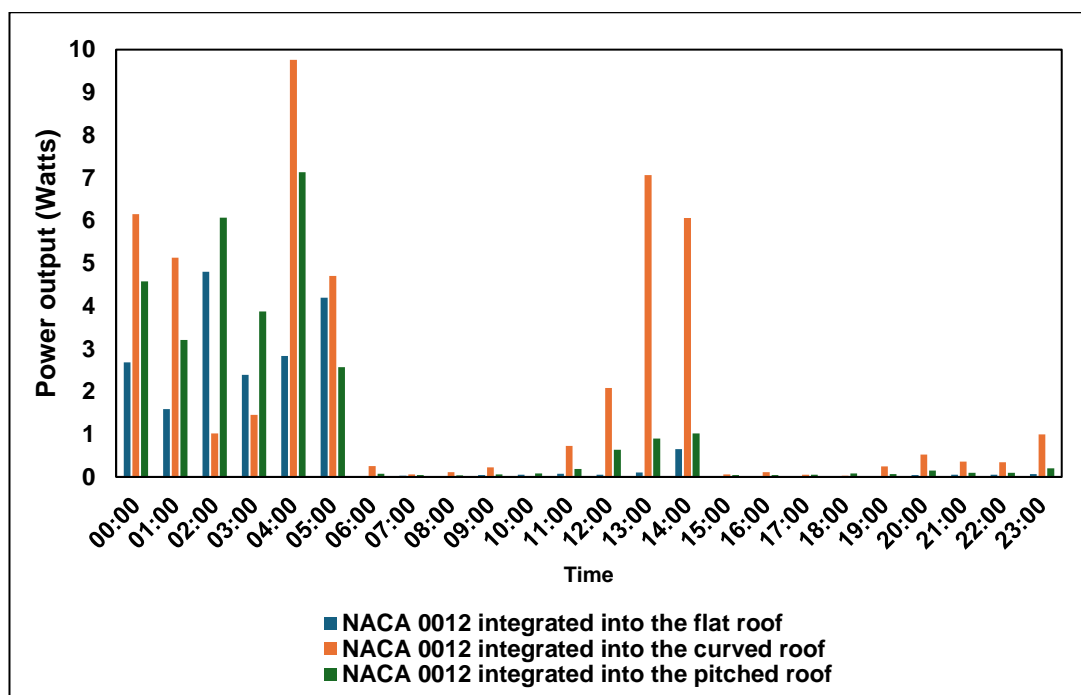


Figure 73. Average predicted power output for 1 day wind data on January 1, 2021

5.7 Power Spectral Density vs Frequency

The Power Spectral Density (PSD) vs frequency plot offers valuable insights into the behaviour of an oscillating aerofoil integrated into a pitched roof building structure in varying wind speeds. This plot illustrates how the distribution of power across different frequencies reflects changes in aerodynamic forces acting on the aerofoil. Understanding the PSD plot provides information about the dynamics of the aerofoil response to wind, which aids in the design and optimisation of structures for improved performance and safety. In summary, the PSD vs frequency plot provides insights into how the aerodynamic forces acting on the oscillating aerofoil integrated into the building roof structure vary with wind speed, which shows the frequency content and intensity of these forces at different wind speeds.

Figure 74 (a-c) shows the PSD vs frequency in three different wind speeds including 3 m/s, 6 m/s, and 9 m/s for the three design parameters of an oscillating aerofoil integrated into the flat, pitched, and curved roof building. In Figure 74 (b and c), these presents a low value of PSD against frequency, and its peak can be observed at 5.8 Hz in 9 m/s for both NACA 0012 integrated into the pitched and curved roof building. While in Figure 74 (a), a very unstable PSD behaviour can be observed from 0 Hz to 8 Hz for NACA 0012 integrated into the flat roof building. In this case (flat), a constant 850 (n-m/rad) for 3 m/s wind speed and 450 (n-m/rad) for 9 m/s wind speed, it indicates that the system has higher damping at 3 m/s. This higher damping would suppress oscillations more effectively, resulting in a lower amplitude of response overall. Therefore, despite the higher wind speed at 9 m/s, the lower damping allows for more significant oscillations and potentially higher peaks in the PSD vs frequency plot compared to the 3 m/s wind speed, where higher damping suppresses oscillations and reduces the peak in the PSD plot.

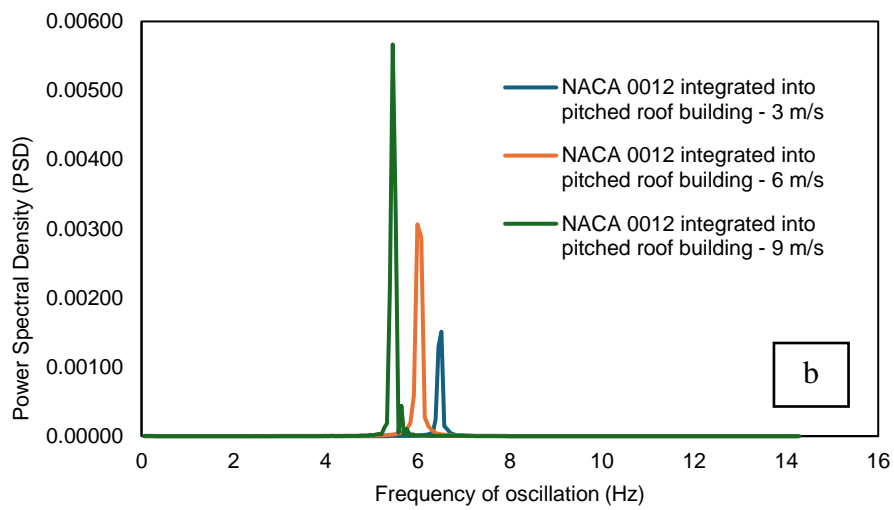
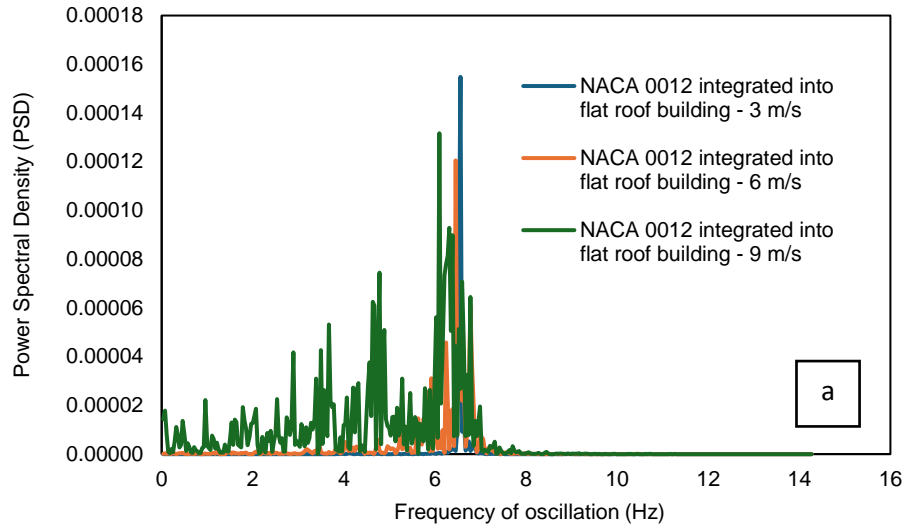
Reducing the spring constant from constant 850 (n-m/rad) to 450 (n-m/rad) to maintain stability at higher wind speeds is a reasonable engineering decision aimed at ensuring the overall performance and safety of the system. Through decreasing the stiffness of the system, engineers can enhance its ability to absorb energy from wind-induced vibrations and mitigate the risk of instability or excessive oscillations. This adjustment allows for greater flexibility and damping, which can improve the dynamic response

of the system and prevent it from reaching critical levels of instability as wind speeds increase. While this approach addresses the immediate concern of stability at higher wind speeds, engineers must carefully consider potential trade-offs in the system's response to lower wind speeds and its overall structural integrity. Through modelling and simulation studies, engineers can analyse the behaviour of the system in various conditions and optimise design parameters to achieve an optimal balance between stability, dynamic response, and structural integrity.

The Power Spectral Density (PSD) value of 0.0059 achieved at 9 m/s for the oscillating aerofoil NACA 0012 integrated into the curved roof building indicates the intensity of the aerodynamic forces experienced by the aerofoil. This higher PSD value suggests that at this wind speed, the aerofoil is subjected to significant fluctuations in aerodynamic forces, which is due to the interaction between the aerofoil shape and the curved roof structure. On the other hand, achieving a nearly identical PSD value of 0.0058 for the oscillating aerofoil NACA 0012 integrated into the pitched roof building suggests that despite differences in the building, the aerodynamic forces experienced by the aerofoil are comparable between the two configurations. This implies that factors other than the roof shape, such as the angle of attack, wind flow patterns, or turbulence, can also play significant roles in determining the aerodynamic response of the aerofoil. Further analysis would be needed to explain the specific mechanisms behind these observations and their implications for the design and performance of the integrated aerofoil systems.

While the lowest value was achieved by the PSD value of less than 0.00002 achieved at 6 m/s for the oscillating aerofoil NACA 0012 integrated into the flat roof building, this indicates relatively lower intensity of aerodynamic forces compared to the other roof configurations, as shown in Figure 74 (a). The difference in PSD values among the three roof types suggests varying degrees of aerodynamic interaction between the aerofoil and the different roof structures. The higher PSD values for the curved and pitched roof buildings suggest potentially more complex airflow patterns and greater aerodynamic loading on the aerofoil compared to the flat roof configuration. However, the nearly identical PSD values of 0.0059 and 0.0058 for the curved and pitched roof buildings at the same wind speed indicate similar aerodynamic responses despite their structural differences, as shown in Figure 74 (b-c). This implies that factors beyond

roof shape, such as angle of attack, wind flow patterns, or turbulence, may significantly influence the aerodynamic behaviour of the integrated aerofoil systems. Further investigation into these factors is essential for optimising the design and performance of such integrated systems in various architectural contexts.



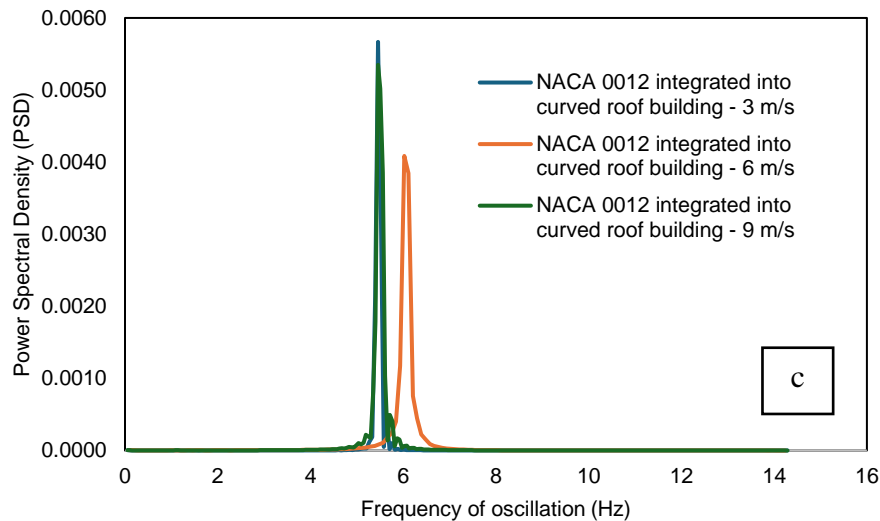


Figure 74. Power Spectral Density vs Frequency NACA 0012 integrated into (a) flat, (b) pitched, and (c) curved roof building at 3 m/s, 6 m/s, and 9 m/s

5.8 Impact of SD7003 aerofoil shape on different roof configuration

Different aerofoil is introduced in this section to see its dynamic behaviour and potential mechanical power output when integrated into the building roof structure. The SD7003 low Reynolds number aerofoil was chosen as it is recognised for their optimal performance at lower speeds, which makes them suitable for areas with low wind speeds, such as rural or urban environments. These aerofoils offer advantages such as an early onset of lift, enabling power generation at lower wind speeds, and a reduced stall speed, which allows continued operation near stall conditions. Moreover, these aerofoils can perform well in turbulent conditions, which are common in urban and rural areas. In addition, these aerofoils adapt to varied wind directions, crucial in areas with complex wind patterns influenced by structures. These aerofoils can also contribute to higher start-up torque, facilitating power generation at lower wind speeds, which is beneficial in regions with intermittent or variable wind conditions.

The dynamic behaviour of the SD7003 including torque and angular velocity will be explored to predict power output for an oscillating aerofoil in a building roof structure. Fluid-structure interaction will be analysed through contours of velocity magnitude and static pressure at different time steps. Figure 75 shows the (a) 3D dimensional SD7003 aerofoil profile and three roof shapes including (b) flat, (c) pitched and (d) curved roof building was created in Designmodeler and Spaceclaim ANSYS software.

The schematic is similar to NACA 0012 aerofoil discussed in section 5.3. Table 14 outlines the investigated parameters and material properties for the SD7003 aerofoil profile at low Reynolds numbers.

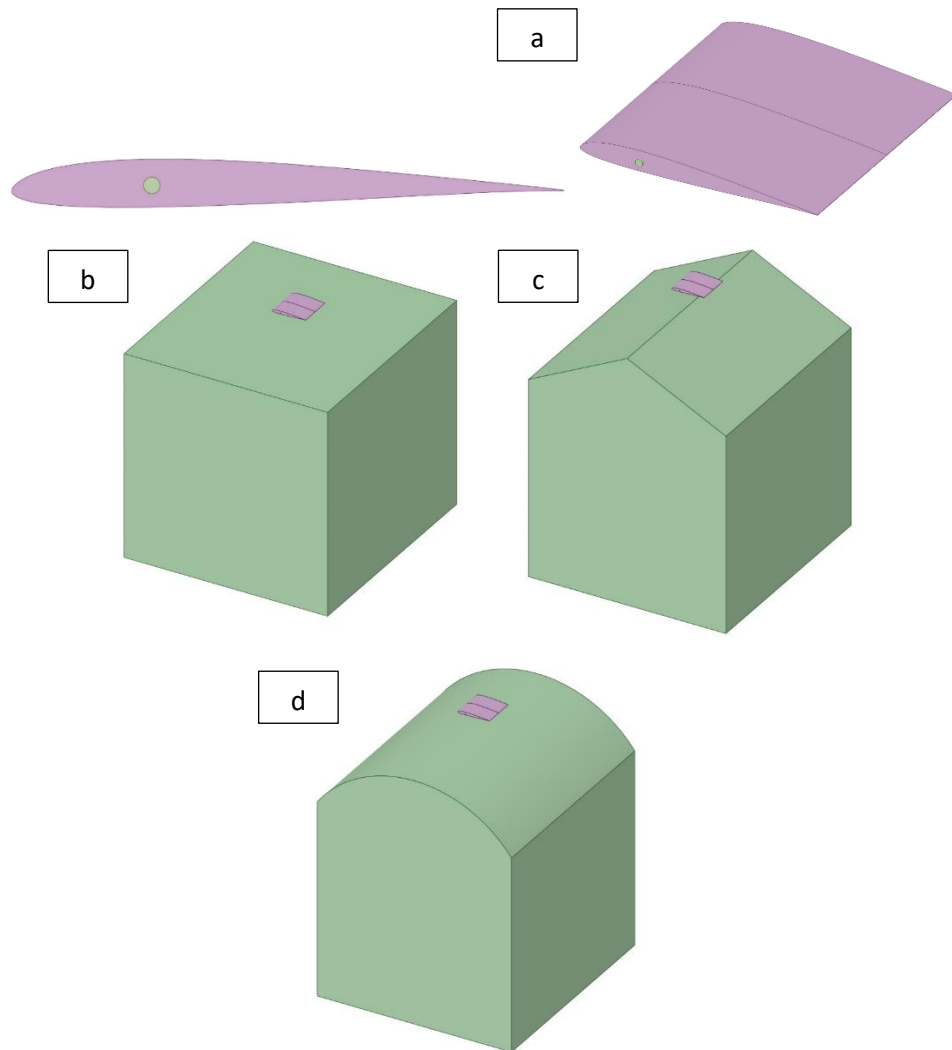


Figure 75. 3D model of (a) non-symmetrical SD7003 aerofoil integrated into the (b) flat, (c) pitched, and (d) curved roof building

Table 14. Parameters and material properties of SD7003 aerofoil profile

Case (s)	Aerofoil profile	Roof shape	Distance between aerofoil and rooftop	Dimension	Material	Mass (kg)	Moment of inertia (kg.m ²)	Centre of rotation (m)
1	SD7003	Flat	600 mm	1 m chord length and 1m span	Foam	2.137	0.12	0.25 m of chord length
2		Pitched						
3		Curved						

5.8.1 Velocity magnitude and static pressure contours for SD7003 integrated into the flat roof at 3 m/s

Figure 76 (a) shows the velocity magnitude contours showed the fluid-structure interaction of SD7003 integrated into the flat roof building. Notably, the wind shear and recirculation patterns in the flow above the flat roof are identified. It is observed that the current placement of the aerofoil within the flat roof building fails to appropriately capture the wind speed acceleration. This inadequacy is attributed to the suboptimal positioning of the aerofoil within the architectural configuration, leading to an inability to effectively harness and amplify the wind speed in the desired manner. The most significant acceleration in wind speed, amounting to a 32.67% increase, is observed from an inlet velocity of 3 m/s to a maximum magnitude of 3.98 m/s. This acceleration is located at the flat roof's edge where the incoming wind is concentrated.

Examining the static pressure distribution alongside the velocity magnitude contours is crucial for gaining insights into the aerodynamic characteristics of a structure, identifying potential areas of lift or drag, and facilitating the design or optimisation of structures for enhanced performance. This analytical approach is supported by existing literature in the field. As illustrated in Figure 76 (b), the analysis reveals notable patterns in static pressure corresponding to specific wind interactions with the flat roof building. Initially, a high static pressure is evident at the windward edge of the flat roof during the initial interaction at 0 seconds. Concurrently, a low static pressure begins to form on the windward side of the flat roof, gradually enveloping the aerofoil as it oscillates under pitch oscillations.

During the oscillations, distinct static pressure variations emerge. At 20 seconds, higher static pressure is observed on the upper side of the aerofoil, contrasting with lower pressure on the lower surface. This dynamic static pressure distribution signifies the complex aerodynamic forces at play during the oscillation process. Moving to 30 seconds, a reverse behaviour is observed, with higher static pressure on the lower surface and lower pressure on the upper surface as the aerofoil continues its pitch oscillations. These findings align with existing literature that emphasises the complex relationship between static pressure distribution and aerodynamic performance during

oscillatory motions. The observed patterns emphasise the importance of considering static pressure in conjunction with velocity magnitude contours for a comprehensive understanding of aerodynamic behaviour over time. Such insights are invaluable for refining designs and optimising structures for sustained and improved performance, as discussed in prior research.

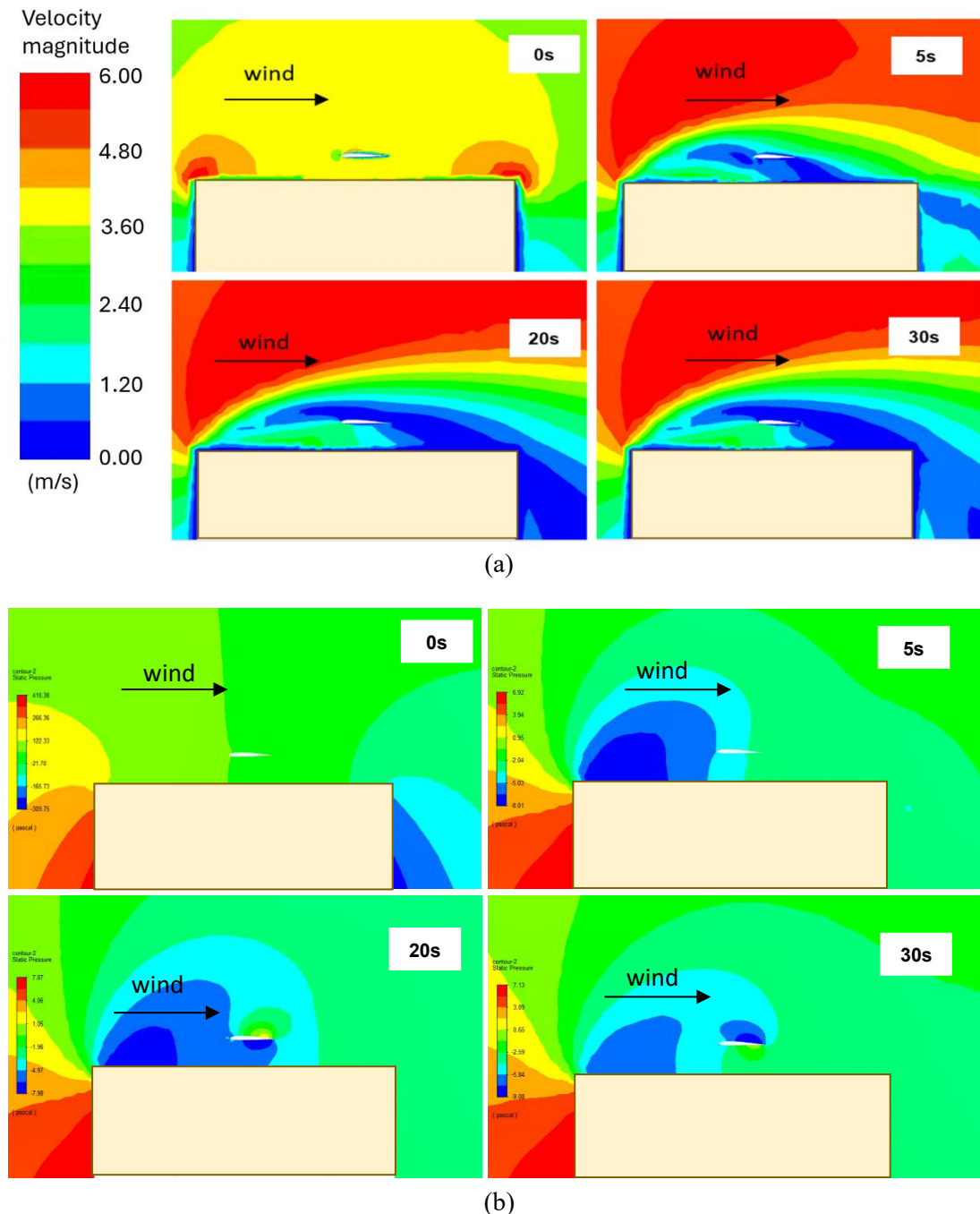


Figure 76. Contours representing (a) velocity magnitude and (b) static pressure for an oscillating aerofoil with the SD7003 profile integrated into flat roof building at 3 m/s for time intervals of 0, 5, 20, and 30 seconds

5.8.2 Velocity magnitude and static pressure contours for SD7003 integrated into the flat roof at 6 m/s

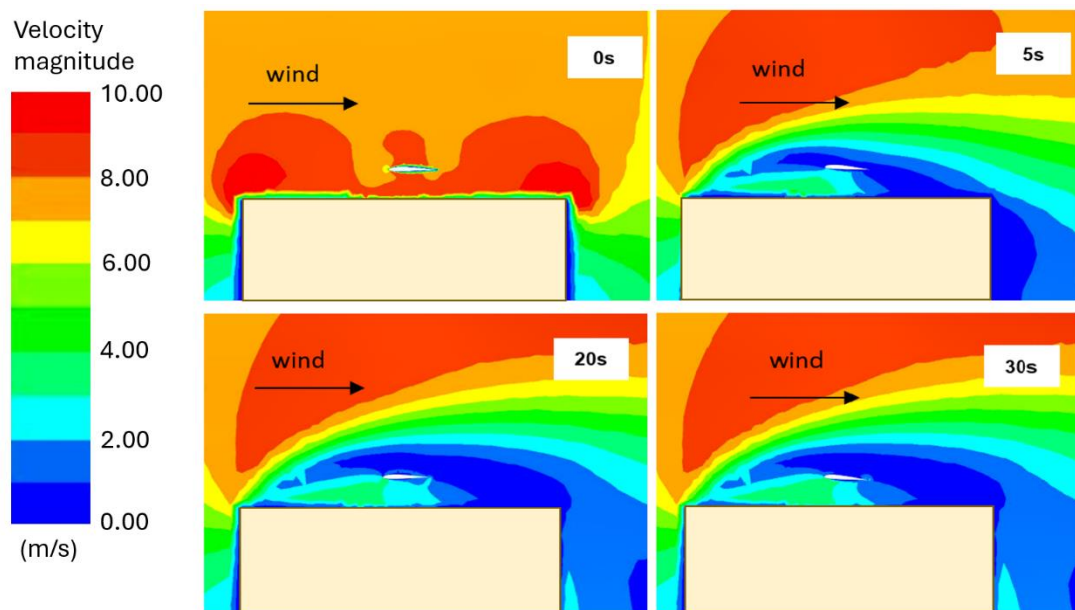
Figure 77 shows a similar configuration with an oscillating SD7003 placed within the flat roof building, maintaining a separation distance of 600 mm from each other. Building upon the insights gained from the previous examination at an inlet velocity of 3 m/s and in line with existing literature, a subsequent analysis was conducted at an increased inlet velocity of 6 m/s. Figure 77 (a) shows the velocity magnitude for the velocity magnitude contours for SD7003 integrated into the flat roof at 6 m/s. The results indicate variations in aerodynamic characteristics. At this higher inlet velocity, distinct issues were identified, including wind shear (directed upwards instead of towards the oscillating aerofoil for wind energy capture), suboptimal placement, and recirculation of the wind flow around the aerofoil. Despite these challenges, there is a notable difference in wind speed acceleration, increasing from 6 m/s to a maximum of 9 m/s. This represents a significant 50% percentage increase in wind speed acceleration.

This finding suggests a potential for harnessing the enhanced wind speed acceleration if the oscillating SD7003 is strategically placed on the rooftop. The implications of this observation align with the broader understanding in existing literature regarding the critical influence of placement on aerodynamic performance and wind energy capture. Considering the outcomes at both 3 m/s and 6 m/s inlet velocities, it becomes evident that the success of wind energy capture is contingent on optimal placement within the architectural configuration. This highlights the importance of future studies to further explore and refine the placement strategies for oscillating aerofoils in rooftop applications, thereby maximising their effectiveness in harnessing wind energy.

Figure 77 (b) shows similar observations in static pressure distribution are noted at the edge of the flat roof where the incoming wind interacts. At the onset, there is apparent high static pressure, transitioning to the development of low static pressure on the windward side of the flat roof at 5 seconds. This evolving low-pressure region progressively surrounds the oscillating aerofoil. The following oscillation sequence

follows a pattern observed in existing literature, where high pressure is evident at the upper surface of the aerofoil, contrasting with low pressure at the lower surface during a specific phase. This dynamic is then reversed, with low pressure at the upper surface and high pressure at the lower surface as the aerofoil continues its oscillations. Connecting these observations to the previously discussed results at 3 m/s wind speed and the ongoing examination at 6 m/s, a consistent theme occurs regarding the complex relationship between velocity magnitude, static pressure distribution, and the aerodynamic behaviour of the system. This emphasises the importance of considering these interrelated factors in the comprehensive analysis of aerofoil performance in different wind conditions.

The insights gained not only contribute to understanding the aerodynamic characteristics at varied wind speeds but also align with established knowledge in the literature. As the study extends to higher wind speeds, these observations provide valuable data for optimising aerofoil placement and harnessing wind energy effectively, echoing the broader context established in existing research.



(a)

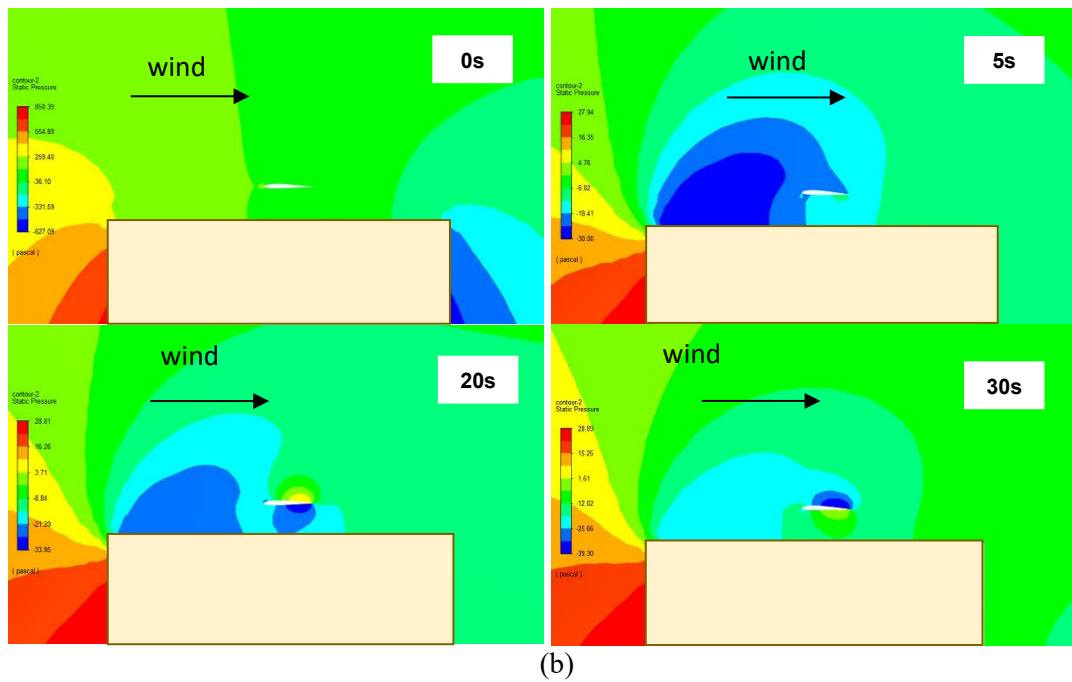


Figure 77. Contours representing (a) velocity magnitude and (b) static pressure for an oscillating aerofoil with the SD7003 profile integrated into flat roof building at 6 m/s for time intervals of 0, 5, 20, and 30 seconds

5.8.3 Velocity magnitude and static pressure contours for SD7003 integrated into the flat roof at 9 m/s

Figure 78 (a) shows the velocity magnitude and static pressure for SD7003 integrated into the flat roof at 9 m/s. Building upon the insights gained from the previous examinations at 3 m/s and 6 m/s, the study further investigates the impact of an increased wind speed, specifically from 6 m/s to 9 m/s. This variation in wind speed reveals a notable wind speed acceleration, with the velocity magnitude escalating from 9 m/s to 13 m/s at different intervals including 0 s, 5 s, 20 s, and 30 s. This corresponds to a substantial 44.44% percentage increase in wind speed acceleration. The comparison with the findings at 6 m/s raises an intriguing observation. Despite the higher wind speed at 9 m/s, the wind speed acceleration at 6 m/s appears to be more favourable, suggesting that the relationship of various factors, such as wind shear and aerofoil placement, plays a crucial role in optimising wind energy capture. This discrepancy aligns with existing literature that emphasises the relationship between wind speed, wind acceleration, and optimal aerofoil performance. It emphasises the importance of considering not only the magnitude of wind speed but also the dynamic

interferences, such as wind shear and aerofoil placement, which can significantly influence the overall efficiency of the system.

In the higher wind speed conditions at an inlet velocity of 9 m/s, notable challenges emerge, including pronounced wind shear and suboptimal placement of the aerofoil for optimal performance. These challenges, when contrasted with the findings at lower wind speeds, highlight the need for a comprehensive understanding of the aerodynamic characteristics in varying conditions. Thus, this study contributes valuable insights that can inform future research endeavors aimed at refining aerofoil designs and placement strategies for enhanced wind energy capture in diverse wind speed scenarios.

Upon further examination of the increased wind speed from 6 m/s to 9 m/s, the study reveals that despite the similar static pressure patterns observed at the same points, there is a noticeable elevation in the static pressure values, as shown in Figure 78 (b). This increase in static pressure values can be attributed to the higher velocity magnitude experienced in the intensified wind conditions. The behaviour of static pressure at these specific locations maintains consistency with the observations made at lower wind velocities of 3 m/s and 6 m/s. This consistency in static pressure patterns across different wind speeds is in alignment with existing literature in the field of aerodynamics. The established principles of fluid dynamics and the known effects of wind speed on static pressure support the idea that while the locations of interest may remain consistent the intensity of static pressure variations is directly influenced by the velocity magnitude.

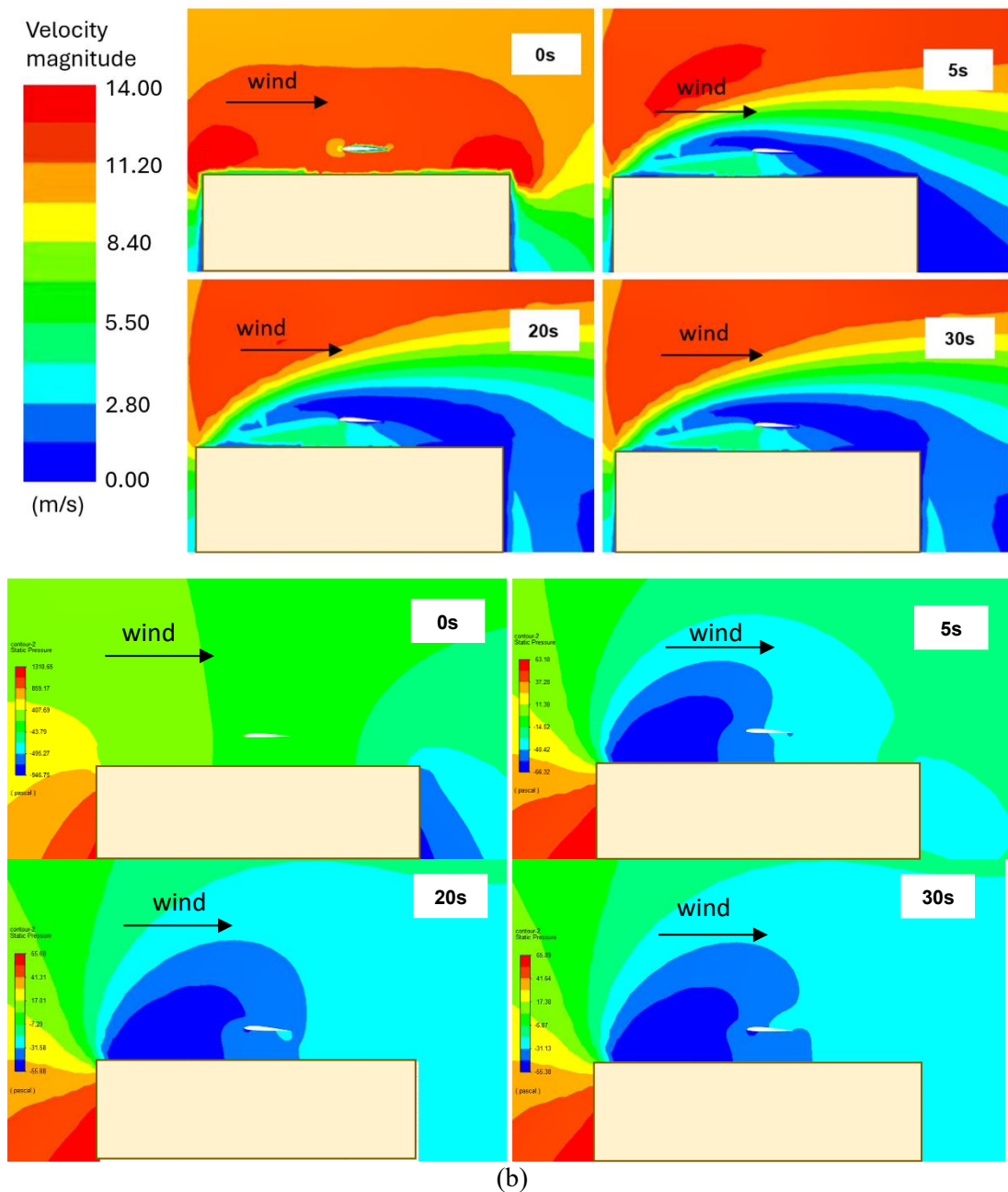


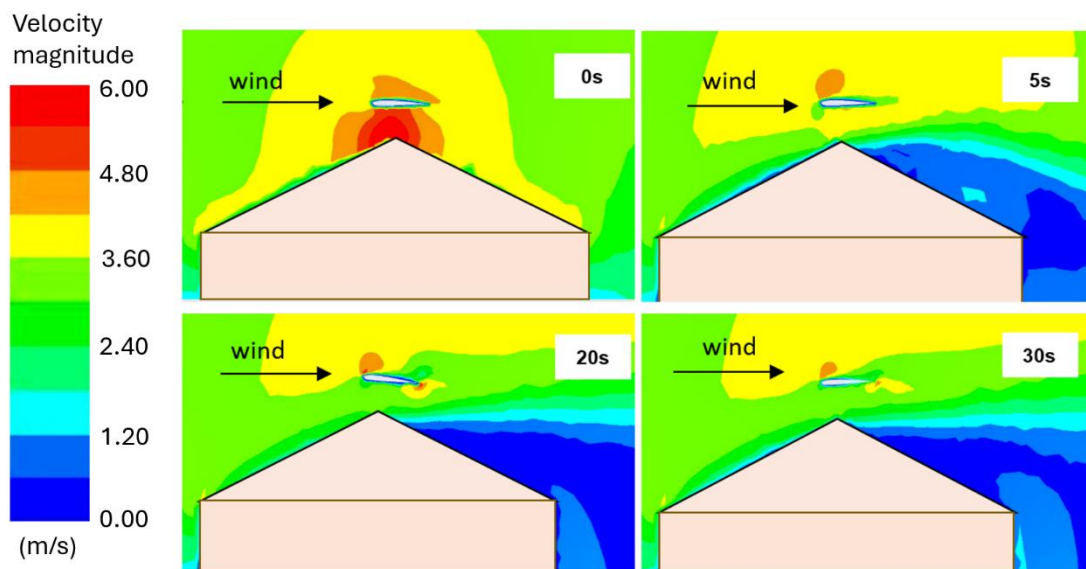
Figure 78. Contours representing (a) velocity magnitude and (b) static pressure for an oscillating aerofoil with the SD7003 profile integrated into flat roof building at 9 m/s for time intervals of 0, 5, 20, and 30 seconds

5.8.4 Velocity magnitude and static pressure contours for SD7003 integrated into the pitched roof at 3 m/s

Figure 79 (a) shows the contours of velocity magnitude and static pressure from 0 s, 5 s, 20 s, and 30 s for the parameter of SD7003 installed into the pitched roof building. Similar to the case of the symmetrical NACA 0012 installed into the pitched roof

building structure, the wind speed acceleration can be observed at the ridge of the aerofoil. The aerofoil is correctly placed where the highest wind speed is located. The ideal placement of the aerofoil is at the windward side slope to the ridge of the pitched roof building structure, while leeward side demonstrates low velocity magnitude which is not beneficial for wind energy harvesting system. In addition, pitch oscillations can be observed from 0 s, 5 s, 20 s, and 30 s as a result of fluid-structure interaction of the wind flow and non-symmetrical aerofoil integrated into the building pitched roof structure.

In Figure 79 (b), it demonstrates the static pressure, the contours initiated at 0 seconds, highlighting the highest static pressure initially. Subsequently, a notable shift occurred, directing the highest static pressure towards the leeward side of the pitched roof for 5 seconds. Concurrently, at this time point, a distinct pattern emerged, with high static pressure observed on the lower surface of the aerofoil and low static pressure on the upper surface. This configuration induced pitch oscillations in the aerofoil, signifying a dynamic response to the aerodynamic forces. The observed pitch oscillations persisted for 20 seconds, characterised by a periodic relationship of upward and downward motion. This continuous oscillatory behaviour extended to 30 seconds, presenting a favourable scenario for a wind energy harvesting system.



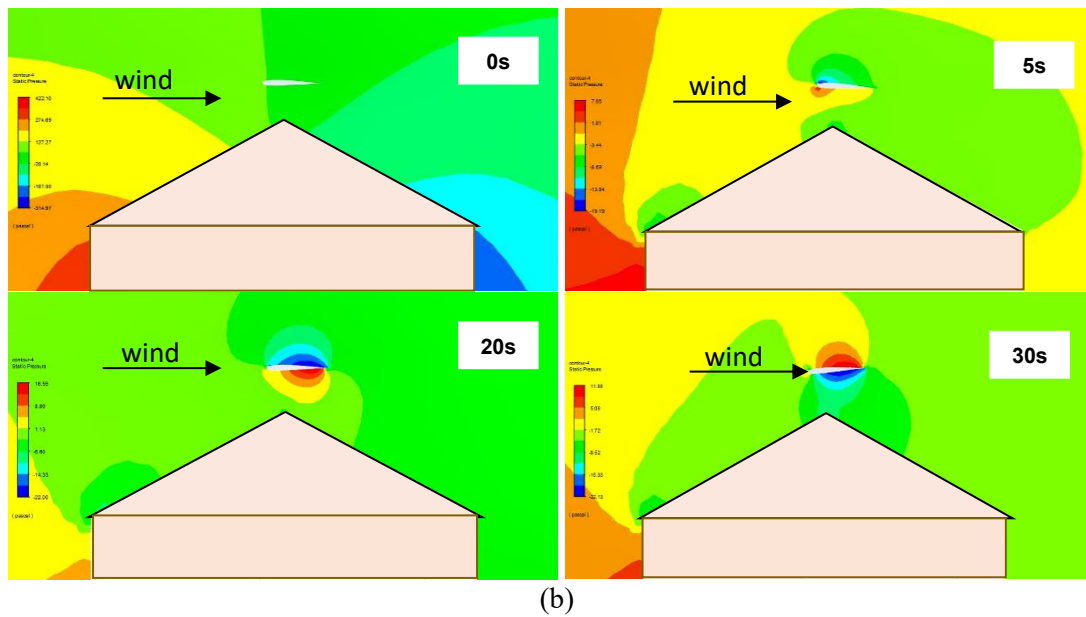


Figure 79. Contours representing (a) velocity magnitude and (b) static pressure for an oscillating aerofoil with the SD7003 profile integrated into pitched roof building at 3 m/s for time intervals of 0, 5, 20, and 30 seconds

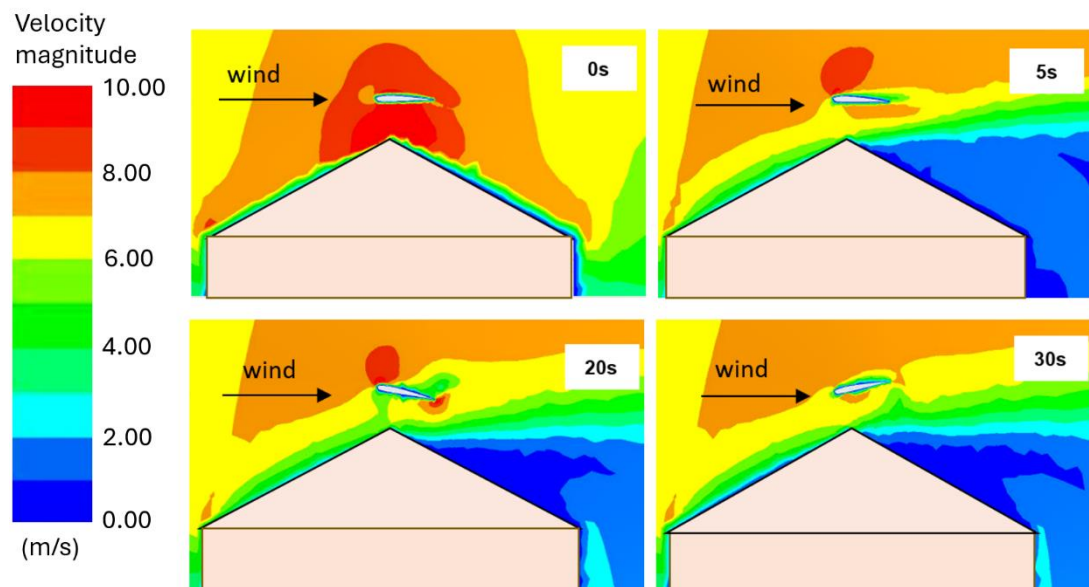
5.8.5 Velocity magnitude and static pressure contours for SD7003 integrated into the pitched roof at 6 m/s

Figure 80 (a) illustrates the velocity magnitude distribution for the SD7003 aerofoil integrated into a pitched roof building. The analysis begins at 0 seconds when the wind initiates from the windward side of the building. Notably, the highest wind speed acceleration is observed at the top of the ridge of the aerofoil, indicating an optimal placement for maximising wind energy harvesting performance. This observation resonates with insights from existing literature, emphasising the importance of strategic aerofoil placement for effective energy capture. Moving to 5 seconds, the wind flow is directed across the windward side of the pitched roof, leading to the emergence of a recirculation of wind flow at the leeward side of the building. Simultaneously, the velocity magnitude highlights elevated wind speeds at the nose or leading edge of the aerofoil, while separation initiates from the mid to the trailing edge of the aerofoil. These findings align with established aerodynamic principles discussed in the literature, emphasising the impact of building geometry on wind flow patterns around aerofoils. Advancing to 20 seconds, the analysis reveals high displacement and lift forces, followed by drag force with substantial displacement at 30 seconds. This dynamic behaviour is identified as beneficial for a wind energy harvest⁸⁰g system, as

it indicates favourable aerodynamic forces acting on the aerofoil. Importantly, the distribution of the aerofoil within the pitched roof building presenting improved performance compared to a flat roof building, as observed in the better distribution of forces and displacements.

In Figure 80 (b), it shows the static pressure at a wind speed of 6 m/s, there is a noticeable increase in static pressure compared to the 3 m/s condition. This higher wind speed contributes to elevated static pressure values. Nonetheless, the interaction between the fluid-structure components, specifically the wind flow and static pressure surrounding the aerofoil, demonstrates behaviour consistent with established principles found in existing literature.

At the initiation of the analysis (0 seconds), higher static pressure is observed on the windward side of the pitched roof building. Subsequently, at 5 seconds, the pressure is directed through the aerofoil, initiating pitch oscillations. This phenomenon aligns with previous studies detailing the dynamic relationship between static pressure, aerofoil response, and the onset of pitch oscillations. Further into the analysis, distinct aerodynamic forces become apparent. At 20 seconds, there is evidence of lift force, followed by the manifestation of drag force at 30 seconds.



(a)

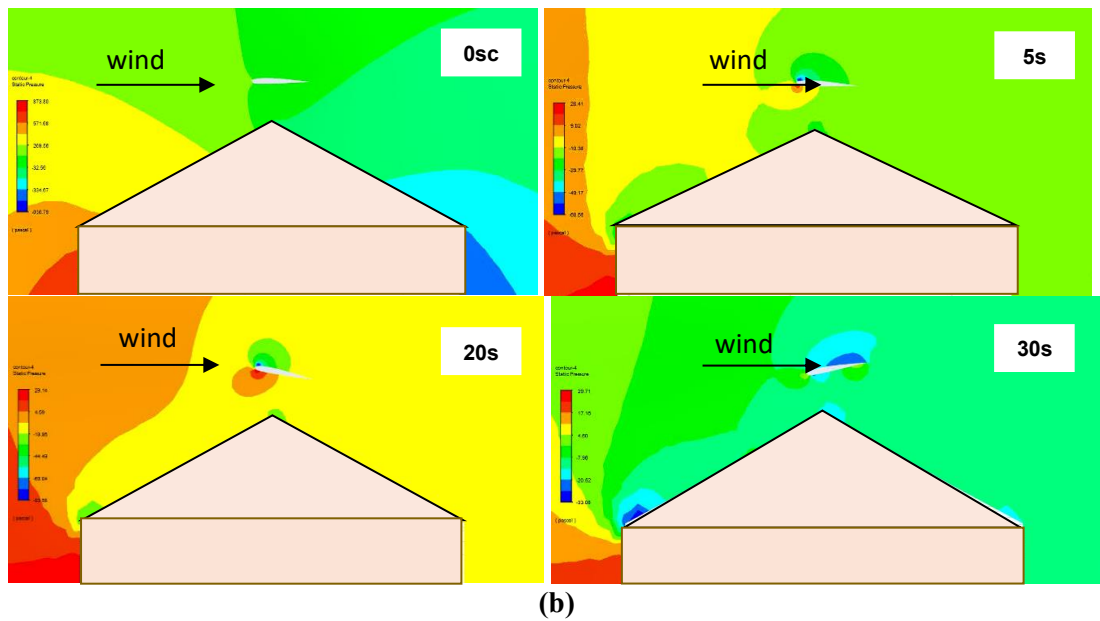
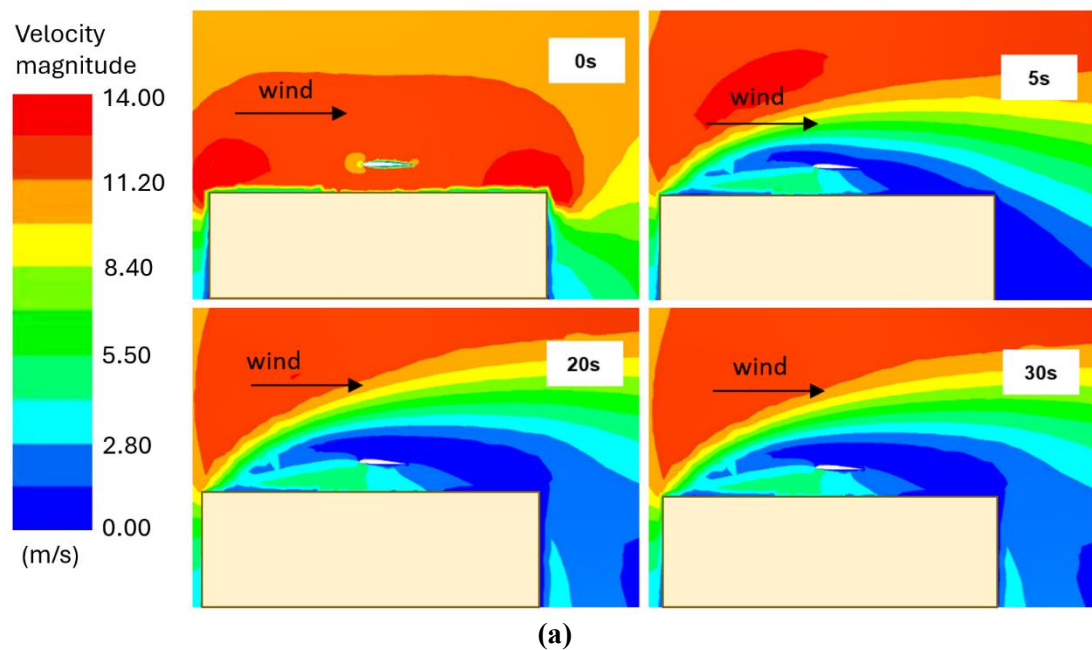


Figure 80. Contours representing (a) velocity magnitude and (b) static pressure for an oscillating aerofoil with the SD7003 profile integrated into pitched roof building at 6 m/s for time intervals of 0, 5, 20, and 30 seconds

5.8.6 Velocity magnitude and static pressure contours for SD7003 integrated into the pitched roof at 9 m/s

Figure 81 (a) shows the velocity magnitude contours for the integration of the SD7003 aerofoil into a pitched roof building structure. At the initial moment (0 seconds), a notable increase in wind speed acceleration is evident at the top ridge of the pitched roof building structure. Commencing from an inlet velocity of 9 m/s, the acceleration reaches up to a velocity magnitude of 14 m/s. The interaction of the wind flow with the aerofoil integrated into the building roof structure initiates lift at 5 seconds. Notably, in comparison to lower wind speeds, the onset of pitch oscillation or a similar heightened lift force is observed earlier, specifically at 20 seconds. This observation aligns with existing literature highlighting the sensitivity of aerofoil dynamics to wind speed variations. Examining the wind flow patterns from the windward side of the pitched roof building to the leeward side at 5 seconds reveals consistent behaviour and separation patterns. The elevated displacements observed at 5 seconds, 20 seconds, and 30 seconds are attributed to the higher lift and drag forces generated. The continuous pitch oscillations observed at 5 seconds, 20 seconds, and 30 seconds further emphasise the dynamic response of the aerofoil to the altered wind conditions.

In Figure 81 (b) it demonstrates the static pressure in the condition of 9 m/s. The results show a consistent pattern emerges, reflecting a similar pressure distribution observed in the cases of 3 m/s and 6 m/s. This uniformity in pressure distribution is noticeable around the aerofoil and the surrounding area of the pitched roof building at key intervals of 0 seconds, 5 seconds, 20 seconds, and 30 seconds. The observed continuity in pressure distribution across varying wind speeds contributes to a comprehensive understanding of aerodynamic behaviour. Contrasting these findings with the previously examined cases at 3 m/s and 6 m/s, it becomes apparent that the static pressure distribution remains consistent even as the wind speed increases to 9 m/s. This coherence in pressure patterns aligns with established principles in existing literature, reinforcing the notion that static pressure variations are linked to aerodynamic forces and aerofoil dynamics. The higher static pressure noted in this analysis corresponds to elevated displacements, primarily induced by increased lift and drag forces. This observation connects back to the earlier results at 3 m/s and 6 m/s, providing a continuum of evidence regarding the relationship between static pressure, aerodynamic forces, and aerofoil performance in varying wind speeds.



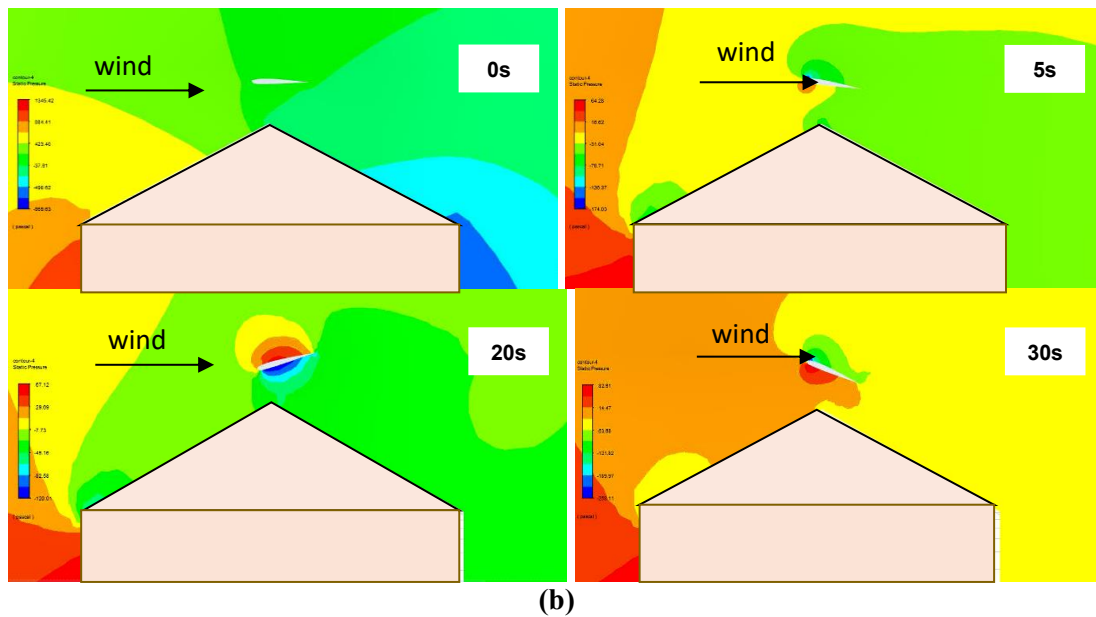


Figure 81. Contours representing (a) velocity magnitude and (b) static pressure for an oscillating aerofoil with the SD7003 profile integrated into pitched roof building at 9 m/s for time intervals of 0, 5, 20, and 30 seconds

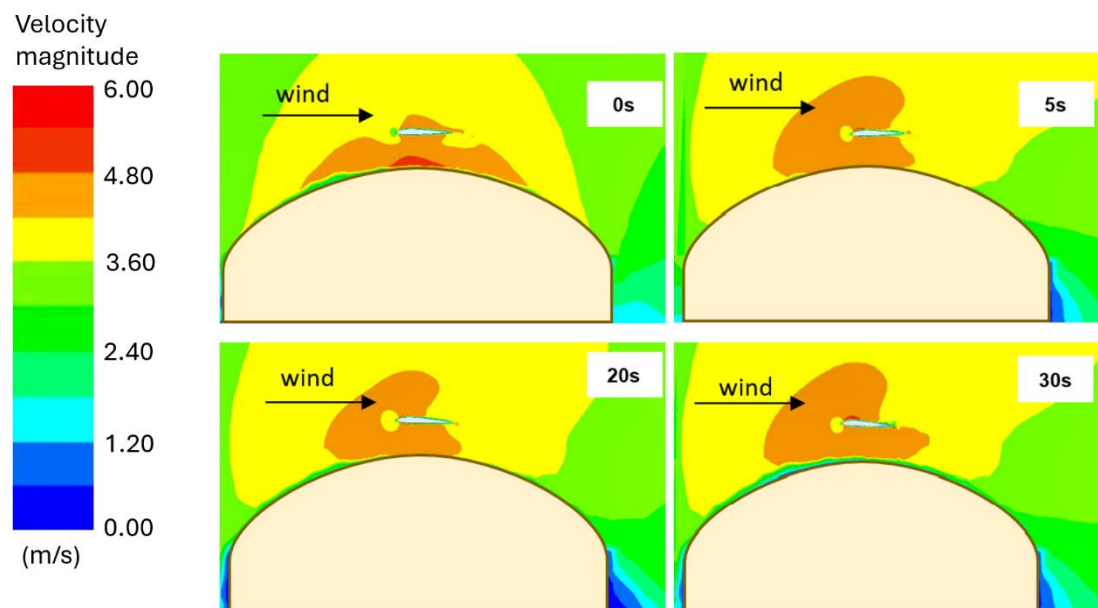
5.8.7 Velocity magnitude and static pressure contours for SD7003 integrated into the curved roof at 3 m/s

Figure 82 (a) illustrates the velocity magnitude for the integration of the SD7003 aerofoil into a building roof structure with a curved design. At the onset (0 seconds), the highest wind speed acceleration is prominently observed at the top ridge of the curved roof building. Simultaneously, the wind demonstrates strong attachment to the curved roof surface at intervals of 0, 5, 20, and 30 seconds.

Upon the initiation of wind interaction with the aerofoil at 5 seconds, a lift force is generated, indicative of the aerofoil's response to the aerodynamic forces. Subsequently, from 20 seconds to 30 seconds, pitch oscillations commence, characterised by relatively low displacement when compared to a pitched roof building. These findings align with existing literature regarding aerofoil behaviour in diverse architectural settings. The elevated wind speed acceleration at the curved roof's top ridge highlights the unique aerodynamic characteristics associated with this roof structure. In addition, the observed pitch oscillations and wind attachment patterns contribute to the broader understanding of aerofoil dynamics in curved roof configurations.

This analysis emphasises the importance of considering building geometry when integrating aerofoils for wind energy harvesting. The observed outcomes provide valuable insights into the specific aerodynamic responses of the SD7003 aerofoil within a curved roof context, contributing to the ongoing body of knowledge in aerodynamics and wind energy capture.

The static pressure contours shown in Figure 82 (b) demonstrated the distinctive patterns when the SD7003 aerofoil is integrated into the building roof structure with a curved design. At the initiation (0 seconds), higher static pressure becomes evident from the windward side extending to the ridge of the curved roof building. This initial static pressure distribution sets the stage for subsequent aerodynamic responses. As time progresses, from 5 seconds onward, the static pressure is propelled throughout the curved roof building. The pressure dynamics contribute to the creation of lift force, particularly noticeable when static pressure is higher at the nose or leading edge of the aerofoil for 5 seconds. This behaviour aligns with established principles in existing literature regarding the correlation between static pressure distribution and lift force generation. Moving to 20 seconds, a shift in static pressure is observed, with lower pressure at the trailing edge of the aerofoil. This alteration in pressure distribution triggers oscillations that persist from 20 seconds to 30 seconds. The observed oscillatory behaviour aligns with the known aerodynamic responses of aerofoils, emphasising the relationship between static pressure variations and aerofoil dynamics.



(a)

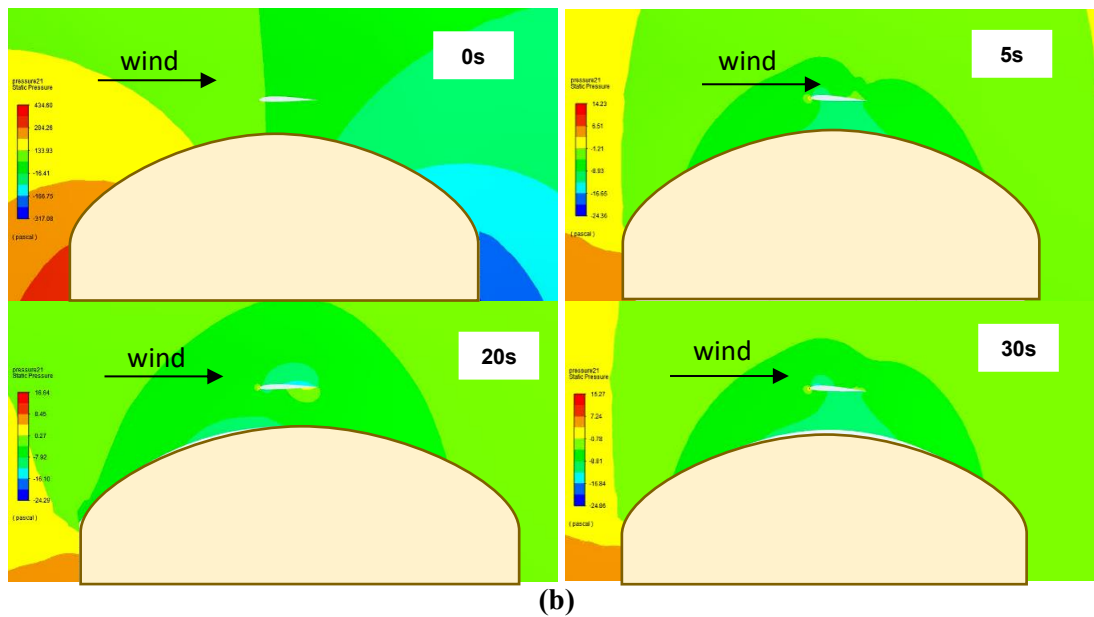


Figure 82. Contours representing (a) velocity magnitude and (b) static pressure for an oscillating aerofoil with the SD7003 profile integrated into curved roof building at 3 m/s for time intervals of 0, 5, 20, and 30 seconds

5.8.8 Velocity magnitude and static pressure contours for SD7003 integrated into the curved roof at 6 m/s

Figure 83 (a) illustrates velocity magnitude contours for the integrated design of SD7003 aerofoil into a curved roof building at a wind speed of 6 m/s, capturing snapshots at 0 s, 5 s, 20 s, and 30 s. The highest wind speed acceleration is notably concentrated at the ridge of the curved roof building, as observed consistently across the showed time intervals.

Commencing at 0 seconds, the wind interacts with the aerofoil, initiating subsequent aerodynamic responses. At 5 seconds, the aerofoil begins to generate lift force, accompanied by the formation of separation bubbles at the trailing edge. These observed phenomena align with existing literature on aerofoil behaviour and lift force generation in specific wind conditions. Advancing to 20 seconds, the aerofoil transitions into generating drag force, leading to the onset of pitch oscillations. This dynamic behaviour is recognised as beneficial for wind energy harvesting systems, as highlighted in the literature. The continuity of pitch oscillations is observed at 30 seconds, accompanied by a subsequent lift force.

Consistent behaviour in static pressure was evident at 0 s, 5 s, 20 s, and 30 s during a lower wind speed scenario of 3 m/s, as shown in Figure 83 (b). However, notably higher static pressure values were observed from the windward to the leeward side of the curved roof building and surrounding the aerofoil when the wind speed increased to 6 m/s. These elevated static pressure values corresponded to increased lift force and displacements, highlighting the impact of higher wind speeds on the aerodynamic performance.

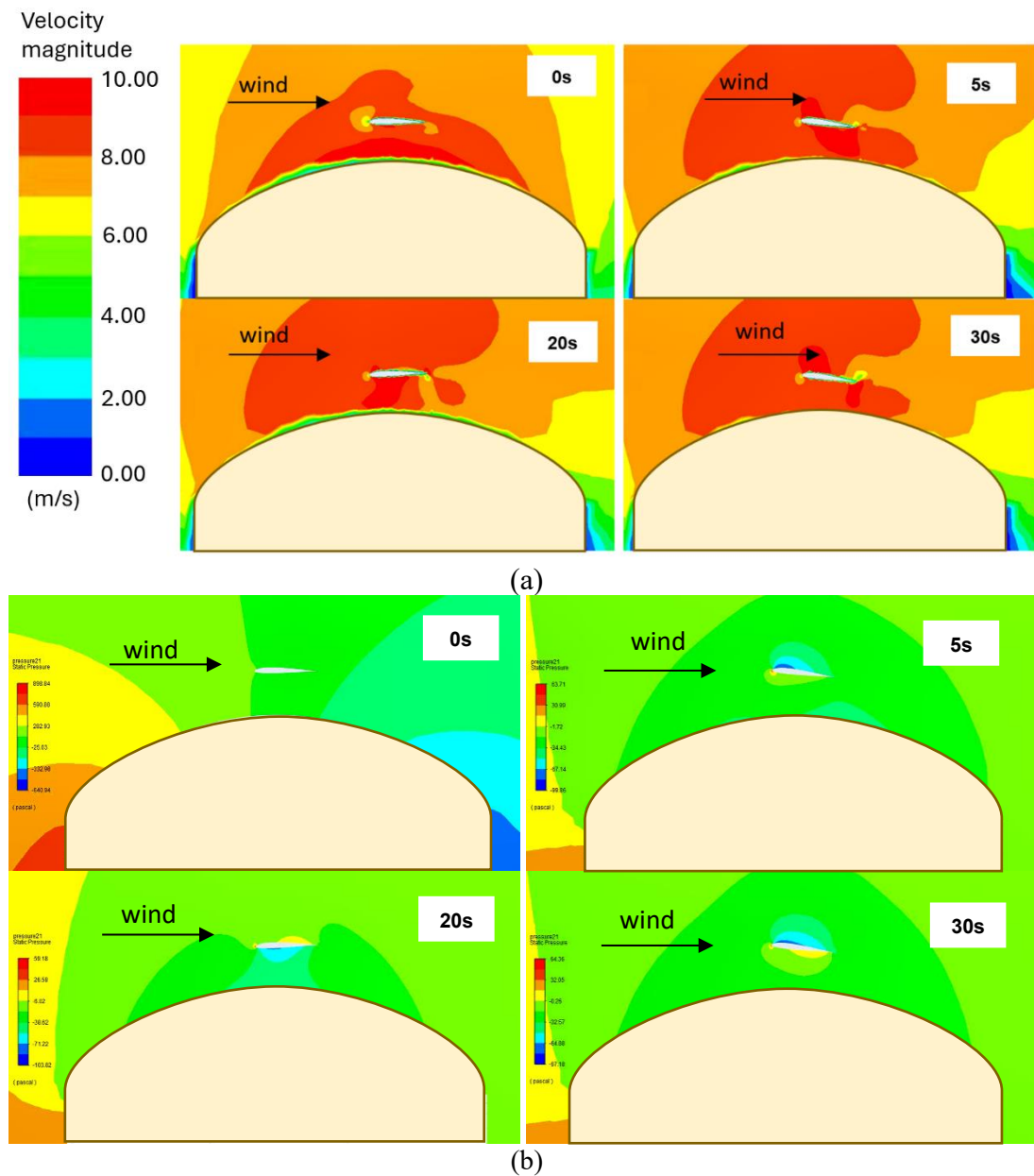


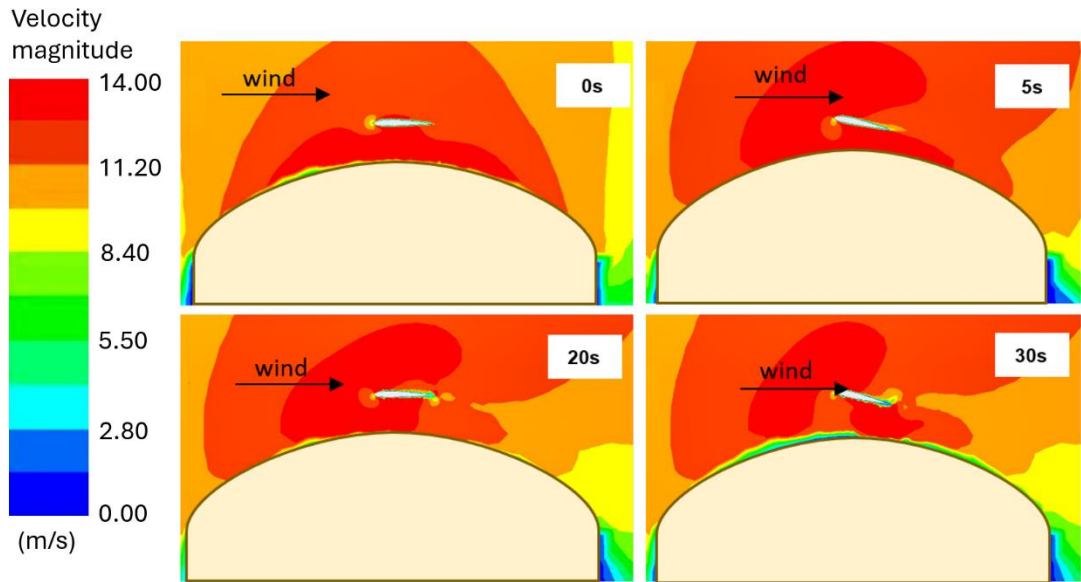
Figure 83. Contours representing (a) velocity magnitude and (b) static pressure for an oscillating aerofoil with the SD7003 profile integrated into curved roof building at 6 m/s for time intervals of 0, 5, 20, and 30 seconds

5.8.9 Velocity magnitude and static pressure contours for SD7003 integrated into the curved roof at 9 m/s

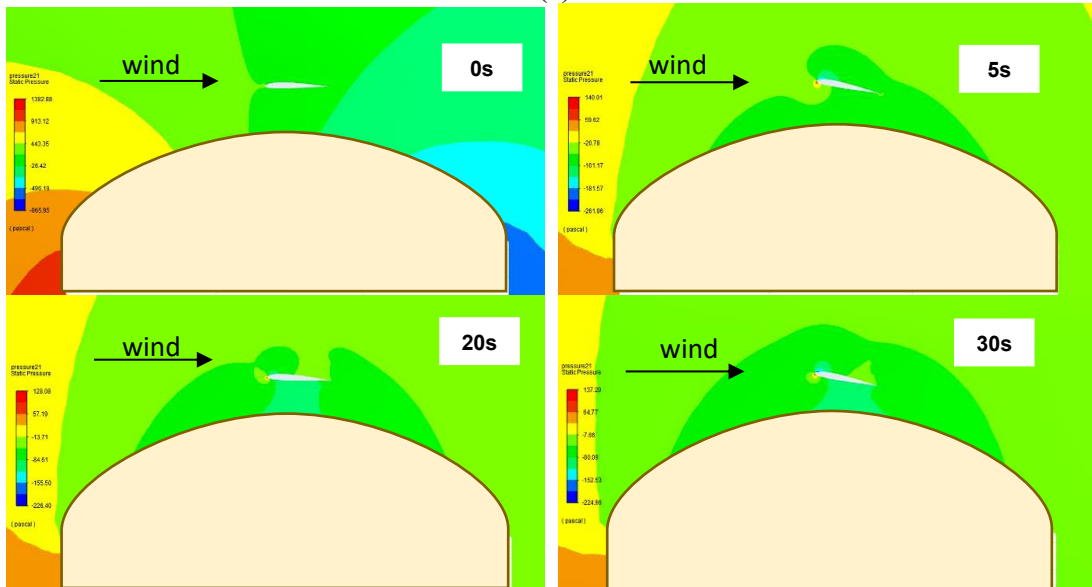
Figure 84 (a) shows the velocity magnitude contours for SD7003 aerofoil on a curved roof building at different time intervals: 0 s, 5 s, 20 s, and 30 s. Similar to observations at lower wind speeds of 3 m/s and 6 m/s, the highest wind speed acceleration is concentrated at the top of the ridge of the curved roof building. In addition, the wind shows strong attachment to the curved roof, distinguishing it from the wind flow pattern observed on a pitched roof. In contrast to the pitched roof, where wind flow is primarily attached from the windward side to the ridge, the curved roof displays consistent attachment, creating a distinct aerodynamic environment.

This wind flow pattern implies potential opportunities for multiple aerofoils to be strategically placed at the leeward side of the building, a notable difference from the pitched roof scenario where wind energy harvesting potential is concentrated mainly on the windward side. The initiation of lift force at 5 seconds, followed by the generation of drag force at 20 seconds and another lift force at 30 seconds, aligns with expected aerodynamic responses. The relationship between wind speed and the observed higher displacements, lift, and drag forces is consistent with existing literature.

The static pressure patterns demonstrated analogous behaviour at lower wind speeds of 3 m/s and 6 m/s, encompassing the regions around the aerofoil, windward side, ridge, and leeward side of the curved roof building at 0 s, 5 s, 20 s, and 30 s. Moreover, the influence of the heightened wind speed of 9 m/s becomes evident, as reflected by the observed increases in displacement, lift, and drag forces, as shown in Figure 84 (b).



(a)



(b)

Figure 84. Contours representing (a) velocity magnitude and (b) static pressure for an oscillating aerofoil with the SD7003 profile integrated into curved roof building at 9 m/s for time intervals of 0, 5, 20, and 30 seconds

In conclusion, the performance of the SD7003 aerofoil demonstrates distinct characteristics when installed in various building structures. When integrated into a curved roof building, the SD7003 shows lower performance, a phenomenon attributed to stagnation points at the top of the curved roof. The inherent nature of the SD7003, with its higher lift force compared to the symmetrical NACA profile aerofoil, contributes to fluid disturbances, particularly as wind flow reaches the top ridge of the

curved roof. This results in the wind being directed upwards on the leeward side of the curved roof building, impacting the overall efficiency of the aerofoil for wind energy harvesting.

Conversely, when the SD7003 is placed in a pitched roof building, it demonstrates more favourable performance compared to the curved roof structure. This highlights the sensitivity of the SD7003 to roof shape and the aerodynamic benefits of the pitched roof configuration. Intriguingly, the SD7003 performs least efficiently when installed in a flat roof structure, emphasising the importance of aerofoil placement within the architectural context. A different pattern emerges when considering a symmetrical NACA 0012 aerofoil in the pitched and curved roof building structures. The NACA 0012 aerofoil shows optimal or superior performance when integrated into the curved roof building, presenting its suitability for wind energy harvesting in this specific configuration. In contrast, the SD7003 non-symmetrical aerofoil demonstrates superior performance in a pitched roof setting. These variations in performance emphasise the relationship between aerofoil design, roof shape, and aerofoil placement within the building structure.

5.8.10 Torque and angular velocity of SD7003 aerofoil integrated into the building roof

Figure 85 shows the comparison of the torque between an oscillating SD7003 aerofoil integrated into flat, pitched, and curved roof at (a) 3 m/s, (b) 6 m/s, (c) 9 m/s with a distance of 600 mm and angular velocity at (d) 3 m/s, (e) 6 m/s, (f) 9 m/s with a distance of 600 mm. This study investigates the dynamic behaviour of the integrated design of non-symmetrical aerofoil integrated into three roof shapes, and at the same time the fluid-structure interactions between the wind flow and integrated design of an oscillating aerofoil and building roof structure. The study will focus on the influence of aerofoil shape and placement within different roof structures.

The observed similarities in torque and angular velocity patterns, particularly after 2 flow times, are attributed to the aerodynamics of the aerofoil shape. Moreover, the study involves different parameters, including the SD7003 aerofoil at varying distances from the rooftop and in different wind speeds. The findings suggest that the aerofoil's initial high oscillations within the first second gradually decrease until 3.5

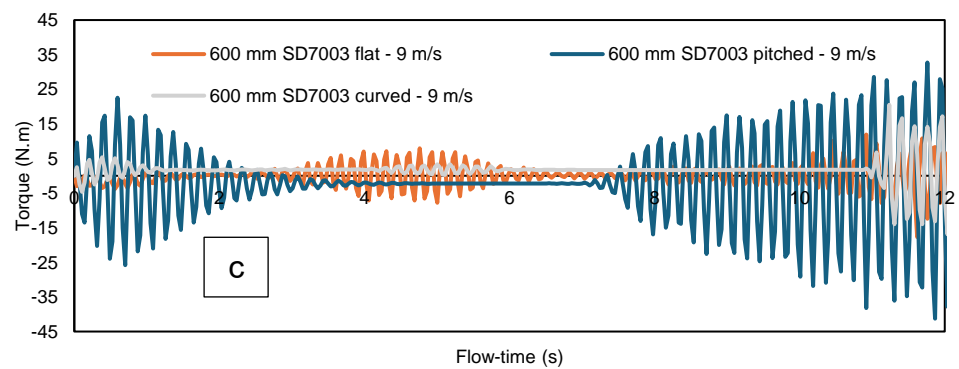
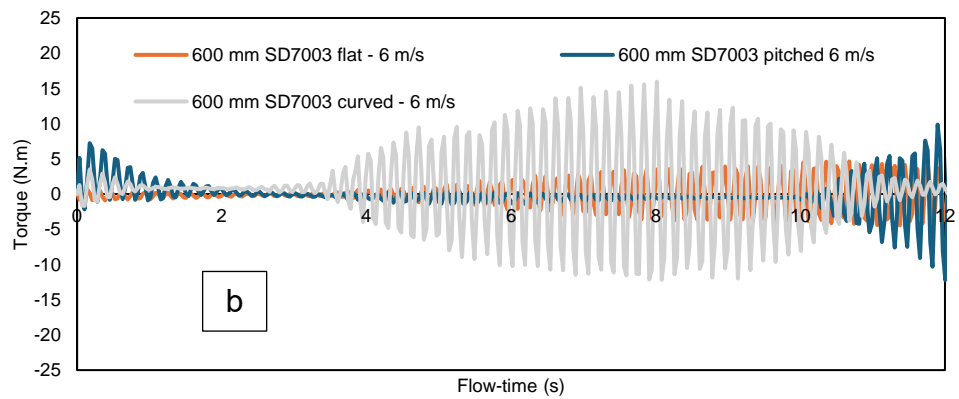
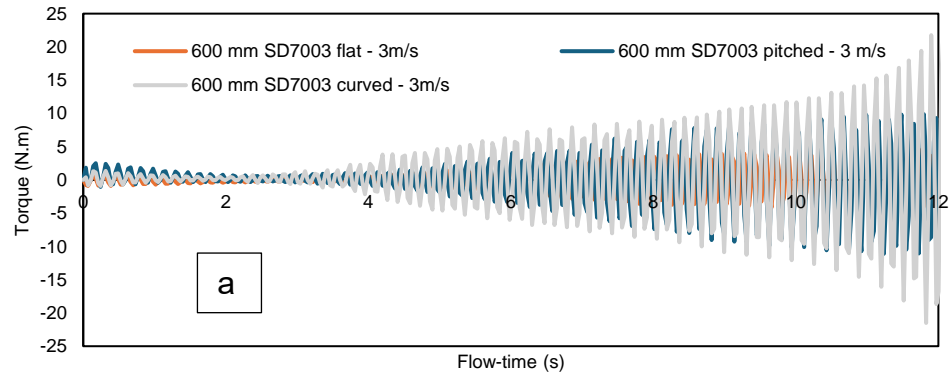
seconds, influenced by the interaction between the aerofoil shape (SD7003) and the integrated design with the building roof structure. The results emphasise the impact of wind shear and recirculation of wind flow around the flat roof building structure on the performance of the SD7003 aerofoil, suggesting the need for sensitivity analyses to optimise aerofoil placement in flat roof structures.

The maximum torque achieved was 35 N.m, which was observed when the SD7003 aerofoil was integrated into a pitched roof building and exposed to wind speeds of 9 m/s. On the other hand, the minimum torque ranged between 1-2 N.m for configurations where the oscillating SD7003 aerofoil was mounted on the building's roof structure. In addition, when the SD7003 was integrated into a curved roof, it generated 24 N.m of torque at a wind speed of 3 m/s. However, increases in wind speed led to instability and chaotic behaviour in the aerofoil, necessitating a reduction in the spring constant, which in turn decreased the torque.

Furthermore, the study reveals that the SD7003 aerofoil, when integrated into a pitched roof, outperforms those in curved roof settings due to the advantageous placement and the aerofoil's higher displacement resulting from its non-symmetrical shape. This configuration provides the aerodynamic benefits more efficiently, enhancing torque output in varying wind speeds. Conversely, the aerofoil integrated into a curved roof benefits from increased wind speed acceleration along the roof's contour, which contributes to higher lift generation. However, at higher wind speeds, specifically 9 m/s, the proximity of the aerofoil to the curved rooftop can lead to interactions that nearly cause the aerofoil to collide with the roof, risking a sudden stop in its operation. This observation emphasises the critical importance of carefully considering the aerofoil's distance from the roof and its placement to prevent operational disruptions and to maximise energy capture.

The analysis also highlights how wind stagnation on the curved roof and the impact of the flat roof's shape on wind shear both significantly affect the power output of the oscillating aerofoil wind energy converter. The flat roof's shape can contribute to a more uniform wind flow, which helps in reducing mechanical stresses and potentially increasing the lifespan of the aerofoil mechanism.

Overall, the study advocates for further research into the optimisation of aerofoil placement within different roof types to enhance the efficiency of wind energy conversion systems. This includes investigating various roof shapes and aerofoil configurations to find the ideal combination that maximises energy output while minimising mechanical risks and inefficiencies.



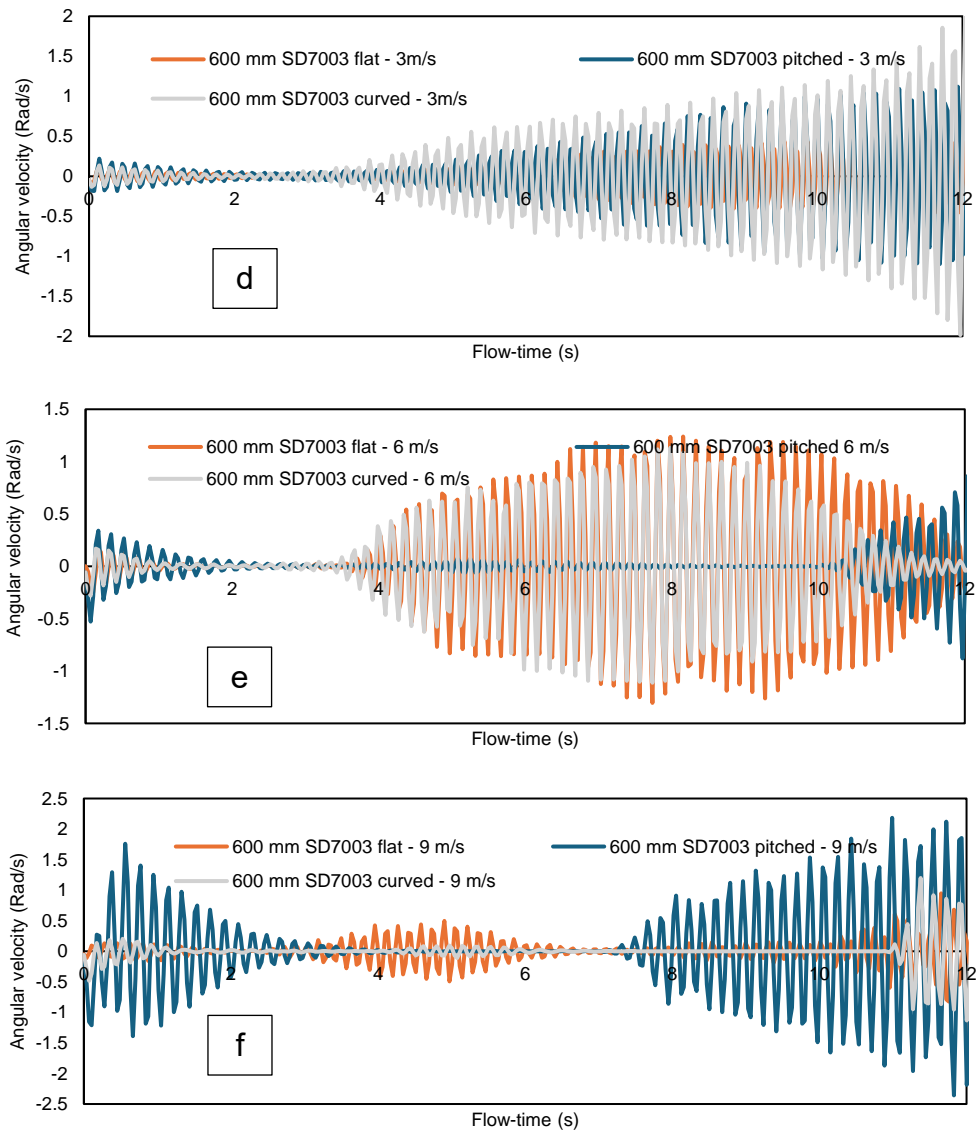


Figure 85. Comparison of the torque between an oscillating SD7003 aerofoil integrated into flat, pitched, and curved roof at (a) 3 m/s, (b) 6 m/s, (c) 9 m/s with a distance of 600 mm and angular velocity at (d) 3 m/s, (e) 6 m/s, (f) 9 m/s with a distance of 600 mm

5.8.11 Effects on mechanical power output of 1 m SD7003 integrated into the building roof

Figure 86 illustrates that the 1-metre SD7003 integrated into the pitched roof building, at an inlet velocity of 9 m/s achieved the highest average power output at 18 watts. The second-highest power output was obtained by the same aerofoil integrated into the pitched roof building, yielding 10 watts. The third-highest power output also belongs to the SD7003 integrated into the pitched roof building. These results suggest that the

non-symmetrical SD7003 when integrated into the pitched roof building, demonstrates the most suitable roof shape for this aerofoil design.

On the other hand, the 1-metre SD7003 integrated into the curved roof building provided useful power outputs of 4.4 watts (at 6 m/s), 3.7 watts (at 9 m/s), and 3.05 watts (at 3 m/s). However, these results indicate that the SD7003 aerofoil integrated into the curved roof building with a distance of 600 mm performed less efficiently compared to the symmetrical NACA 0012 aerofoil in the same conditions. This suggests that the parameters of the SD7003 aerofoil and the curved roof building at a 600 mm distance may not be suitable for a wind energy harvesting system. Therefore, further investigation into the optimal placement of the aerofoil into the curved roof building is warranted. The observed high wind speed acceleration and closely attached wind flow create stagnation points around the aerofoil, making the oscillating wind energy system inefficient. Moreover, the SD7003's non-symmetrical shape is expected to induce higher displacement due to increased lift force, making it less suitable for wind energy harvesting in the curved roof building.

For the case of the 1-metre SD7003 integrated into flat roof buildings, the power output at inlet velocities of 3 m/s, 6 m/s, and 9 m/s showed the least performance. Specifically, the 1-metre SD703 integrated into the flat roof achieved 0.80 watts, 0.7 watts (at 6 m/s), and 0.41 watts (at 9 m/s). These results indicate that increasing wind speed did not improve but rather disturbed the wind flow behaviour for the wind energy harvesting system. This disruption is attributed to wind shear effects at the edge of the flat roof building, where wind speed acceleration directs upwards rather than towards the aerofoil. As a result, low velocity magnitude surrounds the aerofoil, creating recirculation of the wind flow, which is detrimental for wind energy harvesting.

Overall, the results demonstrate that as wind speed increases, power output generally increases. However, the oscillating SD7003 aerofoil integrated into the flat roof building with a distance of 600 mm showed the lowest power output of 0.4 watts, indicating a combination of improper aerofoil placement and compatibility issues between the aerofoil and roof shape.

In conclusion, the findings from this study offer valuable insights into the performance of the SD7003 aerofoil when integrated into various building structures with flat, pitched, and curved roofs. The results emphasise the suboptimal performance of the SD7003 aerofoil when integrated into flat roof buildings, highlighting the impact of factors such as wind shear effects, aerofoil placement, and roof shape on power output. The study emphasises the strategic placement of the SD7003 aerofoil in curved roof structures, capitalising on the strong attachment of wind flow to enhance wind energy harvesting performance. The non-symmetrical design of the SD7003 aerofoil, leading to higher displacement and lift forces, is identified as a key factor influencing its compatibility with different roof structures. This understanding contributes to the optimisation of aerofoil placement for improved wind energy harvesting in diverse architectural configurations.

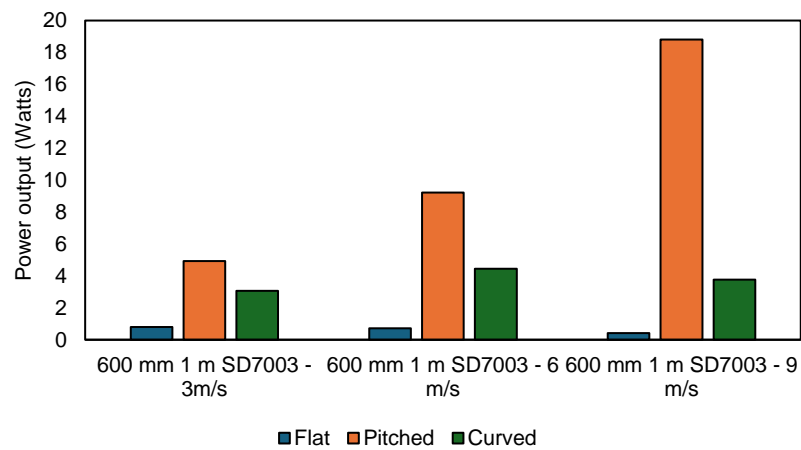


Figure 86. Average power output for the investigated 6 different parameters

5.9 Comparison of NACA 0012 and SD7003 aerofoil shapes

A comparative analysis of symmetrical NACA 0012 and low Reynolds number SD7003 aerofoil profile installed into the building roof structure will be conducted to compare their fluid-structure interaction and power output between the oscillating aerofoil installed into the building roof and wind loads in transient conditions. The two aerofoil shapes of NACA 0012 and SD7003 have different mass and moment of inertia. Table 15 shows the values of mass and moment of inertia taken from ANSYS CAD 3D model of the NACA 0012 and SD7003 aerofoil profile with a foam material. This analysis can provide fundamental understanding of fluid-structure interaction,

dynamic behaviour of pitch oscillations, and predictions of power output through oscillating aerofoil integrated into the building roof structure.

Table 15. Parameters and material properties of NACA 0012 and SD7003 aerofoil profile

Aerofoil profile	Distance between aerofoil and rooftop	Dimension	Material	Mass (kg)	Moment of inertia (kg.m ²)	Centre of rotation
NACA 0012	600 mm	1 m chord length and 1m span	Foam	3.27	0.4	0.25 m of chord length
SD7003 low Reynolds number	600 mm	1 m chord length and 1 m span	Foam	2.137	0.12	0.25 m of chord length

5.9.1 Velocity magnitude contours for SD7003 and NACA 0012 aerofoil integrated into three roof shapes

Figure 87 illustrates velocity magnitude contours for the integration of 1-metre SD7003 and NACA 0012 aerofoils into flat, pitched, and curved roof structures. Moreover, the fluid-structure interaction during pitch oscillations at 30 seconds is showed for both aerofoils in the context of these varied roof configurations. Examining the scenario where the SD7003 and NACA 0012 are installed into a flat roof building, noticeable wind shear is evident at the windward edge of the building. However, a critical observation emerges when the aerofoil is improperly positioned, creating high recirculation zones. Specifically, this occurs when there is a 600 mm distance between the aerofoil and the flat roof building.

Conversely, for pitched and curved roof buildings, there is a notable increase in wind speed acceleration, particularly along the ridge of the rooftop where the aerofoil is strategically placed. The wind-induced flow imparts lift forces on the aerofoils integrated into pitched and curved roof structures, influencing their aerodynamic performance. It is essential to note that when the aerofoil is integrated into a curved roof building, a significant stagnation of wind flow is observed. This phenomenon can have implications for wind energy harvesting systems, potentially affecting the overall wind flow patterns. This observation highlights the importance of optimal aerofoil placement in curved roof configurations to enhance the efficiency of wind energy

capture and conversion. This study contributes valuable insights into the fluid-structure interaction dynamics in different roof structures.

The interaction between the aerofoil and building structure is fundamental in shaping the mechanical power output. Wind interactions with the building induce effects that alter pressure distribution and aerodynamic forces, influencing power generation. To optimise performance, future research should delve deeper into these interactions, investigating the specific aerodynamic conditions induced by the building structure. This may reveal the necessity for aerofoil selection based on the architecture, preventing mismatches that could result in suboptimal performance. In addition, complementing numerical simulations with wind tunnel experiments would provide valuable real-world insights into the aerodynamic behaviour of different aerofoil profiles, aiding in refining design choices for enhanced mechanical power output. Exploring existing literature on aerodynamics, wind energy, and aerofoil performance is crucial for identifying supporting evidence and understanding the factors contributing to the observed variations in mechanical power output.

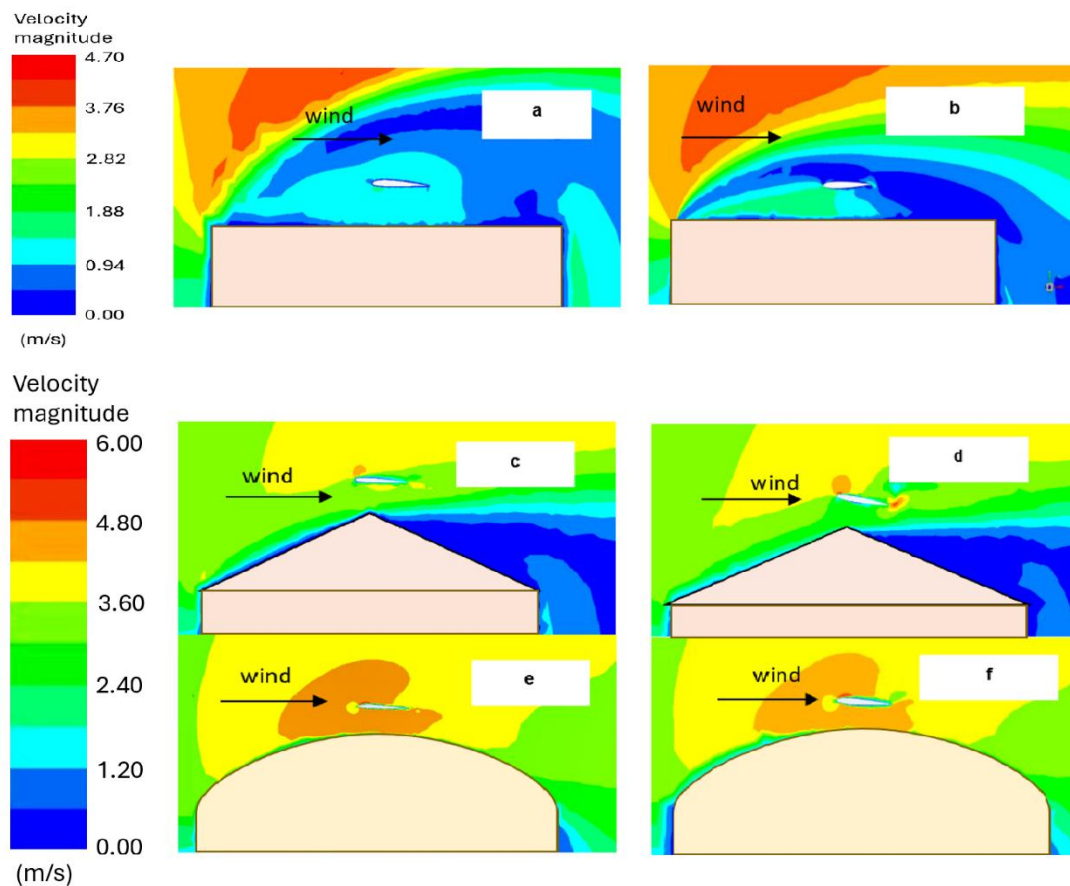


Figure 87. SD7003 aerofoil integrated into (a) flat, (c) pitched, and (e) curved roof shapes at a distance of 600 mm and NACA 0012 aerofoil integrated into (b) flat, (d) pitched, and (f) curved roof shapes at a distance of 600 mm

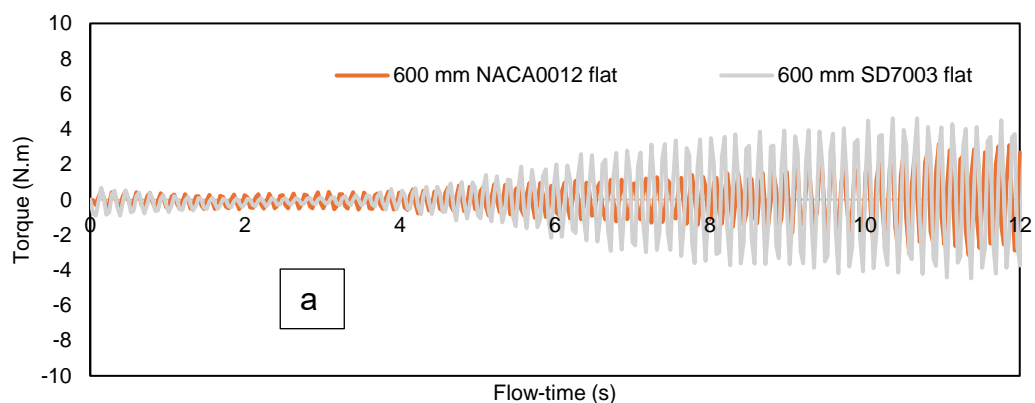
5.9.2 Torque and angular velocity of NACA 0012 and SD7003

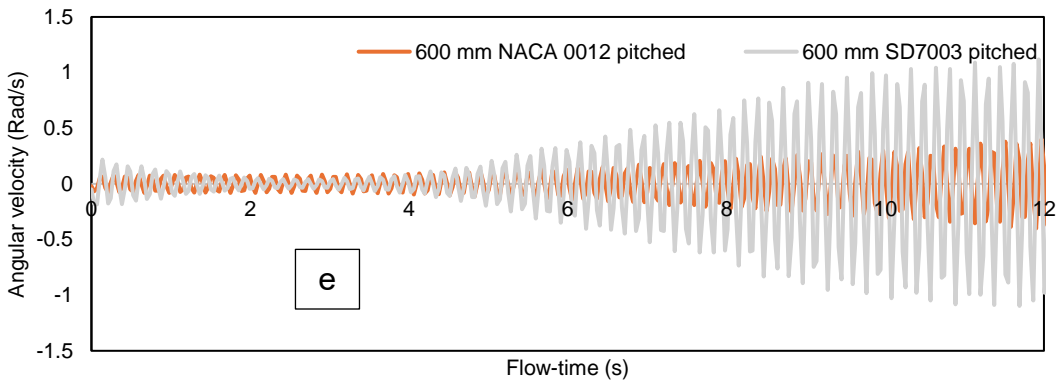
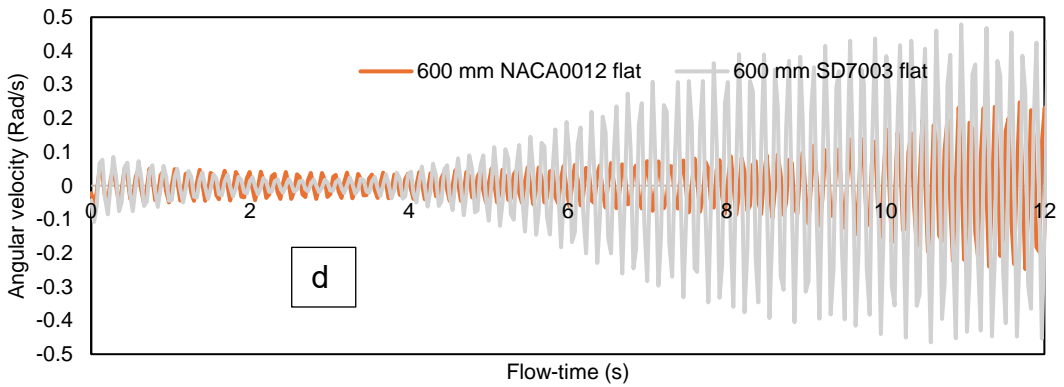
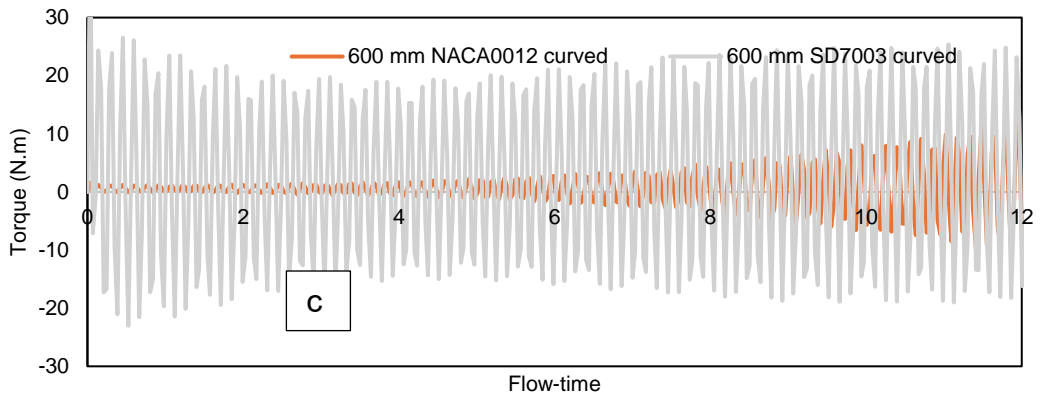
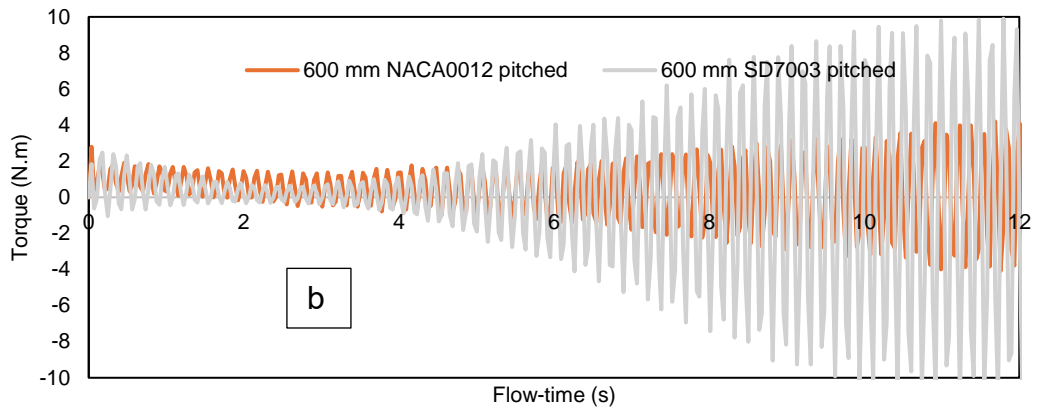
Figure 88 demonstrates the comparison of the torque between an oscillating NACA 0012 and SD7003 aerofoil integrated into (a) flat, (b) pitched, (c) curved roof with a distance of 600 mm and angular velocity for oscillating NACA 0012 and SD7003 aerofoil integrated into (d) flat, (e) pitched, (f) curved roof with a distance of 600 mm. The 1-metre SD7003 aerofoil integrated into the curved roof building demonstrated the highest torque at 28 N.m (Figure 88 c) and an angular velocity of 1.8 rad/s (Figure 88 f). While the 1-metre SD7003 aerofoil integrated into the pitched roof building demonstrated the second-highest torque at 10 N.m (Figure 88b) and an angular velocity of 1 rad/s (Figure 88e). This performance was surpassed only by the same aerofoil configuration on the curved roof building, which achieved even higher metrics.

Conversely, Figure 88 (a and d) demonstrates the SD7003 on the flat roof building, while still outperforming the symmetrical NACA 0012 aerofoils, achieved the third highest results among the configurations tested. This comparison highlights the higher torque and angular velocity of the SD7003 aerofoil when integrated on the curved roof, suggesting an advantage in optimising aerofoil shapes and their placements on different roof types for enhanced wind energy capture. In contrast, all configurations of the symmetrical NACA 0012 aerofoil integrated into flat, pitched, and curved roofs yielded lower torque and angular velocities compared to those achieved with the non-symmetrical SD7003 aerofoil.

The detailed investigation into the aerodynamics of the wind energy harvesting system, integrating an oscillating aerofoil on the building's curved roof, reveals the impact of the structure's shape on wind circulation, disrupting flow and leading to suboptimal conditions for wind energy harnessing. The integration of an oscillating aerofoil strategically disrupts stagnation points, emphasising the significance of the specific 600 mm distance between the oscillating aerofoil and the curved roof in optimising aerodynamic efficiency.

Overall, the use of non-symmetrical SD7003 aerofoils improves the performance of the wind energy harvesting system, highlighting the importance of aerofoil optimisation in future wind energy projects. This optimisation could significantly impact the effectiveness and efficiency of wind energy systems in various building integrations.





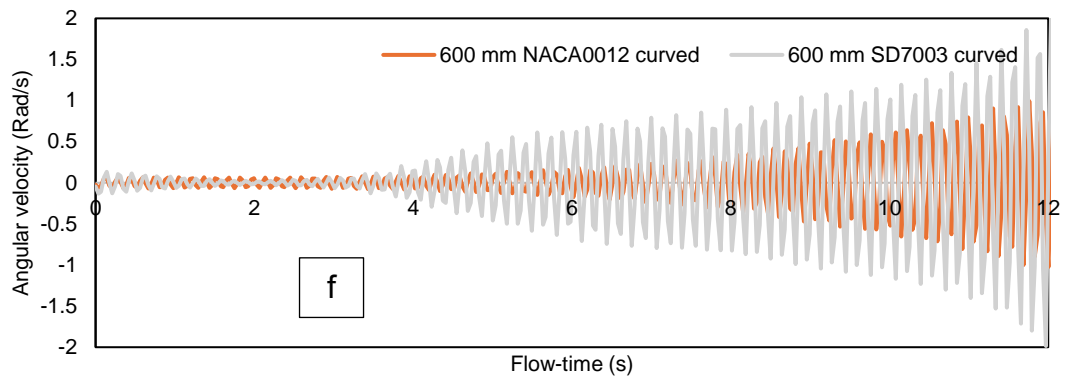


Figure 88. Comparison of the torque between an oscillating NACA 0012 and SD7003 aerofoil integrated into (a) flat, (b) pitched, (c) curved roof with a distance of 600 mm and angular velocity for oscillating NACA 0012 and SD7003 aerofoil integrated into (d) flat, (e) pitched, (f) curved roof with a distance of 600 mm

5.9.3 Effects on mechanical power output of NACA 0012 and SD7003 integrated into the building roof

The presented results in Figure 89 emphasise the substantial impact of aerofoil profile selection and installation location (curved roof or pitched roof) on mechanical power output. The highest power output was achieved by NACA 0012 installed into the curved building roof structure which yielded 5.65 watts, then followed by the SD7003 aerofoil installed into pitched roof building. Symmetrical NACA 0012 aerofoil demonstrates consistent lift and drag characteristics, rendering them well-suited for applications where aerodynamic performance is critical, particularly in curved roof scenarios. Conversely, non-symmetrical profiles such as SD7003 may demonstrate advantages in pitched roof installations, potentially due to improved lift-to-drag ratios at angles typical for pitched roofs. The aerodynamic conditions induced by the unique shapes of curved and pitched roof structures contribute to the observed disparities. Curved roofs create conditions favouring certain aerofoil profiles, such as the NACA 0012, where the curvature influences flow patterns and enhances symmetrical aerofoil performance. between the aerofoil and the rooftop, impeding the fluid circulation and thereby diminishing power generation efficiency. This phenomenon is explained by the distinctive wind speed acceleration dynamics observed at curved roof structures, predominantly concentrated along the curved rooftop or ridges. In pitched roof scenarios, the inclination of the roof alters airflow characteristics, potentially favouring non-symmetrical profiles like the SD7003. While both the NACA 0012 and

SD7003 aerofoil integrated into the flat roof building did not perform well as compared to both aerofoils installed into the pitched and curved roof building.

In the context of the existing scientific literature, these observations align with prior studies on aerofoil aerodynamics and wind energy harvesting. The importance of aerofoil geometry and its interaction with specific building structures has been highlighted in literature, corroborating the significance of the current findings. The comparison of symmetrical and non-symmetrical aerofoils in varying roof configurations adds a dimension to the existing body of knowledge, emphasising the need for tailored solutions based on aerofoil characteristics and structural considerations. Furthermore, the study proposes a future avenue of research, suggesting a sensitivity analysis encompassing diverse rooftop placements for the SD7003 aerofoil. This recommendation aligns with the broader scientific discourse on optimising wind turbine placement and design parameters for increased efficiency, as emphasised by various studies exploring wind flow behaviours and aerodynamic interactions in complex urban and architectural settings. In essence, the presented research contributes to the scientific understanding of aerofoil dynamics in specific building contexts, laying the groundwork for further advancements in the field of building-integrated wind energy systems.

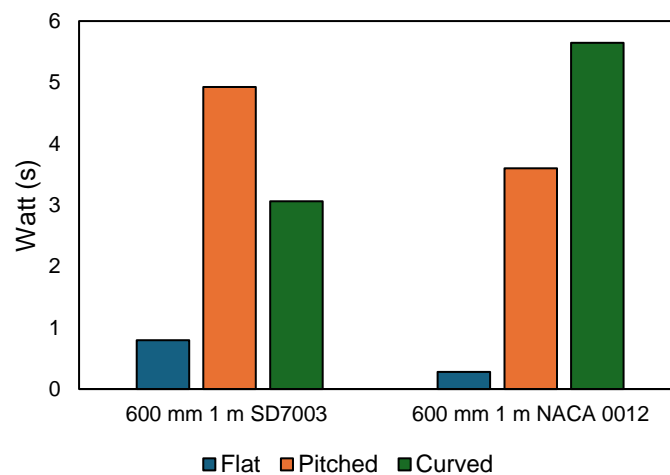


Figure 89. Average power output for the investigated 6 different parameters

5.10 Summary

- Curved building roofs with oscillating aerofoils yielded the highest power output of 12 W at 9 m/s wind speed. While the flat roofs showed the lowest output due to wind shear and recirculation issues. The curved design benefited from elevated static pressure at windward edges.
- Wind direction influenced performance. It affected the angle of attack, lift, drag forces, and energy efficiency. Properly accounting for these variations is crucial during design and operation.
- Nearby buildings caused wind shadow effects that impacted the performance of the oscillating wind energy converter. Understanding and mitigating these effects are essential for accurate performance predictions and optimisation.
- Using hourly wind data from the Copernicus Marine Service (CMEMS) for January 1, 2021, the study evaluated the system's effectiveness in low wind speeds. Curved roofs had the highest predicted power output.
- At wind speeds of 3 m/s, 6 m/s, and 9 m/s, the PSD vs. frequency analysis shows distinct behaviour for the oscillating NACA 0012 aerofoil integrated into flat, pitched, and curved roofs. For the pitched and curved roofs, the PSD peaks at 5.8 Hz with values of 0.0058 and 0.0059 respectively at 9 m/s, indicating significant aerodynamic force fluctuations due to complex airflow patterns and aerodynamic loading. In contrast, the flat roof configuration exhibits unstable PSD behaviour from 0 Hz to 8 Hz and lower PSD values, suggesting less aerodynamic interaction. Higher spring constant at 3 m/s (850 n-m/rad) compared to 9 m/s (450 n-m/rad) suppresses oscillations, resulting in a lower response amplitude. Reducing the spring constant helps maintain stability at higher wind speeds, enhancing energy absorption from wind-induced vibrations while preventing instability. Despite similar PSD values between pitched and curved roofs, further analysis is needed to understand the role of factors such as angle of attack and turbulence in aerodynamic responses.
- The 1-metre SD7003 integrated into pitched roofs achieved the highest power output of 18 watts at 9 m/s and outperformed the NACA 0012 in similar conditions. In curved roofs, the SD7003 produced lower outputs of 4.4 watts at 6 m/s, 3.7 watts at 9 m/s, and 3.05 watts at 3 m/s, making it less efficient

than the NACA 0012 which performed better in these conditions. The flat roof setup showed the least efficiency for both aerofoils with the SD7003 delivering 0.80 watts at 3 m/s, 0.7 watts at 6 m/s, and 0.41 watts at 9 m/s. This indicates that while the SD7003 performs best in pitched roofs, the NACA 0012 provides more consistent performance across different roof shapes.

Chapter 6

Parametric analysis and impact on performance of BI-WEHS

In this chapter, the investigation of different design and optimisation of an oscillating aerofoil wind energy harvesting system integrated into the building roof structure will be conducted to improve the performance of the BI-WEHS. The focus includes examining the effects of aerofoil size, placement, and an additional support arm integrated into different roof shapes at various wind speeds on dynamic performance and mechanical power output. The analysis of each design's performance will involve the utilisation of CFD with a dynamic mesh to predict dynamic parameters such as torque, angular velocity, and mechanical power output. In addition, the transient simulations will investigate velocity magnitude and static pressure, which provides insights into the complex fluid-structure interactions when integrating an aerofoil into the roof structure of a building. This comprehensive exploration aims to contribute to a deeper understanding of how different design configurations impact the overall efficiency and functionality of BI-WEHS.

The chapter begins by examining the impact of aerofoil scale into the dynamic behaviour and mechanical power output. Specifically, aerofoil dimensions featuring a 1-metre chord length and 1 metre span were compared with a larger scale comprising a 2-metres chord length and 2 metres span. This exploration seeks to identify the impact of aerofoil size on wind energy harvesting system efficiency. Subsequently, the optimal placement of the aerofoil within the building rooftop was examined. This investigation considers varying distances of 600 mm and 1000 mm between the

aerofoil and the rooftop at the ridge area. The objective was to determine the influence of placement on the overall performance of the wind energy harvesting system. Lastly, the chapter introduced the concept of an oscillating aerofoil with support arm integrated with the aerofoil to potentially enhance displacement. The hypothesis was that this augmentation could result in improved wind energy harvesting and enhanced power output performance. This exploration further contributes to the comprehensive understanding of the dynamics involved in integrating aerofoils with building structures for renewable energy applications.

6.1 Impact of oscillating aerofoil scale

Scaling is a fundamental aspect in the development and assessment of wind energy harvesters featuring oscillating aerofoils. This practice facilitates practical experimentation within controlled environments such as laboratories and wind tunnels by adjusting the size of models to achieve dynamic similarity with their full-scale counterparts. Moreover, scaling is imperative for preserving precision in aerodynamic testing, validating numerical models, and refining designs. The role of scaling becomes particularly fundamental in ensuring that the behaviours observed in scaled models mirror the performance of full-scale wind energy harvesters. In this study, different scales including a chord length and span of 1 m and 2 m conducting a comparative analysis to determine which size offers the most efficient energy harvesting performance. This exploration aims to shed light on the optimal scaling parameters for enhancing the overall efficiency of wind energy harvesting systems.

Table 16 shows the parameters and material properties of 2-metres NACA 0012 and SD7003 aerofoil profiles. This representation allows for a systematic analysis that highlights the significance and implications of each parameter. The chord length and span were investigated by comparing 1-metre and 2-metres variants to provide insights into the effects of scaling on lift and drag forces and overall wind energy harvesting efficiency. The choice of aerofoil profiles NACA 0012 and SD7003 was examined by considering their distinct lift and drag properties and their suitability for diverse wind conditions. The study also explores the real-world context of different building roof structures (flat pitched and curved) and evaluates how well aerofoils adapt to various architectural configurations. Moreover, the critical parameter of distance between the

aerofoil and roof surface (ranging from 600 mm to 1000 mm) was explored for its influence on airflow patterns and energy capture efficiency. This serves as a valuable reference for researchers and engineers by facilitating the examination of each parameter's effects on the performance of oscillating aerofoils integrated into building roof structures and aiding in drawing meaningful conclusions on optimising wind energy capture in building-integrated systems.

Table 16. Parameters and material properties of 2 m NACA 0012 and 2 m SD7003 with 600 mm distance between the aerofoil and rooftop

Case (s)	Aerofoil profile	Roof shape	Distance between aerofoil and rooftop	Dimension	Material	Mass (kg)	Moment of inertia (kg.m ²)	Centre of rotation (m)
1	NACA 0012	Flat	600 mm	2 m chord length and 2 m span	Foam	6.8	1.52	0.5 m of chord length
2		Pitched						
3		Curved						
4	SD7003 low Reynolds number	Flat	600 mm	2 m chord length and 2 m span	Foam	4.457	0.88	0.77 m of chord length
5		Pitched						
6		Curved						

6.1.2 Velocity magnitude and static pressure contours for 2 m NACA 0012

Figure 90 shows the velocity magnitude contours for 2 metres NACA 0012 with 600 mm distance between (a) flat and (c) pitched, (e) curved roof and the aerofoil integrated into the (b) flat, (d) pitched, and (f) curved roof building with a distance of 1000 mm. The visualisation captures the dynamic interaction between the wind flow and the oscillating aerofoil design which offers valuable insights into the impact of placement within three different roof configurations: flat, pitched, and curved. Similar to findings in existing literature, the observations showed lower velocity magnitudes around the aerofoil when installed in a flat roof building. Moreover, optimising the placement by increasing the distance to 1000 mm in the flat roof building demonstrates improved performance for the 2-metres NACA 0012, which emphasises the significance of placement considerations. In the context of pitched roof buildings, the study recognises more favourable wind flow patterns and behaviours for wind energy harvesting when the aerofoil is installed at a shorter distance of 600 mm compared to a longer distance. Conversely, the installation of the 2-metres NACA 0012 into the curved roof building with 600 mm spacing between the aerofoil presents a notable stagnation point from

the aerofoil to the curved structure, which is indicative of suboptimal conditions for wind energy harvesting. This absence of proper circulation poses challenges for effective wind energy capture.

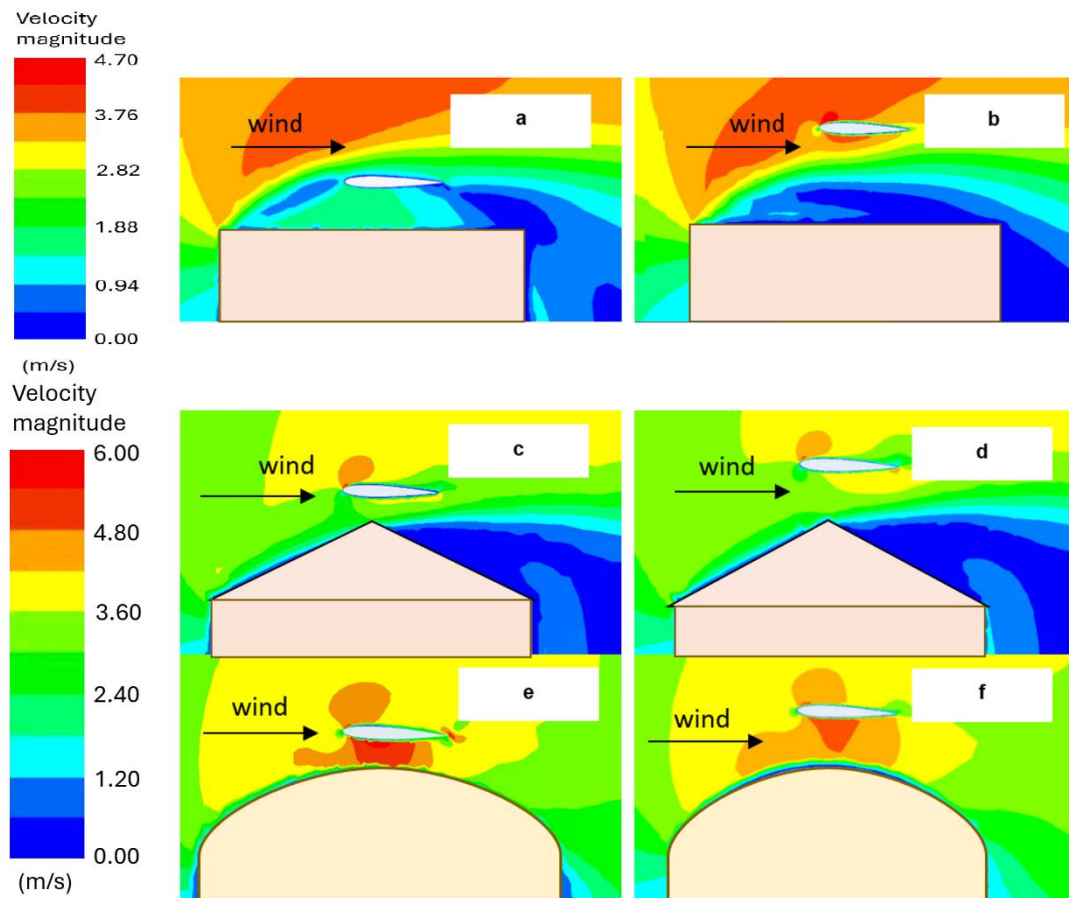


Figure 90. Velocity magnitude contours for 2 metres NACA 0012 with 600 mm distance between (a) flat and (c) pitched, (e) curved roof and 1000 mm distance between the aerofoil and (b) flat, (d) pitched, and (f) curved roof building

6.1.3 Velocity magnitude contours for 600 mm and 1000 mm 2 m SD7003

Figure 91 illustrates the contours of velocity magnitude for an SD7003 aerofoil with a chord length and span of 2 metres, which demonstrates variations for distances of 600 mm and 1000 mm between the aerofoil and the rooftop. These velocity magnitude contours show the cases for 2 metres SD7003 with 600 mm distance between the (a) flat, (c) pitched, (e) curved roof and the aerofoil integrated into the (b) flat, (d) pitched, and (f) curved roof building with 1000 mm distance. The fluid-structure interaction showed similar behaviour for the aerofoil with a notable alteration in the centre of rotation, which transitions from 0.5 m to 0.77 m along the chord length. Comparisons

with existing literature emphasise the influence of aerofoil shape, flat roof configurations, and the distance between the aerofoil and the building roof (ranging from 600 mm to 1000 mm) on the inefficiency of the aerofoil for wind energy harvesting systems. These parameters contribute to suboptimal performance. Consequently, adjustments were made to reposition the centre of rotation at 0.77 m along the chord length to address these inefficiencies.

These findings highlight the need for careful consideration of multiple parameters to enhance the overall efficiency of aerofoils in wind energy harvesting systems. The repositioning of the centre of rotation serves as a strategic adjustment based on empirical data, which further contribute to the evolving body of knowledge on fluid-structure interactions in the context of aerofoil design for wind energy applications.

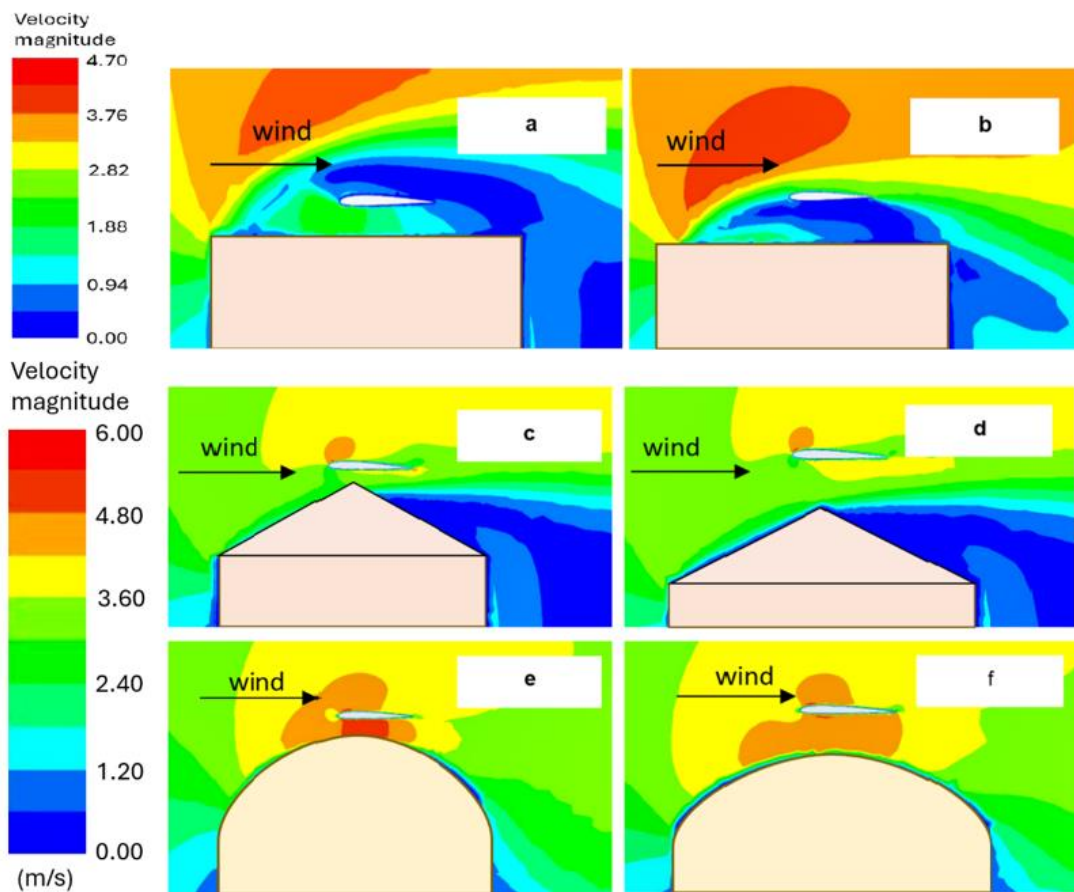


Figure 91. Velocity magnitude contours for 2 metres SD7003 with 600 mm distance between the (a) flat, (c) pitched, (e) curved roof and the aerofoil integrated into the (b) flat, (d) pitched, and (f) curved roof building with 1000 mm distance

6.1.4 Torque and angular velocity of 2 m NACA 0012 and 2m SD7003

Figure 92 shows the comparison of the torque between an oscillating NACA 0012 and SD7003 aerofoils integrated into (a) flat, (b) pitched, (c) curved roof with a distance of 600 mm and angular velocity for oscillating NACA 0012 aerofoil integrated into (d) flat, (e) pitched, (f) curved roof with a distance of 600 mm at a wind speed of 3 m/s. The configurations were assessed to evaluate their efficiency in harnessing wind energy.

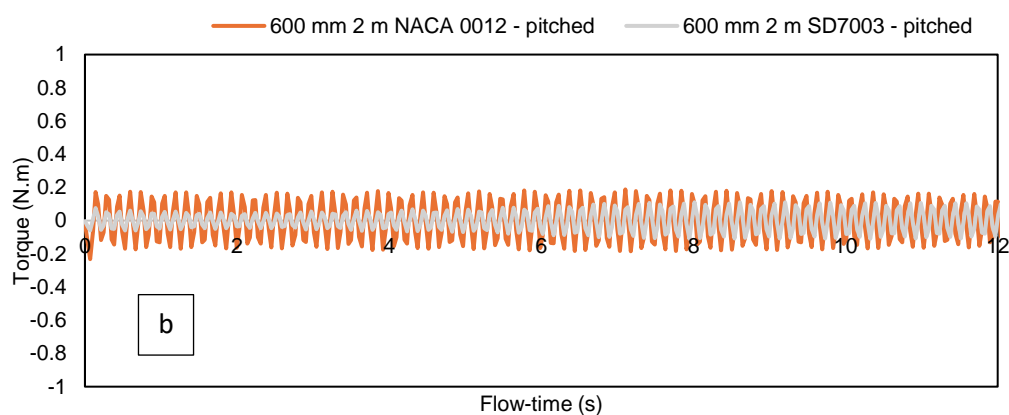
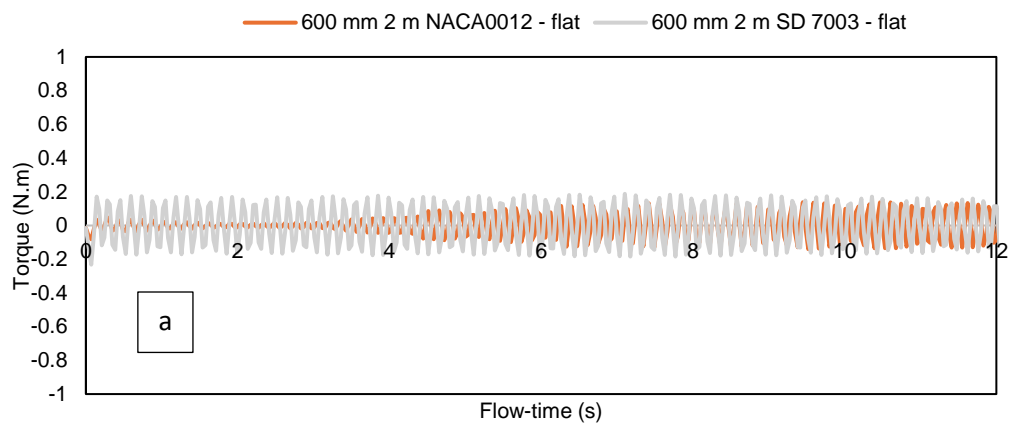
The torque measurements illustrate in Figure 92 highlight significant variations dependent on the aerofoil profiles and roof types. The NACA 0012 aerofoil with a chord and span of 2 metres each installed on a pitched roof achieved the highest torque, peaking at 0.2 N.m (Figure 92b). This setup benefitted from optimal wind flow interaction due to the aerodynamic compatibility of the symmetrical NACA 0012 profile with the angled surface of the pitched roof, enhancing lift and minimising drag. In contrast, the 1-metre version of the NACA 0012, when mounted on a curved roof showed improved aerodynamic flow that maximises torque output, which surpassed the larger 2-metres model in similar wind conditions.

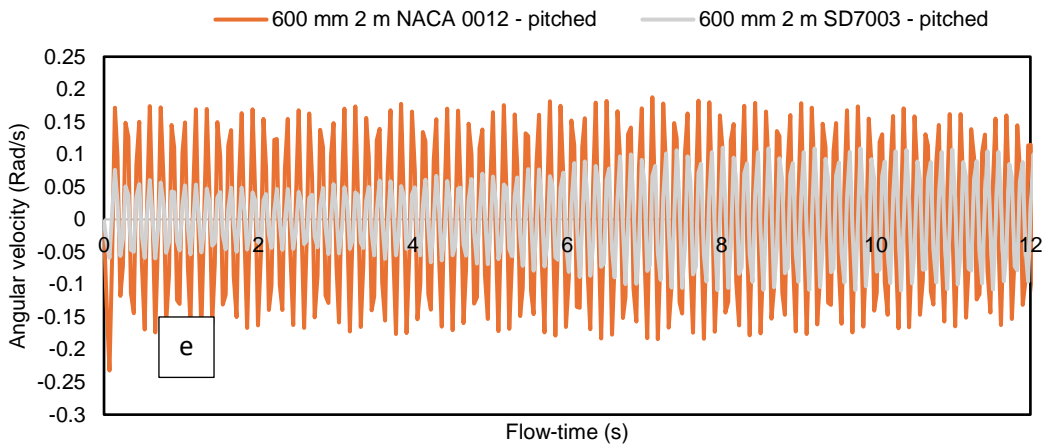
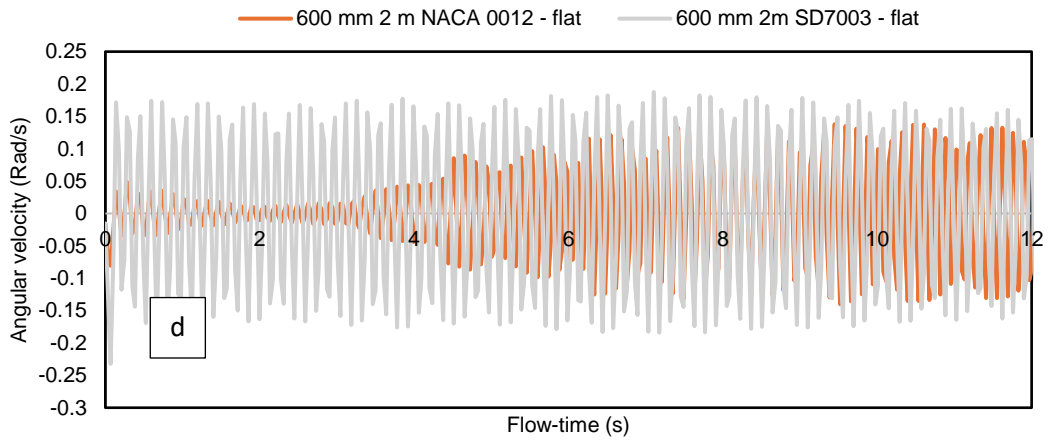
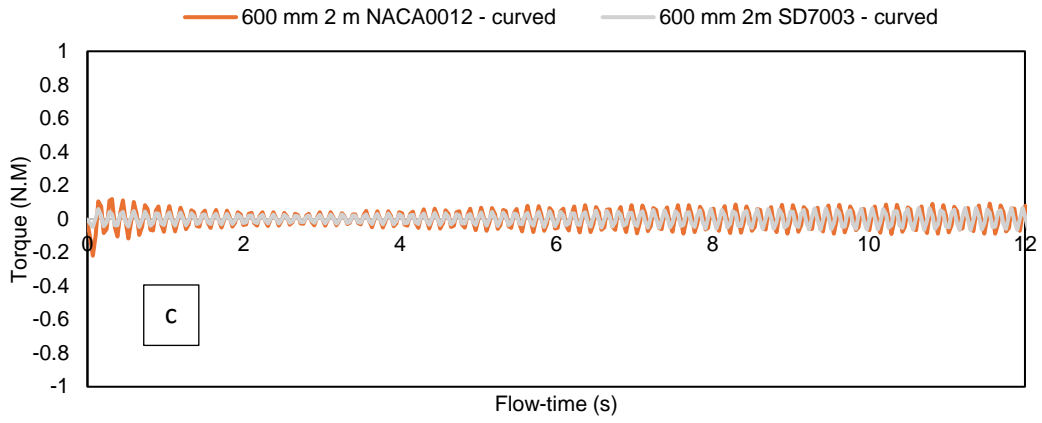
For the 2-metres SD7003 model installed on a flat roof produced the lowest torque recording 0.05 N.m (Figure 92a). The non-symmetrical shape of the SD7003 aerofoil and its interaction with the flat roof architecture created adverse aerodynamic effects such as increased wind shear at the aerofoil's edge, which leads to poor torque performance. This configuration's inefficiency was further worsened by the lift force-induced high displacement of the aerofoil, which nearly reached the rooftop and created a stagnation point that disrupted the wind flow.

Angular velocity results further emphasised the impact of aerofoil and roof type interaction. The 2-metres NACA 0012 on the pitched roof reached a peak angular velocity of 1.8 rad/s (Figure 92e), which was higher than the other 2 cases such as NACA 0012 integrated into the flat (Figure 92d) and curved roof building (Figure 92f). Conversely, the 2-metres SD7003 aerofoil on the flat roof showed an angular velocity of 0.18 rad/s (Figure 92d). The larger scale and increased mass of these 2-metres

installations compared to their 1-metres aerofoil hindered their oscillation capabilities. The reason for this was due to the heavier aerofoil weight and longer chord lengths which approached the rooftop limits, which suggests a necessity for reduced spring constants.

These findings illustrate the influences of aerofoil design, size, and roof architecture on the performance of building-integrated wind energy systems. Proper selection and placement of aerofoils are essential for optimising energy harvesting efficiency. This involves considering factors such as symmetry, displacement potential, and their interaction with building structures. The insights gained from this study enhance the understanding of aerodynamic interactions in wind energy applications. These emphasise the need for tailored system design to maximise the efficiency of wind energy capture in built environments.





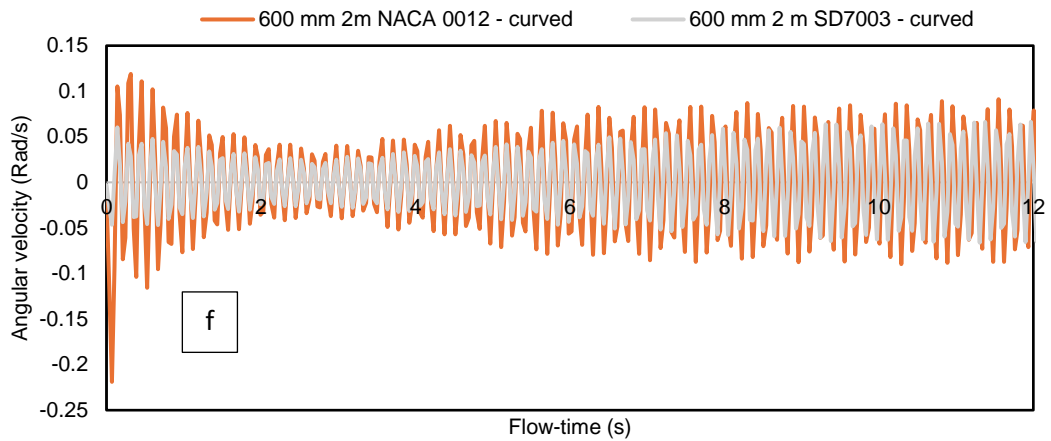


Figure 92. Comparison of the torque between an oscillating NACA 0012 and SD7003 aerofoils integrated into (a) flat, (b) pitched, (c) curved roof with a distance of 600 mm and angular velocity for oscillating NACA 0012 aerofoil integrated into (d) flat, (e) pitched, (f) curved roof with a distance of 600 mm

6.1.5 Effects on mechanical power output of 2m NACA 0012 and 2 m SD7003

Figure 93 shows the average power output for six different investigated parameters. These parameters include the integrated design of 2-metres chord length and 2-metres span NACA 0012 aerofoils into flat, pitched, and curved roof buildings with a spacing of 600 mm apart from each other.

Similarly, the integrated design of 2-metres SD7003 aerofoils into flat, pitched, and curved roof buildings also maintains a 600 mm separation between them. The proximity of the aerofoil to the roof was influenced by its size, which was observed in the integration of both NACA 0012 and SD7003 aerofoils into a curved roof building. In such cases, a reduced in mechanical power output was noted compared to installations on pitched roof buildings. This disparity highlights an issue arising from a 600 mm separation, which affected the efficiency of the wind energy capture system. Consequently, future studies should incorporate a sensitivity analysis on the distance and placement of the aerofoil within curved roof structures to optimise performance.

For NACA 0012 and SD7003 aerofoils with a 2-metres chord length and span achieved the highest performance when integrated into pitched roof building as compared to those installed on flat and curved roof buildings. These NACA 0012 and SD7003 aerofoils integrated into the pitched roof building outperformed installations on flat

and curved roof buildings, with power outputs ranging from 1.3 to 2.6 watts. Conversely, installations on flat roofs yielded 0.6 to 1.2 watts while curved roof installations demonstrated the lowest performance by generating 0.3 to 0.6 watts. Several factors contributed to these variations including the distance between the aerofoil and the curved building, aerofoil size, aerofoil shape, and adjustments to the centre of rotation for the non-symmetrical SD7003 aerofoil at low Reynolds numbers. These modifications were necessitated by the high displacement, which posed a risk of contact with the roof in the curved building scenario.

The results highlight the advantages and disadvantages associated with different installation parameters. Also, it showed that at a 600 mm distance, pitched roofs consistently outperform other configurations for larger scale of 2 metres for both NACA and SD7003 aerofoil profiles. Moreover, the study highlights a trade-off linked to larger-scale aerofoils, which emphasised the challenges posed by increased mass and moment of inertia. This consideration has significant implications for the practicality of implementing larger aerofoils in building-integrated wind energy systems.

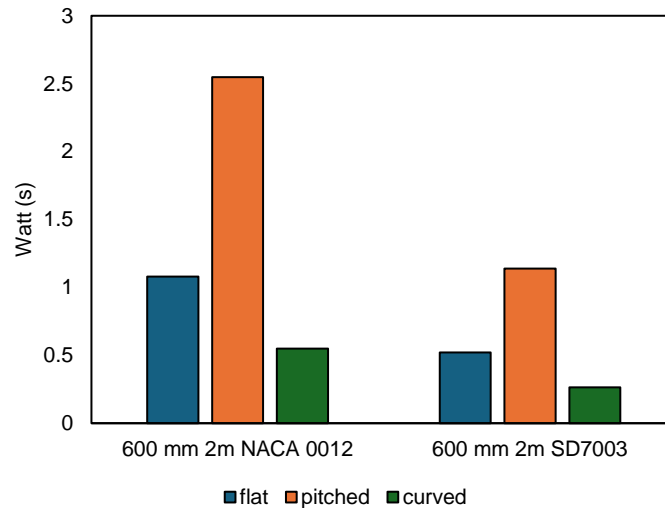


Figure 93. Average power output for the investigated 6 different parameters

In conclusion, the result emphasises the crucial role of roof shape and installation parameters in influencing the performance of building-integrated wind energy harvesting systems. In addition, the larger-scale aerofoils introduced complexities associated with mass and inertia. This study provides practical insights for optimising

wind energy harvesting systems in building structures, which highlights the need for a balanced approach that considers both aerodynamic advantages and structural limitations. Moreover, the study on the 2-metres SD7003 presented challenges associated with low torque and high angular velocity. While the low torque may initially limit rotational force, the high angular velocity provides opportunities for kinetic energy capture. The relationship between these factors highlights a trade-off in power generation, which suggest that while the immediate force may be modest, frequent oscillations at high angular velocity could enhance overall energy conversion efficiency over time. Optimising the system's design and parameters becomes crucial in achieving a balance for maximising power generation in building-integrated wind energy harvesting systems.

6.2 Impact of placement on NACA 0012 performance

To understand the benefit of placement of NACA 0012 at a distance of 600 mm and 1000 mm to the rooftop of the building, 6 cases were investigated including NACA 0012 installed into three different roof shapes including flat, pitched, and curved roof building structure. The goal was to determine the most effective placement for enhancing the performance of the wind energy harvesting system.

In the context of available literature, this research aligns with the broader exploration of aerofoil integration into building structures for energy harvesting purposes. Literature on wind energy and building-integrated renewable energy systems highlights the significance of aerofoil design, placement, and interaction with different roof shapes in maximising power output. The consideration of mass properties, including mass, moment of inertia, and specific dimensions, ensures consistency with established practices in aerofoil analysis.

Through building upon the foundations showed in Chapter 5, which presumably covers aspects like aerodynamic characteristics and mechanical power output, this investigation contributes to the ongoing discourse on the optimal design and placement of aerofoils for effective energy harvesting. It adds valuable insights to the existing body of knowledge, providing practical guidance for engineers and researchers involved in building-integrated wind energy systems. The results of these analyses are

poised to contribute substantively to the advancement of energy harvesting performance and inform future design considerations in building-integrated renewable energy technologies.

6.2.1 Velocity magnitude contours for 600 mm and 1000 mm NACA 0012

Figure 94 shows the contours of velocity magnitude for the NACA 0012 aerofoil integrated into the building roof structure with distances of 600 mm and 1000 mm between the aerofoil and the rooftop. The aerofoil dimensions include a 1-metre chord length and a 1-metre span. Moreover, uniform material properties including mass and moment of inertia of foam were used throughout this analysis. This approach sets as a guideline for a detailed examination of the velocity distribution around the aerofoil at different rooftop distances and provides valuable insights into the aerodynamic behavior of the system.

The comparison of NACA 0012 aerofoil installations at distances of 600 mm and 1000 mm into a curved roof building structure provides valuable insights into the torque, angular velocity, and mechanical power output of a wind energy harvesting system. The results illustrated in Figure 94 (a, c, and e) show that the NACA 0012 aerofoil integrated into the curved roof setting with a 600 mm distance between each unit outperformed other configurations and achieved the highest mechanical power output. Conversely, the least favourable performance was observed when the same aerofoil was installed at 600 mm in a flat roof building structure. This variation suggests a critical influence of the roof shape on the interaction between the aerofoil and the wind flow, which affects the torque and angular velocity dynamics.

Further analysis comparing the 1000 mm distance installations reveals that the NACA 0012 aerofoil in the curved roof structure still demonstrated superior performance compared to installations in pitched and flat roof buildings, as shown in Figure 94 (c, d, and f). Moreover, the 1000 mm NACA 0012 in the flat roof building outperformed its 600 mm counterpart in the same setting. The observation attributes this improvement to the mitigation of intense wind flow recirculation, which emphasised the importance of the specific placement of the aerofoil for optimal wind energy harvesting. These findings highlight the complex relationship between aerofoil

placement, roof shape, and the resulting torque and angular velocity dynamics, which are all crucial factors influencing the overall mechanical power output of the system.

In conclusion, the results suggest that the proposed design with a NACA 0012 aerofoil at a 600 mm distance in a curved roof building structure offers the most promising configuration for enhanced wind energy harvesting performance. The comparison of torque and angular velocity dynamics across different roof shapes and distances provides practical insights for optimising the design and placement of aerofoils in building-integrated wind energy systems. These findings contribute valuable information to the broader understanding of aerodynamic interactions in the context of renewable energy technologies.

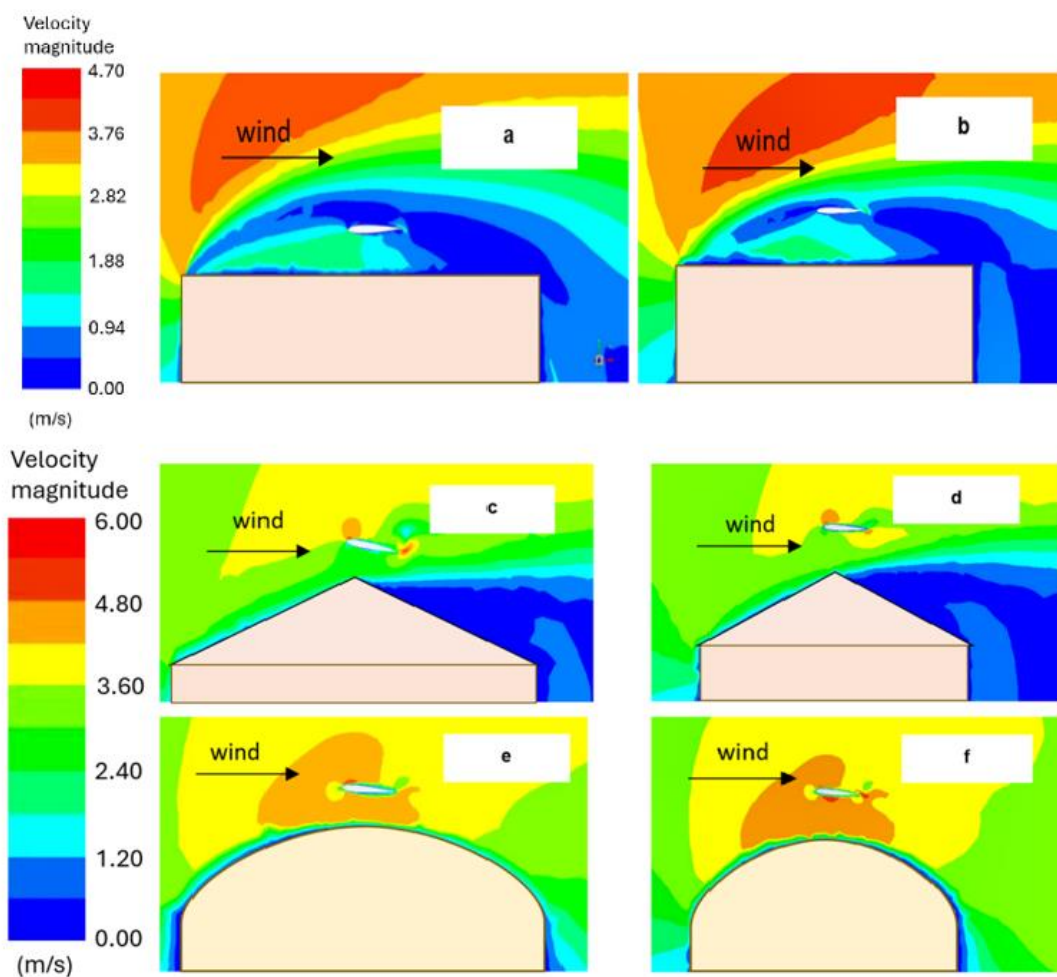


Figure 94. Velocity magnitude contours for oscillating NACA 0012 aerofoil integrated into (a) flat, (c) pitched, and (e) curved roof at 3 m/s with a distance of 600 mm and for oscillating NACA 0012 aerofoil integrated into (b) flat, (d) pitched, and (f) curved roof at 3 m/s with a distance of 1000 mm

6.2.2 Torque and angular velocity of 600 mm and 1000 mm NACA 0012

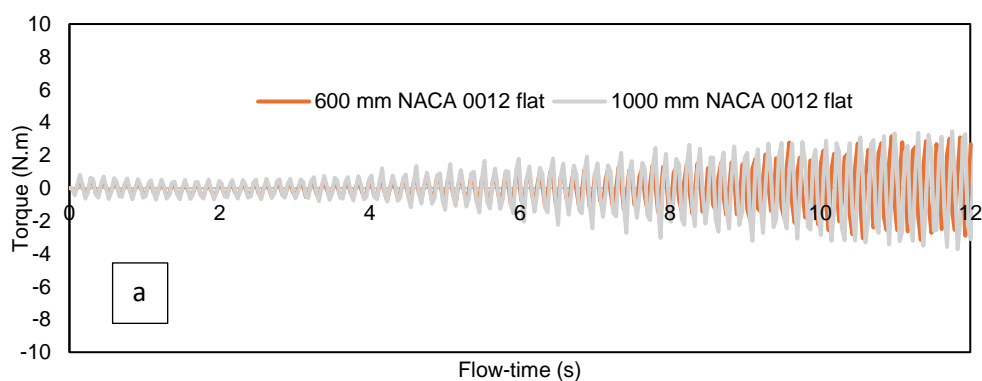
Figure 95 demonstrates the comparison of the torque between an oscillating NACA 0012 aerofoil integrated into (a) flat, (b) pitched, (c) curved roof with a distance of 600 mm and 1000 mm and angular velocity for oscillating NACA 0012 aerofoil integrated into (d) flat, (e) pitched, (f) curved roof with a distance of 600 mm and 1000 mm. The findings regarding torque for the oscillating wind energy converter integrated into the building roof structure show insights. Figure 95 (c) illustrates that the highest torque of 12 N.m occurred with a 600 mm NACA 0012 aerofoil installed on the curved roof building.

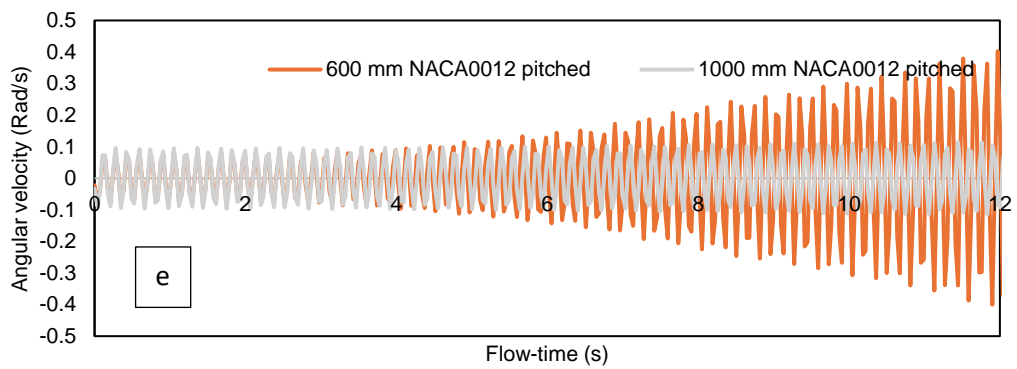
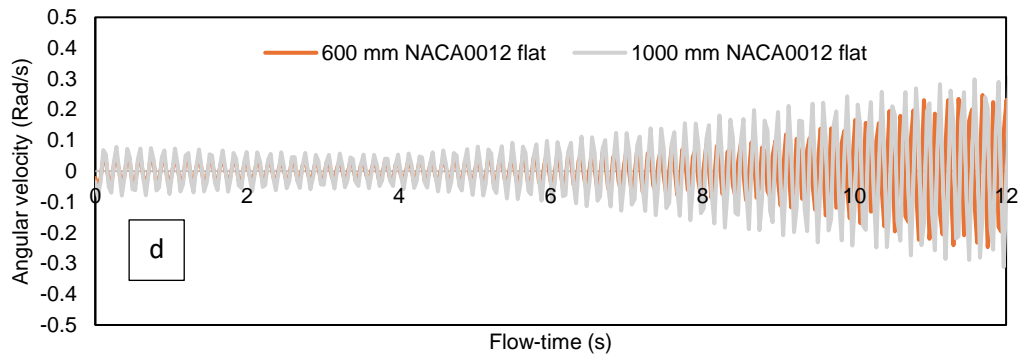
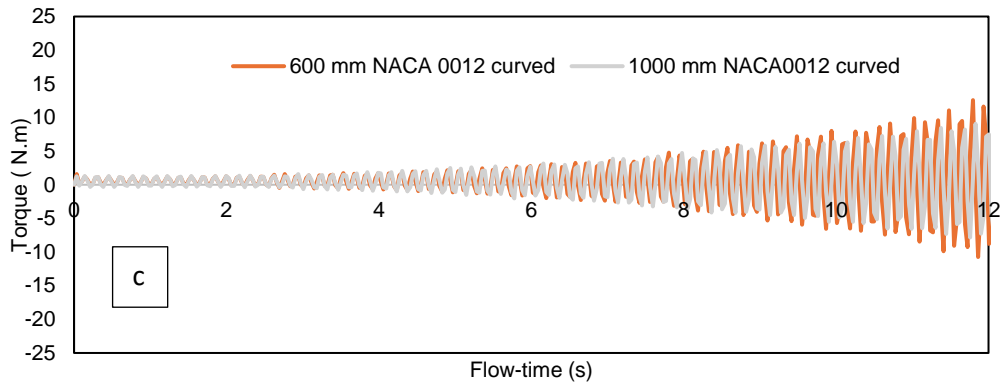
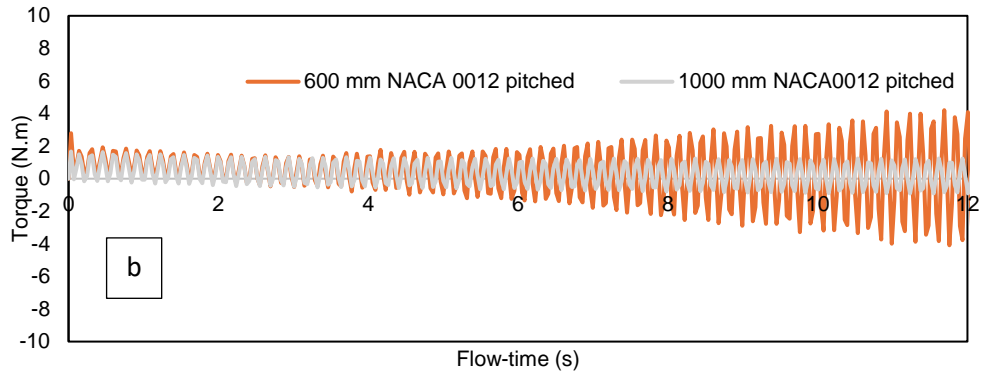
While the lowest torque of 2 N.m can be observed for oscillating aerofoil integrated into flat roof building with a distance of 600 mm, which is almost the same for aerofoil installed near a flat roof with a distance of 1000 mm (Figure 95a). This discrepancy indicates an impact on the aerofoil wind energy converter when positioned close and the shape of flat roof building, which is attributed to significant recirculation of wind flow around the aerofoil and wind shear on the windward side of the flat roof. Contrary to the flat roof scenario, the installation of the aerofoil into the curved roof building yields the highest performance. This aligns with existing literature, which highlights curved roofs as providing higher wind speed acceleration compared to flat and pitched roof shapes. Notably, a different outcome arises when the aerofoil was placed at the curved rooftop with a distance of 1000 mm, indicating a negative impact on the wind energy converter due to the spacing between the aerofoil and the roof. This understanding emphasises the importance of roof shape and aerofoil positioning in optimising the performance of building-integrated wind energy harvesting systems.

In Figure 95 (b), the impact of torque variation is more noticeable for an oscillating NACA 0012 aerofoil integrated into a pitched roof with different spacings of 600 mm and 1000 mm. The 600 mm spacing between the airfoil and the pitched roof achieved a higher torque, reaching up to 5 N.m, compared to a significant reduction to 2 N.m at a 1000 mm spacing. This suggests that the aerofoil's wind energy harvesting efficiency is more favorable with a 600 mm spacing as opposed to 1000 mm when installed on a pitched roof structure.

Conversely, Figure 95 (d) shows that the lowest torque for the same aerofoil near a flat roof was associated with a lower angular velocity. This observation indicates that the proximity of the aerofoil to a flat roof creates unfavourable aerodynamic conditions that reduce rotational motion. The causes of this phenomenon include recirculation of wind flow around the aerofoil and wind shear on the windward side of the roof both of which minimize the efficiency of angular velocity production. In addition, Figure 95 (e) illustrates a drop in angular velocity when comparing the oscillating NACA 0012 aerofoil integrated into a pitched roof building with spacings of 600 mm and 1000 mm. The angular velocity peaked at 0.4 rad/s and decreased to 0.1 rad/s as the spacing between the aerofoil and the pitched roof increased from 600 mm to 1000 mm.

It is important to note that the negative impact observed when the aerofoil is installed at the pitched (Figure 95e) and curved rooftops (Figure 95f) with a distance of 1000 mm resulted in a lower angular velocity. This highlights the system's sensitivity to variations in the spacing between the aerofoil and the roof. This emphasises the need for careful consideration of aerodynamic interactions and optimal positioning to achieve the desired angular velocity for effective wind energy conversion. Also, the dynamics vary with different roof shapes, indicating that further research is necessary to understand the specific interactions between airfoil shapes and building roof configurations. Overall, the findings emphasise the importance of both roof shape and specific installation parameters in influencing angular velocity and the performance of building-integrated wind energy harvesting systems.





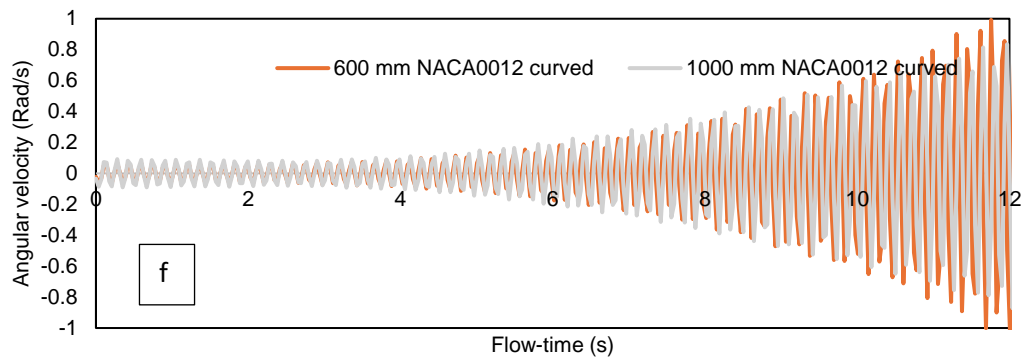


Figure 95. Comparison of the torque between an oscillating NACA 0012 aerofoil integrated into (a) flat, (b) pitched, (c) curved roof with a distance of 600 mm and 1000 mm and angular velocity for oscillating NACA 0012 aerofoil integrated into (d) flat, (e) pitched, (f) curved roof with a distance of 600 mm and 1000 mm

6.2.3 Effects on mechanical power output of 600 mm and 1000 mm NACA 0012

The findings based on torque and angular velocity values of an oscillating aerofoil integrated into various building roof structures offer valuable insights into the predicted power output. Figure 96 shows that the highest power output of 5.6 watts was achieved when a NACA 0012 aerofoil was integrated into a curved roof building with a 600 mm distance between the aerofoil and the rooftop. This outcome highlights the favourable aerodynamic conditions associated with a curved roof, resulting in efficient wind energy conversion. The second highest power output was observed for a NACA 0012 aerofoil installed into a pitched roof building with a 600 mm distance, which demonstrated the significance of roof shape and aerofoil positioning in influencing power generation. Conversely, the least performance was observed for the NACA 0012 aerofoil installed into a flat roof building with a 600 mm distance, which yielded a power output of 0.29 watts. Moreover, a NACA 0012 aerofoil installed into a pitched roof building with a 1000 mm distance showed a power output of 0.18 watts. Moreover, the results indicate that the 1000 mm distance between the aerofoil and the rooftop did not yield better performance for both pitched and curved roof structures. However, a notable exception was observed for a NACA 0012 aerofoil installed into a flat roof building, where a better performance was achieved with the greater distance between the aerofoil and rooftop. In conclusion, the study emphasises the crucial role of roof shape and specific installation parameters in influencing the power output of building-integrated wind energy harvesters.

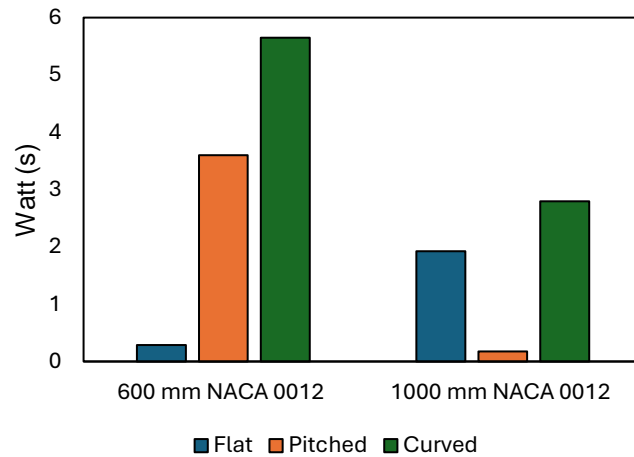


Figure 96. Average power output for the investigated 6 different parameters

The observed highest torque for the 600 mm NACA 0012 aerofoil installed into the curved roof building suggests a corresponding high angular velocity. This indicates that when the aerofoil is positioned on a curved roof it experiences enhanced rotational motion which results in a more efficient conversion of wind-induced mechanical vibrations into angular velocity.

6.3 Impact of placement on SD7003 performance

The study investigates the fluid-structure interaction dynamics between the aerofoil and the building roof structure by using a systematic approach to vary the aerofoil's proximity to the building. Specifically, the aerofoil was positioned at two distinct distances: 1000 mm and 600 mm. This variation aims to assess how placement affects the performance of the wind energy capture system by offering insights into fluid flow characteristics and their effects on power output. The purpose of the study was to examine how proximity affects the aerofoil's interaction with the building roof structure. Figure 97 shows the different parameters of SD7003 aerofoil installed into the three different roof shapes including flat, pitched, and curved roof building structures with a distance of 600 mm and 1000 mm. Table 17 shows the parameters and material properties of SD7003 applied in this study.

Table 17. Parameters and material properties of SD7003 with 1000 mm and 600 mm distance

Aerofoil profile	Roof shape	Distance between aerofoil and rooftop	Dimension	Material	Mass (kg)	Moment of inertia (kg.m ²)	Centre of rotation
SD7003 low Reynolds number	Flat	1000 mm	1 m chord length and 1 m span	Foam	2.137	0.12	0.25 m of chord length
	Pitched						
	Curved						
SD7003 low Reynolds number	Flat	600 mm	1 m chord length and 1 m span	Foam	2.137	0.12	0.25 m of chord length
	Pitched						
	Curved						

6.3.1 Velocity magnitude contours for 600 mm and 1000 mm SD7003

The study shown in Figure 97 (a-f) examines SD7003 non-symmetrical low Reynolds number aerofoil integrated into (a) flat, (c) pitched, and (e) curved roof shapes at a distance of 600 mm and integrated into (b) flat, (d) pitched, and (f) curved roof shapes at a distance of 1000 mm. The non-symmetrical SD7003 aerofoil was expected to generate higher lift compared to the symmetrical NACA 0012 aerofoil. The analysis shows that the curved roof configuration with higher wind speed acceleration and the non-symmetrical aerofoil shape led to increased lift and displacement, which caused the aerofoil to nearly hit the rooftop. The study recommends considering the distance or placement of the aerofoil for improved efficiency in wind energy harvesting. Moreover, the stagnation of wind velocity magnitude at the curved roof and the wind shear effects on the flat roof contribute to variations in power output. In contrast, the symmetrical NACA 0012 aerofoil demonstrates lower lift generation. These findings emphasise the importance of aerofoil shape, roof configuration, and placement for optimising wind energy harvesting efficiency, aligning with existing literature on aerofoil aerodynamics in different architectural contexts.

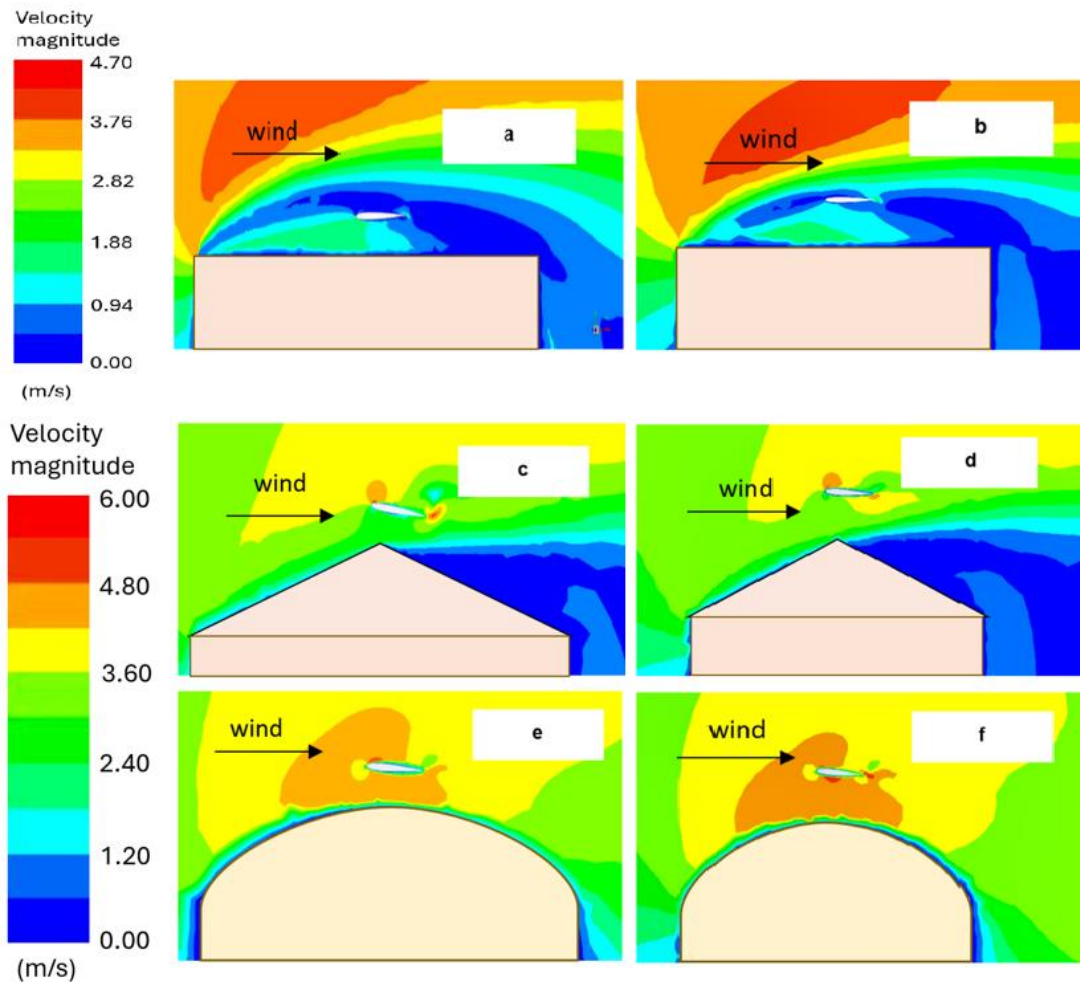


Figure 97. SD7003 non-symmetrical low Reynolds number aerofoil integrated into (a) flat, (c) pitched, and (e) curved roof shapes at a distance of 600 mm and integrated into (b) flat, (d) pitched, and (f) curved roof shapes at a distance of 1000 mm

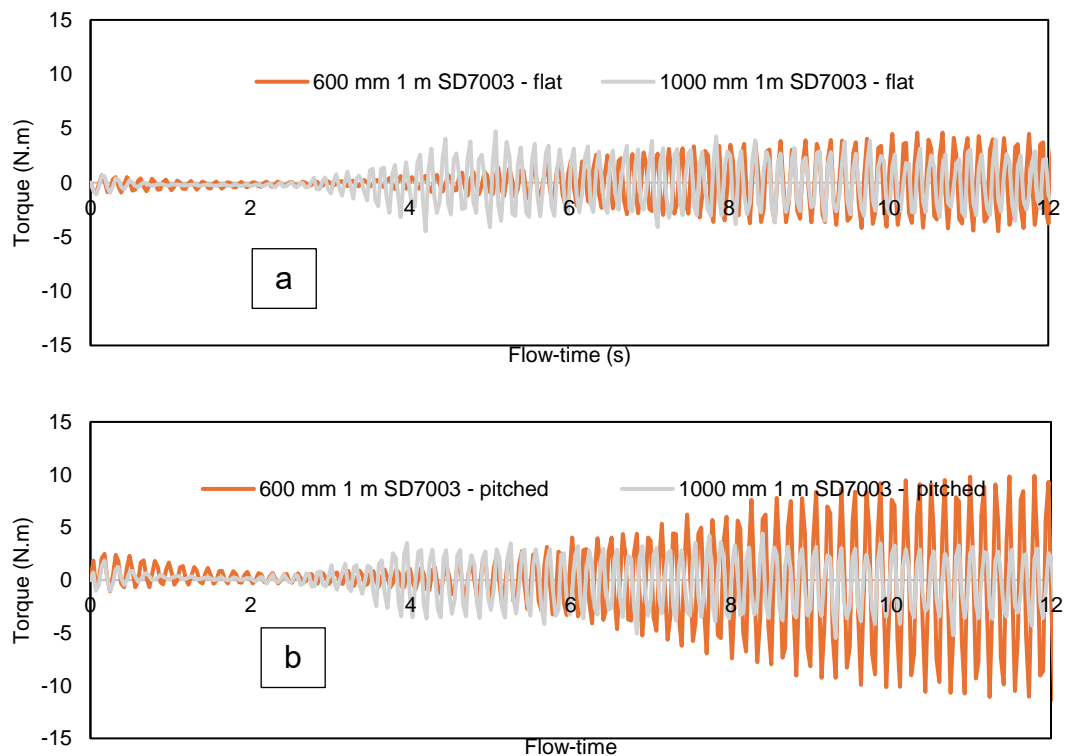
6.3.2 Torque and angular velocity of 600 mm and 1000 mm SD7003

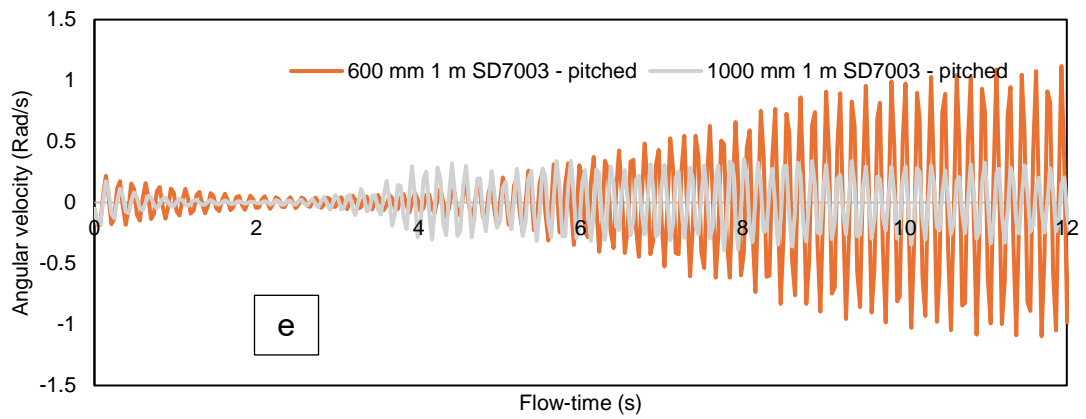
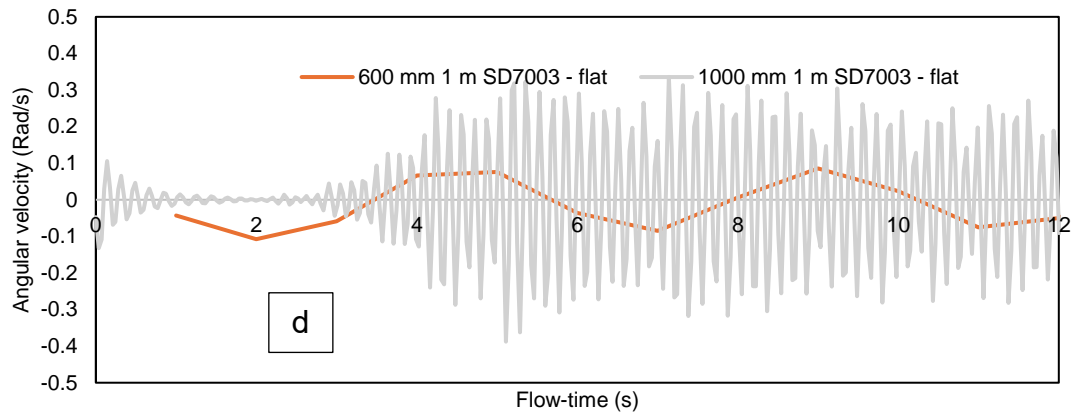
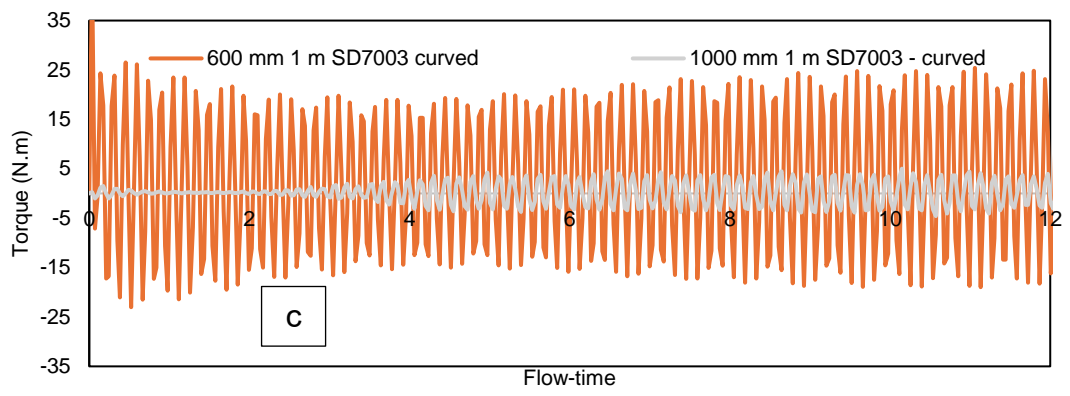
Figure 98 demonstrates the comparison of the torque between an oscillating NACA 0012 and SD7003 aerofoil integrated into (a) flat, (b) pitched, (c) curved roof and angular velocity for oscillating NACA 0012 and SD7003 aerofoil integrated into (d) flat, (e) pitched, (f) curved with a distance of 600 mm and 1000 mm. The integration of the 1-metre SD7003 parameter into the curved roof building at a 600 mm distance resulted in the highest torque of 25 N.m (Figure 98c), which was accompanied by 0.47 rad/s low angular velocity (Figure 98f). This position at the top ridge of the building with a specified distance, demonstrates a system susceptible to rotational forces, which led to a notably slow rotational speed. This phenomenon aligns with Newton's second

law of rotation $\tau = I\alpha$, where the high torque and low angular velocity indicates a significant rotational force countered by resistance from the moment of inertia. This observation resonates with existing literature on mechanical systems and rotational dynamics.

Comparatively, the performance of the 1-metre SD7003 in a pitched roof building resulted in the second-highest torque at 7 N.m and an angular velocity of 0.7 rad/s. The third highest torque was achieved by the same parameter integrated into the curved roof building. Conversely, low performance was noted for the 1-metre SD7003 integrated into the flat roof building at both 600 mm and 1000 mm distances, as well as in the pitched roof building at a 1000 mm distance. These findings contribute to the existing body of knowledge on the adaptability and effectiveness of specific parameters in different architectural contexts.

Overall, the results highlight the suitability of the 1-metre SD7003 for flat, pitched, and curved roof buildings at a 600 mm distance, providing valuable insights into the dynamics of torque and angular velocity in architectural and aerodynamic contexts.





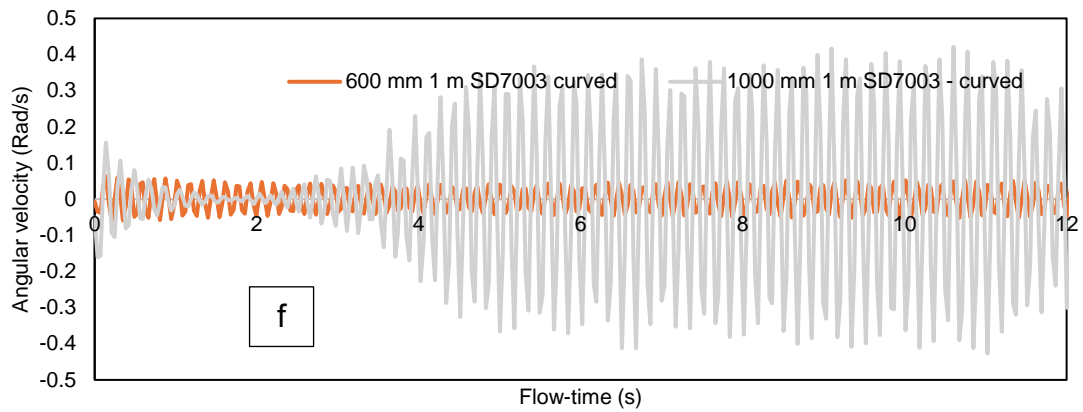


Figure 98. Comparison of the torque between an oscillating NACA 0012 and SD7003 aerofoil integrated into (a) flat, (b) pitched, (c) curved roof and angular velocity for oscillating NACA 0012 and SD7003 aerofoil integrated into (d) flat, (e) pitched, (f) curved with a distance of 600 mm and 1000 mm

6.3.3 Effects on mechanical power output of 600 mm and 1000 mm SD7003

Figure 99 shows the average power output for the investigated 6 different parameters with 600 mm distance demonstrates the study reports varying power outputs for different configurations of the SD7003 aerofoil installed in flat, pitched, and curved roof building structures at two different distances (600 mm and 1000 mm). The highest power output, reaching 5 watts, was achieved when the SD7003 was installed into the pitched roof building with a distance of 600 mm. Conversely, the lowest power output yielded 0.21 watts, which was observed when the same aerofoil was installed in the flat roof building with a distance of 1000 mm. Notably, the overall superior performance of the SD7003 aerofoil was consistently observed when installed at a closer distance of 600 mm, regardless of the roof shape. These findings align with existing literature on aerofoil placement and distance optimisation, highlighting the impact of these parameters on power output in wind energy harvesting systems.

The empirical results indicate that the SD7003 aerofoil, when integrated into the pitched roof, yields superior power output compared to its counterpart in the curved roof setting. This finding aligns with existing literature, which highlights the influence of aerofoil shape and building geometry on energy capture efficiency. Notably, the conclusion is drawn that the aerofoil's proximity to the building structure plays an important role in determining performance outcomes. The study observes that at a distance of 1000 mm, wind resources and speed acceleration are not optimally

captured by the SD7003 aerofoil. This highlights the importance of considering aerofoil placement in the context of fluid dynamics, as insufficient proximity may hinder the efficient utilisation of available wind resources. The suggestion derived from the results advocates for a closer proximity of the aerofoil to the building roof structure for enhanced performance. This proposition aligns with the broader scientific discourse on optimising wind energy harvesting system placement for maximum energy extraction, as documented in literature focusing on wind energy harvesting system array configurations. The implication is that an understanding of fluid-structure interactions, informed by specific aerofoil characteristics and building configurations, can lead to more effective wind energy capture systems.

In summary, the methodology used was combined with findings and recommendations, which contributes to the evolving knowledge regarding dynamic behaviour and fluid-structure interactions in building-integrated wind energy systems. The study features the importance of aerofoil proximity in influencing performance outcomes, aligning with established literature in the field and offering valuable insights for future research and application.

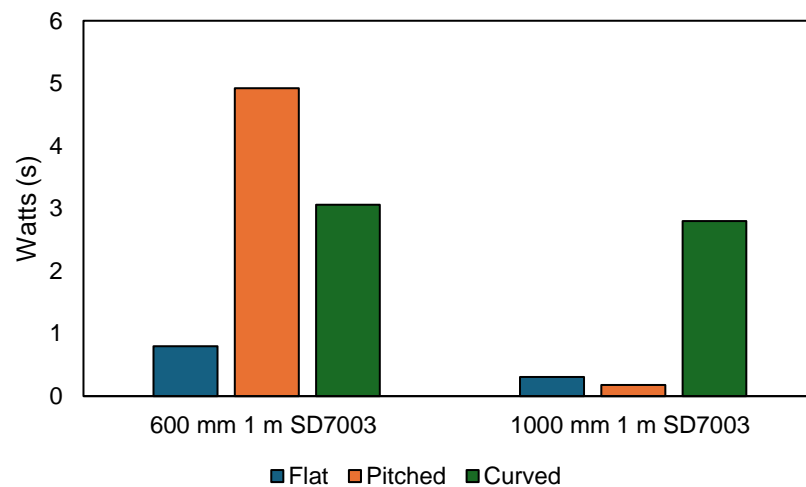


Figure 99. Average power output for the investigated 6 different parameters with 600 mm distance

6.4 Impact of placement of NACA 0012 and SD7003 into the building roof

To enhance the performance of a 2-metres oscillating aerofoil integrated into a building roof structure for wind energy harvesting, this study explores the impact of varying the distance between the aerofoil and the top of the ridge of the building roof. Specifically,

the aerofoil placement was altered from a 600 mm to a 1000 mm distance, maintaining consistency in scale, utilising both the 2-metres NACA 0012 and 2-metres SD7003 aerofoils, along with equivalent mass, moment of inertia, and centre of rotation parameters. Comprehensive details of the relevant parameters and material properties can be found in Table 18. This investigation aims to contribute to the existing literature by providing insights into the effects and significance of optimising the placement of an aerofoil within a building roof structure for effective wind energy harvesting.

Table 18. Parameters and material properties of 2 m NACA 0012 and 2m SD7003 with 1000 mm distance between the aerofoil and rooftop

Case (s)	Aerofoil profile	Roof shape	Distance between aerofoil and rooftop	Dimension	Material	Mass (kg)	Moment of inertia (kg.m ²)	Centre of rotation (m)
1	NACA 0012	Flat	1000 mm	2 m chord length and 2 m span	Foam	6.8	1.52	0.5 m of chord length
2		Pitched						
3		Curved						
4	SD7003 low Reynolds number	Flat	1000 mm	2 m chord length and 2 m span	Foam	4.457	0.88	0.77 m of chord length
5		Pitched						
6		Curved						

6.4.1 Torque and angular velocity of 1000 mm NACA 0012 and 1000 mm SD7003

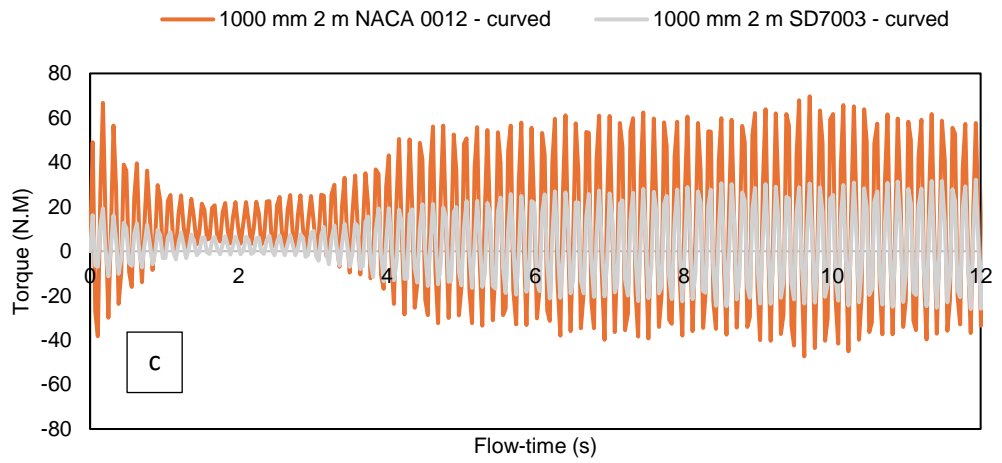
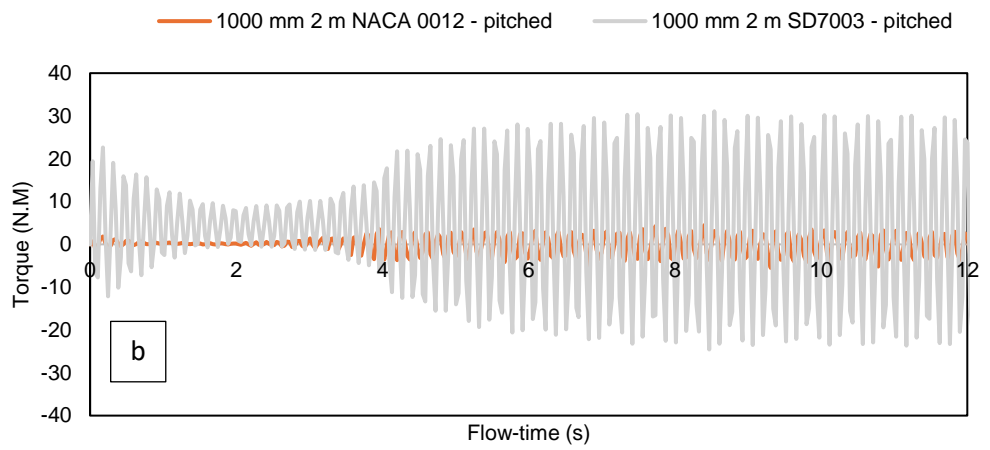
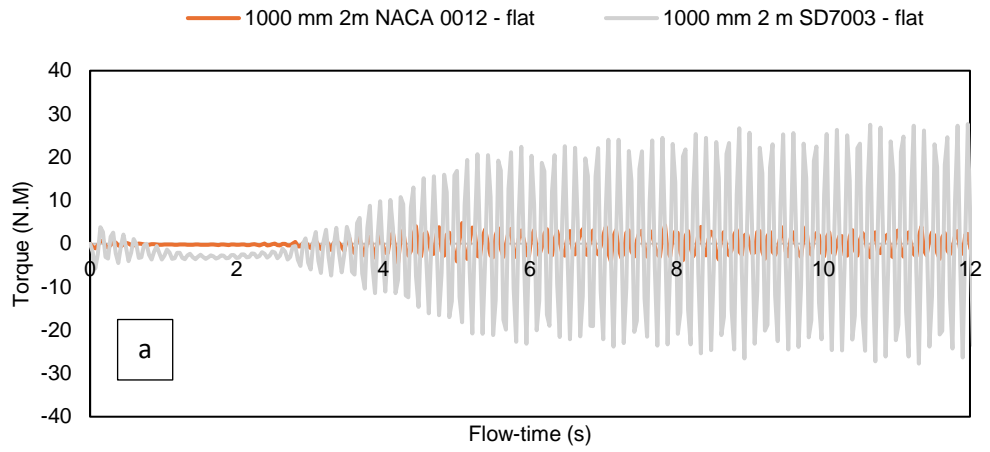
Figure 100 shows the comparison of the torque between an oscillating 2 m NACA 0012 and 2 m SD7003 aerofoil integrated into (a) flat, (b) pitched, (c) curved roof with a distance of 1000 mm and angular velocity for oscillating 2 m NACA 0012 and SD7003 aerofoil integrated into (d) flat, (e) pitched, (f) curved roof with a distance of 1000 mm.

The initial torque surge signifies the aerofoils' prompt response to the wind, leading to rapid rotation. Figure 100 (a-c) shows the transient phase from 0.1 seconds to 2.4 seconds involves adjustments, which is influenced by resistance, resulting in a temporary torque decrease. The subsequent rise and stabilisation of torque between 18 N.m and 55 N.m suggests that the system reaches a more stable state as aerodynamic forces and torques achieve stability. This oscillatory pattern may be influenced by specific aerofoil characteristics, building integration, and natural wind fluctuations,

emphasising the need to comprehend and optimise these dynamics for improved system performance.

Examining torque values, the highest, up to 70 N.m, occurred with the 2 metres NACA 0012 integrated into the curved roof building (Figure 100c). The second highest, peaking at 20 N.m, was noted for the 2 metres SD7003 in the pitched roof building (Figure 100b), while the 2 metres SD7003 in the curved roof building at 1000 mm achieved the third highest, up to 18 N.m (Figure 100c). Conversely, the least performance was observed for the 2 metres SD7003 in the flat roof buildings and the 2 metres NACA 0012 in the flat roof building (Figure 100a). These results suggest divergent performance characteristics among aerofoils integrated into various roofs and distances. The study highlights the significant impact of aerofoil selection and integration into distinct roof configurations on the wind energy harvesting system's overall efficiency. This variability is attributed to aerofoil aerodynamics and their interaction with wind in different roof settings. Moreover, variations in the centre of rotation can influence aerofoil wind interaction, affecting generated torque and angular velocity. In conclusion, the study emphasises the complex connection between aerofoil choice, roof integration, and centre of rotation positioning in determining wind energy harvesting system efficiency.

The oscillating behaviour observed in the wind energy harvesting system integrated into the building roof structure stems from the dynamic interaction between the aerofoils and incoming wind flow. Figure 100 (d-f) illustrate the angular velocity behaviour with a rapid response of the aerofoils to the wind, inducing quick rotation. Subsequently, a transient phase from 0.1 seconds to 2.4 seconds involves adjustments, due to the influence of damping effects or resistance, leading to a temporary decrease in angular velocity. The subsequent increase and stabilisation of angular velocity between 0.05 rad/s and 1 rad/s suggest the system attains a more stable state as aerodynamic forces and torques find equilibrium. This oscillatory pattern may be influenced by the specific aerodynamic characteristics of the aerofoils, building integration, and natural fluctuations in wind dynamics, highlighting the importance of understanding and optimising these dynamics for enhanced system performance.



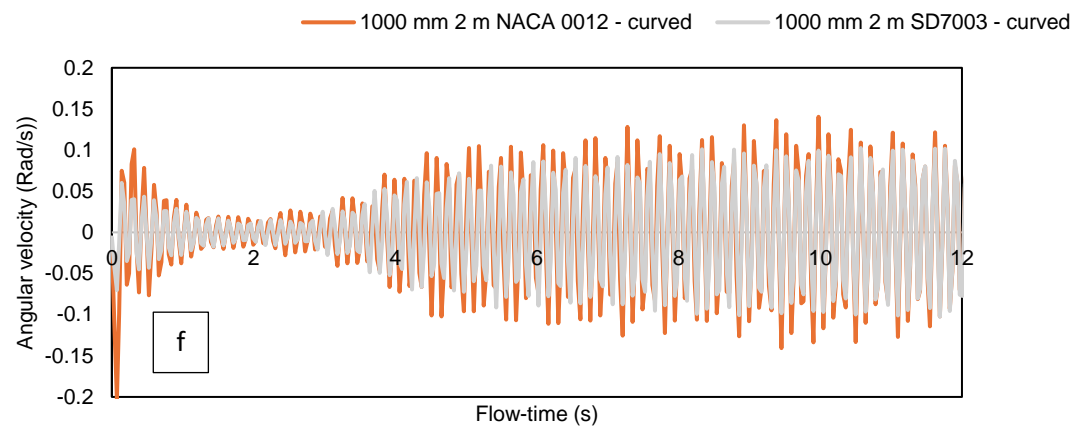
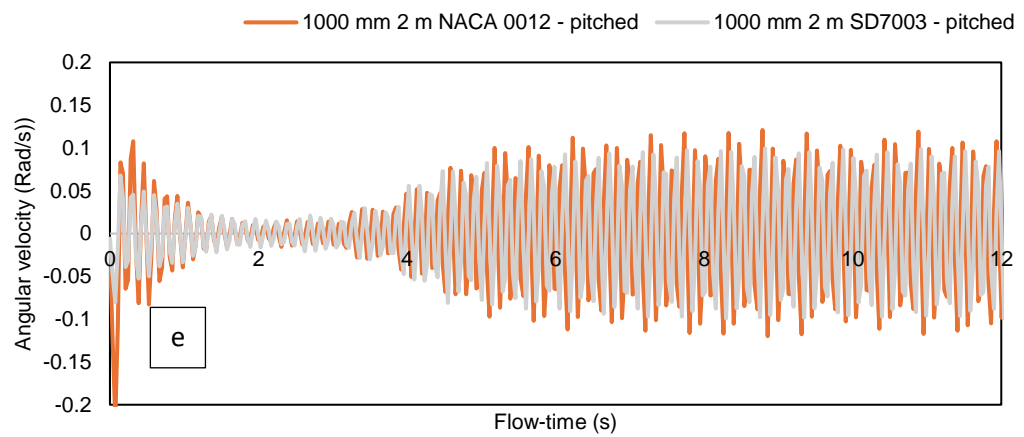
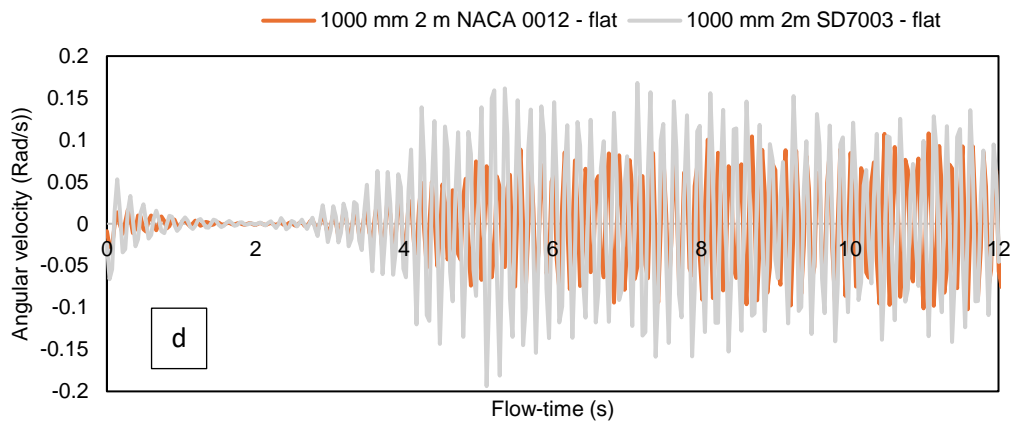


Figure 100. Comparison of the torque between an oscillating 2 m NACA 0012 and 2 m SD7003 aerofoil integrated into (a) flat, (b) pitched, (c) curved roof with a distance of 1000 mm and angular velocity for oscillating 2 m NACA 0012 and 2 m SD7003 aerofoil integrated into (d) flat, (e) pitched, (f) curved roof with a distance of 1000 mm

6.4.2 Effects on mechanical power output of 1000 mm NACA 0012 and 1000 mm SD7003

Figure 101 demonstrates the average power output for the investigated 6 different parameters for 1000 mm 2 m NACA 0012 and 1000 mm 2 m SD7003 integrated into flat, pitched, and curved roof building. This study provides a comparative analysis of various parameters associated with oscillating NACA 0012 and SD7003 aerofoils integrated into flat, pitched, and curved roof buildings. Notably, the 2-metres NACA 0012 integrated into the curved roof building demonstrated the highest power output at 1.2 watts, surpassing other configurations. The second-highest power output, 1.1 watts, was achieved by the 2-metres NACA 0012 integrated into the pitched roof building, while the 2-metres SD7003 parameter in the pitched roof setting attained the third-highest output at 1 watt. Conversely, the lowest power outputs were observed when both symmetrical and non-symmetrical aerofoils were placed in flat roof buildings, with the SD700 non-symmetrical aerofoil yielding 0.6 watts and the NACA 0012 symmetrical aerofoil demonstrating the least performance.

Various factors contribute to the performance of the oscillating wind energy harvesting system in building roof structures, including aerofoil shape, roof shape, aerofoil placement, centre of rotation, weight, mass, moment of inertia, and aerofoil size. Despite expectations that the SD7003 non-symmetrical aerofoil would outperform the NACA 0012 symmetrical profile, the results indicated superior performance by the 2-metres NACA 0012 in the building roof structure. The choice of centre of rotation, aerofoil shape, roof shape, placement, weight, mass, moment of inertia, and size collectively influenced the performance of the oscillating wind energy harvesting system. In particular, the centre of rotation for NACA 0012, located at the quarter of the chord length, is identified as a key parameter for optimisation in future studies. Moreover, the influence of roof shape and the distance between the aerofoil and the building roof was evident, with the performance varying based on aerofoil characteristics and the presence of separation bubbles in the case of the SD7003 non-symmetrical aerofoil. These findings emphasise the complexity of the relationship between these parameters and the need for continued investigation to enhance the efficiency of building-integrated wind energy systems.

Overall, the results indicate that the 2 metres NACA 0012 integrated into the pitched and curved roof building with a distance of 1000 mm provided better performance. While a different behaviour was achieved for 2 metres NACA 0012 integrated into the flat roof building. It shows that 2 metres SD7003 integrated into the flat roof building showed better performance as compared to when installed into the flat roof building with a distance of 1000 mm. In addition, the 2 metres NACA 0012 aerofoil showed best performance for curved roof building as compared to pitched roof building, while the 2 metres SD7003 provided best performance when integrated into the pitched roof building with a distance of 1000 mm. These results show the aerofoil affects the efficiency for wind energy harvesting system, also considering the centre of rotation is different to make it displace to the point that it hits the roof building, which is not suitable for wind energy harvesting system.

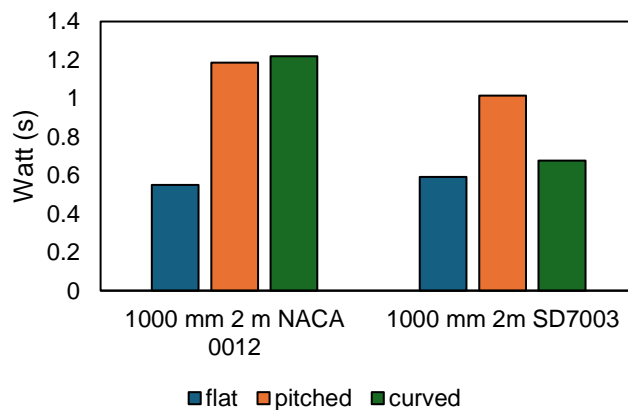


Figure 101. Average power output for the investigated 6 different parameters

In conclusion, the successful integration of wind energy harvesting systems into building structures necessitates a comprehensive consideration of key factors. The scale of the system is influenced by size and capacity, and this is crucial for determining energy output while accounting for space constraints and cost considerations. Aerofoil shape significantly impacts aerodynamic performance and energy conversion efficiency, emphasising the need for alignment with wind speed and operational conditions.

The centre of rotation serves as a fundamental factor in ensuring system stability and responsiveness to wind pattern changes during oscillations. Strategic placement of the wind energy harvesting system on the building, in areas with consistent and strong

wind flow, is essential for maximising energy production. The integration should not only be aesthetically pleasing but also structurally sound, emphasising the importance of the building's roof shape in influencing wind flow patterns and overall system efficiency. Moreover, the consideration of weight, connected to mass and moment of inertia, plays a critical role in the system's performance. The scale of the system not only influences its overall weight but also affects the moment of inertia, influencing the system's responsiveness to changes in wind conditions. Achieving an optimal balance in weight, mass distribution, and moment of inertia is essential for ensuring stability and efficiency in the wind energy harvesting process.

In summary, achieving a successful building-integrated wind energy harvesting system requires a holistic approach encompassing scale, aerofoil shape, centre of rotation, placement, roof shape, and considerations related to weight, mass, and moment of inertia. Optimising these interconnected factors ensures higher energy efficiency, reduces environmental impact, and establishes sustainable solutions for on-site renewable energy generation. Simultaneously, understanding the effects of aerofoil profile, scale, material properties, and the distance between the aerofoil and rooftop is crucial for fine-tuning system performance and enhancing overall efficiency in wind energy capture.

6.5 Impact of support arm on oscillating aerofoil performance

In the pursuit of performance optimisation, a novel model featuring an aerofoil with a support arm was developed to examine its aerodynamic characteristics and assess its impact on the harvesting performance of the aerofoil. The investigation involves correlating the extracted power with the Moment, Oscillation displacement, and frequency, aiming to determine the advantages and trade-offs associated with the introduction of an extension arm on the aerofoil. The primary focus is on evaluating whether increasing the moment and aerofoil displacement by extending the arm length on the foil, while simultaneously reducing the frequency of oscillation, yields a positive impact. This analysis aims to establish a relationship between this configuration approach and the foil-roof geometry, contributing to a comprehensive understanding of the potential benefits derived from altering the aerofoil shape in the context of wind energy harvesting.

In the exploration of an aerofoil wind energy harvesting system integrated into a building's roof structure, the study focuses on assessing the performance of an innovative flow energy harvester utilising oscillating foils. This assessment relies on numerical modelling with dynamic mesh in ANSYS Fluent, addressing the fluid–structure interaction inherent in the dynamics of a pitching foil coupled with an energy harvesting system within the integrated wind energy device. The 3D model is strategically employed around identified areas to precisely predict the system's performance. The investigation investigates the power extraction capacity and efficiency of the system across various geometric, mechanical, and kinematic parameters, aiming to determine the optimal performance of the integrated wind energy harvesting system. This thorough analysis yields valuable insights for enhancing the efficiency and power output of the aerofoil wind energy harvesting system integrated into building roof structures.

Table 19 shows the parameters and material properties of NACA 0012 aerofoil with supporting arm integrated into the flat, pitched, and curved roof building. The centre of rotation is strategically positioned at a distance of 1.8 metres along the x-axis, situated at the end of the support arm. The aerodynamic foil itself features a chord length of 1 metre and a span of 1 metre, while the support arm extends for a length of 0.9 metres. It is noteworthy that the incorporated spring within the system adheres to linear behaviour, characterised by a spring constant, and contributes significantly to the overall dynamics of the foil, particularly with the extension designed to facilitate high displacement.

Table 19. Parameters and material properties of NACA 0012 aerofoil with support arm integrated into the flat, pitched, and curved roof building

Case (s)	Aerofoil profile	Roof shape	Distance between aerofoil and rooftop	Dimension	Material	Mass (kg)	Moment of inertia (kg.m ²)	Centre of rotation (m)
1	NACA 0012	Flat	600	1 m chord length and 1 span + 0.9 m support arm	Foam	6.5	0.8	1.8
2	NACA 0012	Pitched	600	1 m chord length and 1 span + 0.9 m support arm	Foam	6.5	0.8	1.8
3	NACA 0012	Curved	600	1 m chord length and 1 span + 0.9 m support arm	Foam	6.5	0.8	1.8

In Figure 102, it demonstrates the 3D aerodynamic aerofoil, coupled with an additional arm or extension, which is integrated into the structural framework of a building's roof. The foil undergoes a pitching motion characterised by the pitch angle (θ), which is defined by its amplitude ($\Delta\theta$) and frequency of motion (ω).

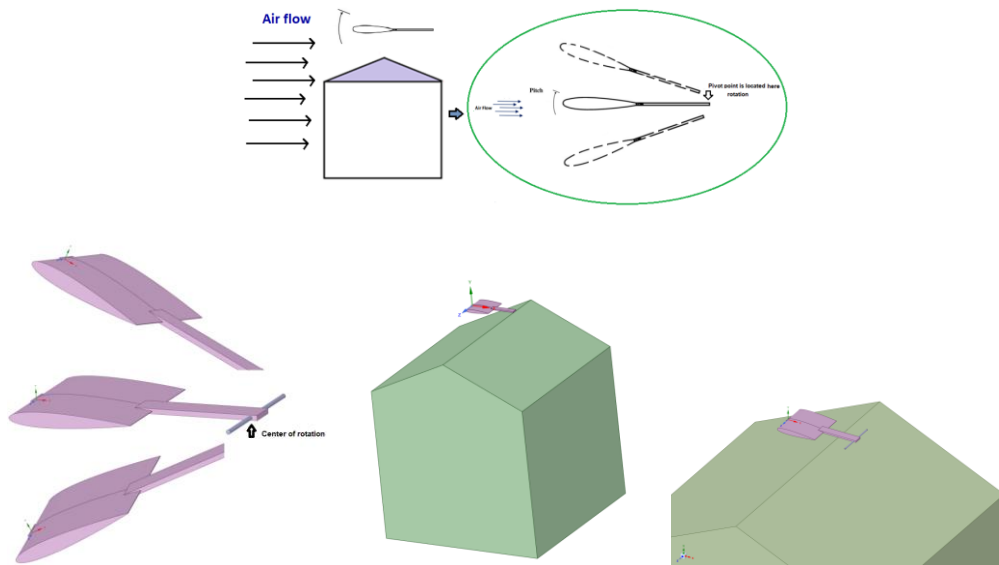


Figure 102. Schematic 3D model of the oscillating aerofoil with support arm integrated into the building roof structure

6.5.1 Velocity magnitude contours for NACA 0012 with arm integrated into building roof

Figure 103 displays velocity magnitude contours for the oscillating NACA 0012 with a support arm integrated into different roof types: (a) flat, (c) pitched, and (e) curved roofs, each with a 600 mm spacing. Moreover, it shows the same setup but with a 1000 mm spacing for the (b) flat, (d) pitched, and (f) curved roofs, which are all at an inlet velocity of 3 m/s. The results provide critical insights into the aerodynamic behaviour of the oscillating aerofoil wind energy harvesting system. Also, the results can be justified by referencing existing literature on aerofoil integration and wind flow interactions with building structures.

The observed fluid behaviour aligns with previous findings in the literature, particularly regarding wind shear effects at the edge of flat roof buildings. The higher displacements noted in all six cases compared to previous results without support arms suggest that the introduced arms significantly influence the wind flow patterns. Notably, in the scenario of NACA 0012 with a support arm integrated into a flat roof at a 600 mm distance, the presence of a large wind flow recirculation is highlighted. This counterproductive phenomenon, where wind flow is directed upwards rather than towards the aerofoil, aligns with literature discussing the impact of roof edges on wind behaviour. The recirculation may hinder the effectiveness of the wind energy harvesting system.

Similarly, in pitched roof buildings, the acceleration of wind speed on the windward side and the detachment or separation of wind flow on the leeward side, consistent with existing literature, is observed. The higher displacement of the aerofoil in this case may be attributed to the specific roof shape effects on wind flow. Furthermore, in the case of NACA 0012 with a support arm integrated into a curved roof building, the stagnation of wind flow is identified, hindering proper circulation for effective wind energy harvesting. This observation aligns with literature discussing challenges associated with curved roof structures.

Overall, these findings contribute to the existing literature on aerofoil integration into building structures, presenting the effects of roof shape, distance, and support arms on

wind flow patterns. The identified limitations, such as recirculation and stagnation, provide valuable insights for optimising wind energy harvesting systems in real-world applications. The damping and spring constants specified for each case also contribute to understanding the dynamic behaviour of the system and its response to varying roof configurations.

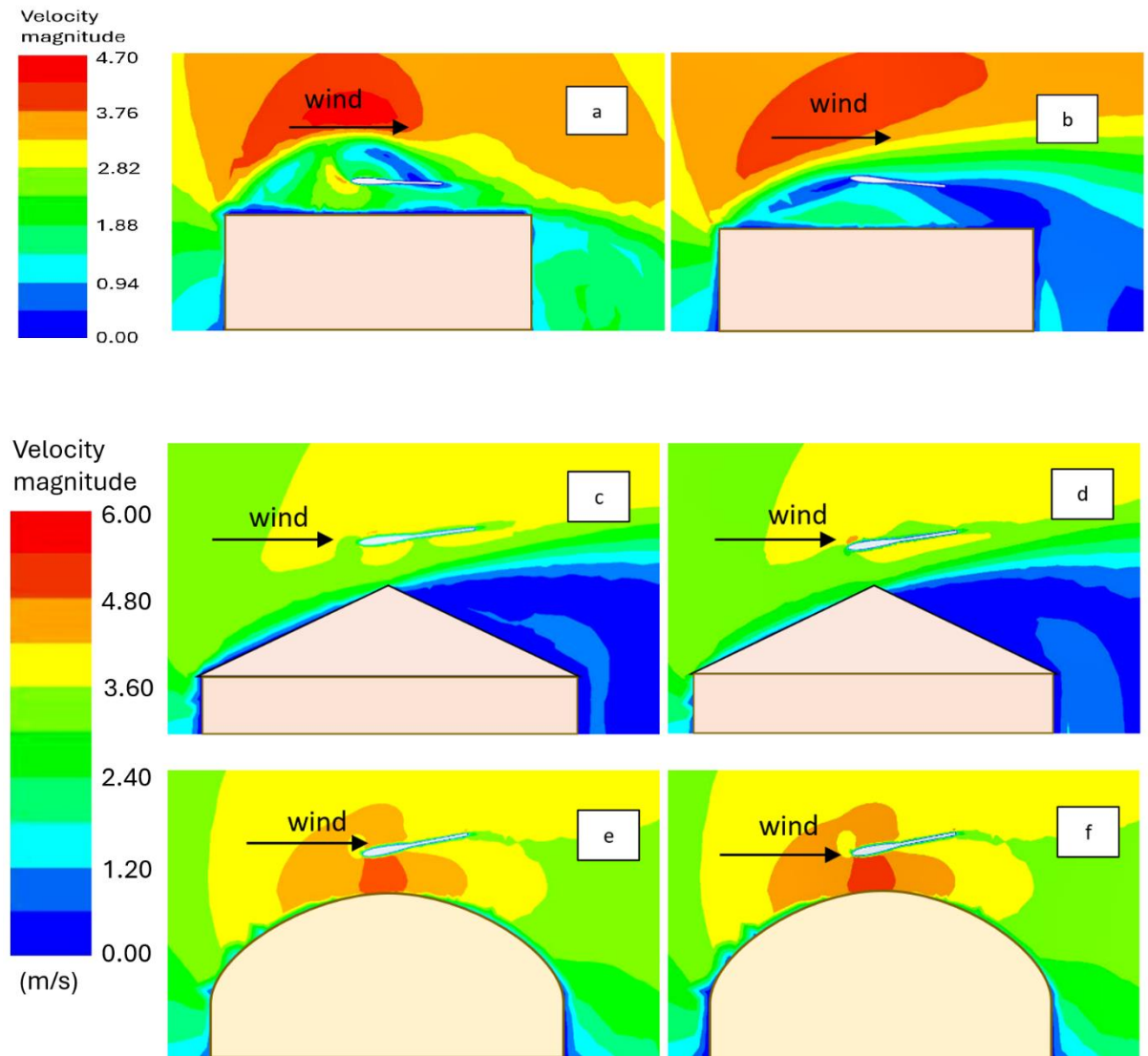


Figure 103. Velocity magnitude contours for oscillating NACA 0012 with support arm integrated into the (a) flat, (c) pitched, and (e) curved roof building with a distance of 600 mm and NACA 0012 with support arm integrated into the (b) flat, (d) pitched, and (f) curved roof building with a distance of 1000 mm and at 3 m/s inlet velocity

6.5.2 Torque and angular velocity of NACA 0012 with support arm

The findings in Figure 104 shows the comparison of the (a-c) torque and (d-f) angular velocity for the case of oscillating NACA 0012 aerofoil with support arm integrated with a distance of 600 mm and 1000 mm, which provide insights into the aerodynamic performance and structural dynamics of these systems.

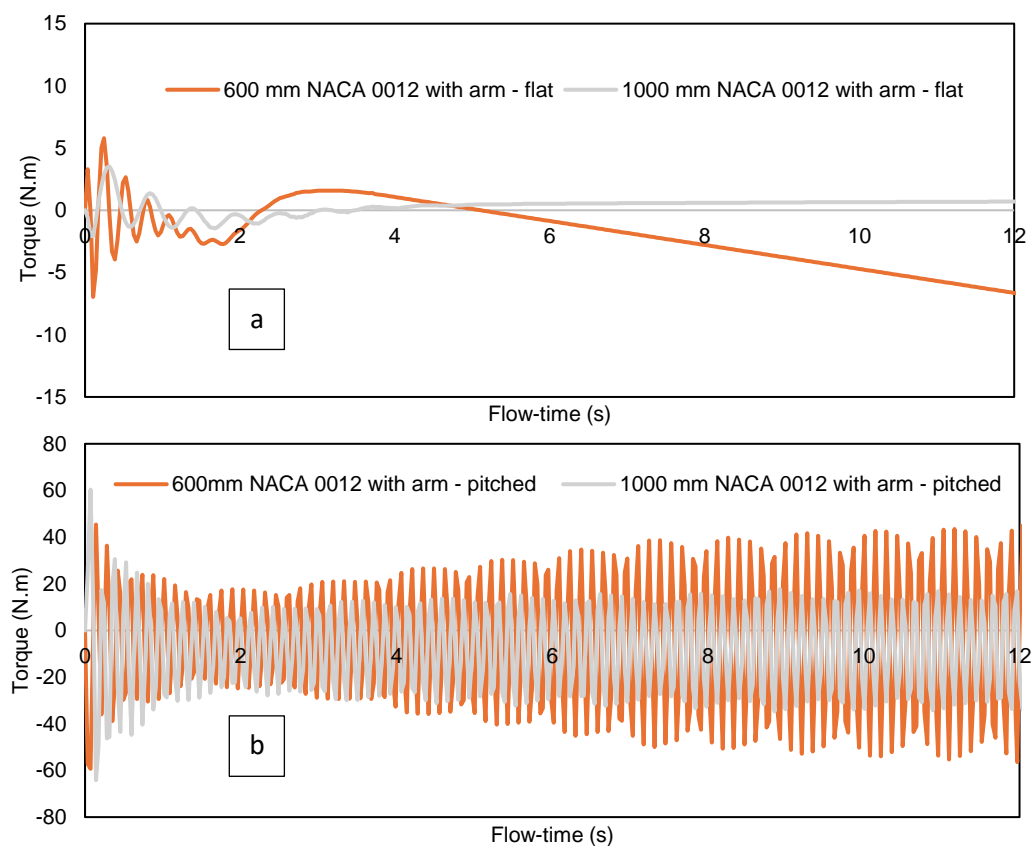
As shown in Figure 104 (a), the observation with the highest torque was achieved by the NACA 0012 aerofoil with a support arm integrated into a curved roof building, with a spacing of 600 mm between them, suggests that this configuration provides optimal aerodynamic efficiency and mechanical stability. The curvature of the roof contributes to smoother airflow patterns around the aerofoil, reducing turbulence and enhancing lift, thereby generating higher torque. In addition, the closer proximity between the aerofoil and the curved roof may facilitate more efficient transfer of aerodynamic forces, further improving torque production. In contrast, while both NACA 0012 configurations with support arms integrated into flat roof buildings showed comparable torque values at 600 mm and 1000 mm spacings, the overall torque generated by these configurations was lower compared to the curved roof scenario. This difference could be attributed to the less favourable aerodynamic conditions and structural interactions inherent in flat roof configurations, which may result in increased drag and reduced lift generation.

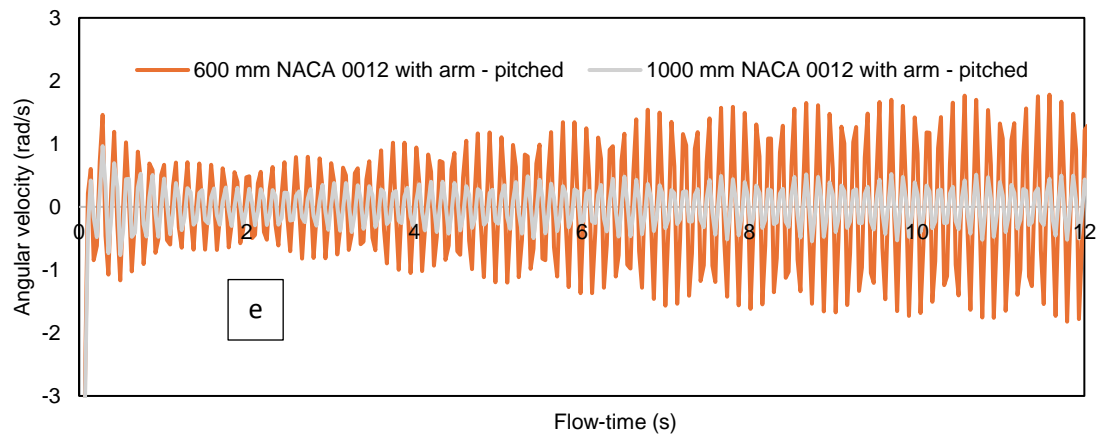
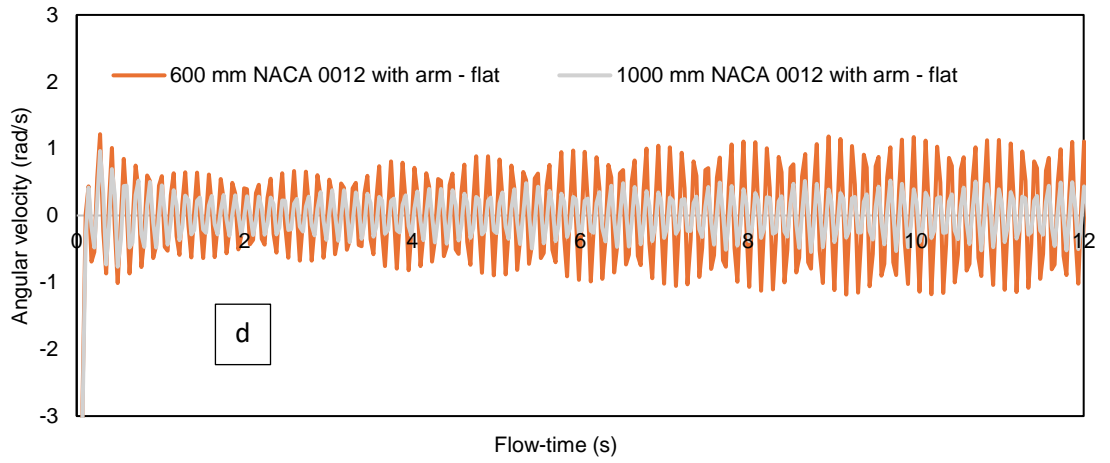
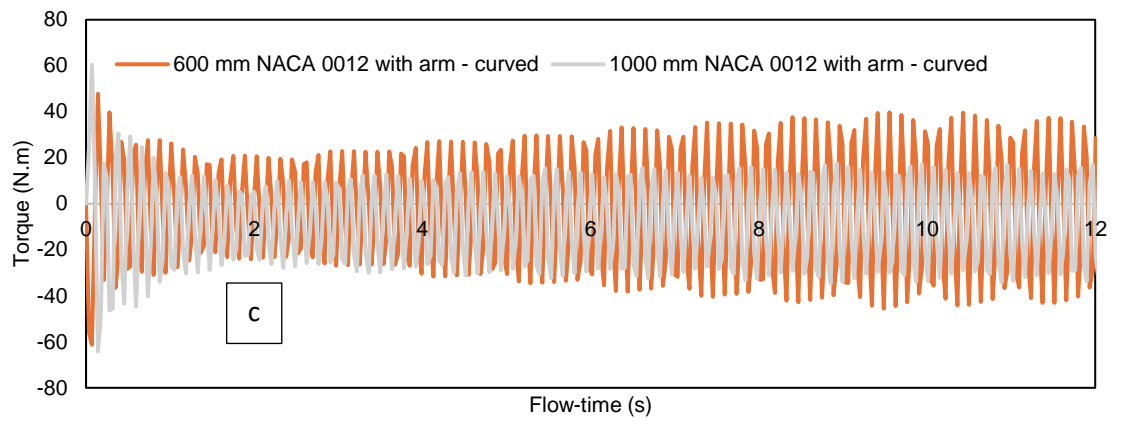
Figure 104 (a-c) illustrates the poor performance of the NACA 0012 aerofoil with a support arm when integrated into a flat roof building, positioned at distances of 600 mm and 1000 mm apart. The results indicate suboptimal performance for both configurations. Specifically, the NACA 0012 with a 1000 mm distance between support arms did not oscillate, while the same aerofoil with support arms spaced 600 mm apart initially oscillated from 0 to 0.4 seconds but then experienced a decrease in torque, rendering it ineffective for power generation.

While in Figure 104 (e-f), it illustrates the dynamic variation of angular velocities over flow time for different configurations featuring the NACA 0012 aerofoil integrated into flat, pitched, and curved roof. The results show that NACA 0012 aerofoil with a support arm integrated into a curved roof building, with a spacing of

600 mm between them, suggests that this configuration provides optimal aerodynamic efficiency and mechanical stability. Furthermore, the correlation between torque and angular velocity is noteworthy, as the highest angular velocity was also observed in the NACA 0012 configuration with support arms integrated into the curved roof building at a spacing of 600 mm. This outcome highlights the interconnected relationship between aerodynamic forces (which produce torque) and the resulting rotational motion of the aerofoil. The efficient torque generation in the curved roof configuration likely translates into higher angular velocity, reflecting the effectiveness of this design in harnessing wind energy and facilitating rotational motion.

Overall, the findings from Figure 104 highlight the importance of roof configuration and spacing in influencing the aerodynamic performance and mechanical behaviour of oscillating aerofoil systems. Through optimising these parameters, designers and engineers can enhance the efficiency and effectiveness of such systems for various applications, including renewable energy generation and structural dynamics analysis.





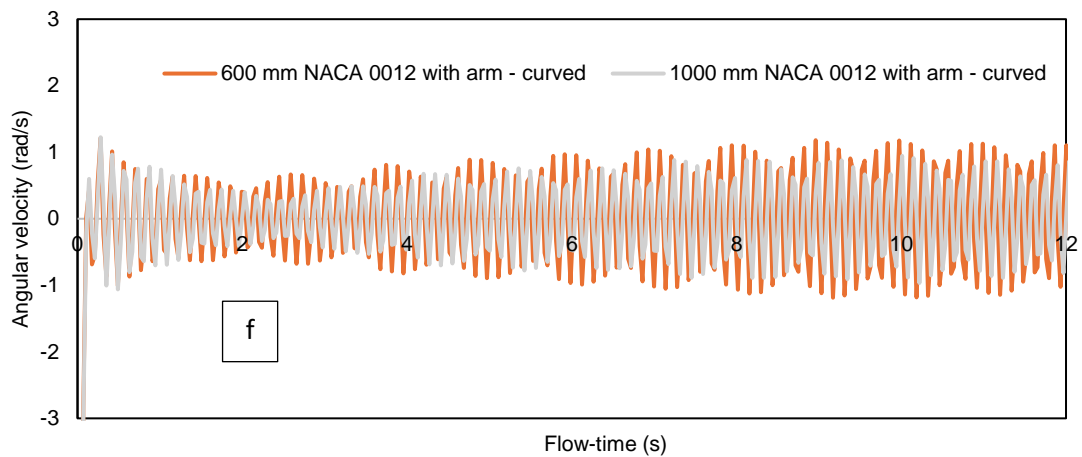


Figure 104. Comparison of the (a-c) torque and (d-f) angular velocity for the case of oscillating NACA 0012 aerofoil with support arm integrated with a distance of 600 mm and 1000 mm

6.5.3 Effects on mechanical power output of NACA 0012 with support arm

Figure 105 illustrates the average power output for six cases involving the integration of NACA 0012 with a support arm into flat, pitched, and curved roof buildings at distances of 600 mm and 1000 mm. The results highlight that the NACA 0012 with a support arm integrated into the pitched roof achieved the highest performance, generating 45 watts at 3 m/s inlet velocity. The second-highest power output was observed for the NACA 0012 with a support arm integrated into the curved roof building, producing 27 watts. The explanation provided for these results appears reasonable, emphasising the impact of aerofoil placement distance on efficiency and drawing comparisons to existing literature.

Comparing the results to existing literature, the findings align with the recognised preference for pitched roofs in wind energy harvesting. Pitched roof configurations are known to enhance wind flow dynamics, resulting in higher power outputs. The acknowledgment of challenges posed by specific roof shapes, such as curved roofs demonstrating high wind speed acceleration but inefficiency for the NACA 0012 with a support arm (27 watts), resonates with existing discussions on the complexities associated with aerodynamics and roof structures. A noteworthy observation is that the NACA 0012 with a support arm integrated into the curved roof performs better than in the pitched roof scenario at a 1000 mm distance. This finding deviates from some literature [208-210] that often emphasises the superiority of pitched roofs, highlighting

the complex nature of aerodynamic interactions and the significance of specific parameters in determining performance. This highlights the importance of an understanding and adaptation of generalisations based on specific conditions. The suboptimal performance of the NACA 0012 in flat roof scenarios aligns with literature acknowledging challenges associated with flat roof configurations in terms of aerodynamic efficiency. In summary, the provided explanation is reasonable and aligns with key principles in wind energy harvesting literature, offering insights that contribute to the ongoing discourse in the field.

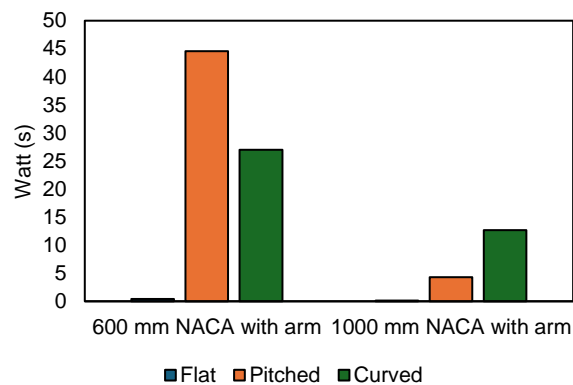


Figure 105. Average power output for the investigated 6 different parameter

6.6 Summary

- Larger-scale aerofoils faced issues with mass and inertia highlighting the need for a balanced design that considers aerodynamic benefits and structural limitations.
- The 2-metres SD7003 aerofoil faced challenges with low torque and high angular velocity suggesting a trade-off in power generation efficiency and highlighting the need for optimised design parameters.
- The 2-metres NACA 0012 in a curved roof configuration achieved the highest power output of 1.2 watts outperforming the SD7003 and other configurations indicating superior performance of the NACA 0012 despite expectations favouring the SD7003.
- Integrating a support arm with the NACA 0012 aerofoil in flat, pitched, and curved roof buildings highlighted pitched roofs' superior performance and revealed that curved roofs despite high wind speed acceleration showed inefficiency challenging conventional expectations.

- The NACA 0012 with the support arm aerofoil achieved the highest power output of 45 watts on a pitched roof at 3 m/s with the curved roof producing 27 watts and the flat roof yielding only 0.1 watts at 1000 mm and 0.4 watts at 600 mm highlighting the complex relationship between roof geometry and aerofoil dynamics.

6.7 Affirmations of research outputs

In response to the research questions outlined in section 1.7, the following sections provide detailed answers and discuss the corresponding outcomes:

What is the effect of different building shapes and configurations on the performance of an oscillating aerofoil integrated into the building roof structure?

In this thesis, the effect of different building shapes and configurations on the performance of an oscillating aerofoil integrated into the building roof structure is a complex relationship of aerodynamics, structural engineering, and architectural design. Building shapes such as rectangular, cylindrical, or irregular can provide distinct influences on wind flow patterns, creating variations in turbulence and vortices around the structure. These airflow dynamics directly impact the efficiency and stability of the oscillating aerofoil. In addition, oscillating aerofoil integrated into the pitched and curved roof building have shown that these roof shapes can induce better wind speed acceleration as compared to flat roof building roof. Through this phenomenon of Venturi effect, resulting in higher velocities for the aerofoil to harness and consequently increasing mechanical power output. The power output for the oscillating NACA 0012 aerofoil integrated into the curved roof increased by approximately 58% when compared to the pitched roof building structure.

How can the wind flow around buildings be optimised to increase the power output of an oscillating aerofoil integrated into the building roof structure?

It has proven in this thesis that several factors must be considered to optimise the wind flow around buildings and increase the power output of an oscillating aerofoil integrated into the building roof structure, Firstly, the shape of the building's roof plays a critical role, particularly in curved roof buildings where wind speed acceleration occurs. In addition, comprehensive investigation should be given to the design of the

aerofoil, including its shape and any additional support arms for increased displacement, even if it means a reduced frequency. CFD simulations are invaluable for the complexities of roof shapes, aerofoil configurations, and placement, which all can impact the system's potential mechanical power output.

What is the optimal placement of oscillating aerofoil integrated into the building roof structure to maximise power output?

The optimal placement of an oscillating aerofoil integrated into a building roof structure greatly depends on the roof type and the desired wind energy harvesting efficiency. However, in this study, it showed that the pitched and curved roof buildings, where wind speed acceleration is significant from the building roof and positioning it at the centre of the rooftop is recommended. According to the current CFD results, this set up suitable for an oscillating NACA 0012 aerofoil profile integrated into pitched and curved roof building with a distance of 600 mm. This placement ensures that the aerofoil can effectively capture wind energy without interference from the building itself. Specifically, for an oscillating NACA 0012 aerofoil with a chord length of 1 metre and a span of 1 metre, maintaining 600 mm from the roof and centre placement optimises performance. In addition, considerations such as mass, moment of inertia, and pitch motion characteristics of the aerofoil should be factored into the design.

However, in different scenarios, particularly when dealing with larger aerofoils with a chord length and span of 2 metres each, such as the SD7003 or NACA 0012 with a 600 mm distance with the building roof structure, outcomes significantly differ. This is primarily because the size of the aerofoil positions it too close to the rooftop, almost hitting the structure. This proximity to the roof not only risks physical contact, which could damage the aerofoil or the structure, but also affects the airflow dynamics around the aerofoil. The closeness to the top boundary of the domain can create stagnation points where the airflow velocity relative to the aerofoil is zero, leading to inefficient aerodynamic performance and potentially unstable aerodynamics characteristics in practical applications. Such effects are crucial to consider in the design and testing phases to avoid performance issues and structural damages.

Conversely, in the case of flat roof buildings, traditional placement at the centre of the roof may not be optimal. Placing the aerofoil at the roof's centre can lead to the creation

of recirculation zones, diminishing its effectiveness in capturing wind energy. Instead, practical placement involves positioning the aerofoil at the edge of the roof where wind shear is generated. This placement takes advantage of the wind shear to enhance energy capture. Furthermore, angling the aerofoil to align with the direction of the wind flow can further optimise wind speed acceleration and energy harvesting efficiency. In both cases, careful consideration of aerodynamic principles and site-specific factors is crucial for determining the optimal placement of the oscillating aerofoil to maximise power output and overall system performance. Iterative testing, modelling, and simulation can help refine placement strategies and ensure effective wind energy harvesting.

How do varying wind speeds and directions affect the performance of an oscillating aerofoil integrated into the building roof structure, and how can this be mitigated?

Using ANSYS CFD, the numerical results showed that the different wind speeds and directions affect the performance of oscillating aerofoils integrated into building roof structures. A study examined this effect using a NACA 0012 profile aerofoil integrated into flat, pitched, and curved roofs. Simulations were conducted for wind directions ranging from 0 to 25 degrees at 3 m/s to assess power output efficiency. Findings revealed a decline in power output starting at 15 degrees of wind direction, emphasising the influence of wind angle on generation. This understanding is vital for optimising aerofoil placement and orientation, particularly considering the contrasting performance among different roof types.

As the wind direction shifts from 0 degrees to 25 degrees, the mechanical power output declines significantly across all roof structures. For the flat roof, the output decreases from 0.2 watts to 0.0001 watts, a drop of 0.1999 watts. The pitched roof experiences a more substantial decline, with power output falling from 6.2 watts to 0.0001 watts, a reduction of 6.1999 watts. The curved roof also sees a notable decline, from 6.8 watts at 0 degrees to 0.0002 watts at 25 degrees, resulting in a decrease of 6.7998 watts. Despite the drop, the curved roof maintains the highest power output compared to the flat and pitched roofs.

Flat roofs suffer from wind recirculation and shear effects, necessitating strategic placement. Conversely, pitched, and curved roofs benefit from enhanced power output due to wind speed acceleration. Adjusting the positioning and angle of attack relative to wind direction can further optimise performance. Conducting a sensitivity analysis of spring constants can help mitigate these effects.

Overall, using CFD modelling and simulations as preliminary investigative tools, followed by their application in wind tunnel experiments and field tests, are crucial steps towards developing highly efficient building-integrated wind energy harvesting systems. In addition, considering the impact of wind direction is vital for optimising energy extraction in oscillating wind energy systems that are integrated into building roofs. This approach ensures that the systems are not only efficient but also reliable in varying wind conditions, maximising the energy harvesting potential.

What is the impact of turbulence on the performance of an oscillating aerofoil integrated into the building roof structure, and how can it be accounted for in simulations?

The impact of turbulence on the performance of an oscillating aerofoil integrated into a building roof structure is substantial. Turbulence induces fluctuating aerodynamic forces on the aerofoil, causing variations in lift and drag coefficients. These fluctuations can lead to unstable oscillations and reduced efficiency in energy capture. The unsteady nature of turbulent flow can also result in erratic torque and angular velocity behaviour, which negatively affects the aerofoil's performance.

To account for turbulence in simulations, advanced CFD techniques should be employed. This involves using turbulence modelling approaches such as URANS with turbulence models such as k-epsilon. These models help capture the complex, unsteady flow characteristics around the aerofoil, providing detailed insights into the effects of turbulence. Furthermore, high-resolution mesh generation is critical to accurately resolve the turbulent boundary layers and flow structures. By incorporating these advanced simulation techniques, designers can better predict and optimize the aerofoil's performance under turbulent conditions, allowing for more reliable and efficient energy harvesting solutions in real-world applications.

The turbulent wind flow introduces unsteady and chaotic aerodynamic forces on the aerofoil, causing fluctuations in lift and drag coefficients. These fluctuations can destabilise the aerofoil's oscillations, reducing its efficiency in harnessing wind energy and increasing mechanical stresses on both the aerofoil and its mounting structure. Consequently, accounting for turbulence is critical in designing and optimizing such systems for reliable and efficient performance.

To effectively model the impact of turbulence, the Unsteady Reynolds-Averaged Navier-Stokes (URANS) approach with a k-epsilon turbulence model can be employed. The URANS method is suitable for capturing the unsteady behavior of turbulent flows over the oscillating aerofoil. The k-epsilon model, a widely used turbulence model in CFD, helps to simulate the turbulent kinetic energy (k) and its dissipation rate (epsilon), providing a robust representation of the turbulence effects on the aerofoil's aerodynamic performance. By integrating the URANS approach with the k-epsilon model, it is possible to capture the dynamic behaviour of the aerofoil, including the effects of varying wind speeds and directions.

What are the key parameters that affect the performance of building integrated wind energy harvesting systems, and how can they be optimised?

According to prior research in the literature and the CFD findings of this study, several factors influence the performance of oscillating wind energy harvesting systems integrated into building roof structures. The aerofoil's shape and the building's roof showed that these factors can influence the wind flow patterns, thus their design needs careful consideration through CFD modelling and simulations to achieve optimal lift and minimise drag. In addition, the placement and scale of the aerofoil should be strategically selected to exploit high wind zones on the roof while avoiding areas that may be negatively impacted by adjacent building structures or turbulent flows.

Key parameters such as the aerofoil's mass, moment of inertia, and the positioning of its centre of rotation significantly affect its oscillatory dynamics and energy harvesting capability. These factors require precise adjustments to balance the aerofoil's displacement and frequency of oscillation, ensuring effective energy capture and minimal mechanical stress. The use of extension arms can further fine-tune this

balance by modifying the aerofoil's amplitude and operational frequency based on wind conditions.

6.8 Research impact

The knowledge and application of CFD techniques in this thesis has contributed to the advancement of novel wind energy harvesting systems product for Katrick Technologies company. Through optimising the novel design of Wind Panel and operation, CFD and research work have been an important role for understanding the effects of neighbouring structures, different building roof shapes, wind channelling, wind speed, wind direction, wind shadow, wind shear, optimal placement for wind energy harvesting technology. These studies are crucial in maximising energy extraction efficiency and driving the transition towards sustainable energy production. Notably, insights gained from research findings on aerodynamic behaviour and wind flow dynamics have informed the optimisation of aerofoil designs and their strategic placement within building structures, resulting in maximised wind energy capture and power output.

CFD modelling and analysis has facilitated the development of predictive models for evaluating product performance in diverse environmental conditions. These models have played a crucial role in identifying areas for improvement and guiding iterative design refinements, ultimately enhancing product efficiency and reliability. Also, the validation of CFD results against wind tunnel experimental data has supported the credibility and accuracy of computational models and simulation techniques at Katrick Technologies, providing valuable insights into product performance in real-world conditions.

Furthermore, the continuous refinement and validation processes employed at Katrick Technologies ensure greater confidence in product performance predictions, ultimately leading to better decision-making and outcomes for investors and the environment. Real-world case studies further contribute to understanding the system's behaviour and effectiveness in various scenarios, providing practical insights for design optimisation and system improvement.

Figure 105 (a) shows the Wind Panel tested in Sports Engineering Hub [211-212] to examine the performance in terms of wind flow behaviour surrounding the aerofoil in the duct. These examinations include the capturing the velocity magnitude and pressure in different points in the duct to better understand the behaviour of the wind when it interacts with the aerofoil and duct. As a result, this can improve the wind energy harvesting system design and better capture wind energy. In Figure 105 (b), it demonstrates different Wind Panels installed alongside the road, streetlight and passing cars. Whereas for Figure 105 (c), it can be observed the streamlines and Figure 105 (d) velocity contours for Glasgow Airport case study [211-212]. The case study was able to identify the optimal placement of the Wind Panel on the building roof structure, understand the effects of different roof shapes, turbulence intensity, better capture the wind energy through to the duct, and at the same improve the design [212].

Both the current CFD study in the PhD thesis and the referenced research (Katrik Technology CFD results) highlighted the significant role of optimal placement, effects of wind speed, wind direction roof shape, and wind speed acceleration in the aerodynamic performance of oscillating aerofoils integrated into building roof structures. Wind speed accelerates through narrow passages, which can substantially increase local wind speeds. Moreover, CFD simulations confirmed that positioning the aerofoil in areas with prominent wind channelling and considering the effects of wind shear enhances energy capture, a finding consistent with the referenced study. Also, both studies emphasised the importance of wind direction, demonstrating that aerofoils aligned perpendicular to prevailing wind directions experience higher lift and more stable oscillations. Incorporating dynamic orientation adjustments in response to changing wind directions was identified as a strategy to optimise energy harvesting further. Moreover, the shape of the roof and the placement of the aerofoil were also critical factors affecting aerodynamic performance. Both studies found that curved and pitched roofs significantly enhanced wind speed acceleration and energy capture compared to flat roofs. This placement minimised adverse effects such as flow separation, recirculation, and the impact of wind shear, which were identified as detrimental to aerofoil performance.

Overall, the transition from academia to industry has enabled the translation of theoretical research into practical applications, driving innovation and advancing sustainable solutions for a greener future. Through collaborative efforts and continuous improvement initiatives, Katrik Technologies remains committed to refining and optimising its products in terms of accelerating the transition to sustainable and renewable energy sources in building applications.

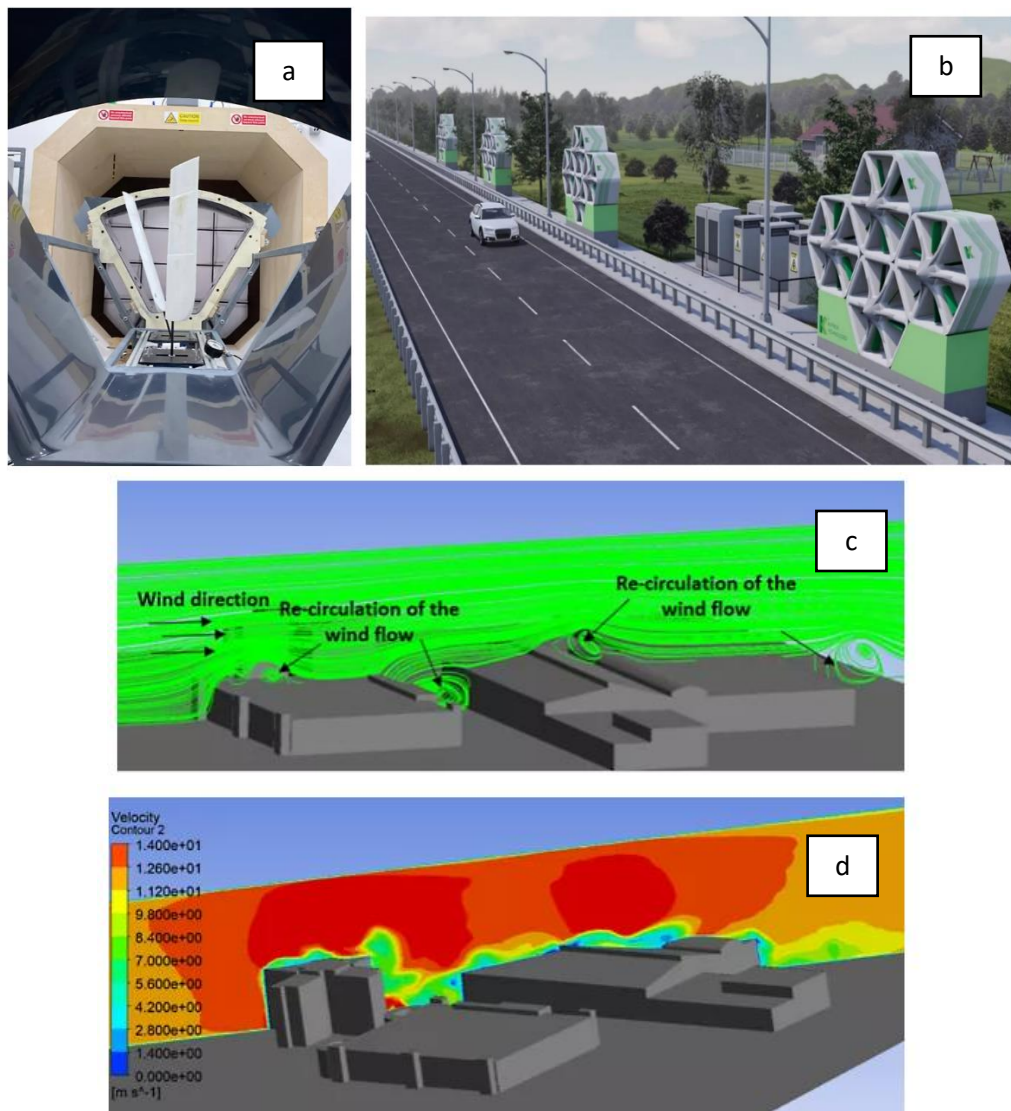


Figure 106. Wind Panel in (a) Wind tunnel tests and (b) application in an environment of the Wind Panel [210] (c) Streamlines and (d) velocity contours for Glasgow Airport case study [211]

Chapter 7

Conclusion and Recommendation for Future Work

The increasing demand for energy efficiency has stimulated the integration of renewable energy solutions into buildings. Micro/small building integrated wind turbines have shown promising energy harvesting performance, their implementation faces challenges. Wind induced vibration harvesting devices such as oscillating aerofoil wind energy harvesting system offers an alternative approach. Yet, their integration into building structures lacks comprehensive study. This research fills this gap by investigating the performance of an oscillating aerofoil integrated into a building through CFD numerical modelling and simulations. A coupled numerical model, employing CFD with a one-degree-of-freedom solver was developed in ANSYS Fluent.

7.1 Conclusions

- The proposed design presents an alternative solution to the ongoing challenges associated with conventional building-integrated wind turbines. It provides a practical power output in watts, suitable for powering low-powered devices such as sensors, LED lights, and small-scale equipment. In addition, it can provide electricity to decentralised communities, functioning as a self-charging unit. Integrating an aerofoil into the roof shape of pitched and curved buildings

accelerates wind flow, resulting in higher power output compared to single aerofoil wind energy harvesters.

- The research methodology has predicted the dynamic behaviour of an oscillating aerofoil integrated into the building roof structure. In addition, a fundamental understanding of the fluid-structure interaction between the wind flow and integrated design of the aerofoil and building roof were shown from the CFD results.
- The wind speed, wind direction, placement, building roof and aerofoil shape, scale, atmospheric boundary layer (ABL) condition, and additional support arm attached to the aerofoil showed that it affects the performance of the aerofoil wind energy harvester.
- The study emphasises the potential of small-scale wind-induced vibration technology to provide cost-effective power to off-grid communities. The simplicity of the wind energy harvester structure and its compatibility with various electronic devices make it an attractive option.

In conclusion, this research contributes to advancing sustainable architectural design and improving energy efficiency through the utilisation of dynamic mesh approaches and wind-induced vibration technologies for building-integrated wind energy harvesting systems. The findings highlight the importance of optimising design parameters and considering specific architectural contexts to maximise the efficiency of wind energy harvesting systems in diverse settings.

7.2 Recommendations for future works

The research described in this thesis establishes the groundwork for future studies, outlining specific areas for further exploration as follows:

- Additional enhancements to the CFD procedure are essential to enhance accuracy and provides greater confidence in the proposed design. This entails measuring the surface roughness of the aerofoil utilised in physical experiments and replicating it in the CFD simulations. Furthermore, analysing the effects of spatial discretisation settings is crucial for refining the procedure.

This refinement is especially imperative for 3D URANS CFD due to its higher associated costs compared to 2D simulations.

- Future endeavours should concentrate on overcoming existing limitations by establishing standardised experimental protocols and methodologies for the study of building-integrated wind energy systems. This approach will enhance comparability across studies and deepen the understanding of the factors impacting system performance. In addition, collaboration with experts from relevant fields can offer valuable insights and elevate the rigor of experimental design and analysis.
- Sensitivity analyses across spring constant values and exploration of adjacent structures' effects on system efficiency are areas for future investigation. Also, understanding turbulence intensity and vortices generated during the interaction between the aerofoil and its surroundings is crucial for comprehending motion influences.
- Exploring different case studies across various environments will provide valuable insights into system performance and applicability.
- Introducing ducts to better capture wind flow directed towards the aerofoil wind energy harvesting system.
- In this study, the focused was on a single degree of freedom, specifically pitch motion for the oscillating aerofoil. However, an aerofoil can have 2 degrees of freedom, including both pitch and heave motions. Future research should investigate the impact of incorporating both pitch and heave motions to determine if this dual approach offers any additional benefits or drawbacks for the proposed wind energy harvesting system integrated into the building roof structure.
- Further studies focusing on transducers, power management, and energy storage for self-charging power units are necessary to enhance system efficiency and sustainability.

7.3 Contributions to the knowledge

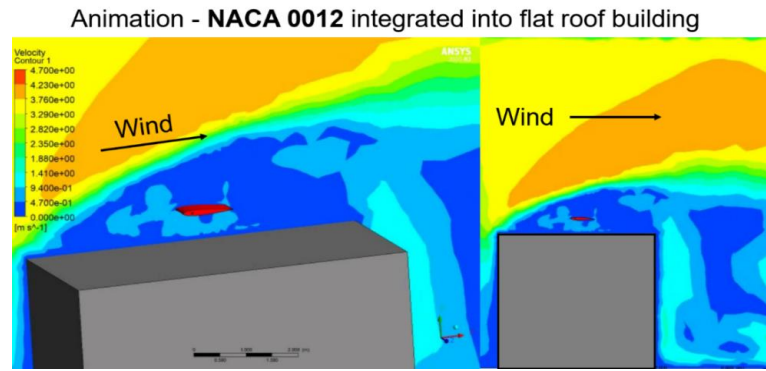
As per section 2.5, gaps in research concerning small-scale wind energy harvesting systems integrated into building roof structures were identified through a literature

review. This thesis addressed these gaps and contributed to knowledge in the following ways:

- Introduced a new design of wind energy capture system of oscillating aerofoil integrated into the building roof structure.
- Introduced new approach of ANSYS Fluent using 1 degree of freedom rotational motion to predict and examine the dynamic behaviour and power output of an oscillating aerofoil wind energy capture integrated into the building roof structure
- The results of the study provided the fundamental understanding of fluid-structure between the wind flow and integrated design of an oscillating aerofoil and building roof structure.
- Findings in this showed the potential for wind energy harvesting of an oscillating aerofoil integrated into building roof structure with different boundary conditions and parameters.

Appendix A

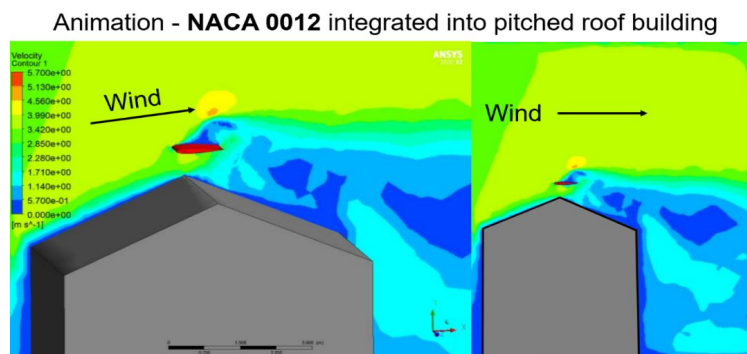
Dynamic Behaviour and Fluid-Structure Interaction of an Oscillating Aerofoil Integrated into the Flat Roof Building Structure Motion Animation



Video 1. Air flow distribution above and around oscillating aerofoil with the NACA 0012 profile integrated into flat roof building (*the playable video is available in the Appendix) Video 1 - Flat roof.mp4*

Appendix B

Dynamic Behaviour and Fluid-Structure Interaction of an Oscillating Aerofoil Integrated into the Pitched Roof Building Structure Motion Animation

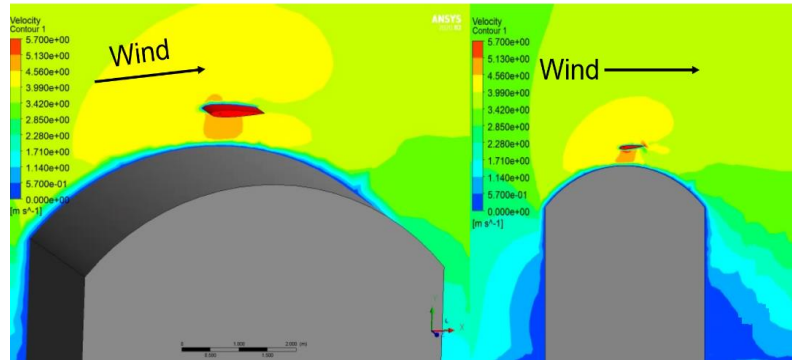


Video 2. Air flow distribution above and around the oscillating aerofoil with the NACA 0012 profile integrated into pitched roof building (*the playable video is available in the Appendix) Video 2 - Pitched roof.mp4*

Appendix C

Dynamic Behaviour and Fluid-Structure Interaction of an Oscillating Aerofoil Integrated into the Curved Roof Building Structure Motion Animation

Animation - **NACA 0012** integrated into curved roof building



Video 3. Air flow distribution above and around the oscillating aerofoil with the NACA 0012 profile integrated into curved roof building (*the playable video is available in the Appendix*) Video 3 - Curved roof.mp4

Bibliography

- [1] IEA 2022; *CO2 Emissions in 2022*, <https://www.iea.org/reports/co2-emissions-in-2022>, License: CC BY 4.0;
- [2] Met office, [Accessed on March 2023] at <https://www.metoffice.gov.uk/weather/climate-change/causes-of-climate-change>.
- [3] International Energy Agency: IEA: 2019, (Accessed at https://iea.blob.core.windows.net/assets/23f9eb39-7493-4722-aced-61433cbffe10/Global_Energy_and_CO2_Status_Report_2018.pdf), [Accessed on 10 Jan 2021].
- [4] Intergovernmental Panel on Climate Change, 2022, (Accessed at https://www.ipcc.ch/report/ar6/wg3/downloads/report/IPCC_AR6_WGIII_SPM.pdf), [Accessed on 21 January 2022].
- [5] IEA, 2024, Energy Systems – Buildings (Accessed at <https://www.iea.org/energy-system/buildings>), [Accessed on June 2024]
- [6] IRENA, 2024, Future of Solar Photovoltaic - Executive Summary, https://www.irena.org//media/Files/IRENA/Agency/Publication/2019/Nov/IRENA_Future_of_Solar_PV_2019.pdf, Accessed on June 2024]
- [7] Tamesol, 2024, Solar Panel Power Revealed: Surprising Facts on Energy Output, (Accessed at <https://tamesol.com/solar-panel-power-2024/>), [Accessed on June 2024]
- [8] Ragheb, M., Ragheb, A., Wind Turbines Theory - The Betz Equation and Optimal Rotor Tip Speed Ratio, IntechOpen, 2011.
- [9] Santamouris, M., Vasilakopoulou, K., Present and future energy consumption of buildings: Challenges and opportunities towards decarbonisation, e-Prime – Advances. *Electrical Engineering, Electronics and Energy*, Vol. 1, 100002, 2021.
- [10] Höök, M. and Tang, X., Depletion of fossil fuels and anthropogenic climate change—A review. *Energy policy*, 52, pp.797-809, 2013.
- [11] Jones, G.A. and Warner, K.J., The 21st century population-energy-climate nexus. *Energy Policy*, 93, pp. 206-212, 2016.

- [12] Chevalier, J., M., *The new energy crisis*, Palgrave Macmillan UK, pp. 6-59. 2009.
- [13] International Energy Agency. *Technical Guidelines for Passive Ultra-low Energy use Green Buildings (Trial Implementation in Residential Buildings)*, (Accessed at <https://www.iea.org/policies/7923-technical-guidelines-for-passive-ultra-low-energy-use-green-buildings-trial-implementation-in-residential-buildings>), [Accessed: 10 January 2024].
- [14] Zhao, J., *Passivhaus Standard as a Social Housing Model in the UK: Barriers and Opportunities*. In: Leal Filho, W., Dinis, M.A.P., Moggi, S., Price, E., Hope, A. (eds) *SDGs in the European Region. Implementing the UN Sustainable Development Goals – Regional Perspectives*. Springer, Cham, 2023.
- [15] Gielen, D., Boshell, F., Saygin, D., Bazilian, M., Wagner, N., Gorini, R., *The role of renewable energy in the global energy transformation*, *Energy Strategy Reviews*, Volume 24, 2019, pp. 38-50.
- [16] Østergaard, P. A., Duic, N., Noorollahi, Y., Kalogirou, A., *Recent advances in renewable energy technology for the energy transition*. *Renewable Energy*, Vol. 179, pp. 877-884, 2021.
- [17] Xu, W., Li, G., Zheng, X., Li, Y., Li, S., Zhang, C., Wang, F., *High-resolution numerical simulation of the performance of vertical axis wind turbines in urban area: Part I, wind turbines on the side of single building*. *Renewable Energy*, Vol. 177, pp. 461-474, 2021.
- [18] Xu, W., Li, Y., Li, G., Li, S., Zhang, C., Wang, F., *High-resolution numerical simulation of the performance of vertical axis wind turbines in urban area: Part II, array of vertical axis wind turbines between buildings*. *Renewable Energy*, Vol. 176, pp. 25-39, 2021.
- [19] Aquino, A., I., Calautit, J., K., Hughes, B., R., *Evaluation of the integration of the Wind-Induced Flutter Energy Harvester (WIFEH) into the built environment: Experimental and numerical analysis*. *Applied Energy*, Vol. 207, pp. 61-77, 2017.
- [20] Abohela, I., Hamza, N., Dudek, S., *Effect of roof shape, wind direction, building height and urban configuration on the energy yield and positioning of roof mounted wind turbines*. *Renewable Energy*, Vol. 50, pp. 1106-1118, 2013.

- [21] Ntinias, G. K., Zhang, G., Fragos, V. P., Bochtis, D. D. Nikita-Martzopoulou, C., Airflow patterns around obstacles with arched and pitched roofs: Wind tunnel measurements and direct simulation. *European Journal of Mechanics - B/Fluids*, Vol. 43, pp. 216-229, 2014.
- [22] Lu, L., Ip, K., Investigation on the feasibility and enhancement methods of wind power utilization in high-rise buildings of Hong Kong. *Renewable and Sustainable Energy Reviews*, Vol. 13(2), pp. 450-461, 2009.
- [23] Ledo, L., Kosasih, P. B., Cooper, P., Roof mounting site analysis for micro-wind turbines. *Renewable Energy*, Vol. 36(5), pp. 1379-1391, 2011.
- [24] Cao, Y., Taslimi, M., Dastjerdi, S. M., Ahmadi, P., Ashjaee, M., Design, dynamic simulation, and optimal size selection of a hybrid solar/wind and battery-based system for off-grid energy supply. *Renewable Energy*, Vol. 187, pp. 1082-1099, 2022.
- [25] Aravindhana, N., Natarajan, M. P., Ponnuvel, S., Devan, P. K., Recent developments and issues of small-scale wind turbines in urban residential buildings - A review. *Energy & Environment*, 2022.
- [26] Department of Energy and Climate Change (2011b) Low Carbon Buildings Programme, Communities Project Case Study – Wind Turbine. (Available at: <http://www.decc.gov.uk/assets/decc/11/meeting-energydemand/microgeneration/2122-communities-case-studybeckington.pdf>), [Accessed: 13 December 2021].
- [27] Rafailidis, S., Influence of Building Areal Density and Roof Shape on the Wind Characteristics Above a Town, *Boundary-Layer Meteorology*, Vol. 85(2), pp. 255-271, 1997.
- [28] Dutton, A., G., Halliday, J., A., Blanch, M., J., Energy Research Unit, CCLRC, The Feasibility of Building-Mounted/Integrated Wind Turbines (BUWTs): Achieving their potential for carbon emission reductions, May 2, 2005, (at: https://ukerc.rl.ac.uk/pdf/BUWT_final_v004_full.pdf) [Accessed: 21 October 2022].
- [29] WINEUR, 2007, Wind Energy Integration in the Urban Environment: Report on Resource Assessment 5.1, (Accessed at:

http://www.ieelibrary.eu/images/all_ieelibrary_docs/514%20wineur.pdf),

[Accessed: 29 January 2021].

- [30] Blackmore, P., Siting micro-wind turbines on house roofs. *Watford: BRE*, 2008.
- [31] Mithraratne, N., Roof-top wind turbines for microgeneration in urban houses in New Zealand. *Energy and Buildings*, Vol. 41(10), pp. 1013- 1018, 2009.
- [32] Sievert, T., 2009, Product Pick of the Week - The Mag-Wind™ wind turbine. (Accessed at <http://windfair.net/press/5739.html>), [Accessed: 19 April 2021].
- [33] Mertens, Sander. The Energy Yield of Roof Mounted Wind Turbines. *Wind Engineering*. Vol. 27, pp.507-518, 2003.
- [34] Phillips, R., Blackmore, P., Anderson, J., Clift, M., Aguilo-Rullan, A. and Pester, S., Micro-wind turbines in urban environments-An assessment, *IHS BRE Press for BRE Trust*, Bracknell, 2007.
- [35] AWEA, AWEA Small Wind Global Market Study, 2010, AWEA, Washington, DC, 2010.
- [36] Renewable UK, UK Market Report, 2010, Small Wind Systems, United Kingdom, 2010.
- [37] Hyams, M., A., Chapter 20 - Wind energy in the built environment, Editor(s): Frank Zeman, *In Woodhead Publishing Series in Energy, Metropolitan Sustainability, Woodhead Publishing*, pp. 457-499, 2012.
- [38] Wen, Q., He, X., Lu, Z., Streiter, R., Otto, T., A comprehensive review of miniaturized wind energy harvesters. *Nano Materials Science*, Vol. 3(2), pp.170-185, 2021.
- [39] Micallef D, Van Bussel G. A Review of Urban Wind Energy Research: Aerodynamics and Other Challenges. *Energies*. Vol. 11(9), p. 2204, 2018.
- [40] Du, X., Zhang, M., Chang, H., Wang, Y., Yu, H., Micro windmill piezoelectric energy harvester based on vortex-induced vibration in tunnel. *Energy*, Vol. 238, Part A, 2022.
- [41] Li, Z., Zhou, S., Yang, Z., Recent progress on flutter-based wind energy harvesting. *International Journal of Mechanical System Dynamics*, Vol. 2: pp. 82- 98, 2022.

- [42] Millward-Hopkins, J., Tomlin, A., Linsha, M., Ingham, D., Pourkashanian, M., Assessing the potential of urban wind energy in a major UK city using an analytical model. *Renewable Energy*, Vol. 60, pp. 701-710, 2013.
- [43] Sunderland, K., Mills, G., Conlon, M., Estimating the wind resource in an urban area: A case study of micro-wind generation potential in Dublin, Ireland. *Journal of Wind Engineering and Industrial Aerodynamics*, Vol. 118, pp. 44–53, 2013.
- [44] Baniotopoulos, C., Borri, C., Hemida, H., Veljkovic, M., Morbiato, T., Borg, R., P., Huber, S., Efthymiou, E., Rebelo, C., Trends and challenges for wind energy harvesting. Portugal: University of Coimbra, 2015.
- [45] Westerlund, M., Social Acceptance of Wind Energy in Urban Landscapes. *Technology Innovation Management Review*, Vol. 10(9), 2020.
- [46] Clifton, A., Barber, S., Stökl, A., Frank, H., and Karlsson, T., Research challenges and needs for the deployment of wind energy in hilly and mountainous regions. *Wind Energy Science*, Vol. 7, pp. 2231–2254, 2022.
- [47] Bhat, S. and Govardhan, R. Stall flutter of NACA 0012 airfoil at low Reynolds numbers. *Journal of Fluids and Structures*, Vol. 41, pp.166-174, 2013.
- [48] Poirel, D., Harris, Y., Benaissa, A., Self-sustained aeroelastic oscillations of a NACA0012 airfoil at low-to-moderate Reynolds numbers, *Journal of Fluids and Structures*, Vol. 24, No. 5, pp.700-719, 2008.
- [49] Tang, D. and Dowell, E. H., Experimental Aeroelastic Models Design and Wind Tunnel Testing for Correlation with New Theory. *Aerospace*, Vol. 3, No. 12, 2016.
- [50] Hamlehdar, M., Kasaeian, A., Safaei, M. R., Energy harvesting from fluid flow using piezoelectrics: A critical review. *Renewable Energy*, Vol. 143, pp. 1826-1838, 2019.
- [51] Chong, W. T., Pan, K. C., Poh, S. C., Fazlizan, A., Oon, C. S., Badarudin, A., Nik-Ghazali, N., Performance investigation of a power augmented vertical axis wind turbine for urban high-rise application. *Renewable Energy*, Vol. 51, pp. 388-397, 2013.

- [52] Wang, Q., Wang, J., Hou, Y., Yuan, R., Luo, K., Fan, J., Micrositing of roof mounting wind turbine in urban environment: CFD simulations and lidar measurements. *Renewable Energy*, Vol. 115, pp. 1118-1133, 2018.
- [53] Li, K., Yang, Z., Gu, Y., He, S., Zhou, S., Nonlinear magnetic-coupled flutter-based aeroelastic energy harvester, Modeling, simulation and experimental verification. *Smart Materials and Structures*. 28, 2018.
- [54] Naseer, R., Dai, H., Abdelkefi, A., Wang, L., Piezomagnetoelastic energy harvesting from vortex-induced vibrations using monostable characteristics. *Applied Energy*, Vol. 203, pp. 142–153, 2017.
- [55] Chai, Y, Gao, W, Ankay, B, Li, F, Zhang, C. Aeroelastic analysis and flutter control of wings and panels: A review. *International Journal of Mechanical System Dynamics*, Vol. 1, No. 2, pp. 5- 34, 2021.
- [56] Quy, V. D., Sy, N. V., Hung, D. T., Huy, V. Q., Wind tunnel and initial field tests of a micro generator powered by fluid-induced flutter, *Energy for Sustainable Development*, Vol. 33, pp. 75–83, 2016.
- [57] Stathopoulos, T. and Wu, H., Using computational fluid dynamics (CFD) for pedestrian winds. In: *Proceedings of Structures, Building on the Past, Securing the Future*, 2004.
- [58] Zhang, Y., Zhou, Z., Wang, K., Li, X., Aerodynamic Characteristics of Different Airfoils under Varied Turbulence Intensities at Low Reynolds Numbers. *Applied Science*, Vol. 10, 1706, 2020.
- [59] Fu, C., Uddin, M., Zhang, C., Computational Analyses of the Effects of Wind Tunnel Ground Simulation and Blockage Ratio on the Aerodynamic Prediction of Flow over a Passenger Vehicle. *Vehicles* Vol, 2, pp. 318-341, 2020.
- [60] Energy Follower, 2022, Energy Follower (Accessed at: <https://energyfollower.com/types-of-wind-turbines/> [Accessed: 10-Mar-2022])
- [61] Kasinadhuni, C., Experimental Investigation of Wind Loading on a Ducted Wind Turbine, PhD Thesis, 2022.
- [62] Tumewu, Y., Petrone, C., Sivaselvan, M., Numerical Simulation of the Influence of Platform Pitch Motion on Power Generation Steadiness in Floating Offshore Wind Turbines. *International Journal of Environmental Science & Sustainable Development*, Vol. 1(2): 9, 2017.

- [63] Park, J., Jung, H., J., Lee, S.-W.; Park, J., A New Building-Integrated Wind Turbine System Utilizing the Building. *Energies*, 8, pp. 11846-11870, 2015.
- [64] Stanciu, M., D., The design of a test bench for wind blades bending with small dimension, 2015.
- [65] Sugathapala, T., M., Boteju, S. Withanage, P., B., Wijewardane, S., Aerodynamic modeling of simplified wind turbine rotors targeting small-scale applications in Sri Lanka. *Energy for Sustainable Development*, Vol. 59, pp. 71–82, 2020.
- [66] Abdelsalam, A., M., El-Askary, W., A., Kotb, M., A., Sakr, I., M., Experimental study on small scale horizontal axis wind turbine of analytically-optimized blade with linearized chord twist angle profile. *Energy*, Vol. 216, p. 119304, 2021.
- [67] Lee, M., Shiah, Y., C., Bai, C., Experiments and numerical simulations of the rotor-blade performance for a small-scale horizontal axis wind turbine. *Journal of Wind Engineering and Industrial Aerodynamics*, Vol. 149, pp. 17-29, 2016.
- [68] Rahgozar, S., Pourrajabian, A., Kazmi, S., A., A., Kazmi, S., M., R., Performance analysis of a small horizontal axis wind turbine under the use of linear/nonlinear distributions for the chord and twist angle. *Energy for Sustainable Development*, Vol. 58, pp. 42–49, 2020.
- [69] Pourrajabian, A., Nazmi Afshar, P., A., Ahmadizadeh, M., Wood, D., Aero-structural design and optimization of a small wind turbine blade. *Renewable Energy*, Vol. 87, pp. 837–848, 2016.
- [70] Gupta, R., K., Warudkar, V., Purohit, R., Singh Rajpurohit, S., Modeling and aerodynamic analysis of small scale, mixed airfoil horizontal axis wind turbine blade, *Materials Today Proceedings*, Vol. 4, No. 4, pp. 5370–5384, 2017.
- [71] Hasan, M., El-Shahat, A., Rahman, M., Performance investigation of three combined airfoils bladed small scale horizontal axis wind turbine by BEM and CFD analysis,” *Journal of Power and Energy Engineering*, Vol. 05, No. 05, pp. 14–27, 2017.
- [72] Muhsen, H., Al-Kouz, W., Khan, W., Small wind turbine blade design and optimization. *Symmetry*, Vol. 12, No. 1, p. 18, 2019.
- [73] Pholdee, N., Bureerat, S., Nuantong, W., Kriging surrogate-based genetic algorithm optimization for blade design of a horizontal Axis Wind turbine.

- Computer Modeling in Engineering and Sciences*, Vol. 126, No. 1, pp. 261–273, 2021.
- [74] Singh, R., Ahmed, M., R., Blade design and performance testing of a small wind turbine rotor for low wind speed applications. *Renewable Energy*, Vol. 50, pp. 812-819, 2013.
- [75] Volkmer, K., Kaufmann, N., Carolus, T., Mitigation of the aerodynamic noise of small axial wind turbines - methods and experimental validation. *Journal of Sound and Vibration*, Vol.500, p. 116027, 2021.
- [76] Ghorani, M., M., Karimi, B., Mirghavami, S., M., Saboohi, Z., A numerical study on the feasibility of electricity production using an optimized wind delivery system (Invelox) integrated with a Horizontal axis wind turbine (HAWT). *Energy*, Vol. 268, p. 126643, 2023.
- [77] Dar, A., Armengol, G., Porté-Agel, F., An experimental investigation of a roof-mounted horizontal-axis wind turbine in an idealized urban environment. *Renewable Energy*, Vol. 193, No.9, 2022.
- [78] Ali, M., H., Experimental Comparison Study for Savonius Wind Turbine of Two & Three Blades at Low Wind Speed. *International Journal of Modern Engineering Research (IJMER)*, Vol. 3, No. 5, pp. 2978-2986, 2013.
- [79] Ragheb, M., Vertical Axis Wind Turbines. *Scientific Research*, 2015.
- [80] Windside, 2023, (Accessed at <https://windside.com/products/ws-4/>), [Accessed: 12 January 2023].
- [81] Kumara, E., A., D., Hettiarachchi, N., Jayathilake, R.,. Review Paper: Overview of the Vertical Axis Wind Turbines. *International Journal of Scientific Research and Innovative Technology*, Vol. 4, pp. 2313-3759, 2017.
- [82] Kuang, L., Su, J., Chen, Y., Han, Z., Zhou, D., Zhang, K., Zhao, Y., Bao, Y., Wind-capture-accelerate device for performance improvement of vertical-axis wind turbines: External diffuser system. *Energy*, Vol. 239, Part B, 2022.
- [83] Li, S., Li, Y., Yang, C., Wang, Q., Zhao, B., Li, D., Zhao, R., Ren, T., Zheng, X., Gao, Z., Xu, W., Experimental investigation of solidity and other characteristics on dual vertical axis wind turbines in an urban environment. *Energy Conversion and Management*, Vol. 229, 2021.

- [84] Jooss, Y., Rønning, E., B., Hearst, R., J., Bracchi, T., Influence of position and wind direction on the performance of a roof mounted vertical axis wind turbine. *Journal of Wind Engineering and Industrial Aerodynamics*, Vol. 230, p. 105177, 2022.
- [85] Zamre, P., Lutz, T., CFD analysis of a Darrieus Vertical-Axis Wind turbine installation on the rooftop of a buildings under turbulent inflow conditions. *Wind Energy Science*, 2021.
- [86] Allard, M., A., Performance and Wake Analysis of a Darrieus Wind Turbine on the Roof of a Building using CFD. *Masters thesis*, Concordia University, 2020.
- [87] Allard, M., A., Paraschivoiu, M., Power enhancement CFD based study of Darius wind turbine via roof corner placement. *Journal of Renewable and Sustainable Energy*, Vol.14, p. 033301, 2022.
- [88] Chen, T., Y., Hung, C., W., Liao., Y., T., Experimental study on aerodynamics of micro-wind turbines with large-tip non-twisted blades. *Journal of Mechanics*, Vol. 29, No. 3, pp. 15–20, 2013.
- [89] Chong, W., T., Yip, S., Y., Fazlizan, A., Poh, S., C., Hew, W., P., Tan, E.,P., Lim, T.,S., Design of an exhaust air energy recovery wind turbine generator for energy conservation in commercial buildings. *Renewable Energy*, Vol. 67, pp. 252-256, 2014.
- [90] Sridhar, S., Zuber, M., Shenoy S., B., Kumar, A., Ng, Eddie Y.K., Radhakrishnan, J., Aerodynamic comparison of slotted and non-slotted diffuser casings for Diffuser Augmented Wind Turbines (DAWT). *Renewable and Sustainable Energy Reviews*, Vol. 161, 2022.
- [91] Krishnan, A., Paraschivoiu, M., 3D analysis of building mounted VAWT with diffuser shaped shroud. *Sustainable Cities and Society*, Vol. 27, pp.160-166, 2016.
- [92] Bhakare, A., Ranka, P., Telkapalliwar, A., Design and Analysis of Ducted Wind Turbine for Rooftop installation. *Thesis*, 2018
- [93] Agha, A., The integration of Diffuser Augmented Wind Turbines (DAWT) into the built environment. *Doctoral Thesis*, 2018.
- [94] Dilimulati, A., Stathopoulos, T., Paraschivoiu, M., Wind turbine designs for urban applications: A case study of shrouded diffuser casing for turbines. *Journal of Wind Engineering and Industrial Aerodynamics*, Vol. 175, 2018, pp. 179-192.

- [95] Abu-Thuraia, H., Aygun, C., Paraschivoiu, M., Allard, M., A., Computational fluid dynamic analysis of roof-mounted vertical-axis wind turbine with diffuser shroud, flange, and vanes. *Transactions of the Canadian Society for Mechanical Engineering*, Vol. 42, No. 4, pp. 404-415, 2018.
- [96] Chong, W., Muzammil, W., K., Wong, K., Wang, C., Gwani, M., Chu, Y., Poh, S., Cross axis wind turbine: Pushing the limit of wind turbine technology with complementary design. *Applied Energy*, Vol. 207, pp. 78-95, 2017.
- [97] Chong, W., T., Wang, X., H., Wong, K., H., Mojumder, J., C., Poh, S., C., Saw, L., H., Lai, S., H., Performance assessment of a hybrid solar-wind-rain eco-roof system for buildings. *Energy and Buildings*, Vol. 127, pp. 1028-1042, 2016.
- [98] Moreno-Armendáriz, M., A., Duchanoy, C., A., Calvo, H., Ibarra-Ontiveros, E., Salcedo-Castañeda, J., S., Ayala-Canseco, M., García, D. Wind Booster Optimization for On-Site Energy Generation Using Vertical-Axis Wind Turbines. *Sensors*, Vol. 21, p. 4775, 2021.
- [99] Wang, W., Huang, J., Yao, Z., Cut-corner prism piezoelectric energy harvester based on galloping enhancement mechanism. *Energy Reports*, Vol. 7, pp.6366-6374, 2021.
- [100] Yang, Y., Zhao, L., Tang, L., Comparative study of tip cross-sections for efficient galloping energy harvesting. *Applied Physics Letters*, Vol. 102, 064105, 2013.
- [101] Zhao, D., Hu, X., Tan, T., Yan, Z., Zhang, W., Piezoelectric galloping energy harvesting enhanced by topological equivalent aerodynamic design. *Energy Conversion and Management*, Vol. 222, 2020.
- [102] Le, D., Kwon, S. D., Design and Experiments of a Galloping-Based Wind Energy Harvester Using Quadruple Halbach Arrays. *Energies*. Vol. 14, pp. 6094, 2021.
- [103] Zhang, L., B., Dai, H., L., Abdelkefi, A., Lin, S.,X., Wang, L., Theoretical modeling, wind tunnel measurements, and realistic environment testing of galloping-based electromagnetic energy harvesters. *Applied Energy*, Vol. 254, p. 113737, 2019.
- [104] Lim, Y., Y., Padilla, R., V., Unger, A., Barraza, R., Thabet, A., M., Izadgoshasb, I., A self-tunable wind energy harvester utilising a piezoelectric cantilever beam

- with bluff body under transverse galloping for field deployment. *Energy Conversion and Management*, Vol. 245, p. 114559, 2021.
- [105] Aquino, A., Calautit, J. K., Hughes, B., Urban Integration of Aeroelastic Belt for Low-Energy Wind Harvesting, *Energy Procedia*, Vol. 105, pp.738-743, 2017.
- [106] Zhang, C., He, X. F., Li, S. Y., Cheng, Y. Q., Rao, Y., A Wind Energy Powered Wireless Temperature Sensor Node. *Sensors*, Vol. 15, pp. 5020-5031, 2015.
- [107] Chawdhury, S., Morgenthal G., Numerical simulations of aeroelastic instabilities to optimize the performance of flutter-based electromagnetic energy harvesters. *Journal of Intelligent Material Systems and Structures*, Vol. 29, No. 4, pp. 479-495, 2018.
- [108] Shan, X., Tian, H., Cao, H., Feng, J., Xie, T., Experimental Investigation on a Novel Airfoil-Based Piezoelectric Energy Harvester for Aeroelastic Vibration. *Micromachines* Vol. 11, p. 725, 2020.
- [109] Bo, F., Jiwen, F., Jiuchun, Z., Chong, L., Jia, W., Mingming, L., Bionic flutter wing piezoelectric-electromagnetic composite energy harvesting system. *Energy Conversion and Management*, Vol. 271, p. 116319, 2022.
- [110] Ramírez, J., M., A coupled formulation of fluid-structure interaction and piezoelectricity for modeling multi-body energy harvester from vortex-induced vibrations. *Energy Conversion and Management*, Vol. 249, p.114852, 2021.
- [111] De Sousa, V., C., and Junior, D., C., Airfoil-based piezoelectric energy harvesting by exploiting the pseudoelastic hysteresis of shape memory alloy springs, *Smart Materials and Structures*, Vol. 24, No. 12, 2015.
- [112] Perez, M., Boisseau, S., Gasnier, P., Willemin, J., Reboud, J. L., An electret-based aeroelastic flutter energy harvester, *Smart Materials and Structures*, Vol. 24, 035004, 2015.
- [113] Yin, P., Tang, L., Li, Z., Guo, H., Aw, K., C., Circuit representation, experiment and analysis of parallel-cell triboelectric nanogenerator. *Energy Conversion and Management*, Vol. 278, 2023.
- [114] Lee, Y., J., Qi, Y., Zhou, G., Lua, K., B., Vortex-induced vibration wind energy harvesting by piezoelectric MEMS device in formation. *Scientific Reports* Vol. 9, No. 20404, 2019.

- [115] Jin, Z., Li, G., Wang, J., Zhang, Z., Design, Modeling, and Experiments of the Vortex-Induced Vibration Piezoelectric Energy Harvester with Bionic Attachments, *Complexity*, pp. 13, 2019.
- [116] Hu, Y., Yang, B., Chen, X., Wang, X., Liu, J., Modeling and experimental study of a piezoelectric energy harvester from vortex shedding-induced vibration, *Energy Conversion and Management*, Vol. 162, pp. 145-158, 2018.
- [117] Zhang, L., Meng, B., Tian, Y., Meng, X., Lin, X., He, Y., Xing, C., Dai, H., Wang, L., Vortex-induced vibration triboelectric nanogenerator for low speed wind energy harvesting. *Nano Energy*, Vol. 95, p.107029, 2022.
- [118] Vortex Bladeless, 2022, (Accessed at: <https://vortexbladeless.com/technology/> [Accessed: 10-May-2022]).
- [119] Hemida, H., Šarkić Glumac, A., Vita, G., Kostadinović Vranešević, K., Höffer, R., On the Flow over High-rise Building for Wind Energy Harvesting: An Experimental Investigation of Wind Speed and Surface Pressure. *Applied Science.*, Vol. 10, p. 5283, 2020.
- [120] Mohamed, K., Prakash, S., A Systematic Review on Wind Energy Resources Forecasting by Neural Network. *Proceedings of the 2020 5th IEEE International Conference on Recent Advances and Innovations in Engineering, Institute of Electrical and Electronics Engineers Inc*, 2020.
- [121] Wu, Z., Luo, G., Yang, Z., Guo, Y., Li, K., Xue, Y., A comprehensive review on deep learning approaches in wind forecasting applications. *CAAI Transactions on Intelligence Technology*, Vol. 7, No. 2, pp. 129– 143, 2022.
- [122] Calautit, K., Aquino, A., Calautit, J., K., Nejat, P., Jomehzadeh, F.; Hughes, B.R. A Review of Numerical Modelling of Multi-Scale Wind Turbines and Their Environment. *Computation*, Vol. 6, No. 1, p. 24, 2018.
- [123] Lu, L., Sun, K., Wind power evaluation and utilization over a reference high-rise building in urban area. *Energy and Buildings*, Vol. 68, Part A, pp. 339-350, 2014.
- [124] Weekes, S., M., *Small-scale wind energy: methods for wind resource assessment. Integrated Doctoral and Master thesis, University of Leeds, 2014.*

- [125] Bashirzadeh, A., Whale, J., Lyon, T., Urmee, T., Performance and safety of rooftop wind turbines: Use of CFD to gain insight into inflow conditions. *Renewable Energy*, 67, 2013.
- [126] Arteaga-López, E., Ángeles-Camacho, C., Bañuelos-Ruedas, F., Advanced methodology for feasibility studies on building-mounted wind turbines installation in urban environment: Applying CFD analysis, *Energy*, Vol. 167, pp. 181-188, 2019.
- [127] Heo, Y., G., Choi, N., K., Choi, K., H., Ji, H., S., Kim, K., C., CFD study on aerodynamic power output of a 110 kW building augmented wind turbine. *Energy and Buildings*, Vol. 129, pp. 162–173, 2016.
- [128] Tabrizi, A., B., Whale, J., Lyons, T., Urmee, T., Performance and safety of rooftop wind turbines: Use of CFD to gain insight into inflow conditions. *Renewable Energy* Vol. 67, pp. 242–251, 2014.
- [129] Larin, P., Paraschivoiu, M., Aygun, C., CFD based synergistic analysis of wind turbines for roof mounted integration. *Journal of Wind Engineering and Industrial Aerodynamics*, Vol. 156, pp. 1-13, 2016.
- [130] Elbakheit, A., R., Effect of turbine resistance and positioning on performance of Aerofoil wing building augmented wind energy generation. *Energy and Buildings*, Vol. 174, pp. 365-371, 2018.
- [131] Bayoumi, M., Fink, D., Hausladen, G., Extending the feasibility of high-rise façade augmented wind turbines. *Energy and Buildings*, Vol. 60, pp. 12-19, 2013.
- [132] Chaudhry, H., N., Calautit, J., K., S., Hughes, B., R., The influence of structural morphology on the efficiency of building integrated wind turbines (BIWT). *AIMS Energy*, Vol. 2, pp. 219–236, 2014.
- [133] Petković, D., Shamshirband, S., Čojbašić, Z., Nikolić, V., Anuar, N., B., Sabri, A., Q., M., Akib, S., Adaptive neuro-fuzzy estimation of building augmentation of wind turbine power. *Computers & Fluids*, Vol. 97, pp.188-194, 2014.
- [134] Toja-Silva, F., Peralta, C., Lopez-Garcia, O., Navarro, J., Cruz, I. Roof region dependent wind potential assessment with different RANS turbulence models. *Journal of Wind Engineering and Industrial Aerodynamics*, Vol. 142, pp. 258–271, 2015.

- [135] Wang, B., Cot, L., D., Adolphe, L., Geoffroy, S., Morchain, J., Estimation of wind energy over roof of two perpendicular buildings. *Energy and Buildings*, 2015, Vol. 88, pp. 57–67.
- [136] Veena, K., Asha, V., Shameem, C., A., Venkatesh, T.N. CFD analysis for siting of wind turbines on high-rise buildings. *Journal of Physics: Conference Series*, Vol. 822, p. 012013, 2017.
- [137] Kono, T., Kogaki, T., Kiwata, T., Numerical Investigation of Wind Conditions for Roof-Mounted Wind Turbines: Effects of Wind Direction and Horizontal Aspect Ratio of a High-Rise Cuboid Building. *Energies*, Vol. 9(11), p. 907, 2016.
- [138] Nishimura, A., Ito, T., Murata, J., Ando, T., Kamada, Y., Hirota, M., Kolhe, M., Wind Turbine Power Output Assessment in Built Environment. *Smart Grid and Renewable Energy*, Vol. 4, pp. 1-10, 2013.
- [139] Sun, H., Miniature Wind Energy Harvesters. *University of Southampton, PhD Thesis*, 2017.
- [140] Aljadiri, R., T., Modelling and Design of Electrostatic Based Wind Energy Harvester. *PhD Thesis*, 2014.
- [141] Romanic, D., Rasouli, A., Hangan, H., Wind Resource Assessment in Complex Urban Environment. *Wind Engineering*, Vol 39, pp. 193-212, 2015.
- [142] Khlaifat, N., Altaee, A., Zhou, J., Huang, Y., Braytee, A., Optimization of a Small Wind Turbine for a Rural Area: A Case Study of Deniliquin, New South Wales, Australia. *Energies*, Vol. 13, 2020.
- [143] Abu-Zidan, Y., Mendis, P., Gunawardena, T., Impact of atmospheric boundary layer inhomogeneity in CFD simulations of tall buildings. *Heliyon*, Vol. 6(7), 04274, 2020.
- [144] Dagneu, A., Bitsuamlak, G. Computational evaluation of wind loads on buildings: A review, *Wind and Structures*, Vol. 16(6), 2013.
- [145] Blocken, B., Stathopoulos, T., Carmeliet, J., CFD simulation of the atmospheric boundary layer: wall function problems. *Atmospheric Environment*, Vol. 41(2), pp. 238-252, 2007.
- [146] Arumugam, P., Ramalingam, V., Bhaganagar, K., A pathway towards sustainable development of small capacity horizontal axis wind turbines –

- Identification of influencing design parameters & their role on performance analysis, *Sustainable Energy Technologies and Assessments*, Vol. 44, 2021.
- [147] Gwani, M., Ibrahim, A., Muhammad, U., Joshua, B., W., Design and Testing of Building Integrated Hybrid Vertical Axis Wind Turbine. *Journal of Electrical and Electronic Engineering*, Vol. 9(3), pp. 69-77, 2021.
- [148] Emejeamara, F., C., *Urban Wind Resource Assessment: Predicting the Turbulence Intensity, Excess Energy Available and Performance of Roof Mounted Wind Turbines in a Built Environments*. PhD thesis, University of Leeds, 2017.
- [149] Siddiqui, M., S., Khalid, M., H., Zahoor, R., Butt, F., S., Saeed, M., Badar, A., W., A numerical investigation to analyze effect of turbulence and ground clearance on the performance of a roof top vertical-axis wind turbine. *Renewable Energy*, Vol. 164, pp. 978-989, 2021.
- [150] Dunbar, A., Craven, B., Paterson, E., Development and validation of a tightly coupled CFD/6-DOF solver for simulating floating offshore wind turbine platforms, *Ocean Engineering*, Vol. 110, pp. 98-105, 2015.
- [151] Wicaksono, H., Hadi, S., Pranoto, B., Fakhrudin, M., Initial Rotation Characteristic Investigation of a Hybrid Savonius - Darrieus Wind Turbine using 6 DOF Computational Fluid Dynamics, *Mekanika: Majalah Ilmiah Mekanika*, Vol. 20, No. 1, 2021.
- [152] Tran, Thanhtoan, Donghyun Kim, and Jinseop Song. 2014. "Computational Fluid Dynamic Analysis of a Floating Offshore Wind Turbine Experiencing Platform Pitching Motion" *Energies* 7, No. 8, pp. 5011-5026.
- [153] Cheng, P., Huang, Y., Wan, D. A numerical model for fully coupled aerohydrodynamic analysis of floating offshore wind turbine, *Ocean Engineering*, Vol. 173, pp. 183-196, 2019.
- [154] Wang, B., Li, Y., Gao, S., Kanmin, S., Hu, Z., Zheng, X., Motion characteristics and aero-elastic responses of floating offshore wind turbine under coupling action of waves and winds, *Frontiers in Environmental Science*, 2022.
- [155] Ayhan, D., Sağlam, S., A technical review of building-mounted wind power systems and a sample simulation model. *Renewable and Sustainable Energy Reviews*, Vol. 16(1), pp. 1040-1049, 2012.

- [156] Walker, S., L., Building mounted wind turbines and their suitability for the urban scale—A review of methods of estimating urban wind resource. *Energy and Buildings*, Vol. 43(8), pp. 1852-1862, 2011.
- [157] Reja, R., K., Amin, R., Tasneem, Z., Ali, M., F., Islam, M., R., Saha, D., K., Badal, F., R., Ahamed, M., H., Moyeen, S., I., Das, S., K., A review of the evaluation of urban wind resources: challenges and perspectives. *Energy and Buildings*, Vol. 257(2), p. 111781, 2022.
- [158] Sanderasagran, A. Azizuddin, A., Oumer, A. Comparative CFD power extraction analysis of novel nature inspired vertical axis wind turbines Comparative CFD power extraction analysis of novel nature inspired vertical axis wind turbines. *IOP Conference Series Materials Science and Engineering*, 863, 2020.
- [159] Zhu, H., Zhou, D., Han, Z., Ma, J., Bao, Y., Fu, S., The Performance Assessment of a Semisubmersible Platform Subjected to Wind and Waves by a CFD/6-DOF Approach. Flow-induced Vibration Control and Energy Harvesting. *Shock and Vibration*, Vol. 2020, pp. 1-16, 2020.
- [160] Dong, L., Xie, P., Zhu, J., Wang, C., Zhang, Po., Study on the power extraction performance of a flapping airfoil power generator using jet flow method. *Journal of the Brazilian Society of Mechanical Sciences and Engineering*. Vol. 45, 2023.
- [161] Simscale, 2023, Accessed at <https://www.simscale.com/docs/simwiki/cfd-computational-fluid-dynamics/what-is-cfd-computational-fluid-dynamics/>. [Accessed on Jan 2023].
- [162] ANSYS, 2021 (Accessed at <https://www.afs.enea.it/project/neptunius/docs/fluent/html/th/node41.htm>. [Accessed on 10-Jan 2021.
- [163] Wilcox, D., Turbulence Modeling in CFD, *DCW Industries, Incorporated, Third Edition*, 2006.
- [164] Blazek, J., Computational Fluid Dynamics: Principles and Applications. *Elsevier Science*, 2005.
- [165] Moureau, V., Lartigue, G., Sommerer, Y., Angelberger, C., Colin, O., Poinot, T., Numerical methods for unsteady compressible multi-component reacting flows

- on fixed and moving grids. *Journal of Computational Physics*, Vol. 202(2), 2005, pp. 710-736.
- [166] Asyikin, M., H., CFD Simulation of Vortex Induced Vibration of a Cylindrical Structure, Thesis, Norwegian University of Science and Technology, 2012.
- [167] Patel, M., Henderson, A., On the modeling of a floating offshore wind turbine. *Wind Energy*, Vol. 6 pp. 53-76, 2003.
- [168] Tan, J., H., C., Magee, A., Kim, J., W., Teng, Y., J., Zukni, N., A., CFD Simulation for Vortex Induced Motions of a Multi-Column Floating Platform. *Proceedings of the ASME 2013 32nd International Conference on Ocean, Offshore and Arctic Engineering*, Vol. 7, 2013.
- [169] Xu, S., Gao, Z., Xue, W., CFD database method for roll response of damaged ship during quasi-steady flooding in beam waves. *Applied Ocean Research*, Vol. 126, p.103282, 2022.
- [170] Kim, J., W., Magee, A., Guan, K., Y., H., CFD Simulation of Flow-Induced Motions of a Multi-Column Floating Platform. *Proceedings of the ASME 2011 30th International Conference on Ocean, Offshore and Arctic Engineering*. Vol. 7, pp. 319-326, 2011.
- [171] Yasuda, T., Fukui, K., Matsuo, K., Minagawa, H., Kurimoto, R., Effect of the Reynolds Number on the Performance of a NACA0012 Wing with Leading Edge Protuberance at Low Reynolds Numbers. *Flow Turbulence Combust*, Vol. 102, pp. 435–455, 2019.
- [172] Anyoji, M. High-performance airfoil with low reynolds-number dependence on aerodynamic characteristics. *Fluid Mechanics research International Journal*. 3. 76-80. 2019.
- [173] Izquierdo, D., O., D., Dos Santos, C., R., Marques, F., D., Nonlinear oscillations of a low Reynolds SD7003 airfoil at higher angles of attack, *Proceedings of Isma*, 2020.
- [174] Carta, M., Putzu, R., Ghisu, T., A comparison of plunging- and pitching-induced deep dynamic stall on an SD7003 airfoil using URANS and LES simulations, *Aerospace Science and Technology*, Vol. 121, 2022.

- [175] Tominaga, Y., Stathopoulos, T., Numerical simulation of dispersion around an isolated cubic building: Model evaluation of RANS and LES. *Building and Environment*, Vol. 45(10), pp. 2231-2239, 2010.
- [176] Negi, P., S., Hanifi, A., Henningson, D., S., On the onset of aeroelastic pitch-oscillations of a NACA0012 wing at transitional Reynolds numbers, *Journal of Fluids and Structures*, Vol. 105, 2021.
- [177] Jamil, M., Javed, A., Shah, S., I., A., Mansoor, M., Hameed, A., Djidjeli, K., Performance Analysis of Flapping Foil Flow Energy Harvester Mounted on Piezoelectric Transducer using Meshfree Particle Method. *Journal of Applied Fluid Mechanics*, 13 (6), pp. 1859-1872, 2020.
- [178] Pantua, C., A., J., Calautit, J., K., Wu, Y., A fluid-structure interaction (FSI) and energy generation modelling for roof mounted renewable energy installations in buildings for extreme weather and typhoon resilience. *Renewable Energy*, Vol. 160, pp. 770-787, 2020.
- [179] Rostamzadeh, N., Kelso, R., Dally, B., Tian, Z., An Experimental and Computational Study of Flow over a NACA 0021 Airfoil with Wavy Leading Edge Modification, *Conference: 18th Australasian Fluid Mechanics Conference At: Launceston*, 2012.
- [180] Maalouly, M., Souaiby, M., ElCheikh, A., Issa, J., S., Elkhoury, M., Transient analysis of H-type Vertical Axis Wind Turbines using CFD. *Energy Reports*, 8, pp. 4570-4588, 2022.
- [181] Jaohindy, P., McTavish, S., Garde, F., Bastide, A., An analysis of the transient forces acting on Savonius rotors with different aspect ratios. *Renewable Energy*, Vol. 55, pp. 286-295, 2013.
- [182] Abdizadeh, G., Farokhinejad, M., Ghasemloo, S., Numerical investigation on the aerodynamic efficiency of bio-inspired corrugated and cambered airfoils in ground effect. *Scientific Reports*, Vol.12(1), 19117, 2022.
- [183] Gao, Y., Xie, L., Lam, T., L., A Novel and More Efficient Oscillating Foil for Wave-Driven Unmanned Surface Vehicles. *Frontiers in Robotics AI.*, Vol. 9, 759200, 2022.
- [184] Menon, K., Mittal, R., Flow physics and dynamics of flow-induced 1 pitch oscillations of an airfoil. *Journal of Fluid Mechanics*, Vol. 877, pp.582-613, 2019.

- [185] Sazesh, S., Shams, S., Nonlinear aeroelastic analysis of an airfoil with control surface free-play using stochastic approach. *Journal of Fluids and Structures*, 72, pp. 114-126, 2017.
- [186] Rad, M., P., Khoshnevis, A., B., Experimental investigation of flow structure over pitching airfoil in the wake of circular cylinder. *Ocean Engineering*, 284, p. 115103, 2023.
- [187] Roothaan, S., Williams, C., Guerrero, S., Acioli, P., Optimization of Small Scale Wind Turbine in Urban Areas, *Conference: Society for Advancement of Hispanics/Chicanos and Native Americans in Science National Conference*, 2012.
- [188] Batay, S., Baidullayeva, A., Zhao, Y., Wei, D., Baigarina, A., Sarsenov, E., Shabdan, Y., Aerostructural Design Optimization of Wind Turbine Blades. *Processes*, Vol. 12, p. 22, 2024.
- [189] Hernandez-Estrada, E., Lastres-Danguillecourt, O., Robles-Ocampo, J., Lopez-Lopez, A., Sevilla-Camacho, P., Perez-Sariñana, B., Dorrego-Portela, J., Considerations for the structural analysis and design of wind turbine towers: A review. *Renewable and Sustainable Energy Reviews*, Vol. 137, p. 110447, 2021.
- [190] Copernicus Marine Service (CMEMS) (Accessed at https://data.marine.copernicus.eu/viewer/expert?view=dataset&dataset=WIND_GLO_PHY_L4_NRT_012_004). [Accessed: 12 March 2023].
- [191] Google Earth V 10.65.1.2. (December 14, 2015). Basilan, Philippines. 6°25'48"N 121°08'43"E, elevation 610 m. Data SIO, NOAA, U.S. Navy, NGA, GEBCO, Maxar Technologies, Airbus. <http://www.google.com/earth/index.html> [July 1, 2024].
- [192] Google Earth V 10.65.1.2. (December 14, 2015). Basilan, Philippines. 6°25'42"N 121°59'16"E, elevation 97 m. Maxar Technologies, Data SIO, NOAA, U.S. Navy, NGA, GEBCO, TerraMetrics, Landsat / Copernicus. <http://www.google.com/earth/index.html> [July 1, 2024].
- [193] Global Wind Atlas, 2024, Assessed at <https://globalwindatlas.info/en>, Accessed on: July 2024.
- [194] UIUC Airfoil Coordinates Database - Airfoil Tools, 2021, (Accessed at <http://airfoiltools.com/airfoil/details?airfoil=n0012-il>) [Accessed: 10-Jan 2021].

- [195] Willis, D., J., Niezrecki, C., Kuchma, D., Hines, E., Arwade, S., R., Barthelmie, R., J., DiPaola, M., Drane, P., J., Hansen, C., J., Inalpolat, M., Mack, J., H., Myers, A. T., Rotea, M. Wind energy research: State-of-the-art and future research directions, *Renewable Energy*, Vol. 125, pp. 133-154, 2018.
- [196] Alrawashdeh, H., Stathopoulos, T., Wind loads on solar panels mounted on flat roofs: Effect of geometric scale. *Journal of Wind Engineering and Industrial Aerodynamics*, 206, p. 104339, 2020.
- [197] Yu-Hsien, L., Ahmad, H. Transient analysis of the slamming wave load on an offshore wind turbine foundation generated by different types of breaking waves. *Journal of Renewable and Sustainable Energy*, 14, p. 053302, 2022.
- [198] Abdessemed, C., Yao, Y., Abdessalem, B., Narayan, P., Morphing airfoils analysis using dynamic meshing. *International Journal of Numerical Methods for Heat & Fluid Flow*, 5, (2018).
- [199] Yoshie, R., Mochida, A., Tominaga, Y., Kataoka, H., Harimoto, K., Nozu, T., Shirasawa, T. Cooperative project for CFD prediction of pedestrian wind environment in the Architectural Institute of Japan. *Journal of Wind Engineering and Industrial Aerodynamics*, Vol. 95(9–11), pp. 1551-1578, 2007.
- [200] Werner, H., Wengle, H. Large eddy simulation of turbulent flow over and around a cube in plane channel. *Proceedings of 8th symposium on turbulent shear flows*, p. 155–168, 1993.
- [201] Ishihara, T., Hibi, K. Turbulent measurements of the flow field around a high-rise building. *Journal of Wind Engineering*. Vol. 76. 55-64, 1998.
- [202] Meng, Y. Hibi, K. Turbulent measurements of the flow field around a high-rise building. *Wind Engineers, JAWE*, Vol. 76, pp. 55-64, 1998.
- [203] Mathai, V., Neut, M., Poel, E., Sun, C., Translational and rotational dynamics of a large buoyant sphere in turbulence. *Experiments in Fluids*. Vol. 57, 2016.
- [204] Meyer, C., Byron, M., Variano, E. Rotational Diffusion of Particles in Turbulence. *Limnology and Oceanography: Fluids and Environments*, pp. 89-102, 2013.
- [205] Sicot, C., Devinant, P., Loyer, S. Hureau, J., Rotational and turbulence effects on a wind turbine blade. Investigation of the stall mechanisms. *Journal of Wind Engineering and Industrial Aerodynamics*, Vol 96, pp. 1320-1331.

- [206] Boudis, A., Benzaoui, A., Oualli, H., Guerri, O., Bayeul-Lainé, A., C., Coutier Delgosha, O, Energy Extraction Performance Improvement of a Flapping Foil by the Use of Combined Foil. *Journal of Applied Fluid Mechanics*, Vol 11(6), 1651-1663, 2018.
- [207] Xiao, Q., Zhu, Q., A review on flow energy harvesters based on flapping foils, *Journal of Fluids and Structures*, Vol. 46, pp. 174-191, 2014.
- [208] Xing, F., Mohotti, D., Chauhan, K., Study on localised wind pressure development in gable roof buildings having different roof pitches with experiments, RANS and LES simulation models. *Building and Environment*, Vol. 143. 240-257, 2018.
- [209] Al-Chalabi, R., Elshaer, A, Aerodynamic mitigation of low-rise building with complex roof geometry. *Frontiers in Built Environment*, Vol. 9, 2023.
- [210] Quan, Y., Tamura, Y., Matsui, M., Mean Wind Pressure Coefficients on Surfaces of Gable-Roofed Low-Rise Buildings. *Advances in Structural Engineering*, Vol.10(3), pp. 259-271, 2007.
- [211] Katrick Technologies, 2023, (Accessed at <https://www.katricktechnologies.com/news/katrick-technologies-completes-alpha-testing>). [Accessed: 28-Dec 2023].
- [212] ANSYS blog, 2023, (Accessed at <https://www.ansys.com/en-gb/blog/katrick-technologies-advances-wind-energy-with-simulation>). [Accessed: 28-Dec 2023].